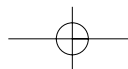
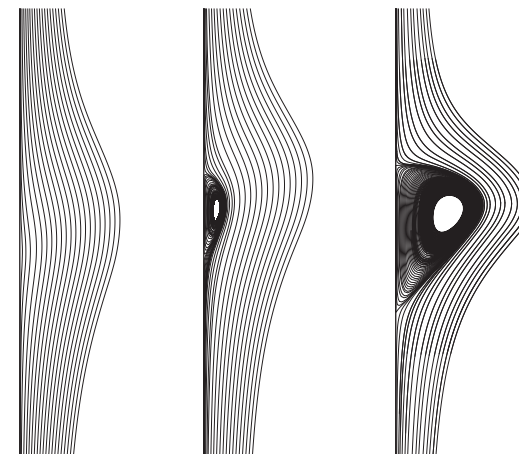




Georg F. Dietze **Flow Separation in Falling Liquid Films**



Flow Separation in Falling Liquid Films



Georg F. Dietze

SV SierkeVerlag

ISBN 13 978-3-86844-259-5



9 783868 442595

Flow Separation in Falling Liquid Films

Von der Fakultät für Maschinenwesen der
Rheinisch-Westfälischen Technischen Hochschule Aachen
zur Erlangung des akademischen Grades eines
Doktors der Ingenieurwissenschaften
genehmigte Dissertation

vorgelegt von

Georg Friedrich Dietze

Berichter: Universitätsprofessor Dr.-Ing. R. Kneer
Universitätsprofessor Dr.-Ing. C. Tropea

Tag der mündlichen Prüfung: 19. April 2010

Bibliografische Information der Deutschen Nationalbibliothek – CIP-Einheitsaufnahme

Die Deutsche Bibliothek verzeichnet diese Publikation in der Deutschen Nationalbibliografie; detaillierte bibliografische Daten sind im Internet über <<http://dnb.ddb.de>> abrufbar.

D 82 (Diss. RWTH Aachen University, 2010)

Georg F. Dietze

Flow Separation in Falling Liquid Films

ISBN 13: 978-3-86844-259-5

© **SV** SierkeVerlag
Am Steinsgraben 19 · 37085 Göttingen
Tel. 0551- 503664-7 · Fax 0551-3894067
www.sierke-verlag.de

Einband: Grafik Sierke Verlag

Das Werk einschließlich aller seiner Teile ist urheberrechtlich geschützt.
Jede Verwertung außerhalb der engen Grenzen des Urheberrechtsgesetzes ist ohne Zustimmung des Verlanges unzulässig und strafbar. Das gilt insbesondere für Vervielfältigungen, Übersetzungen, Mikroverfilmungen und die Einspeicherung und Verarbeitung in elektronischen Systemen.

1. Auflage 2010

Dedicated to my parents, my sister and Kerstin.

“... au lieu de ce grand nombre de préceptes dont la logique est composée, je crus que j’aurais assez des quatre suivants, pourvu que je prisse une ferme et constante résolution de ne manquer pas une seule fois à les observer.”

René Descartes, *Discours de la méthode, Seconde partie*

Abstract

The subject of this matter is flow separation in the capillary wave region of falling liquid films. The discovery of this hitherto unknown phenomenon as well as the elucidation of its governing dynamics represent a basis for the unifying explanation of several as yet unexplained empirical observations in falling liquid films. Further, they constitute a valuable input for the development of wave dynamics models. The study is based on highly resolving experimental and numerical investigations of 2-dimensional laminar falling liquid films with externally excited monochromatic surface waves. In addition, one 3-dimensional numerical simulation was also performed.

Experimentally, an optical test setup was specifically designed to enable the application of standard optical techniques for the measurement of the velocity field in the film cross section as well as the instantaneous local film thickness. Thereby, optical access to the falling liquid film was enabled by matching the refractive indices of working liquid and glass test section. Velocity measurements were performed using Laser Doppler Velocimetry (LDV) and Particle Image Velocimetry (PIV), whereas film thickness measurements were performed with a Confocal Chromatic Imaging (CCI) technique. Resulting experimental data clearly show the existence of a separation eddy at the first capillary minimum preceding a large wave. This capillary separation eddy (CSE) is shown to outgrow the minimal film thickness, assuming an open shape with streamlines ending at the liquid-gas interface. Through systematic variations of the Reynolds number and wave frequency it was established that the separation of large waves, which influences the number, wavelength and amplitude of preceding capillary waves, determines the size of the CSE in its developed state. Thereby, large wave separation (caused either by large Reynolds number values

or small values of the wave frequency) leads to large amplitude capillary waves of small wavelength, causing a large CSE. Decreasing wave separation leads to the gradual reduction and eventual suppression of capillary waves and, as a consequence, the disappearance of the CSE. Further, on the basis of high-speed PIV recordings, the effect of wave dynamics on the liquid phase velocity field at different times in the wave evolution was elucidated. Finally, through the simultaneous measurement of velocity (using LDV) and film thickness (using CCI) time traces it was established that the streamwise velocity component in the residual layer of the film is strongly correlated with the local film thickness. Thereby, streamwise velocity time traces display periodic flow reversal in the capillary wave region, coinciding with the CSE.

Numerical investigations focused on completing the picture established by the experimental data, which were confined to the developed region of the falling liquid film. Therefore, the full Navier-Stokes equations were solved numerically for both the liquid and gaseous phase, using the Volume of Fluid (VOF) method. Numerical results in the developed region of the flow are in good agreement with experimental data both in terms of wave kinematics and velocity field kinematics. On the basis of these data, the spatio-temporal evolution of the CSE, covering its inception, growth and subsequent breakup into the open shape was elucidated. Further, a mechanistic explanation of the dynamics governing these processes was developed. Results show that flow separation in the capillary wave region is caused by an adverse pressure distribution, itself induced by the strong third order deformation (i.e. change in curvature) of the liquid-gas interface there. This deformation acts on the interfacial pressure jump, and thereby the wall pressure distribution, as a result of surface tension forces. It is shown that only the capillary waves, due to their short wavelength and large curvature, impose a wall pressure distribution that satisfies the conditions for flow separation. Furthermore, the effect of Reynolds number and wave frequency on the magnitude of the adverse wall pressure derivative at the first capillary minimum was studied, showing the latter to increase with wave separation, which explains the experimental observations concerning the CSE's size. In a further step, the effect of the CSE on liquid phase scalar transport

was elucidated. Thereby, it was established that this effect is to be understood from a Lagrangian rather than from an Eulerian perspective. Indeed, fluid elements traveling in the residual layer of the film are only temporarily subjected to the streamlines of the CSE as the capillary waves pass over their position, owing to the fact that wave celerity exceeds local fluid velocity. Resulting pathlines are characterized by “loop-” or “hook”-shaped distortions caused by the CSE, which represent convective transport normal to the wall. This convective transport is shown to intensify wall-side heat transfer to the falling liquid film. Moreover, the crosswise distribution of the mixing length, characterizing the pathline distortions, was investigated in greater detail, showing it to increase with wall distance. This results from the associated increase in relative velocity between fluid elements and capillary waves and could explain experimental observations, showing interfacial scalar transfer to be enhanced more significantly by surface waves than wall-side transfer.

Finally, capillary flow separation in falling liquid films with 3-dimensional wave topology was investigated based on a single 3-dimensional simulation. Results show that a 3-dimensional CSE (assuming the form of a vortex tube) arises in front of horseshoe-shaped large wave fronts, its axis following the position of the first capillary minimum. Moreover, the region where large wave fronts interact exhibits several pronounced precursory capillary minima, which are respectively associated with a large open CSE. Further downstream, a checkerboard or herringbone pattern of 3-dimensional capillary interaction takes hold. In this region, strong spanwise flow was observed, which is caused by the same mechanism as the capillary flow separation, i.e. a spanwise pressure derivative resulting from spanwise interfacial distortion. This spanwise flow could cause a strong wave-induced intensification of scalar transfer to 3-dimensional falling liquid films.

Zusammenfassung

Die vorliegende Dissertation befasst sich mit der Strömungsablösung im Kapillarwellenbereich laminarer Rieselfilme. Die Entdeckung dieses bisher unbekanntes Phänomens sowie die Aufklärung des zugrunde liegenden Mechanismus stellen eine Basis für die Erklärung einiger ungeklärter empirischer Beobachtungen in Rieselfilmen dar. Des Weiteren bedeuten sie einen wertvollen Beitrag für die Entwicklung von Modellen zur Beschreibung der Wellendynamik solcher Rieselfilme. Im Rahmen der Dissertation wurden dazu hoch aufgelöste experimentelle und numerische Untersuchungen 2-dimensionaler laminarer Rieselfilme mit monochromatisch aufgeprägten Oberflächenwellen durchgeführt. Zusätzlich wurde eine 3-dimensionale Simulation durchgeführt.

Auf der experimentellen Seite wurde eine optische Messstrecke entwickelt, welche die Anwendung optischer Messtechniken zur Messung des Geschwindigkeitsfeldes im Filmquerschnitt sowie der Filmdicke ermöglicht. Dabei wurde der erforderliche optische Zugang durch Anpassung der Brechungsindizes von Filmflüssigkeit und gläserner Messstrecke gewährleistet. Geschwindigkeitsmessungen wurden mit zwei verschiedenen Messtechniken durchgeführt, nämlich Laser Doppler Velocimetry (LDV) und Particle Image Velocimetry (PIV), wohingegen zur Filmdickenmessung Confocal Chromatic Imaging (CCI) verwendet wurde. Die so erfassten experimentellen Daten zeigen eindeutig die Existenz eines Ablösewirbels im Bereich des ersten kapillaren Minimums stromab einer großen Oberflächenwelle. Die Größe dieses *kapillaren Ablösewirbels* kann dabei die lokale Filmdicke überschreiten, so dass Letzterer eine offene Form annimmt, deren Stromlinien an der Phasengrenze (zwischen Flüssigkeit und Gas) enden. Durch systematische Variation der Reynolds-Zahl und der Wellenfrequenz konnte gezeigt werden, dass die Größe des kapillaren Ablösewirbels im

ausgebildeten Zustand durch den Abstand aufeinander folgender großer Oberflächenwellen bestimmt wird, da diese die Anzahl, Wellenlänge und Amplitude der vorgelagerten Kapillarwellen festlegt. Bei großem Wellenabstand (entweder durch große Werte der Reynolds-Zahl oder kleine Werte der Wellenfrequenz bedingt) entstehen Kapillarwellen mit großer Amplitude und kleiner Wellenlänge, die einen großen Ablösewirbel verursachen. Mit abnehmendem Wellenabstand nimmt die Ausprägung der Kapillarwellen bis hin zu deren Unterdrückung ab, wodurch ebenfalls der kapillare Ablösewirbel verschwindet. Durch Einsatz der PIV-Messtechnik wurde darüber hinaus das Geschwindigkeitsfeld im Querschnitt des Rieselfilms zu unterschiedlichen Zeitpunkten der Wellenentwicklung erfasst. Schließlich konnte durch simultane Geschwindigkeits- (mit LDV) und Filmdickenmessungen (mit CCI) festgestellt werden, dass die Geschwindigkeitskomponente in Hauptströmungsrichtung innerhalb des Residualfilms stark mit der Filmdicke korreliert. Dabei zeigen die zeitlichen Verläufe der Geschwindigkeitskomponente das periodische Auftreten von Rückströmung im Kapillarwellenbereich in Übereinstimmung mit der kapillaren Strömungsablösung.

Die numerischen Untersuchungen konzentrierten sich indes auf die Vervollständigung des durch experimentelle Daten (welche auf den ausgebildeten Bereich des Rieselfilms beschränkt waren) erzeugten Bildes. Dazu wurden die vollständigen Navier-Stokes Gleichungen sowohl in der flüssigen als auch in der gasförmigen Phase unter Verwendung der Volume of Fluid (VOF) Methode gelöst. Die resultierenden numerischen Daten weisen im ausgebildeten Bereich des Rieselfilms eine gute Übereinstimmung mit den entsprechenden experimentellen Daten bzgl. Wellenkinematik und Geschwindigkeitsfeld auf. Auf Grundlage dieser numerischen Daten konnte die zeitlich-örtliche Entwicklung des kapillaren Ablösewirbels von dessen Entstehung über das Wachstum bis zur Ausprägung der ausgebildeten (offenen) Form aufgezeigt werden. Des Weiteren wurde der diesem Entwicklungsprozess zugrunde liegende physikalische Mechanismus aufgeklärt. Demzufolge wird die Strömungsablösung im Kapillarwellenbereich durch eine der Strömung entgegengerichtete starke Druckzunahme verursacht, welche aus der starken Krümmungsänderung der

Phasengrenze in diesem Bereich resultiert. Letztere beeinflusst den durch Oberflächenspannungskräfte verursachten Drucksprung über die Phasengrenze und damit die Druckverteilung auf der Wand. Es konnte dabei gezeigt werden, dass ausschließlich im Kapillarwellenbereich, in Folge der geringen Wellenlänge und großen Amplitude der Kapillarwellen, die Bedingungen für die Strömungsablösung erfüllt werden. Des Weiteren wurde der Einfluss der Reynolds-Zahl und der Wellenfrequenz auf die Zunahme des Wanddruckes im Bereich des ersten kapillaren Minimums untersucht und gezeigt, dass diese mit zunehmendem Wellenabstand ansteigt, wodurch sich die zuvor erwähnten experimentellen Beobachtungen hinsichtlich der Größe des kapillaren Ablösewirbels erklären lassen.

In einem weiteren Schritt wurde der Einfluss der kapillaren Strömungsablösung auf den konvektiven Transport (einer beliebigen skalaren Transportgröße) innerhalb des Rieselfilms untersucht. Dabei wurde erkannt, dass sich dieser Einfluss in einer Lagrangeschen Betrachtungsweise besser verstehen lässt als in einer Eulerschen. In der Tat werden Fluidelemente, die innerhalb des Residualfilms strömen, den Stromlinien des kapillaren Ablösewirbels nur für eine begrenzte Zeit ausgesetzt, während der Kapillarwellenbereich ihre momentane Position überstreicht. Dies resultiert aus der Tatsache, dass die Wellengeschwindigkeit die Strömungsgeschwindigkeit im Residualfilm überschreitet. Die sich ergebenden Bahnlinien weisen charakteristische Auslenkungen in Form einer "Schleufe" bzw. eines "Hakens" auf, welche durch den kapillaren Ablösewirbel verursacht werden und einen konvektiven Transport senkrecht zur Wand darstellen. Es konnte gezeigt werden, dass dieser konvektive Transport den wandseitigen Wärmeübergang im Rieselfilm intensiviert. Des Weiteren wurde der durch die Bahnlinienauslenkungen verursachte Mischungsweg näher untersucht und gezeigt, dass dieser mit dem Wandabstand zunimmt. Dieses Verhalten folgt aus der Abnahme der Relativgeschwindigkeit zwischen Fluidelementen und Kapillarwellen mit zunehmendem Wandabstand und könnte experimentelle Beobachtungen erklären, welche eine stärkere wellenbedingte Intensivierung des Wärmeübergangs an der freien Oberfläche des Rieselfilms im Vergleich zum wandseitigen Wärmeübergang aufweisen.

Abschließend wurde die kapillare Strömungsablösung in Rieselfilmen mit 3-dimensionaler Wellendynamik auf Grundlage einer 3-dimensionalen numerischen Simulation untersucht. Die Ergebnisse zeigen, dass sich ein 3-dimensionaler Ablösewirbel (in Form einer Wirbelröhre) stromab der hufeisenförmigen Fronten großer Wellen, welche die Grenzflächentopologie 3-dimensionaler Rieselfilme kennzeichnen, ausbildet. Die Achse dieses 3-dimensionalen Ablösewirbels folgt dabei der Position des ersten kapillaren Minimums. Außerdem entstehen im Bereich der Interaktion großer Wellen mehrere stark ausgeprägte Kapillarwellen, welche jeweils einen kapillaren Ablösewirbel ausbilden. Weiter stromab entsteht indes ein Schachbrett- bzw. Fischgrätenmuster in Folge der 3-dimensionalen Interaktion zwischen einzelnen Kapillarwellen. In diesem Bereich wurden starke Strömungsbewegungen in Querrichtung festgestellt, welche durch denselben Mechanismus wie die kapillare Strömungsablösung getrieben werden, d.h. durch Druckvariationen in Querrichtung in Folge entsprechender Variationen der Filmdicke. Diese Querströmungen könnten eine starke Intensivierung des Wärmeübergangs in 3-dimensionalen Rieselfilmen verursachen.

Acknowledgements

Almost a century has passed since Wilhelm Nusselt in 1916 first took interest in the transport processes occurring inside a thin water film. Today, although a great deal has been revealed about falling liquid films, it is still the elucidation and modelling of these transport processes that is at the center of research efforts.

This thesis is based on studies I conducted as a research assistant at the Institute of Heat and Mass Transfer at RWTH Aachen University between April 2005 and November 2009. Funding was provided by Deutsche Forschungsgemeinschaft (DFG) within Collaborative Research Center SFB 540 “Model-Based Experimental Analysis of Kinetic Phenomena in Fluid Multi-Phase Reactive Systems”.

I would like to express my sincere gratitude to my doctoral adviser Professor Kneer for giving me the opportunity to unfold my curiosity and thirst for discovery as well as for providing such excellent working conditions. I am also profoundly thankful to Professor Zeller for his encouragement, his unwavering personal and scientific council and for the continuous interest he took in my work. Further, I would like to thank Professor Renz for putting me on the path of scientific research. I am very grateful to Professor Tropea for agreeing to be second examiner and for his continued interest in the thesis as well as his support.

I am indebted to many colleagues inside and outside the institute for various contributions and for a collaborative working environment. I am grateful to Dr. Lel for introducing me to the subject of falling liquid films and to Dr. Stratmann for introducing me to Laser Doppler Velocimetry as well as to Dr. Förster for his guidance. I would like to thank Hans Dautzenberg, Andreas

Panagos, Stefan Mohl and Dmitri Hospital from the electronics laboratory as well as Hans-Dieter Hilgers, Hartmut Moosmayer and Friedrich Nickel from the mechanical work shop for their contributions to the optical test section and measurement setup. Further, I would like to thank Kurt Nährich and Christian Schüller from the IT-group for their help with respect to computer hard- and software. I also thank Dr. Bückner from the department of Scientific Computing for his friendship and for being a reliable scientific barometer. Special thanks go to Erika Aminatey who kept me healthy through these years.

Over these years I have had the privilege to work with a number of very bright students while supervising their undergraduate research. This was not only very rewarding from a teaching perspective, but their work also provided valuable inputs to this thesis. For this I would like to thank them and I wish them a successful future.

My most profound gratitude is due those who are closest to me and have thus experienced the ups and downs almost as intensely as myself. I thank my parents Hartmut and Gertrud Dietze for their relentless support, guidance and council as well as for being such fine role models. I thank Kerstin Sack for her unfailing willingness to understand me, for all the sacrifices she has made as well as her continuing interest in my research and ultimately for freeing my mind. I also thank my little sister Charlotte Dietze for reminding me that there is a real world out there, which I have visited too seldom.

Finally, my thoughts dwell on Paulette Thienpöndt and Magdalene Berhausen who did not live to read these words.

Georg Friedrich Dietze
Aachen, April 2010

Contents

Acknowledgements	xiii
List of Figures	xvii
List of Tables	xxvii
List of Symbols	xxix
1 Introduction	1
2 Falling film dynamics	7
2.1 Governing equations	7
2.2 Wave dynamics	14
2.2.1 Film instability	14
2.2.2 Wave evolution	22
2.2.3 Wave modeling	31
2.3 Liquid phase transport	47
2.3.1 Momentum transport	47
2.3.2 Scalar transport	83
3 Numerical simulation using the Volume of Fluid method	109
3.1 Employed numerical multiphase methods	110
3.1.1 The Volume of Fluid method	113
3.1.2 Interface reconstruction	116
3.1.3 The Continuum Surface Force method	121
3.2 Specification of performed numerical simulations	124
3.2.1 Computational domain and grid topology	124
3.2.2 Discretization of governing equations	128
3.2.3 Numerical algorithms	131
3.2.4 Initial and boundary conditions	136
3.2.5 Quantification of simulated cases	145

3.3	Consistency tests	148
3.3.1	Grid dependence analysis	149
3.3.2	Interfacial spurious currents	153
3.3.3	Outlet boundary condition	160
3.3.4	Comparison with experimental data	161
4	Experimental	173
4.1	Test setups	174
4.1.1	Optical test setup	174
4.1.2	Inclined test setup	187
4.2	Measurement techniques	195
4.2.1	Confocal Chromatic film thickness measurement	195
4.2.2	Laser Doppler Velocimetry	202
4.2.3	Particle Image Velocimetry	216
5	Capillary flow separation	227
5.1	Kinematics	228
5.1.1	Spatio-temporal visualisation	228
5.1.2	Velocity field	232
5.1.3	Vorticity field	243
5.2	Governing dynamics	247
5.3	Effect on wall-side heat transfer	267
5.4	Influence of control parameters	281
5.4.1	Reynolds number influence	282
5.4.2	Wave frequency influence	291
5.5	3-dimensional capillary flow separation	300
6	Conclusion	315
	References	321

List of Figures

1.1	Complexity of liquid films	2
1.2	Free surface topology of a falling liquid film	3
2.1	Coordinate systems for a falling liquid film in 3-dimensional space	8
2.2	Horizontal liquid film	15
2.3	Linear growth rates for 2-dimensional waves	20
2.4	Linear stability bound for 2-dimensional waves	21
2.5	Hierarchy of falling liquid film instability	22
2.6	Linear stability bound for 3-dimensional waves	23
2.7	Linear growth rates for 3-dimensional waves	24
2.8	Wave celerity as a function of wave frequency according to Nosoko <i>et al.</i> (1996)	28
2.9	Wave celerity as a function of wave amplitude according to Nosoko <i>et al.</i> (1996)	29
2.10	Hierarchy of wave dynamics models	31
2.11	Liquid phase streamwise velocity field in smooth and wavy falling liquid films	48
2.12	Liquid phase streamwise velocity profiles ($Re=10.7$, $Ka=509$, $f=16$ Hz)	52
2.13	Liquid phase streamwise velocity profiles ($Re=20$, $Ka=124$, $f=20$ Hz)	53
2.14	Liquid phase streamlines in a wave-fixed coordinate system . .	59
2.15	Flow pattern at the wave trough of a vertically falling liquid film with harmonic surface waves according to Kapitza (1948) . . .	66

2.16	Wall shear stress distribution in smooth and wavy falling liquid films	74
2.17	Wall pressure distribution in smooth and wavy falling liquid films	76
2.18	Temperature profiles in a smooth developed falling liquid film .	85
2.19	Nusselt number time traces for different wavy falling liquid films	95
2.20	Mechanisms of scalar transport intensification in wavy falling liquid films	100
3.1	Dynamic conditions for a finite control volume containing two phases	111
3.2	One-dimensional convection of volume fraction	118
3.3	Interface reconstruction and computation of volume fluxes at cell faces according to Youngs (1982)	119
3.4	Computational domain for the simulation of 2-dimensional falling liquid films	124
3.5	Evolution of the streamwise velocity profile within the inlet channel of the 2-dimensional computational domain	125
3.6	Close-up of the computational grid near the liquid inlet	126
3.7	Computational domain employed for the 3-dimensional simulation	127
3.8	Flowchart of the numerical algorithm implemented in the CFD code employed for 2-dimensional simulations	132
3.9	Flowchart of the PISO loop contained in the complete algorithm of figure 3.8	133
3.10	Convergence history of static pressure as well as streamwise and crosswise velocity components for an exemplary simulation . .	135
3.11	Boundary conditions for the 2-dimensional simulations	138
3.12	Boundary conditions for the 3-dimensional simulation	143
3.13	Grid dependence analysis for case 1	151
3.14	Grid dependence analysis for case 8	152
3.15	Static drop test case simulations for cases 1 and 8	155
3.16	Interfacial streamwise velocity for cases 1 and 8	156
3.17	Horizontal capillary wave test case simulations for cases 1 and 8	158

3.18	Film thickness time traces for the horizontal capillary wave test case simulations	159
3.19	Computed streamwise wave evolution (case 1)	161
3.20	Computed instantaneous film thickness distributions (cases 1-4)	162
3.21	Computed instantaneous film thickness distributions (cases 5-8)	163
3.22	Computed instantaneous film thickness distributions (cases 9 and 10)	164
3.23	Comparison of film thickness time traces from experiment and numerical simulation (case 1)	165
3.24	Comparison of film thickness time traces from experiment and numerical simulation (cases 2-4)	166
3.25	Comparison of film thickness time traces from experiment and numerical simulation (cases 5-7)	167
3.26	Comparison of film thickness time traces from experiment and numerical simulation (cases 8-10)	168
3.27	Comparison of streamwise velocity time traces from experiment and numerical simulation (cases 5-7)	169
3.28	Comparison of streamwise velocity time traces from experiment and numerical simulation (cases 8-10)	170
3.29	Comparison of numerical and experimental wave topology for the 3-dimensional simulation (case 11)	171
4.1	Computer aided design of the optical test setup	174
4.2	Photograph of the optical test setup	175
4.3	Enlarged view of the falling liquid film flowing down the inside of the glass body in the optical test setup	177
4.4	Temperature dependence of the refractive index for quartz glass body and working liquids	178
4.5	Close-up view of liquid inlet conditions in the optical test setup	179
4.6	Photograph of 2-dimensional wave fronts in the optical test setup ($Re=10.7$, $Ka=509.5$, $f=24$ Hz)	181

4.7	Photograph of 2-dimensional wave fronts in the optical test setup ($Re=12.9$, $Ka=509.5$, $f=18$ Hz)	182
4.8	Film thickness time traces measured in the optical test setup at two different streamwise positions in the region of developed waves	183
4.9	Growth rates for wavy regimes realized in the optical test setup	184
4.10	Film thickness time traces measured in the optical test setup ($Re=15.0$, 10.7)	185
4.11	Film thickness time traces measured in the optical test setup ($Re=10.7$, 8.6)	186
4.12	Film thickness time traces measured in the optical test setup ($Re=6.8$)	187
4.13	Sketch of the inclined test setup	188
4.14	Photograph of wave fronts in the inclined test setup ($Re=15.6$, $Ka=133.6$, $f=15$ Hz)	189
4.15	Film thickness time traces measured in the inclined test setup ($Re=21.4$, $Ka=139.8$, $f=5-24$ Hz)	191
4.16	Streamwise evolution of film thickness time traces measured in the inclined test setup ($Re=21.4$, $Ka=139.8$, $f=5.0$ Hz)	193
4.17	Streamwise evolution of film thickness time traces measured in the inclined test setup ($Re=21.4$, $Ka=139.8$, $f=24.0$ Hz) . . .	194
4.18	Measurement principle of the CCI technique	197
4.19	Calibration relation for the CCI distance measurement: wave- length versus measurement distance	198
4.20	Application of the CCI film thickness measuring technique to the optical test setup	199
4.21	Spectral dependence of the refractive index for quartz glass body and DMSO-water solution at $T=25.2$ °C	200
4.22	Sketch of the integrated fiber-based emitting and receiving optics employed for LDV measurements	202
4.23	Close-up schematic view of the intersection volume of LDV laser beams, illustrating the measurement ellipsoid	204

4.24	Photograph of intersecting LDV laser beams in the optical test setup	205
4.25	Signal processing operations performed by the Burst Spectrum Analyzer	206
4.26	Sketch of the LDV measurement ellipsoid in the optical test setup with Cartesian and radial coordinates	207
4.27	Frequency response of the Titanium dioxide tracer particles employed for velocity measurements	210
4.28	Analytical and experimental radial streamwise velocity profiles in a smooth water-glycerol film ($Re=1.1$, $Ka=5.6$)	211
4.29	Liquid phase streamwise velocity time traces in the residual layer measured with LDV in the optical test setup ($Re=15.0$, $Ka=509.5$, $f=16.0$ Hz)	213
4.30	Liquid phase streamwise velocity time traces in the large wave humps measured with LDV in the optical test setup ($Re=15.0$, $Ka=509.5$, $f=16.0$ Hz)	214
4.31	Liquid phase streamwise velocity time traces in the residual layer and intermediate region measured with LDV in the inclined test setup ($Re=15.6$, $Ka=133.6$, $f=15.0$ Hz)	215
4.32	Liquid phase streamwise velocity time trace in the large wave humps measured with LDV in the inclined test setup ($Re=15.6$, $Ka=133.6$, $f=15.0$ Hz)	216
4.33	Photograph of the PIV laser light sheet illuminating the wavy liquid film in the optical test setup	217
4.34	Two successive digital PIV images recorded with the CMOS camera	218
4.35	Typical illumination and imaging sequence employed for PIV recordings	220
4.36	Displacement vectors obtained from the application of the PIV algorithm to an exemplary image pair	222
4.37	Calibration procedure for PIV measurements	224

5.1	Streamlines in the capillary wave region obtained from numerical simulation (case 1)	229
5.2	Streamlines in the capillary wave region obtained from numerical simulation (case 8)	230
5.3	Simulated near-wall streamlines and streamwise velocity profiles at the first capillary minimum during wave development (case 1)	233
5.4	Simulated near-wall streamlines and streamwise velocity profiles at the first capillary minimum in the developed region (case 1)	234
5.5	Simulated near-wall streamlines and streamwise velocity profiles at the first capillary minimum in the developed region (case 8)	236
5.6	Velocity vectors in the capillary wave region measured in the optical test setup using PIV ($Re=15.0$, $f=16.0$ Hz)	238
5.7	Streamwise velocity time traces in the residual layer (near-wall region) measured in the optical test setup using LDV ($Re=15.0$, $f=16.0$ Hz)	240
5.8	Streamwise velocity time traces in the residual layer (intermediate region) measured in the optical test setup using LDV ($Re=15.0$, $f=16.0$ Hz)	241
5.9	Streamwise velocity time traces in the large wave humps measured in the optical test setup using LDV ($Re=15.0$, $f=16.0$ Hz)	242
5.10	Out of plane vorticity component in the CSE region obtained from PIV measurements in the optical test setup ($Re=15.0$, $Ka=509.5$, $f=16.0$ Hz)	244
5.11	Sketch illustrating the relation between interface topology and liquid phase static pressure	250
5.12	Simulated wave topology, streamwise velocity contours and corresponding wall pressure distribution (case 1)	253
5.13	Simulated wave topology, streamwise velocity contours and corresponding wall pressure distribution (case 8)	254
5.14	Dynamic conditions in the capillary wave region corresponding to streamlines in figure 5.3(a)	256

5.15	Dynamic conditions in the capillary wave region corresponding to streamlines in figure 5.3(c)	257
5.16	Dynamic conditions in the capillary wave region corresponding to streamlines in figure 5.4(a)	258
5.17	Simulated kinematic and dynamic conditions at the first capillary minimum (case 8)	261
5.18	Simulated kinematic and dynamic conditions in the region of the wave front (case 8)	262
5.19	Simulated kinematic and dynamic conditions at the second capillary minimum (case 8)	263
5.20	Simulated kinematic and dynamic conditions at the first capillary maximum (case 8)	264
5.21	Simulated streamlines and dynamic conditions in the capillary wave region at $t=2.97000$ s (case 8)	265
5.22	Simulated streamlines and dynamic conditions in the capillary wave region at $t=2.98250$ s (case 8)	266
5.23	Simulated streamlines and dynamic conditions in the capillary wave region at $t=2.99500$ s (case 8)	267
5.24	Simulated streamlines and dynamic conditions in the capillary wave region at $t=3.02000$ s (case 8)	268
5.25	Simulated temperature contours in a single wave (cases 1 and 8)	269
5.26	Simulated temperature profiles in a single wave (cases 1 and 8)	270
5.27	Simulated fluid element pathlines in the residual layer during the transition of the first capillary minimum (case 1)	272
5.28	General and close-up view of simulated near-wall fluid element pathlines (case 1)	273
5.29	Simulated time traces of film thickness, wall shear stress and Nusselt number evaluated over one period length (case 1) . . .	276
5.30	Simulated fluid element pathlines in the residual layer during the transition of the first capillary minimum (case 8)	279
5.31	General and close-up view of simulated near-wall fluid element pathlines (case 8)	280

5.32	Simulated time traces of film thickness, wall shear stress and Nusselt number evaluated over one period length (case 8) . . .	281
5.33	Simulated Streamwise film thickness distribution over a single wave (cases 5 to 8)	283
5.34	Film thickness and streamwise velocity time traces measured in the optical test setup ($Re=8.6, 10.7, f=16.0$ Hz)	284
5.35	Film thickness and streamwise velocity time traces measured in the optical test setup ($Re=12.9, 15.0, f=16.0$ Hz)	285
5.36	Streamlines at the first capillary minimum obtained from PIV measurements in the optical test setup: Reynolds number influence	286
5.37	Streamlines and dynamic conditions at the first capillary minimum obtained from numerical simulation (cases 5 and 6) . . .	288
5.38	Streamlines and dynamic conditions at the first capillary minimum obtained from numerical simulation (cases 7 and 8) . . .	289
5.39	Simulated Streamwise film thickness distribution over a single wave (cases 9 and 10)	291
5.40	Film thickness and streamwise velocity time traces measured in the optical test setup ($Re=10.7, f=24.0, 20.0$ Hz)	292
5.41	Film thickness and streamwise velocity time traces measured in the optical test setup ($Re=10.7, f=18.0, 16.0$ Hz)	293
5.42	Streamlines at the first capillary minimum obtained from PIV measurements in the optical test setup: wave frequency influence	294
5.43	Streamlines and dynamic conditions at the first capillary minimum obtained from numerical simulation (cases 9 and 10) . . .	296
5.44	Simulated Streamwise film thickness distribution over a single wave (cases 1 to 4)	297
5.45	Streamlines and dynamic conditions at the first capillary minimum obtained from numerical simulation (cases 2 and 3) . . .	298
5.46	Streamlines and dynamic conditions at the first capillary minimum obtained from numerical simulation (cases 4 and 1) . . .	299
5.47	Interface topology for the 3-dimensional simulation (case 11) .	300

5.48	Contours of film thickness as well as streamwise and spanwise wall shear stress for the 3-dimensional film (case 11)	302
5.49	Streamlines and velocity vectors near the first two capillary minima of the 3-dimensional film (case 11)	304
5.50	Streamlines and velocity vectors near the first two capillary minima of the 3-dimensional film (case 11)	305
5.51	Liquid phase streamlines in the capillary wave region of the 3-dimensional film (case 11): perspective and top view.	307
5.52	Liquid phase streamlines in the capillary wave region of the 3-dimensional film (case 11): inner and outer side views.	308
5.53	Velocity vectors at different x-positions in the region of capillary interference of the 3-dimensional film (case 11)	310
5.54	Velocity vectors at different x-positions in the region of capillary interference of the 3-dimensional film (case 11)	311
5.55	Velocity vectors at different x-positions in the region of capillary interference of the 3-dimensional film (case 11)	312

List of Tables

2.1	List of long-wave equation models based on the asymptotic expansion method by Benney (1966)	37
2.2	List of recent multiple-equation models based on the method by Shkadov (1967)	43
2.3	List of experimental investigations of the velocity field in falling liquid films	49
2.4	List of investigations pertaining to backflow in falling liquid films	64
2.5	Classification of falling liquid film regimes according to Brauer (1956)	79
2.6	Classification of falling liquid film regimes according to Ishigai <i>et al.</i> (1972)	80
2.7	Liquid phase temperature profile and Nusselt number for smooth fully developed films	86
3.1	Flow regimes for the performed numerical simulations of falling liquid films	145
3.2	Liquid properties for the performed numerical simulations of falling liquid films	146
3.3	Dimensions of the computational domain for the performed numerical simulations of falling liquid films	146
3.4	Spatio-temporal discretization for the performed numerical simulations of falling liquid films	147
3.5	Conditions for the 2-dimensional heat transfer simulations . . .	147
3.6	Spatio-temporal discretization for the grid dependence analysis of cases 1 and 8	149

4.1	Liquid properties of the two refractively matched aqueous solutions employed as working liquids in the optical test setup . . .	176
4.2	Flow regimes investigated in the optical test setup	180
4.3	Liquid properties for working liquids employed in the inclined test setup	190
4.4	Flow regimes investigated in the inclined test setup	190
4.5	Specifications of the CCI measurement system employed for film thickness measurements	198
4.6	Optical quantities specifying the fiber-optic LDV-probe	203
4.7	Dimensions of the LDV-ellipsoid in the liquid film	208
4.8	Settings and properties of the CMOS camera and copper vapour laser employed for PIV image acquisition	220

List of Symbols

Physical quantities		
Symbol	Quantity	Unit
δ	Film thickness	m
c	Wave celerity	m/s
f	Wave frequency	1/s
ω	Angular frequency	1/s
Λ	Wavelength	m
α	Streamwise wave number	1/m
β	Spanwise wave number	1/m
Δ	Wave amplitude	m
ε	Relative amplitude	-
κ	Interfacial curvature	1/m
t	Time coordinate	s
Δt	Time difference	s
u	Streamwise velocity component	m/s
v	Crosswise velocity component	m/s
\tilde{v}	Characteristic crosswise velocity	m/s
w	Spanwise velocity component	m/s
ω_z	Spanwise vorticity component	1/s
Q	Volume flow rate	m ³ /s
q	Volume flow rate per unit width	m ² /s
Ψ	Ratio of streamwise pressure force to gravitational force at the wall	-

Physical quantities (continued)

Symbol	Quantity	Unit
Ψ	Stream function	m^2/s
ϕ	Amplitude of stream function perturbation	-
p	Static pressure	N/m^2
τ_{wx}	Streamwise wall shear stress	N/m^2
τ_{wz}	Spanwise wall shear stress	N/m^2
g	Gravitational acceleration constant	m/s^2
g_x	Streamwise gravitational acceleration component	m/s^2
g_y	Crosswise gravitational acceleration component	m/s^2
T	Temperature	K
h	Heat transfer coefficient	$\text{W}/\text{m}^2\text{K}$
h_m	Mass transfer coefficient	$\text{kg}/\text{m}^2\text{s}$
L	Characteristic length of the falling liquid film	m
W	Width of the falling liquid film	m
φ	Inclination angle with respect to horizontal plane	deg
R	Radius of the glass body bore	m
d	Diameter	m
H	Height of the computational domain	m

Thermophysical properties

Symbol	Quantity	Unit
σ	Surface tension	N/m
μ	Dynamic viscosity	$\text{kg}/\text{m}\text{s}$
ν	Kinematic viscosity	m^2/s
ρ	Density	kg/m^3

Thermophysical properties (continued)

Symbol	Quantity	Unit
α	Thermal diffusivity	m^2/s
k	Thermal conductivity	W/mK
c	Specific heat capacity	J/kgK
c_p	Specific heat capacity (isobaric)	J/kgK
c_v	Specific heat capacity (isochoric)	J/kgK
D	Diffusion coefficient	m^2/s

Scales for non-dimensionalization

Symbol	Quantity	Definition
δ_{Nu}	Crosswise length scale	$\left[\frac{3q\nu_1}{g_x} \right]^{1/3}$
L	Streamwise length scale	e.g. Λ
\bar{u}_{Nu}	Streamwise velocity scale	$\frac{g_x \delta_{\text{Nu}}^2}{3\nu_1}$
t_{Nu}	Time scale	L/\bar{u}_{Nu}

Dimensionless groups

Symbol	Quantity	Definition
Re	Reynolds number	$\frac{\bar{u}_{\text{Nu}} \delta_{\text{Nu}}}{\nu_1}$
We	Weber number	$\frac{\sigma}{\rho_1 \delta_{\text{Nu}} \bar{u}_{\text{Nu}}^2}$
Ka	Kapitza number	$\frac{\sigma}{\rho_1 g_x^{1/3} \nu_1^{4/3}}$
Fr	Froude number	$\frac{\bar{u}_{\text{Nu}}}{(g_y \delta_{\text{Nu}})^{1/2}}$
ϵ	Length scale ratio	δ_{Nu}/L

Dimensionless groups (continued)

Symbol	Quantity	Definition
Π_{BL}	Dimensionless group for boundary layer equations	$\frac{3^{2/3} We^{1/3}}{Re^{2/3}}$
Π_{μ}	Dynamic viscosity ratio	μ_g/μ_l
Π_{ρ}	Density ratio	ρ_g/ρ_l
Pr	Prandtl number	ν_l/α_l
Nu	Nusselt number	$\frac{h \delta_{Nu}}{k_l}$
Π_k	Thermal conductivity ratio	k_g/k_l
Π_{α}	Thermal diffusivity ratio	α_g/α_l
Sc	Schmidt number	ν_l/D
Sh	Sherwood number	$\frac{h_m \delta_{Nu}}{\rho_l D}$
St	Stokes number	$\frac{\Delta t \nu_l}{2\pi d_p^2}$

Mathematical notation

Notation	Signification
x	Streamwise coordinate
y	Crosswise coordinate
z	Spanwise coordinate
s	Interfacial line coordinate
r	Radial coordinate
ξ	Wave-fixed streamwise coordinate
V	Volume
A	Area

Mathematical notation (continued)

Notation	Signification
$\bar{\phi}$	1-dimensional spatial, volume or temporal average of ϕ
$\hat{\phi}$	Area average of ϕ
$\bar{\bar{\phi}}$	Spatial and temporal average of ϕ
ϕ_i	Einstein notation for vector $\vec{\phi}$
x_i	Position vector: $[x, y, z]^T$
u_i	Velocity vector: $[u, v, w]^T$
$\vec{\nabla}$	Nabla vector: $[\partial/\partial x, \partial/\partial y, \partial/\partial z]^T$
\vec{n}	Normal interfacial unit vector
\hat{n}	Normal distance to the interface
$\vec{\tau}$	First tangential interfacial unit vector
$\vec{\bar{\tau}}$	Second tangential interfacial unit vector
\vec{g}	Gravitational acceleration vector
τ_{xy}	Shear stress acting in (or opposed to the) y direction on a surface with outward normal pointing in (or opposed to the) x-direction
Φ_{ij}	Einstein notation for matrix Φ
S_{ij}	Stress tensor
δ_{ij}	Kronecker Delta
ε_{ijk}	Levi-Civita permutation tensor
$\hat{\delta}$	Delta function
$\Delta\Phi$	Discrete amount of the extensive quantity Φ in a computational cell
i	Complex variable: $\sqrt{-1}$
ϕ_r	Real part of the complex scalar ϕ
ϕ_i	Imaginary part of the complex scalar ϕ
$\vec{\phi}^T$	Transpose of the vector $\vec{\phi}$
φ	Volume fraction
ϕ	Area fraction
α	Weight factor

Subscripts

Symbol	Reference to
x	Streamwise direction
y	Crosswise direction
z	Spanwise direction
g	Gaseous phase; glass
l	Liquid phase
δ	Liquid-gas interface
w	Bounding wall
F	Film
C	Channel; camera
f	Film; finely resolved computational subdomain
d	Diabatic boundary
0	Initial state; state at the liquid inlet; ambient air
Nu	Nusselt (1923) (i.e. laminar, smooth and developed film)
m	Mean or bulk; mass transfer; measurement
∞	Fully developed region; far field
eff	Effective or apparent
max	Maximality
min	Minimality
res	Residual layer
c	Criticality; capillary wave
SP	Stagnation point
sp.	Spurious currents
BL	Boundary layer equations
\perp	Normal projection
P	Particles

Subscripts (continued)

Symbol	Reference to
R	Red
G	Green
B	Blue

Superscripts

Symbol	Reference to
x	Streamwise direction
y	Crosswise direction
z	Spanwise direction
0	Initial state
*	Non-dimensionalization
'	Perturbation, differentiation
"	Area specific
'''	Volume specific
i	Time step

Abbreviations

Acronym	Significance
CSE	Capillary Separation Eddy
lhs	Left hand side
rhs	Right hand side
rms	Root mean square
RIM	Refractive Index Matching
LDV	Laser Doppler Velocimetry

Abbreviations (continued)

Acronym	Significance
PIV	Particle Image velocimetry
PTV	Particle Tracking Velocimetry
CCI	Confocal Chromatic Imaging
CFD	Computational Fluid Dynamics
VOF	Volume of Fluid
CSF	Continuum Surface Force
CCF	Cross Correlation Function

1 Introduction

Liquid films are thin liquid layers of approximately 1 mm thickness flowing along a bounding wall. Depending on the mechanism of their formation one can distinguish shear-driven liquid films, falling liquid films, which are accelerated only by gravity, liquid films developing as a result of vapor condensation and liquid films resulting from jet impingement (see figure 1.1).

Such flows develop naturally, as can be observed on the windshield of a car, driving in rainy weather, but are also present in many industrial applications. In cooling towers for example, water is sprayed onto corrugated sheets, generating a falling liquid film from which it evaporates into the counter-flowing air (see e.g. Ibrahim *et al.* (1995); Fisenko *et al.* (2002)). In nuclear fusion research, falling liquid lithium films are employed to cool chamber walls surrounding the plasma (see e.g. Abdou (1999)). In modern nuclear reactors, water in the primary circuit flows along fuel elements in the shape of an evaporating film, driven by water vapor (see e.g. Takase *et al.* (2003)). Conversely, films develop on the outside of horizontal or vertical tubes in power plant condensers (see e.g. Sarma *et al.* (1998)) or in absorption-cooling machines (see e.g. Killion & Garimella (2004); Nosoko *et al.* (2002)). In certain gas turbines, liquid fuel is injected as an air-driven film, which atomizes in the combustion chamber (see e.g. Gerendas & Wittig (2001)). Liquid films also develop in reciprocating combustion engines as oil films on the inside of the cylinder (see e.g. Yilmaz (2003)). In process technology, falling film evaporators are employed for inspissation (see e.g. Jebson & Chen (1997)) or distillation (see e.g. Brotherton (2002)) including desalination (see e.g. Uche *et al.* (2002)). For example, such falling film apparatuses consist of vertical tubes along the inside of which a falling film develops. Thereby, the liquid is accessible for thermal control through the tube

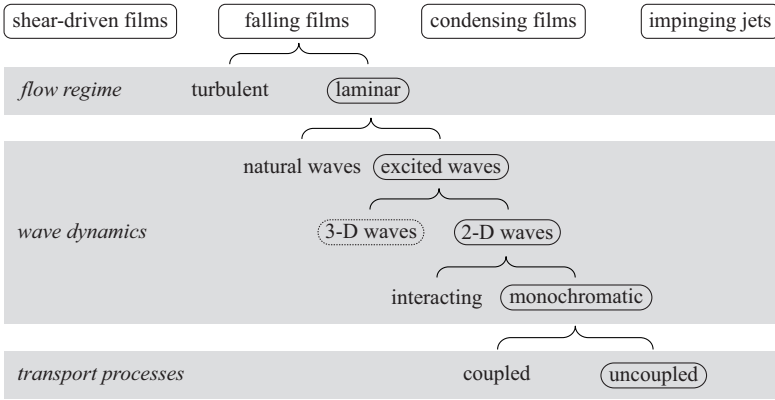


Figure 1.1: Diagram showing the complexity levels of liquid films and highlighting conditions principally investigated in this thesis with rounded boxes (a single 3-dimensional falling film was also investigated).

wall. This property is relevant for processes requiring the limitation of product temperature. A considerably more complex flow is encountered in distillation or absorption columns with structured packings where the film develops on non smooth surfaces (see e.g. Valluri *et al.* (2005)). Further examples can be found in the comprehensive review of liquid film applications compiled by Fulford (1964).

In the context of this thesis, only falling liquid films (i.e. liquid films driven by gravity) are of interest. Their most notable characteristic is the presence of waves on the *liquid-gas free surface*, which subsequently will be referred to as *liquid-gas interface* or simply *interface*. Brooke Benjamin (1957) established that a smooth vertically falling film is unstable to interface perturbations for all values of the film Reynolds number. Thus, such flows are generally wavy in technical applications. The full complexity displayed by falling liquid film dynamics is broken down in figure 1.1. On a higher level, the flow in the liquid phase can be either turbulent or laminar. Thereby, even laminar falling films can display very complex wave dynamics. Owing to film instability, surface

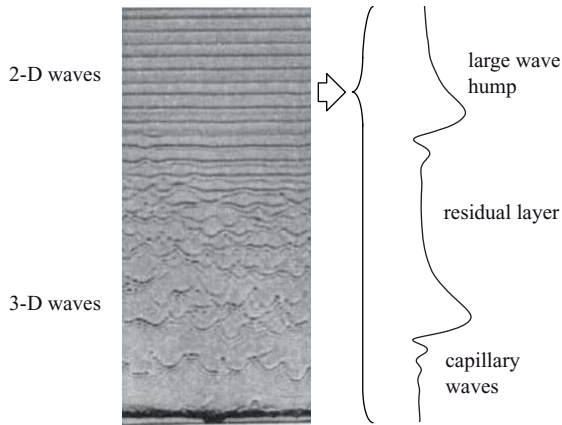


Figure 1.2: Shadowgraph of a vertical water film with excited surface waves (taken from Nosoko *et al.* (1996)) and typical wave profile in the region of 2-dimensional wave fronts.

waves arise either naturally or due to controlled external perturbations. The kinematics of these waves can be two- or three-dimensional. Further, single waves either travel well separated from one another or interact with one another due to dispersion effects. On an additional complexity level, one can distinguish flows displaying strong coupling between heat- and mass-transport (i.e. scalar transport) and momentum transport from flows where scalar transport is passive. Thereby, coupling between scalar and momentum transport can result from the temperature or concentration dependence of fluid properties such as surface tension and viscosity.

In most technical systems, falling films display maximal complexity, characterized by turbulent flow regimes, 3-dimensional interacting surface waves, occurring naturally with coupled and superimposed transport mechanisms. This complexity prohibits an integral modelling approach which is traditionally applied in heat- and mass transfer through the use of transfer coefficients. Rather, a more detailed approach must be chosen, focused on mechanistically modelling

distinct phenomena and their interaction. Thereby, efforts have traditionally been divided between two main areas: modelling of wave dynamics and modelling of liquid phase transport phenomena.

A prerequisite for the mechanistic modelling of falling liquid films is the elucidation of relevant transport phenomena and their governing dynamics. It is to this task that this thesis seeks to contribute. Thereby, investigations are constrained to the case of laminar falling liquid films with externally excited monochromatic 2-dimensional surface waves, with the exception of one 3-dimensional simulation (see section 5.5). As can be deduced from figure 1.1 this constitutes the path of least complexity. However, even under these more simple conditions the understanding of liquid phase transport mechanisms is still incomplete. Figure 1.2 illustrates the wave topology of a falling liquid film under these conditions as visualized experimentally by Nosoko *et al.* (1996). One can discern waves of two dimensional wave fronts and equal spacing near the film inlet at the top of the shadowgraph. Farther downstream, plane wave fronts break-up into 3-dimensional structures, interacting with one another and rendering the interface topology considerably more complex. The profile on the right side of figure 1.2 shows a typical shape of the liquid-gas interface in the 2-dimensional region of the flow, consisting of large wave humps preceded by small so called *capillary waves* (to be understood in the sense that the effect of surface tension dominates the effect of gravity, as stated by Whitham (1974)) and separated by a smooth *residual layer* .

A principal object of interest has been the investigation of the effect of wave dynamics on transport in the liquid film. Several studies (see e.g. Frisk & Davis (1972)) have shown that due to the presence of surface waves on the film, scalar transfer between the bounding wall and the liquid or between the liquid and its gaseous atmosphere is intensified. Thereof, a few studies (see e.g. Adomeit *et al.* (2000)) have shown that the intensification is strongest in the region of capillary waves. Because no sufficiently resolved numerical and experimental data, relative to the velocity and scalar fields in the liquid phase have been available, no unifying physically based explanation of this phenomenon has been provided. Concurrently, the capillary wave region has been the focus of

attention due to another reason. Ever since Kapitza (1948) (see also the English translation Kapitza & Kapitza (1965)), based on his long-wave approximation of the film flow, hypothesized that upward flow exists in the region of the wave trough, the possibility of such back flow in a falling liquid film (which *nota bene* is vertical in most cases) has been debated.

Consequently, in an attempt to elucidate these two open questions, detailed numerical and experimental investigations of the kinematics and dynamics in the capillary wave region were performed in this thesis. The thesis is structured as follows. In chapter 2, a summary of established knowledge concerning falling film wave dynamics (section 2.3) as well as liquid phase transport mechanisms (section 2.2) is provided in the form of a literature review.

Chapters 3 and 4 introduce the employed investigative methodology. Thereof, chapter 3 addresses the numerical simulation of falling liquid films comprising a description of the employed numerical multiphase methods (section 3.1), the quantification of performed simulations (section 3.2) as well as a series of consistency tests (section 3.3), including comparison with experimental data. Chapter 4 introduces the test setups employed for the experimental investigations (section 4.1) as well as the optical measurement techniques (section 4.2).

Results are summarized in chapter 5. These constitute a complete numerical and experimental picture of the phenomenon of *capillary flow separation* in falling liquid films discovered in the context of this thesis. The kinematics and governing dynamics are elucidated in sections 5.1 and 5.2 respectively, whereas its effect on heat transfer is explained in section 5.3. In section 5.4, the effect of two principal control parameters, namely the Reynolds number and wave frequency, is demonstrated and the chapter is concluded with an analysis of 3-dimensional capillary flow separation (section 5.5). Final conclusions are drawn in chapter 6.

2 Falling film dynamics

The body of research on falling liquid films, preceding the year 2000 is summarized in two landmark books by Alekseenko *et al.* (1994) on general aspects of falling films and by Chang & Demekhin (2002) on falling film wave dynamics. In this chapter, some contents of these works as well as more recent research results are reviewed in order to contextualize the contributions of this thesis.

2.1 Governing equations

Assuming Newtonian fluids, the flow of a falling liquid film down an inclined plane [†] (see figure 2.1) in a quiescent gaseous atmosphere is governed by the following system of equations in both the liquid and gaseous phase:

$$\begin{aligned} \rho \frac{\partial u_i}{\partial t} + \rho u_j \frac{\partial u_i}{\partial x_j} &= -\frac{\partial p}{\partial x_i} + \frac{\partial}{\partial x_j} \left(\mu \frac{\partial u_i}{\partial x_j} + \mu \frac{\partial u_j}{\partial x_i} \right) - \frac{2}{3} \frac{\partial}{\partial x_i} \left(\mu \frac{\partial u_j}{\partial x_j} \right) + \rho g_i, \\ \frac{\partial \rho}{\partial t} + \frac{\partial}{\partial x_i} (\rho u_i) &= 0, \quad i, j = 1, 2, 3, \end{aligned} \tag{2.1}$$

where Einstein's summation convention is to be applied, yielding the continuity equation and the Navier-Stokes equations for the 3 Cartesian coordinates. In order for the solutions to these equations to be well defined in the respective phases, 7 inter-phase *coupling conditions* need to be formulated. Three of these result from the continuity of velocity across the interface. Further conditions result from a local interfacial force balance. Thereby, the discontinuity of

[†]Only inclination angles smaller or equal to 90° with respect to the horizontal plane shall be considered in this thesis.

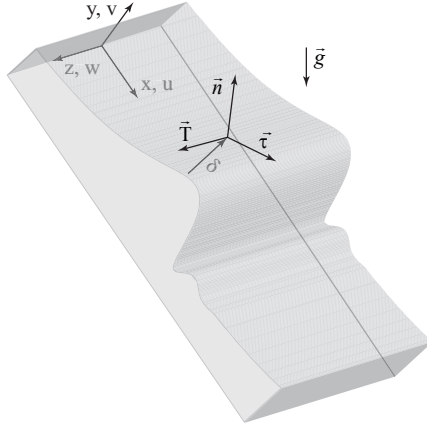


Figure 2.1: Sketch of a wavy falling liquid film in 3-dimensional space, showing the wall fixed Cartesian coordinate system and the orthonormal surface coordinate system defined in equation 2.2.

the stress tensor across the interface, due to the presence of interfacial tensile forces, must be accounted for. Conventionally, the interfacial force balance is formulated in an orthonormal *surface coordinate system* (see figure 2.1), yielding three scalar coupling equations. The surface coordinate system chosen here is given by the following definitions (see Slattery (1990) or Kreyszig (1991)):

$$\begin{aligned}
 \vec{n} &= \left[-\frac{\partial\delta}{\partial x}, 1, -\frac{\partial\delta}{\partial z} \right] \left(\frac{\partial\delta^2}{\partial x} + 1 + \frac{\partial\delta^2}{\partial z} \right)^{-\frac{1}{2}}, \\
 \vec{\tau} &= \left[1, \frac{\partial\delta}{\partial x}, 0 \right] \left(1 + \frac{\partial\delta^2}{\partial x} \right)^{-\frac{1}{2}}, \\
 \vec{T} &= \left[0, \frac{\partial\delta}{\partial z}, 1 \right] \left(1 + \frac{\partial\delta^2}{\partial z} \right)^{-\frac{1}{2}}.
 \end{aligned} \tag{2.2}$$

Thereby, the interface is represented by the scalar equation $y = \delta(x, z)$. Consequently, \vec{n} signifies the unit normal vector (pointing away from the liquid phase) and $\vec{\tau}, \vec{T}$ span the tangent plane to the interface at the considered interface point.

According to Brackbill *et al.* (1992), the resulting tensile force per unit area $F''_{\sigma i}$ acting on an infinitesimal interfacial surface element can be written as follows:

$$F''_{\sigma i} = \frac{\partial \sigma}{\partial x_i} - n_i \left(\sigma \frac{\partial n_j}{\partial x_j} + n_j \frac{\partial \sigma}{\partial x_j} \right). \quad (2.3)$$

With this, the interfacial force balance yields the following coupling conditions between gaseous (superscript g) and liquid (superscript l) phase formulated in surface coordinates:

$$\begin{aligned} S^l_{ij} n_j n_i - n_i \left(\sigma \frac{\partial n_j}{\partial x_j} + n_j \frac{\partial \sigma}{\partial x_j} \right) &= S^g_{ij} n_j n_i, \\ S^l_{ij} n_j \tau_i + \frac{\partial \sigma}{\partial x_i} \tau_i \tau_i &= S^g_{ij} n_j \tau_i, \\ S^l_{ij} n_j \Gamma_i + \frac{\partial \sigma}{\partial x_i} \Gamma_i \Gamma_i &= S^g_{ij} n_j \Gamma_i. \end{aligned} \quad (2.4)$$

For the formulation of the tangential balances (i.e. the last two equations of 2.4), the first term of equation 2.3 was projected in the directions of the surface coordinates $\vec{\tau}$ and \vec{T} . Further, S_{ij} designates the stress tensor:

$$S_{ij} = -\delta_{ij} \left(p + \frac{2}{3} \mu \frac{\partial u_k}{\partial x_k} \right) + \mu \left(\frac{\partial u_i}{\partial x_j} + \frac{\partial u_j}{\partial x_i} \right). \quad (2.5)$$

The film thickness δ , which appears in the above equations, is related to the velocity field by the so called *kinematic condition* (i.e. the seventh coupling condition):

$$v|_{y=\delta} = \frac{d\delta}{dt}, \quad (2.6)$$

which simply states that the position of the interface moves in crosswise direction with the local crosswise velocity of the fluid. At the wall, assuming no slip

and no penetration, the following boundary conditions apply:

$$u|_{y=0} = v|_{y=0} = w|_{y=0} = 0. \quad (2.7)$$

When additional heat transport is considered, the energy equation is added to the equations in 2.1:

$$\frac{\partial}{\partial t} (\rho c_v T) + \frac{\partial}{\partial x_j} (\rho u_j c_p T) = \frac{\partial}{\partial x_j} \left(k \frac{\partial T}{\partial x_j} \right) + S_{ij} \frac{\partial u_i}{\partial x_j}, \quad (2.8)$$

where the last term on the right side signifies the dissipation rate per unit volume. In addition to the continuity of temperature across the interface a second thermal inter-phase coupling condition can be derived from an interfacial heat balance:

$$-k_l \frac{\partial T_l}{\partial x_j} n_j = -k_g \frac{\partial T_g}{\partial x_j} n_j. \quad (2.9)$$

In the above equation as in the rest of the text, the *subscripts* g and l have been introduced to refer to the gaseous and liquid phase respectively, as opposed to equation 2.4 where *superscripts* were exceptionally employed for convenience. Finally, assuming an isothermal bounding wall, the following thermal boundary condition applies:

$$T|_{y=0} = T_w. \quad (2.10)$$

The investigations presented in this thesis are mainly focused on 2-dimensional flow dynamics with constant fluid properties. For these conditions the governing equations presented above are considerably reduced in complexity. By further assuming a constant pressure p_0 in the gaseous phase and a smooth liquid-gas interface, Nusselt (1923) solved the resulting 2-dimensional equations in the limit of developed flow. This solution describes the *primary flow* of the film and can be written as follows:

$$\begin{aligned} \delta_{\text{Nu}} &= \left[\frac{3q\nu_l}{g_x} \right]^{\frac{1}{3}}, \quad p(y) = p_0 + \rho_l g_y (\delta_{\text{Nu}} - y), \\ u_{\text{Nu}}(y) &= \frac{g_x}{\nu_l} \left(\delta_{\text{Nu}} y - \frac{y^2}{2} \right), \quad v_{\text{Nu}} = w_{\text{Nu}} = 0, \end{aligned} \quad (2.11)$$

where q signifies the volume flow rate per unit width. The properties of this primary flow are conventionally introduced as reference values for non dimensionalization. The reference values for length, velocity and time thus are:

$$\delta_{\text{Nu}} = \left[\frac{3q\nu_1}{g_x} \right]^{\frac{1}{3}}, \quad \bar{u}_{\text{Nu}} = \frac{1}{\delta_{\text{Nu}}} \int_0^{\delta_{\text{Nu}}} u_{\text{Nu}}(y) dy = \frac{g_x \delta_{\text{Nu}}^2}{3\nu_1}, \quad t_{\text{Nu}} = \frac{L}{\bar{u}_{\text{Nu}}}, \quad (2.12)$$

whereby the subscript Nu refers to the work of Nusselt (1923) and L signifies an adequate characteristic length in streamwise direction.

Cerro & Whitaker (1971) calculated the film thickness distribution in the *developing region* of the smooth film based on a boundary layer approach for different heights of the inlet channel. Their results show that the film thickness asymptotically approaches δ_{Nu} over the developing region. Finally, an analytical solution for smooth developed vertical film flow in *cylindrical coordinates* (see e.g. Mudawar & Houpt (1993a)) can be derived:

$$u(r) = \frac{1}{2} \frac{g}{\nu_1} \left[\frac{1}{2} (R^2 - r^2) - R_\delta^2 \ln \left(\frac{R}{r} \right) \right], \quad v = w = 0, \quad p = p_0, \quad (2.13)$$

where R designates the radial distance of the bounding wall and R_δ the radial distance of the liquid-gas interface. No closed relation for the film thickness can be derived under these conditions. However, by integrating the radial velocity profile over the film thickness, the latter can be related implicitly to the volume flow rate per unit width.

Introducing the dimensionless quantities:

$$x^* = \frac{x}{L}, \quad y^* = \frac{y}{\delta_{\text{Nu}}}, \quad t^* = \frac{t \bar{u}_{\text{Nu}}}{L}, \quad p^* = \frac{p}{\rho_1 \bar{u}_{\text{Nu}}^2}, \quad u^* = \frac{u}{\bar{u}_{\text{Nu}}}, \quad v^* = \frac{v}{\bar{u}_{\text{Nu}} \delta_{\text{Nu}}} \quad (2.14)$$

the Navier-Stokes and continuity equations in 2.1 reduce to the following non-dimensional form for the considered 2-dimensional case with constant fluid properties:

$$\frac{\partial u^*}{\partial t^*} + u^* \frac{\partial u^*}{\partial x^*} + v^* \frac{\partial u^*}{\partial y^*} = -\gamma \frac{\partial p^*}{\partial x^*} + \frac{\chi}{Re} \left(\epsilon \frac{\partial^2 u^*}{\partial x^{*2}} + \frac{1}{\epsilon} \frac{\partial^2 u^*}{\partial y^{*2}} \right) + \frac{3\chi}{\epsilon Re},$$

$$\begin{aligned} \frac{\partial v^*}{\partial t^*} + u^* \frac{\partial v^*}{\partial x^*} + v^* \frac{\partial v^*}{\partial y^*} &= -\frac{\gamma}{\epsilon^2} \frac{\partial p^*}{\partial y^*} + \frac{\chi}{Re} \left(\epsilon \frac{\partial^2 v^*}{\partial x^{*2}} + \frac{1}{\epsilon} \frac{\partial^2 v^*}{\partial y^{*2}} \right) - \frac{1}{\epsilon^2 Fr^2}, \\ \frac{\partial u^*}{\partial x^*} + \frac{\partial v^*}{\partial y^*} &= 0, \end{aligned} \quad (2.15)$$

where χ and γ have been introduced to distinguish the formulations for the respective phases. In the gaseous phase $\chi = \Pi_\mu/\Pi_\rho$, $\gamma = 1/\Pi_\rho$ and in the liquid phase $\chi = \gamma = 1$ with the density ratio $\Pi_\rho = \rho_g/\rho_l$ and the dynamic viscosity ratio $\Pi_\mu = \mu_g/\mu_l$. As the surrounding atmosphere of the falling liquid film is quiescent gas, the scales in both the liquid and the gaseous phase are imposed by the flow in the liquid phase (see equation 2.12). The dimensionless Navier-Stokes and continuity equations yield the Reynolds number Re , the Froude number Fr and the ratio of length scales ϵ :

$$Re = \frac{\bar{u}_{Nu} \delta_{Nu}}{\nu_l}, \quad Fr = \frac{\bar{u}_{Nu}}{(|g_y| \delta_{Nu})^{1/2}}, \quad \epsilon = \frac{\delta_{Nu}}{L}. \quad (2.16)$$

The inter-phase *coupling conditions* in equation 2.4 reduce to:

$$\begin{aligned} p_l^* - p_g^* + \frac{We \epsilon^2}{\beta^{3/2}} \frac{\partial^2 \delta^*}{\partial x^{*2}} &= \\ \frac{2\epsilon}{\beta Re} \left[\epsilon^2 \frac{\partial u_1^*}{\partial x^*} \left(\frac{\partial \delta^*}{\partial x^*} \right)^2 + \frac{\partial v_1^*}{\partial y^*} + \frac{\partial \delta^*}{\partial x^*} \left(\frac{\partial u_1^*}{\partial y^*} + \epsilon^2 \frac{\partial v_1^*}{\partial x^*} \right) \right] &- \\ \frac{2\epsilon \Pi_\mu}{\beta Re} \left[\epsilon^2 \frac{\partial u_g^*}{\partial x^*} \left(\frac{\partial \delta^*}{\partial x^*} \right)^2 + \frac{\partial v_g^*}{\partial y^*} + \frac{\partial \delta^*}{\partial x^*} \left(\frac{\partial u_g^*}{\partial y^*} + \epsilon^2 \frac{\partial v_g^*}{\partial x^*} \right) \right] &, \quad (2.17) \\ \epsilon^2 \frac{\partial \delta^*}{\partial x^*} \left(\frac{\partial u_1^*}{\partial x^*} - \frac{\partial v_1^*}{\partial y^*} \right) + \left(\frac{\beta}{2} - 1 \right) \left(\frac{\partial u_1^*}{\partial y^*} + \epsilon^2 \frac{\partial v_1^*}{\partial x^*} \right) &= \\ \Pi_\mu \epsilon^2 \frac{\partial \delta^*}{\partial x^*} \left(\frac{\partial u_g^*}{\partial x^*} - \frac{\partial v_g^*}{\partial y^*} \right) + \Pi_\mu \left(\frac{\beta}{2} - 1 \right) \left(\frac{\partial u_g^*}{\partial y^*} + \epsilon^2 \frac{\partial v_g^*}{\partial x^*} \right) &, \end{aligned}$$

where the following definitions were introduced:

$$We = \frac{\sigma}{\rho_1 \delta_{Nu} \bar{u}_{Nu}^2} = \left[\frac{3 \sigma^3 \nu_1}{\rho_1^3 g_x q^5} \right]^{1/3}, \quad \beta = 1 + \epsilon^2 \left(\frac{\partial \delta^*}{\partial x^*} \right)^2, \quad \delta^* = \frac{\delta}{\delta_{Nu}} \quad (2.18)$$

and We designates the Weber number. The non-dimensional form of the kinematic condition 2.6 is:

$$v^*|_{y^*=\delta^*} = \frac{d\delta^*}{dt^*}, \quad (2.19)$$

and the velocity boundary conditions 2.7 at the wall take the form:

$$u^*|_{y^*=0} = v^*|_{y^*=0} = w^*|_{y^*=0} = 0. \quad (2.20)$$

Finally, non-dimensionalizing equations 2.8 (without the dissipation term), 2.9 and 2.10 yields:

$$\begin{aligned} \frac{\partial \Theta^*}{\partial t^*} + u^* \frac{\partial \Theta^*}{\partial x^*} + v^* \frac{\partial \Theta^*}{\partial y^*} &= \frac{\chi \epsilon}{Pr Re} \left(\frac{\partial^2 \Theta^*}{\partial x^{*2}} + \frac{1}{\epsilon^2} \frac{\partial^2 \Theta^*}{\partial y^{*2}} \right), \\ -\frac{\partial \Theta_1^*}{\partial x^*} \frac{\partial \delta^*}{\partial x^*} + \frac{1}{\epsilon} \frac{\partial \Theta_1^*}{\partial y^*} &= -\Pi_k \frac{\partial \Theta_g^*}{\partial x^*} \frac{\partial \delta^*}{\partial x^*} + \frac{\Pi_k}{\epsilon} \frac{\partial \Theta_g^*}{\partial y^*}, \quad \Theta^*|_{y^*=0} = 1, \end{aligned} \quad (2.21)$$

where in the gaseous phase $\chi = \Pi_\alpha$ and in the liquid phase $\chi = 1$ with the thermal diffusivity ratio $\Pi_\alpha = \alpha_g/\alpha_l$ and thermal conductivity ratio $\Pi_k = k_g/k_l$, the Prandtl number Pr and the dimensionless temperature difference Θ^* :

$$Pr = \frac{\nu_1}{\alpha_l}, \quad \Theta^* = \frac{T - T_0}{T_w - T_0}, \quad (2.22)$$

whereby T_0 is the liquid inlet temperature and T_w the wall temperature (depending on the thermal boundary conditions, a different reference temperature may be introduced). Consequently the dimensionless groups scaling falling liquid films are:

$$Re, Fr, We, \frac{\delta_{Nu}}{L}, Pr, \Pi_\mu, \Pi_\rho, \Pi_k, \Pi_\alpha.$$

It is interesting to note that the Weber number and not the Kapitza number $Ka = \sigma \rho_1^{-1} g_x^{-1/3} \nu_1^{-4/3}$ (which is used frequently in literature pertaining to

film flow) results from the non-dimensionalization. However, the principal advantage of the Kapitza number is that it contains only liquid properties. Both dimensionless groups are related by $We = 3^{1/3} Ka Re^{-5/3}$ and are both used in this thesis. Finally, Panga & Balakotaiah (2003) argued that the Weber number, which relates inertial forces to viscous and capillary forces, accounts for the relative importance of “inertial forces” more accurately than the Reynolds number. They further showed that, as a consequence, neutral stability curves (see figure 2.4 in subsection 2.2.1) for different liquids collapse into one curve when plotted against the Weber number instead of the Reynolds number.

2.2 Wave dynamics

According to equation 2.11, the primary flow of falling liquid films can be described analytically. Yet in most instances such films are covered with interfacial waves yielding a complex topology. These waves are the cause for deviation from the characteristics of the primary flow, and understanding their dynamics as well as modelling these is of principal technical interest. Thereby, it is important to note that different waves or different stages in the evolution of a wave result from different modes of instability.

2.2.1 Film instability

As stated previously, the primary flow of a vertically falling liquid film displays instability at all values of the film Reynolds number Re , meaning that infinitesimal disturbances are amplified under these conditions. Before addressing this instability, the case of a horizontal liquid layer shall be considered here. The corresponding conditions are illustrated in figure 2.2, wherein the liquid-gas interface is disturbed harmonically in space. As can be observed when a rain drop impinges on a water surface in a recipient, the film thickness $\delta(x, t)$ at a given position oscillates periodically in time as a result of the initial disturbance. This film thickness oscillation propagates over the interface in the shape of a traveling wave. For the case of inviscid flow, the resulting waves are

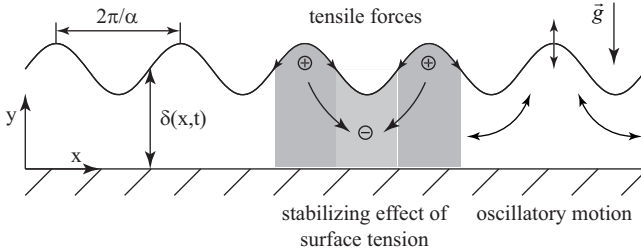


Figure 2.2: Sketch of a horizontal liquid layer with harmonic interfacial disturbance, showing the oscillatory liquid motion and the stabilizing effect of surface tension. Tensile forces cause large values of static pressure in the wave humps (plus sign) and small values in the wave troughs (minus sign).

neutral, meaning that the amplitude of the oscillation neither decays nor grows in time nor space, and their angular frequency is given by (see e.g. Whitham (1974)):

$$\omega = \left[\left(g + \frac{\sigma}{\rho_1} \alpha^2 \right) \alpha \tanh(\alpha \delta_0) \right]^{\frac{1}{2}}, \quad (2.23)$$

whereby δ_0 specifies the mean film thickness and α the wave number in x -direction. For this case, the cause for the sustained oscillation is the inertia of the liquid, the effect of which is stabilized by the effects of surface tension and gravity. From a dynamical point of view, the stabilizing effect of surface tension results from its influence on the liquid pressure distribution. Indeed, the interfacial pressure jump between liquid and gaseous phase is negative in regions of positive interface curvature and vice versa as can be derived from equation 2.17 for the inviscid case:

$$p_1 - p_g = -\sigma \kappa, \quad \kappa = \frac{\partial^2 \delta / \partial x^2}{(1 + (\partial \delta / \partial x)^2)^{3/2}}, \quad (2.24)$$

introducing the *interface curvature* κ . Assuming negligible pressure variations in the gaseous phase, this leads to a pressure distribution forcing the liquid from

the humps to the troughs (see figure 2.2) thus acting to suppress the waves. The effect of gravity is also stabilizing as it accelerates liquid flowing from hump to trough and decelerates liquid flowing from trough to hump (see figure 2.2). From a thermodynamical point of view, the film thickness oscillation transforms kinetic energy of the flow into potential and surface energy and vice versa, the total mechanical energy remaining constant. When fluid friction is considered, the total mechanical energy is gradually transformed into internal energy through dissipation, leading to decaying waves, which can be observed in the example of the rain drop impinging on a water surface. Thereby, the effect of viscous forces in the liquid is stabilizing as they always act counter to the flow.

When considering a vertically falling liquid film instead of a horizontal layer, the gravitational acceleration vector \vec{g} pictured in figure 2.2 is to be rotated so that it acts in x-direction. This change has several key consequences. First of all it leads to the development of a mean flow in x-direction. In the undisturbed developed case this is the primary flow in which potential energy is fully converted into internal energy. Further, as the component of \vec{g} in y-direction vanishes, gravity no longer exerts a stabilizing effect on the disturbed film. The stabilizing effect of surface tension remains unaltered nonetheless. However, the wavy motion of the interface can no longer be fully stabilized by the tensile forces due to the asymmetry introduced by the orientation of the gravitational acceleration vector. Indeed, the capillary-induced pressure force acting from wave hump to wave trough is countered by gravity if it is oriented upstream and supported by gravity if it is oriented down stream. The effect of gravity is thus destabilizing. Due to this, the importance of viscous forces grows. Whereas in the horizontal case even an inviscid liquid film is not unstable, owing to the stabilizing effect of surface tension and gravity, viscous forces are essential to stabilizing the vertical film.

The cause driving the ever growing deformation of the interface is the inertia of the liquid as is the case in the horizontal film. Consequently, it is to be expected that the falling liquid film can be fully stabilized for low values of the Reynolds number and for conditions under which the stabilizing effect of

surface tension is strong. Having developed a physical understanding of the film stability for the limiting horizontal and vertical cases, the behaviour of inclined films can be interpolated accordingly.

The reasoning developed above provides a physical insight into the film instability but cannot yield any quantitative analysis. This however can be obtained by applying *linear stability analysis* to the problem of falling liquid films, which was first performed by Yih (1954) and later by Brooke Benjamin (1957) and Yih (1963) (see Lin (1983) for a summary). When investigating the instability of the primary flow, a 2-dimensional analysis suffices as according to Squire (1933) and Yih (1955) every 3-dimensional instability is paired with a 2-dimensional one, appearing at a lower Reynolds number.

The basis for linear stability analysis of falling liquid films is the *Orr-Sommerfeld equation* written here in non-dimensional form (see e.g. Brooke Benjamin (1957)):

$$\begin{aligned} \phi'''' + \phi'' [iRe\alpha^* (\tilde{c}^* - 3y^* + 1.5y^{*2}) - 2\alpha^{*2}] + \\ \phi [iRe\alpha^* (-3 - \alpha^{*2} (\tilde{c}^* - 3y^* + 1.5y^{*2})) + \alpha^{*4}] = 0, \end{aligned} \quad (2.25)$$

where primes denote differentiation with respect to y^* and the dimensionless wave number α^* and *complex wave celerity* \tilde{c}^* are introduced according to:

$$\alpha^* = \alpha \delta_{Nu}, \quad \tilde{c}^* = \frac{\tilde{c}}{\bar{u}_{Nu}}. \quad (2.26)$$

It can be derived from the dimensionless Navier-Stokes equations in 2.15 by first eliminating the pressure terms through cross differentiation. Subsequently, the resulting single equation is linearized around the primary solution (given by the non-dimensional form of equations 2.11), yielding a differential equation for the velocity perturbations $u^{*'} and v^{*}' , which express the departure from the primary flow velocity field. Then, the velocity perturbations are expressed through the corresponding stream function perturbation Ψ^{*}' for which the following ansatz is chosen:$

$$\Psi^{*'} = \phi(y^*) \exp(i\alpha^*(x^* - \tilde{c}^*t^*)), \quad (2.27)$$

2 Falling film dynamics

where ϕ is a dimensionless function of the crosswise coordinate, and the stream-wise coordinate is non-dimensionalized using δ_{Nu} (i.e. $L=\delta_{Nu}$).

Four boundary conditions for the function ϕ can be derived (see e.g. Yih (1963)) (similarly to the procedure adopted for the derivation of the Orr-Sommerfeld equation) from the velocity boundary conditions at the wall (equations 2.20):

$$\phi|_{y^*=0} = 0, \quad \phi'|_{y^*=0} = 0, \quad (2.28)$$

and the inter-phase coupling conditions given by equations 2.17, yielding:

$$(1.5 - \tilde{c}^*) \left(\phi''|_{y^*=1} + \alpha^{*2} \phi|_{y^*=1} \right) + 3 \phi|_{y^*=1} = 0, \quad (2.29)$$

and:

$$(1.5 - \tilde{c}^*) \left(\phi'''|_{y^*=1} - 3\alpha^{*2} \phi'|_{y^*=1} \right) - i Re \alpha^* (1.5 - \tilde{c}^*)^2 \phi'|_{y^*=1} \\ - i We Re^{-1} \alpha^{*3} \phi|_{y^*=1} - i 3 \alpha^* \frac{g_y}{g_x} \phi|_{y^*=1} = 0, \quad (2.30)$$

where the kinematic condition (equation 2.19) was employed additionally. It should be noted that viscous forces in the gaseous phase have been neglected here. The fourth order Orr-Sommerfeld equation (equation 2.25) and the four boundary conditions in 2.28, 2.29 and 2.30 define the function ϕ uniquely for given values of Re , We , α^* , \tilde{c}^* and g_y/g_x .

From a physical standpoint, as shown in section 2.1, the flow in the liquid phase under the conditions considered here is well-defined by the dimensionless quantities Re , Ka , Fr (Fr can be expressed in terms of g_y/g_x using the other dimensionless groups) in addition to α^* which defines the initial condition for the dimensionless stream function. The complex wave celerity \tilde{c}^* therefore does not constitute a degree of freedom. Consequently, a condition for non trivial solutions of ϕ in the following form can be derived:

$$\tilde{c}^* = f(Re, Ka, Fr, \alpha^*), \quad (2.31)$$

whereby the complex wave celerity is defined by[†] $\tilde{c} = c_r + i c_i$. Thus, the above condition can be split into two equations:

$$c_r^* = f_r(Re, Ka, Fr, \alpha^*), \quad c_i^* = f_i(Re, Ka, Fr, \alpha^*). \quad (2.32)$$

The determination of these relations depends on the method employed to solve the Orr-Sommerfeld equation and shall not be detailed here (see Brooke Benjamin (1957); Yih (1963); Anshus & Goren (1966); Pierson & Whitaker (1977) for details). From the perspective of stability analysis the second relation in 2.32 is of interest. Indeed, inserting the complex wave celerity into the ansatz given by equation 2.27 yields:

$$\Psi' = \phi(y^*) \exp(\alpha^* c_i^* t^*) \exp(i \alpha^* (x^* - c_r^* t^*)), \quad (2.33)$$

which shows that for $c_i < 0$ initial perturbations are damped, hence the primary flow is stable and for $c_i > 0$ perturbations are amplified, hence the primary flow is unstable. Consequently, the case $c_i = 0$ defines the stability bound for the primary film flow. Anshus & Goren (1966) developed a procedure to determine equations 2.32 based on a simplified solution of the Orr-Sommerfeld equation, by assuming that the streamwise velocity of the primary flow is constant over the film thickness and corresponds to the surface velocity[‡]. Later, Liu *et al.* (1993) and Liu & Gollub (1994) showed that this approximate procedure yields good agreement with experimental data. Thereby, the authors reformulated the expression for the complex part c_i^* in equations 2.32 as a function of dimensionless wave frequency f^* as opposed to dimensionless wave number α^* , owing to the fact that, to induce surface waves in experiments, temporal perturbations are generally employed:

$$c_i^* = f_i(Re, Ka, Fr, f^*), \quad f^* = \frac{\alpha^* c_r^*}{2\pi} = \frac{f \delta_{Nu}}{\bar{u}_{Nu}}. \quad (2.34)$$

[†]Here c_r designates the physical *wave celerity*.

[‡]Two entries of matrix F (defined by equation 10 in the article) contain typographical errors and should correctly read $F(4,1) = (\frac{3}{2} - c) \beta_1 [i\alpha N_{Re} (\frac{3}{2} - c) + 3\alpha^2 + \beta_1^2]$ and $F(4,3) = (\frac{3}{2} - c) \beta_2 [i\alpha N_{Re} (\frac{3}{2} - c) + 3\alpha^2 + \beta_2^2]$.

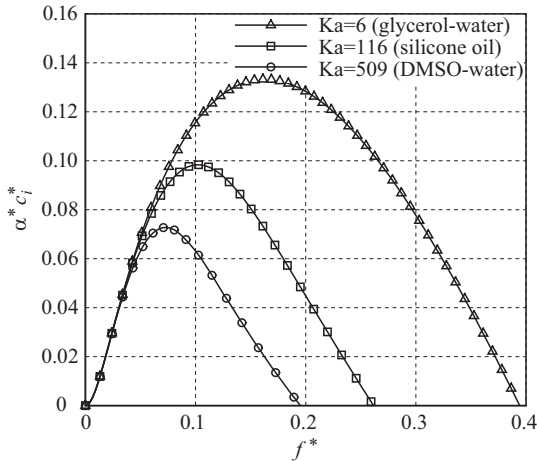


Figure 2.3: Dimensionless growth rate as a function of dimensionless wave frequency for a vertical film computed according to Anshus & Goren (1966) for different film liquids encountered in this work: $Re=15$.

Figure 2.3 depicts the dimensionless growth rate $\alpha^* c_i^*$ as a function of the dimensionless perturbation frequency f^* for different Ka values of the Kapitza number as calculated with the method by Anshus & Goren (1966). All graphs are plotted for $Re = 15$ and vertical conditions (i.e. $Fr = \infty$). The liquids (see tables 4.1 and 4.3) corresponding to the different graphs as well as the Reynolds number value are representative for conditions encountered in the context of this thesis. All pictured graphs display positive growth rates (associated with amplified disturbances) for small excitation frequencies (the region of negative growth rates is not pictured here). It can also be observed that disturbances are amplified selectively with respect to the excitation frequency, yielding growth rate maxima for specific values of f^* . The intersection points of the different graphs with the f^* axis (for $f^* > 0$) define the respective stability thresholds. Determining these for different values of the Reynolds number, yields the stability bounds of the primary film flow plotted in figure

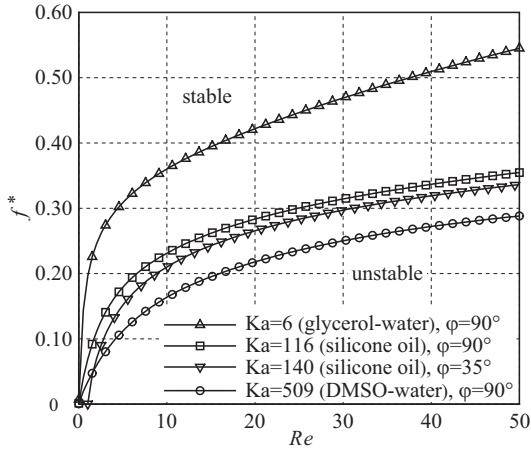


Figure 2.4: Linear stability bound computed according to Anshus & Goren (1966) for different film liquids and inclination angles $\varphi = \arctan(g_x/g_y)$ encountered in this work.

2.4, whereby an additional curve corresponding to an inclined film flow was included (for its calculation the method by Anshus & Goren (1966) was applied to inclined films). The respective plots validate all principal conclusions drawn in the previous physical discussion of film instability. Indeed, instability of the film flow is seen to occur for small frequencies i.e. large wavelengths, which weaken the stabilizing effect of tensile forces. Further, figure 2.4 shows that the film flow can be destabilized by increasing the Reynolds number, owing to the growing importance of inertia in relation to viscous forces. Finally, reducing the *inclination angle* $\varphi = \arctan(g_x/g_y)$ of the film has a stabilizing effect as the crosswise component of gravity increases. Indeed, in this case the intersection of the corresponding graph with the Re -axis, which corresponds to the *critical Reynolds number* Re_c (i.e. the Reynolds number below which the flow is stable for all perturbations) does not lie at the origin. Thus, inclined films as opposed to vertical films do not display instability for all values of the Reynolds num-

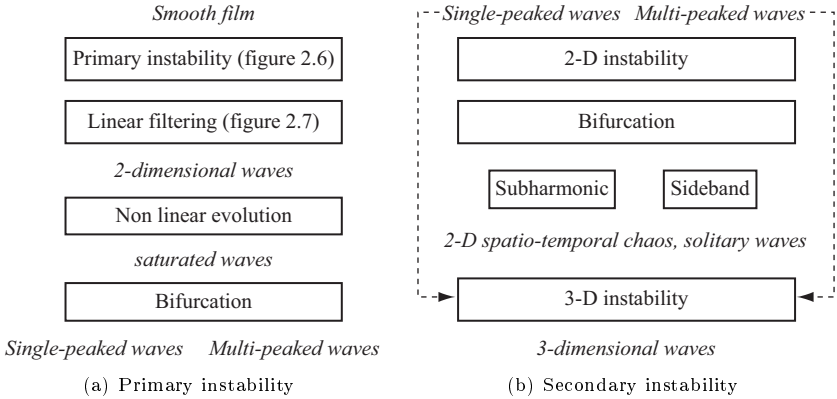


Figure 2.5: Hierarchy of the liquid film instability and associated wave dynamics.

ber. Accordingly, the critical Reynolds number is given by $Re_c = 5g_y/6g_x$ (see e.g. Yih (1955)). It should be reminded here that the linear stability analysis is only accurate for infinitesimal disturbances of the interface and can consequently only describe the inception of waves. Indeed, according to equation 2.33, surface waves would grow indefinitely for positive growth rates, which is refuted by experimental observations. This aberration results from the fact that for increasing wave amplitude the linearized governing equations no longer describe all relevant dynamical effects.

2.2.2 Wave evolution

Having discussed the origin of falling film instability, attention here is directed toward explaining the subsequent wave evolution, which leads to the interface topology pictured in figure 1.2. The hierarchy of different stages of wave development is illustrated in figure 2.5. Starting point of the following discussion shall be the primary flow of a vertical film, which is subjected to spatial noise in streamwise and spanwise direction at a position that shall be designated

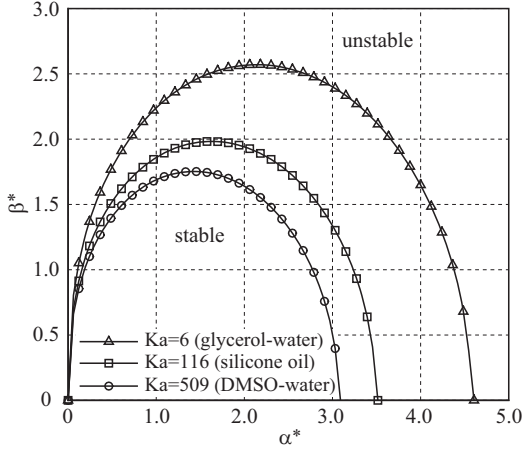


Figure 2.6: Linear stability bound for 3-dimensional perturbations as a function of streamwise (α^*) and spanwise (β^*) dimensionless wave number computed according to Chang *et al.* (1993) for different film liquids encountered in this work: $Re=15$.

as inlet. As pointed out by Pierson & Whitaker (1977), the development of the primary flow from an inlet channel influences the wave dynamics of the film at large values of the Reynolds number. This influence is neglected in the following analysis.

Although according to Squire's theorem it suffices to consider two dimensional perturbations when investigating the onset of film instability, the primary film flow is in fact unstable to 2- and 3-dimensional perturbations (see Brooke Benjamin (1961); Chang *et al.* (1993)). This is evidenced by figure 2.6, which shows the stability bound of the primary flow with respect to 3-dimensional perturbations of the form:

$$\Psi^{*l} = \phi(y^*) \exp(i(\alpha^* x^* + \beta^* z^* - c^* \alpha^* t^*)), \quad (2.35)$$

where β^* designates the dimensionless spanwise wave number. Results were

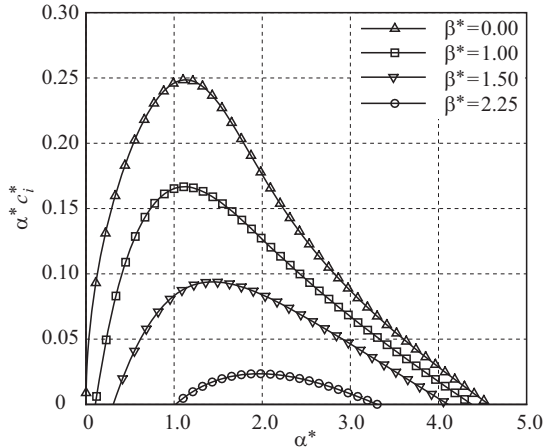


Figure 2.7: Dimensionless linear growth rates $\alpha^* c_i^*$ for 3-dimensional waves of different dimensionless spanwise wave number β^* computed according to Chang *et al.* (1993) for the glycerol-water mixture ($Ka=6$): $Re=15$.

computed on the basis of the dispersion relation given by Chang *et al.* (1993) (see equation 16 there), obtained by linear stability analysis, for the previously considered liquids. The corresponding growth rates for the glycerol-water mixture are plotted in figure 2.7. In addition to the influence of the streamwise wave number α^* , these graphs show that the wave displaying maximal growth rate is in fact 2-dimensional (i.e. $\beta^*=0$). It can thus be deduced that waves caused by 3-dimensional inlet disturbances are filtered through a linear mechanism, yielding a 2-dimensional wave of defined streamwise wave number α^* (see also Chang (1994)). As this 2-dimensional wave grows in amplitude, it is increasingly dominated by non-linear mechanisms leading to its saturation (Lin (1983) showed that the wave celerity decreases during this process which is associated with a slight shift in wavelength as reported by Chang (1994)). Experimental evidence of this saturation of surface waves was first published by Kapitza & Kapitza (1949) (see also Kapitza & Kapitza (1965) for an En-

glish translation). Subsequently, Lin (1969) and Gjevik (1970) (see also Pumir *et al.* (1983)) on the basis of long-wave equation models derived from the governing equations of the film flow according to the method by Benney (1966) (see subsection 2.2.3), provided analytical proof of wave saturation. In contrast to Benney (1966), who did not observe the saturation, Lin (1969) and Gjevik (1970) accounted for tensile forces in their models. Consequently, the effect of surface tension is essential to the stabilization of non-linear 2-dimensional surface waves. Kapitza & Kapitza (1949) showed that the saturated waves can adopt two distinct forms, depending on their wave number. For large wave numbers (i.e. small wavelengths), surface waves travel close to one another and exhibit a single maximum (see e.g. figure 4.12 in subsection 4.1.1). For smaller wave numbers (i.e. larger wavelengths), waves develop subsidiary maxima as their separation increases. Decreasing the wave number further, neighbouring waves become well separated by a residual film layer and travel independently as so called *solitary waves* (according to Drazin & Johnson (1989) “so-called because it often occurs as this single entity and is localised”) characterized by a main wave hump and one or several preceding capillary waves, which develop from the subsidiary maxima (see e.g. figure 3.21 in subsection 3.3.3). The different non-linear waveforms were also predicted by Trifonov & Tsvlodub (1991), Tsvlodub & Trifonov (1992) and Chang *et al.* (1993) (they refer to the two wave forms as γ_1 and γ_2) based on a multiple-equation model and a boundary layer model (see subsection 2.2.3) respectively. A clear picture of these different wave topologies is provided in the numerical works of Ramaswamy *et al.* (1996); Miyara (1999, 2000, 2001); Gao *et al.* (2003); Nosoko & Miyara (2004) and Trifonov (2008). Further, Liu *et al.* (1993), on the basis of highly resolving film thickness measurements for inclined films, determined the bound separating single-peaked and multi-peaked waves, showing that noise-driven waves filtered by the linear mechanism illustrated in figure 2.7 are multi-peaked.

The saturated amplitude waves described above are the result of primary film instability (see subfigure 2.5(a)). Liu *et al.* (1993) proved experimentally that these waves are subject to a secondary instability (see subfigure 2.5(b)) of 2-dimensional nature. Indeed, their experiments show that residual inlet

noise causes neighboring wave peaks to coalesce. Further, by applying Fourier analysis to the measured film thickness time traces they distinguish two different secondary instabilities of the saturated waves, depending on their wave number. The *subharmonic instability* appearing at small wave numbers and the *sideband instability* for large wave numbers. At the onset of both secondary instabilities, the film thickness power spectra display the emergence of additional peaks in the neighborhood of the saturated wave number. In terms of the film interface topology this corresponds to the coalescence of neighboring wave peaks. Liu *et al.* (1993) determined that the bound between the two instabilities in terms of wave number lies above the bound delimiting single-peaked and multi-peaked waves. The physical demarcation of these respective instabilities was elucidated by Cheng & Chang (1995). The authors find that the principal difference between these instabilities is the number of wave peaks remaining in a given region after the coalescence has taken place. For the subharmonic instability they show that always two neighboring wave peaks coalesce (associated with the appearance of a subsidiary wave number peak at half the initial wave number [†]), while the sideband instability leads to the simultaneous coalescence of three wave peaks (associated with the appearance of a subsidiary wave number peak on either side of the initial wave number). They also show that the subsidiary peaks in the power spectrum are not monochromatic but rather broad, leading to an irregular wave pattern bearing the characteristics of 2-dimensional spatio-temporal chaos (see Liu & Gollub (1993)). Liu & Gollub (1994) argue that the local defects introduced by this irregularity lead to the localized appearance of solitary waves due to further wave peak coalescence and the inelastic nature of wave interactions (waves of different amplitude and thus different celerity merge instead of passing through one another; see also Malamataris *et al.* (2002)). Further, Chang *et al.* (1996b) (see also Meza & Balakotaiah (2008)) show that the resulting solitary waves then coalesce to form even larger ones, designating this mechanism as *coarsening dynamics*. The cascade comes to a halt when the wave separation is such that new waves

[†]This period-doubling was previously identified experimentally by Brauner & Moalem Maron (1982) and confirmed numerically by Prokopiou *et al.* (1991).

develop on the residual layer between wave peaks as a result of the primary film instability. The halting of the cascade is in accordance with the observation by Chang *et al.* (1994) that there exists a threshold wave number for solitary waves underneath which these are stable with respect to 2-dimensional disturbances.

Because the different instabilities mentioned above are *noise sustained* (i.e. perturbations over a wide range of wave numbers or frequencies are amplified) the falling film wave dynamics are considerably influenced by the inlet conditions, based on which two main wave evolution scenarios can be discerned. When disturbances at the inlet consist of white noise, so called *natural waves* develop. These result from the linear (and non-linear) filtering mechanism of the primary instability and the subsequent subharmonic instability, development of solitary waves and coarsening dynamics (see Chang *et al.* (1996 *a, b*, 2002); Nosoko & Miyara (2004)). More simple wave dynamics are encountered when a relatively strong monochromatic (temporal) excitation is superimposed on the white inlet noise (see e.g. Nosoko *et al.* (1996)). In that case, a wave of corresponding wave number develops close to the inlet, bypassing the linear filtering mechanism. Due to the strong forcing, such *excited waves* saturate close to the inlet and are maintained over a long distance before residual inlet noise leads to the development of spatio-temporal chaos due to the secondary instabilities. Nosoko *et al.* (1996) determined empirical expressions for the dimensionless physical *wave celerity*[†] c^* (see figure 2.8) and amplitude δ_{max}/δ_{Nu} (see figure 2.9) of these monochromatically excited 2-dimensional saturated waves. Their results show that wave celerity decreases with increasing excitation frequency and increases with wave amplitude. Natural saturated waves have a considerably shorter lifespan since, due to their slower development, the secondary perturbations are already more pronounced at the time of saturation.

Joo & Davis (1992) (see also Chang *et al.* (1993)), on the basis of a strongly non-linear film thickness evolution equation, showed that saturated 2-dimensional waves are unstable with respect to spanwise perturbations of small wave num-

[†]The symbol c will be used instead of c_r in the remaining text.

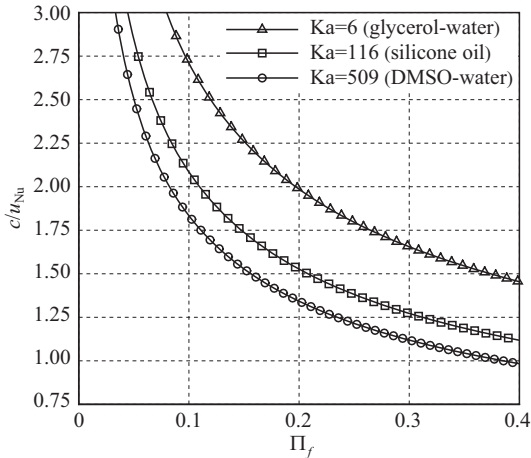


Figure 2.8: Wave celerity as a function of wave frequency computed according to the empirical relations of Nosoko *et al.* (1996) for different film liquids encountered in this work.

ber[†]. Thereby, they determined the stability bound for this 3-dimensional instability and found that it depends on the wave number of the considered 2-dimensional wave (the critical spanwise wave number is shown to increase with the wave number of the 2-dimensional wave). Due to this instability, residual inlet noise can cause 2-dimensional saturated waves to transit into 3-dimensional structures directly. Therefore, it shall be considered as a secondary instability (see figure 2.5(b)). First experimental evidence of this 3-dimensional instability was published by Tailby & Portalski (1962) in the form of photographs of the naturally developing film interface (similar photographs were published later by Alekseenko *et al.* (1994)). Results show a highly irregular 3-dimensional interface topology sufficiently far downstream of the inlet. The most compelling feature of the photographs are horseshoe-shaped wave

[†]Chang *et al.* (1994) established that this is not the case for the non-linear evolution leading up to saturation.

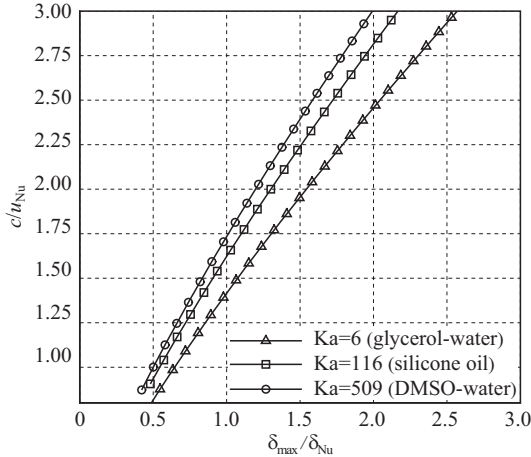


Figure 2.9: Wave celerity as a function of wave amplitude computed according to the empirical relations of Nosoko *et al.* (1996) for different film liquids encountered in this work.

crests (*horseshoe waves*) preceded by capillary waves with equally shaped wave fronts. Different horseshoe-waves are either separated from one another or represent spanwise modulations of a connected originally 2-dimensional wave front. According to Chang *et al.* (1994) the transition of saturated waves from 2- to 3-dimensional wave dynamics can take two paths in the considered case of natural waves, depending on the level of residual spanwise noise in relation to residual streamwise noise. If sufficiently large spanwise perturbations are present, the 2-dimensional wave fronts distort into a *checkerboard pattern*, characterized by spanwise modulations which are out of phase for successive wave fronts. If spanwise residual noise is weak, the 2-dimensional secondary instability dominates further evolution of the saturated wave[†]. As stated above, this evolution culminates in the development of large well separated solitary

[†]Consequently, if the inlet noise does not favor perturbations of a specific direction the onset of 2- and 3-dimensional secondary instability roughly coincides.

waves, which are stable with respect to 2-dimensional perturbations. According to Chang *et al.* (1994) they are however unstable to spanwise disturbances, which cause the 2-dimensional wave fronts to distort in spanwise direction. As opposed to the *checkerboard instability*, the resulting spanwise modulations on successive wave fronts are in phase (see figure 3.7 in subsection 3.2.1 and figure 5.47 in subsection 5.5). Thereby, their crests distort into a horseshoe shape. If these horseshoe crests expand sufficiently downstream, they pinch-off due to the interaction of successive wave fronts. Waves then travel as solitary isolated 3-dimensional disturbances, constituted by a large horseshoe-shaped wave crest and several preceding capillary waves. Petviashvili & Tsvelodub (1978) were the first to numerically construct a 3-dimensional wave of this kind (strictly speaking they constructed a soliton as established in subsection 2.2.3). Recently, Alekseenko *et al.* (2005) validated the results of Petviashvili & Tsvelodub (1978) experimentally using a *Laser Induced Fluorescence* (LIF) technique to measure the film thickness as a function of stream- and spanwise coordinates. Finally, the second of the above described evolution scenarios proposed by Chang *et al.* (1994) was validated by Kunugi & Kino (2005), who solved the full Navier-Stokes equations numerically for a vertical water film.

Trifonov (1990) was the first to differentiate the two 3-dimensional instabilities discussed above based on numerical solutions of a multiple-equation model (see subsection 2.2.3). Subsequently, Liu *et al.* (1992) (see also Liu *et al.* (1995) for a detailed account) proved their existence experimentally. The authors introduced the term *synchronous instability* to describe the second case. Based on their experiments, the authors determined a bound delimiting the two resulting wave regimes in terms of the saturated 2-dimensional wave's wave number, showing that single-peaked waves develop checkerboard spanwise patterns and waves with large separations develop synchronous spanwise patterns. A very clear picture of the wave topology resulting from synchronous instability is provided by the experiments of Park & Nosoko (2003). In their experiments, the authors imposed a monochromatic spatial excitation in spanwise direction in addition to the temporal excitation, thus bypassing the 2-dimensional secondary wave dynamics and yielding 3-dimensional waves of prescribed span-

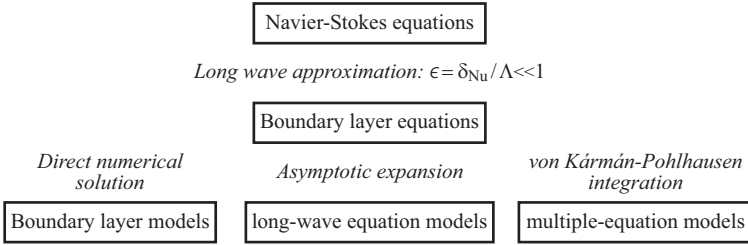


Figure 2.10: Hierarchy of models describing the dynamics of falling film surface waves.

and streamwise wavelength near the inlet[†]. Subsequently, Scheid *et al.* (2006) calculated the interface topology numerically for the regimes considered by Park & Nosoko (2003) based on a multiple-equation model (see subsection 2.2.3), showing excellent agreement.

2.2.3 Wave modeling

Having established the physical basics and phenomenology of falling liquid film wave dynamics, this section is dedicated to their modelling. As will be shown, the detailed elucidation of transport processes in the falling film, to which this thesis is devoted, can contribute to the improvement of such models. The most common modelling strategies for film flows are listed in figure 2.10 in a hierarchical manner. The common basis for the models are the boundary layer equations of film flow, which can be derived from the Navier-Stokes equations under the assumption that the *wavelength* Λ of surface waves is much larger than the characteristic film thickness δ_{Nu} . This assumption is often designated as *long-wave approximation* and is similar to the assumption underlying the classical boundary layer theory by Prandtl (1938) (see also Schlichting (1951)). Introducing the long-wave approximation $\epsilon = \delta_{\text{Nu}} / \Lambda \ll 1$ in the 2-dimensional Navier-Stokes and continuity equations 2.15 for the liquid phase and discarding

[†]One of the cases considered by Park & Nosoko (2003) was simulated in this thesis (see section 5.5).

terms containing ϵ to the second or higher order, yields the first order boundary layer equations:

$$\begin{aligned} \frac{\partial u^*}{\partial t^*} + u^* \frac{\partial u^*}{\partial x^*} + v^* \frac{\partial u^*}{\partial y^*} &= -\frac{\partial p^*}{\partial x^*} + \frac{1}{\epsilon Re} \frac{\partial^2 u^*}{\partial y^{*2}} + \frac{3}{\epsilon Re}, \\ 0 &= -\frac{\partial p^*}{\partial y^*} + \frac{\epsilon}{Re} \frac{\partial^2 v^*}{\partial y^{*2}} - \frac{1}{Fr^2}, \quad \frac{\partial u^*}{\partial x^*} + \frac{\partial v^*}{\partial y^*} = 0, \end{aligned} \quad (2.36)$$

and analogously the inter-phase coupling conditions 2.17 (neglecting viscous forces in the gaseous phase: $\Pi_\mu \ll 1$) reduce to:

$$p_1^* - p_g^* + We \epsilon^2 \frac{\partial^2 \delta^*}{\partial x^{*2}} = \frac{2\epsilon}{Re} \frac{\partial v_1^*}{\partial y^*}, \quad \frac{\partial u_1^*}{\partial y^*} = 0. \quad (2.37)$$

Importantly, in the normal coupling condition the term containing the Weber number is retained, although it includes ϵ^2 . Omitting this term would eliminate the effect of tensile forces, which are crucial to falling film wave dynamics as was established in subsection 2.2.1[†]. From figure 2.7 it can be discerned that $Re=15$ and $\epsilon=\alpha^*/2\pi\approx 0.2$. Consequently, the orders of magnitude neglected in the above equations are $\mathcal{O}(\epsilon^2/Re)=0.003$, $\mathcal{O}(\epsilon^2)=0.04$ and $\mathcal{O}(\epsilon^3/Re)=0.0005$, and the retained orders of magnitude are $\mathcal{O}(\epsilon)=0.2$, $\mathcal{O}(1/Re)=0.07$, $\mathcal{O}(\epsilon/Re)=0.01$ and $\mathcal{O}(\epsilon^2 We)=0.004$. It is evident here that due to the relatively large value of Re (and relatively small value of $We=0.1$) the long-wave approximation is not very accurate for the considered case. However, its quality increases drastically with decreasing values of Re (strictly speaking $\mathcal{O}(Re)=1$). The above equations can be further simplified by integrating the crosswise momentum equation from y^* to δ^* using the normal inter-phase coupling condition. This yields the pressure distribution which can then be inserted into the streamwise momentum equation, taking the form:

$$\frac{\partial u^*}{\partial t^*} + u^* \frac{\partial u^*}{\partial x^*} + v^* \frac{\partial u^*}{\partial y^*} = We \epsilon^2 \frac{\partial^3 \delta^*}{\partial x^{*3}} - \frac{1}{Fr^2} \frac{\partial \delta^*}{\partial x^*} + \frac{3}{\epsilon Re} + \frac{1}{\epsilon Re} \frac{\partial^2 u^*}{\partial y^{*2}}, \quad (2.38)$$

[†]Strictly speaking the term can only be retained if the order of magnitude of the Weber number is $\mathcal{O}(We)=\epsilon^{-1}$.

whereby pressure variation in the gaseous phase was neglected ($p_g = \text{const}$). Introducing the following estimation for the wavelength Λ :

$$\Lambda = \left(\frac{WeRe^2\nu_l^2}{g_x} \right)^{\frac{1}{3}} \rightarrow \epsilon = \frac{\delta_{Nu}}{\Lambda} = \left(\frac{3}{WeRe} \right)^{\frac{1}{3}}, \quad (2.39)$$

and adding the kinematic condition as well as the tangential inter-phase coupling condition and the wall boundary conditions, finally yields the 2-dimensional first order *boundary layer equations* of film flow:

$$\begin{aligned} \frac{\partial u^*}{\partial t^*} + u^* \frac{\partial u^*}{\partial x^*} + v^* \frac{\partial u^*}{\partial y^*} &= \Pi_{BL} \left[\frac{\partial^3 \delta^*}{\partial x^{*3}} + \frac{1}{3} \frac{\partial^2 u^*}{\partial y^{*2}} + 1 \right] - \frac{1}{Fr^2} \frac{\partial \delta^*}{\partial x^*}, \\ \frac{\partial u^*}{\partial x^*} + \frac{\partial v^*}{\partial y^*} &= 0, \quad \frac{\partial u^*}{\partial y^*} \Big|_{y^*=\delta^*} = 0, \quad u^*|_{y^*=0} = v^*|_{y^*=0} = 0, \quad (2.40) \\ \frac{\partial \delta^*}{\partial t^*} &= v^*|_{y^*=\delta^*} - \frac{\partial \delta^*}{\partial x^*} u^*|_{y^*=\delta^*}, \quad \Pi_{BL} = 3^{2/3} \frac{We^{1/3}}{Re^{2/3}}, \end{aligned}$$

which depend only on two dimensionless groups namely Fr and Π_{BL} . Note also that the superscript l , differentiating interfacial conditions on the liquid side from those on the gas side, has been dropped, as only the liquid phase is of interest here.

Different modelling strategies pictured in figure 2.10 differ with respect to the level of further approximation to the governing equations. A comprehensive overview of available models as well as a characterization of their quality is provided by the collectivity of the works by Demekhin *et al.* (1987); Alekseenko *et al.* (1994); Chang *et al.* (1994); Frenkel & Indireskumar (1996); Ruyer-Quil (1999); Chang & Demekhin (2002); Mudunuri & Balakotaiah (2006) and Trifonov (2008).

So called boundary layer models rely on the direct numerical solution of the boundary layer equations 2.40. Such calculations have been performed by Demekhin *et al.* (1983, 1987) and Chang *et al.* (1993, 1996 *a*) for 2-dimensional film flows, and by Chang *et al.* (1994) for 3-dimensional conditions. Thereby, Demekhin *et al.* (1987) performed calculations under the same conditions as the

measurements by Alekseenko *et al.* (1985), showing good agreement between numerical and experimental data. In general, the mentioned works show that the boundary layer equations of film flow describe its dynamics with good accuracy. This accuracy however, bears a considerable computational cost as the numerical solution of equations 2.40, as is the case for the full system of governing equations, has to be performed in the temporally varying liquid phase domain, the free surface of which has to be tracked.

Due to this complexity, simplified modelling approaches for the prediction of falling film wave dynamics have been studied ever since the pioneering work of Kapitza (1948). One such approach consists of deriving a single evolution equation for the film thickness, the so called *long-wave equation*, from the boundary layer equations presented above. The first step in this approach is the *asymptotic expansion* of the dimensionless stream function Ψ^* in terms of the length scale ratio ϵ :

$$\begin{aligned} \Psi^* &= \Psi_{\text{Nu}}^* + \Psi^{*'} = \Psi_{\text{Nu}}^* + \Psi_0^{*'} + \epsilon \Psi_1^{*'} + \epsilon^2 \Psi_2^{*'} + \dots, \\ \frac{\partial \Psi^*}{\partial y} &= u^*, \quad -\frac{\partial \Psi^*}{\partial x} = v^*, \quad \Psi_{\text{Nu}}^* = \frac{3}{2}y^{*2} - \frac{3}{6}y^{*3}, \end{aligned} \tag{2.41}$$

whereby Ψ_{Nu}^* signifies the dimensionless stream function for the developed smooth film (Ψ_{Nu}^* and consequently Ψ^* are arbitrarily set to zero at the wall) and $\Psi^{*'}$ the departure from that solution. This ansatz must then satisfy equation 2.38 written for the dimensionless stream function $\Psi^* = \Psi_{\text{Nu}}^* + \Psi^{*'}$:

$$\begin{aligned} \frac{\partial^3 \Psi^{*'}}{\partial y^{*3}} &= \epsilon Re \left[\frac{\partial^2 \Psi^{*'}}{\partial y^* \partial t^*} + \frac{\partial^2 \Psi^{*'}}{\partial y^* \partial x^*} \left[\frac{\partial \Psi^{*'}}{\partial y^*} + u_{\text{Nu}}^* \right] - \frac{\partial \Psi^{*'}}{\partial x^*} \left[\frac{\partial^2 \Psi^{*'}}{\partial y^{*2}} + \frac{\partial u_{\text{Nu}}^*}{\partial y^*} \right] \right] \\ -Re We \epsilon^3 &\frac{\partial^3 \delta^*}{\partial x^{*3}} + \frac{\epsilon Re}{Fr^2} \frac{\partial \delta^*}{\partial x^*}, \end{aligned} \tag{2.42}$$

and the reformulated wall boundary, tangential inter-phase coupling and kine-

matic conditions of equation 2.40:

$$\begin{aligned} \left. \frac{\partial \Psi^{*'}}{\partial y^*} \right|_{y^*=0} &= \left. \frac{\partial \Psi^{*'}}{\partial x^*} \right|_{y^*=0} = 0, & \left. \frac{\partial^2 \Psi^{*'}}{\partial y^{*2}} \right|_{y^*=\delta^*} + \left. \frac{\partial u_{\text{Nu}}^*}{\partial y^*} \right|_{y^*=\delta^*} &= 0, \\ \frac{\partial \delta^*}{\partial t^*} &= - \left. \frac{\partial \Psi^{*'}}{\partial x^*} \right|_{y^*=\delta^*} - \frac{\partial \delta^*}{\partial x^*} \left. \frac{\partial \Psi^{*'}}{\partial y^*} \right|_{y^*=\delta^*} - \frac{\partial \delta^*}{\partial x^*} u_{\text{Nu}}^* \Big|_{y^*=\delta^*}. \end{aligned} \quad (2.43)$$

The different coefficients $\Psi_i^{*'}$ of the stream function expansion are successively determined from equations 2.42 and 2.43 by neglecting all terms of orders higher than the considered one (i.e. $< \epsilon^i$). That is, to determine $\Psi_0^{*'}$ all terms of order ϵ or higher in equation 2.42 are neglected, yielding a third order differential equation for $\Psi_0^{*'}$. This equation is then solved with the boundary conditions and the tangential coupling condition in 2.43. The obtained solution for $\Psi_0^{*'}$ is then inserted into the normal coupling condition yielding a differential equation for the dimensionless film thickness δ^* . This zeroth-order approximation yields:

$$\Psi_0^{*'} = \frac{3}{2} (\delta^* - 1) y^{*2}, \quad \frac{\partial \delta^*}{\partial t^*} = - \frac{\partial}{\partial x^*} (\delta^{*3}). \quad (2.44)$$

The procedure can be repeated to determine all remaining coefficients Ψ_i^* , the final result always being a differential equation for δ^* . Thereby it should be noted that at every step all lower order coefficients Ψ_{i-1}^* have been previously determined and are thus known so that equation 2.42 always yields a differential equation for the current coefficient Ψ_i^* . The result for the first-order approximation $\Psi_1^{*'}$ consequently is:

$$\begin{aligned} \Psi_1^{*'} &= \frac{3}{40} y^{*5} Re \frac{\partial \delta^*}{\partial x^*} \delta^* - \frac{3}{8} y^{*4} Re \delta^{*2} \frac{\partial \delta^*}{\partial x^*} + \frac{1}{6} y^{*3} \left[\frac{Re}{Fr^2} \frac{\partial \delta^*}{\partial x^*} - \epsilon^2 Re We \frac{\partial^3 \delta^*}{\partial x^{*3}} \right] \\ &+ \frac{1}{2} y^{*2} \left[3 Re \delta^{*4} \frac{\partial \delta^*}{\partial x^*} - \frac{Re}{Fr^2} \delta^* \frac{\partial \delta^*}{\partial x^*} + \epsilon^2 Re We \delta^* \frac{\partial^3 \delta^*}{\partial x^{*3}} \right], \end{aligned} \quad (2.45)$$

yielding the first order film thickness evolution equation:

$$\frac{\partial \delta^*}{\partial t^*} = - \frac{6}{5} \epsilon Re \delta^{*6} \frac{\partial^2 \delta^*}{\partial x^{*2}} - \frac{36}{5} \epsilon Re \delta^{*5} \frac{\partial \delta^*}{\partial x^*} \frac{\partial \delta^*}{\partial x^*} - \frac{1}{3} \delta^{*3} \left[\epsilon^3 Re We \frac{\partial^4 \delta^*}{\partial x^{*4}} \right]$$

$$-\epsilon \frac{Re}{Fr^2} \frac{\partial^2 \delta^*}{\partial x^{*2}} \Big] - \delta^{*2} \frac{\partial \delta^*}{\partial x^*} \left[\epsilon^3 Re We \frac{\partial^3 \delta^*}{\partial x^{*3}} - \epsilon \frac{Re}{Fr^2} \frac{\partial \delta^*}{\partial x^*} + 3 \right], \quad (2.46)$$

whereby the temporal film thickness derivatives resulting from 2.42 were expressed as spatial derivatives using the zeroth-order approximation in 2.44 (this is not a necessary step but simplifies the resulting long-wave equation). To determine higher order approximations, the boundary layer equations considered here can no longer be used as they themselves (with the exception of tensile terms) only retain terms of magnitude ϵ . In that case the full Navier-Stokes equations along with corresponding boundary and coupling conditions have to be considered.

The asymptotic expansion procedure described above was first applied to falling liquid films by Benney (1966), which is why the resulting long-wave equation is frequently designated as Benney equation or *Benney-type equation*. However, Benney (1966) did not retain tensile terms in his first order approximation, as he assumed $\mathcal{O}(We)=1$. Strictly speaking, equation 2.46 was first published by Gjevik (1970), who required $\mathcal{O}(We)=\epsilon^{-2}$, leading to the incorporation of tensile effects. As mentioned previously, Gjevik (1970) as opposed to Benney (1966) showed his equation to predict saturated surface waves, proving that accounting for tensile effects is essential to modelling falling film wave dynamics. Thus, to avoid any confusion, the film thickness evolution equation resulting from the asymptotic expansion method shall simply be designated as long-wave equation. It is a non-linear partial differential equation for the local instantaneous film thickness that can be solved numerically for given initial and streamwise boundary conditions.

Table 2.1 lists different long-wave equation models along with the order at which the underlying asymptotic expansion is truncated and the scaling employed to simplify the governing equations. Based on the works by Benney (1966) and Gjevik (1970), Lin (1974) and Nakaya (1975) derived long-wave equations by truncating the asymptotic expansion at second and third order respectively. Thereby, the authors were able to impose less stringent restrictions on the Weber number in order to retain tensile terms. An evaluation

Source	Order	Scaling	Blow up
Benney (1966)	1	$\mathcal{O}(We)=1, \mathcal{O}(Re)=1$	yes
Gjevik (1970)	1	$\mathcal{O}(We)=\epsilon^{-2}, \mathcal{O}(Re)=1$	yes
Lin (1974)	2	$\mathcal{O}(We)=\epsilon^{-1}, \mathcal{O}(Re)=1$	yes
Nakaya (1975)	3	$\mathcal{O}(Re)=1$	yes
Ooshida (1999)	2	$\mathcal{O}(We)=\epsilon^{-2}, \mathcal{O}(Re)=1$	no
Panga & Balakotaiah (2003)	6/5	$\mathcal{O}(We)=\epsilon^{-2}, \mathcal{O}(Ka)=1$	yes
Panga <i>et al.</i> (2005)	6/5	$\mathcal{O}(We)=\epsilon^{-2}, \mathcal{O}(Ka)=1$	no

Table 2.1: List of long-wave equation models based on the asymptotic expansion method by Benney (1966).

of the quality of predictions produced by the long-wave equations of Gjevik (1970), Lin (1974) and Nakaya (1975) is provided in Panga *et al.* (2005) and Ruyer-Quil & Manneville (2000). There, the authors compared linear stability bounds and non-linear saturated wave celerities predicted by the respective model equations. Results show that stability bounds for all mentioned long-wave equations correspond well with those computed from the Orr-Sommerfeld equation for large values of the Weber number as the employed scaling calls for (see discussion regarding equation 2.37). Indeed, it is a general property of long-wave equations, resulting from asymptotic expansion that the absolute stability threshold (for vertical films $We_c=\infty$) is predicted accurately. This stems from the fact that the long-wave assumption is exactly fulfilled i.e. $\alpha_c^*=\epsilon_c=0$ under critical conditions. For smaller values of the Weber number Panga *et al.* (2005) showed that long-wave linear stability bounds diverge considerably from the Orr-Sommerfeld bounds. Interestingly they also demonstrate that increasing the order of the expansion does not improve linear predictions. Concerning the prediction of non-linear saturated wave celerity, Ruyer-Quil & Manneville (2000) established a similar behaviour for the respective long-wave equations. While at large values of the Weber number model predictions correspond well with direct solutions of the first order boundary layer equations, they diverge

considerably for smaller ones. Most importantly, the authors showed that below a certain Weber number threshold the long-wave equations do not yield saturated wave solutions. This behaviour was investigated by Pumir *et al.* (1983) on the basis of the long-wave equation of Gjevik (1970). These authors showed that below the threshold Weber number value an unlimited local increase in film thickness arises, causing calculations to abort. They designated this behaviour as *finite time blow up* and associated it with the presence of highly non-linear terms in the film thickness evolution equation (up to δ^{*6} in equation 2.46). It is evident that finite time blow up constitutes a major limitation of standard long-wave equations and attention here is now directed toward remedies for this unwanted property.

As mentioned above, the strong non-linearity of standard long-wave equations causes finite time blow up. Consequently, the latter can be suppressed by considering weakly non-linear forms of the long-wave equations, which are derived under the assumption of small wave amplitudes. Therefore, the dimensionless film thickness in the considered long-wave equation is expressed by $\delta^* = 1 + \gamma\eta^*$, whereby $\gamma\eta^*$ designates the departure of the film thickness from the smooth developed state and γ is a small parameter ($\gamma \ll 1$) quantifying the amplitude of that deviation. Inserting this into the first order long-wave equation derived by Gjevik (1970) (equation 2.46) yields:

$$\begin{aligned}
 4 \frac{\partial \eta^*}{\partial t^*} + 6\gamma \eta^* \frac{\partial \eta^*}{\partial \xi^*} + \frac{6}{5} \epsilon (Re - Re_c) \frac{\partial^2 \eta^*}{\partial \xi^{*2}} + \epsilon^3 \gamma Re W e \frac{\partial \eta^*}{\partial \xi^*} \frac{\partial^3 \eta^*}{\partial \xi^{*3}} \\
 + \frac{1}{3} \epsilon^3 Re W e \frac{\partial^4 \eta^*}{\partial \xi^{*4}} + \frac{18}{5} \epsilon \gamma (2Re - Re_c) \frac{\partial \eta^*}{\partial \xi^*} \frac{\partial \eta^*}{\partial \xi^*} = 0,
 \end{aligned}
 \tag{2.47}$$

where the moving coordinate $\xi^* = x^* + t^*$ was introduced and only terms of order $\gamma \epsilon$ or larger were retained. Further $\partial \eta^* / \partial \xi^*$ was replaced with $\partial \eta^* / \partial t^*$ in one instance. It is evident that the strong non linear terms of equation 2.46 are no longer present in this weakly non-linear equation. Assuming $\mathcal{O}(\gamma) = \epsilon$ and retaining only terms of order ϵ the amplitude equation takes the following

form:

$$\frac{\partial H}{\partial T} + H \frac{\partial H}{\partial \Xi} + \frac{\partial^2 H}{\partial \Xi^2} + \frac{\partial^4 H}{\partial \Xi^4} = 0, \quad (2.48)$$

where Ξ , T and H are conveniently chosen substitutions for amplitude, time and moving coordinate:

$$\Xi = \xi^* \left[\frac{18 (Re - Re_c)}{5 Re We} \right]^{\frac{1}{2}}, \quad T = t^* \frac{18}{5} \frac{3}{10} \frac{(Re - Re_c)^2}{Re We}, \quad (2.49)$$

$$H = \eta^* 5 \left[\frac{5}{18} \right]^{\frac{1}{2}} (Re We)^{\frac{1}{2}} (Re - Re_c)^{-\frac{3}{2}}.$$

In the literature, equation 2.48 is designated as *Kuramoto-Shivasinsky equation* and was first published by Kuramoto & Tsuzuki (1974) (see also Kuramoto & Tsuzuki (1976)) in the context of reaction kinetics. Later, Sivashinsky & Michelson (1980) identified its applicability to film flows and used it to simulate falling film wave dynamics. Chang (1986) evaluated predictions of the equation on the basis of experimental data by Alekseenko *et al.* (1985) with respect to maximal film thickness and non-linear wave celerity, showing reasonable agreement for small wave amplitudes. However, the equation has a serious shortcoming as it does not describe dispersion i.e. the dependence of wave growth rates on wavelength. Another weakly non-linear equation can be obtained in a similar manner on the basis of the third order long-wave equation (see e.g. Nakaya (1975)). The equation is designated as *Korteweg-de Vries equation* (see Korteweg & de Vries (1895) and Chang & Demekhin (2002)) and shall simply be written here without derivation:

$$\frac{\partial H}{\partial T} + H \frac{\partial H}{\partial \Xi} + v \frac{\partial^3 H}{\partial \Xi^3} = 0. \quad (2.50)$$

Thereby, the quantities H , T and Ξ are defined differently to equation 2.49. A significant property of the equation is its ability to describe the behaviour of *solitons* i.e. solitary waves that preserve their properties after interacting with one another (see Drazin & Johnson (1989)). Inertial and tensile effects however are not accounted for. The 3-dimensional form of the equation was employed

by Petviashvili & Tsvelodub (1978) to construct the first published solution of a 3-dimensional soliton on a falling liquid film.

Another method of suppressing finite time blow up is by regularizing the long-wave equations. This was first performed by Ooshida (1999) on the basis of the second order long-wave equation of Gjevik (1970), deriving a regularized long-wave equation model. Although predictions of the linear stability bound for small Weber number values are considerably better than those of standard long-wave equations (see e.g. Panga *et al.* (2005) for a comparison), Ruyer-Quil & Manneville (2000) showed that non-linear wave celerities are considerably underpredicted by the model. A further improvement was obtained by Panga & Balakotaiah (2003) who introduced different scaling ($\mathcal{O}(Ka)=1$ instead of $\mathcal{O}(Re)=1$) to derive a long-wave equation on the basis of an expansion up to order $6/5$. The model predicts the linear stability bound quite accurately up to Weber number values of unity but is not free of finite time blow up as shown by Ruyer-Quil & Manneville (2004). Later, Panga *et al.* (2005) regularized their model using the same approach as Ooshida (1999), eliminating finite time blow up. Although model predictions of linear stability suffer slightly in quality due to this, the authors showed (see also Balakotaiah & Mudunuri (2004)) that their regularized model predicts considerably higher non-linear wave celerities than that of Ooshida (1999), however still underpredicting the boundary layer equation results by about 10% (see Panga *et al.* (2005) and Ruyer-Quil & Manneville (2000)). In their article, Panga *et al.* (2005) also developed the corresponding long-wave equation for 3-dimensional flow conditions. A drawback of the regularized version of the model is the fact that it contains two equations i.e. for the film thickness and the local instantaneous flow rate per unit width. This serves as proof that an accurate prediction of linear and non linear falling film dynamics is not possible through the modelling of just one kinematic quantity (in this case the film thickness) expected to enslave all others. Consequently, other kinematic and dynamic quantities such as flow rate and wall shear stress should be considered and modelled using adequate evolution equations. Such so called *multiple-equation models* constitute the third class of wave dynamics models distinguished in figure 2.10, and shall be addressed next.

A considerable simplification of the boundary layer equations can be achieved by applying the von Kármán-Pohlhausen approach to the liquid film i.e. integrating the streamwise momentum equation and the continuity equation in 2.40 from the wall ($y^* = 0$) to the interface ($y^* = \delta^*$). The critical modelling step being the assumption of a realistic instantaneous local profile for the streamwise velocity u^* , this method leads to two evolution equations for the film thickness δ^* and instantaneous local flow rate per unit width q^* . Applying Leibniz's integration rule and allowing for the wall and interface boundary conditions (as well as the kinematic condition) in 2.40, the integral streamwise momentum and continuity equations take the form:

$$\begin{aligned} \frac{\partial q^*}{\partial t^*} + \frac{\partial}{\partial x^*} \int_0^{\delta^*} u^{*2} \partial y^* &= \Pi_{BL} \left[\delta^* \frac{\partial^3 \delta^*}{\partial x^{*3}} + \delta^* \right] \\ -\frac{\delta^*}{Fr^2} \frac{\partial \delta^*}{\partial x^*} - \frac{\Pi_{BL}}{3} \frac{\partial u^*}{\partial y^*} \Big|_{y^*=0}, \quad \frac{\partial q^*}{\partial x^*} + \frac{\partial \delta^*}{\partial t^*} &= 0. \end{aligned} \quad (2.51)$$

The first authors to use this approach for falling films were Kapitza (1948) and Shkadov (1967) (see also Prokopiou *et al.* (1991)). Thereby, Shkadov (1967) assumed a *self-similar semi-parabolic* local instantaneous velocity profile:

$$u^* = \frac{3q^*}{\delta^*} \left[y^* - \frac{y^{*2}}{2} \right], \quad (2.52)$$

the resulting model being referred to as *Shkadov's 2-equation model*. In physical terms the above equation signifies that the flow is locally developed at all times, which is clearly not the case in real films. Shkadov and co-workers (see Demekhin *et al.* (1987)) later reviewed his model by comparing its results to experimental data and direct solutions of the boundary layer equations. Thereby linear stability analysis of Shkadov's model showed that it yields differing primary stability bounds compared to those obtained from the Orr-Sommerfeld equation (the authors also show that this deviation is already present in stability bounds obtained from the boundary layer equations). Considering the evolution scenario of natural waves outlined in subsection 2.2.1, this is an im-

portant restriction. Further analysis of the model by Demekhin *et al.* (1987) showed that it predicts the nonlinear wave dynamics for monochromatically excited waves reasonably well, also predicting wave saturation. With respect to capillary wave dynamics however, the model deviates significantly from experimental data and the solution of the boundary layer equations. Demekhin *et al.* (1987) stated that this is due to the complexity of the capillary wave region's velocity field. Interestingly, the boundary layer solution exhibits backflow in this region, which in the course of this thesis will be shown to coincide with significant deceleration and acceleration of the flow. In fact, as will be developed, backflow is the result of flow separation, nucleating at the wall. Therefore the streamwise velocity profile has to be at least of third order to capture this effect, which is not the case for the assumed profile in equation 2.52. Due to the importance of the capillary wave region for scalar transfer, this is another important restriction of the model.

In the last 10 years up until most recently, significant advances in the modelling of film flows based on Shkadov's approach have been achieved by the groups of Professor Balakotaiah at the University of Houston and Professor Manneville at the École Polytechnique in Paris. Different multiple-equation models developed by both groups are listed in table 2.2 (only the most important models are described in the text). The first significant improvement was achieved by Yu *et al.* (1995) by applying Shkadov's approach to the second order boundary layer equations, obtained by retaining terms containing ϵ^2 in equations 2.15 and 2.17. Thereby, the authors employed the traditional boundary layer scaling of $\mathcal{O}(Re) \gg 1$ (as opposed to the scaling employed to derive equations 2.36 and 2.37), and their calculations were consequently performed for extremely high values of the Reynolds number ($Re=600$). Under such conditions falling films are generally turbulent. Nonetheless, the authors show that linear stability bounds obtained from the second order boundary layer equations correspond far better to solutions of the Orr-Sommerfeld equation than those obtained from the first order boundary layer equations and attribute this improvement to the retention of the $\partial^2 u / \partial x^2$ term in the streamwise momentum equation. Using Shkadov's approach, the authors constructed a second

Source	Model order	Equation number	Order of velocity profile	Ka	Re	Linear predictions	Non-linear predictions
Shkadov (1967)	1	2	2	193	3	Not good	Reasonable
Yu <i>et al.</i> (1995)	1	4	4	3550	600	Not shown	Reasonable
Yu <i>et al.</i> (1995)	2	4	4	3550	600	Good	Reasonable
Ruyer-Quil & Manneville (1998)	1	2	4	700	<20	Not good	Not shown
Ruyer-Quil & Manneville (1998)	2	3	8	700	<20	Very good	Excellent
Nguyen & Balakotaiah (2000)	2	3	2	<100	<100	Excellent	Good
Ruyer-Quil & Manneville (2000)	1	2	6	252	<10	Restricted	Not shown
Ruyer-Quil & Manneville (2000)	2	4	14	252	<10	Excellent	Not shown
Ruyer-Quil & Manneville (2000)	2	2	2	252	<10	Excellent	Very good
Scheid <i>et al.</i> (2006)	2	4 (3-D)	6	-	-	-	Not shown
Scheid <i>et al.</i> (2006)	2	2 (3-D)	6	1106	<60	-	Excellent
Mudunuri & Balakotaiah (2006)	2	2	2	500	<100	Not shown	Excellent

Table 2.2: List of recent multiple-equation models based on the method by Shkadov (1967). Values of the Reynolds- and Kapitza number respectively refer to the conditions under which the models were compared with experimental data (validation of the models by Ruyer-Quil & Manneville (2000) was performed in Ruyer-Quil & Manneville (2002)).

order four-equation model, which predicts experimental film thickness statistics reasonably well. The addition of two further equations (compared to Shkadov's model) is owed to the assumption of a fourth-order polynomial for the streamwise velocity profile and thus the introduction of two additional degrees of freedom. Interestingly, the authors mention as a quality of their model the fact that it does not predict negative wall shear stress. However, the presence of negative wall shear stress in falling liquid films is by no means unphysical as will be shown in this thesis.

Ruyer-Quil & Manneville (1998), on the basis of the second order boundary layer equations (derived with usual film scaling i.e. $\mathcal{O}(Re)=1$, $\mathcal{O}(We)=\epsilon^{-1}$), and by assuming an eighth order polynomial for the streamwise velocity profile, derived a three-equation model (for the flow rate per unit width, film thickness and a wall shear stress correction respectively). Thereby, the authors limited the number of evolution equations by deriving relations for the additional polynomial coefficients from the governing equations by so called collocation (see e.g. Villadsen & Michelson (1978); Brauner & Moalem Maron (1983)). These relations are chosen such that an asymptotic expansion of the model yields the corresponding long-wave equation. Thus, by design the model predicts the stability threshold accurately. Importantly, it is shown that the 3-equation model relaxes coupling between wall shear stress, film thickness and flow rate per unit width. On the basis of a comparison with experimental data, this relaxation is shown to improve the model predictions of non-linear wave dynamics. Indeed, as opposed to Shkadov's model, the three-equation model predicts the number of capillary waves preceding a solitary wave accurately although slightly overestimating their amplitude. Moreover, model predictions of multi-peaked interacting waves are excellent and linear stability predictions are good. However, the model has a significant drawback as it fails to predict wave saturation for large Reynolds numbers (caused by finite time blow up). Ruyer-Quil & Manneville (2000) later remedied this deficiency with a 4-equation second order model assuming a 14th-order polynomial for the velocity profile. Thereby, instead of using the collocation approach to determine polynomial coefficients they applied a weighted integration technique to the streamwise momentum

equation using weight functions of different orders. The authors subsequently derived a second order two-equation model from the four-equation model assuming a parabolic velocity profile. Linear predictions of both models are reported in Ruyer-Quil & Manneville (2002) and display excellent agreement with experimental data. For the two-equation model, Ruyer-Quil & Manneville (2002) also show that non linear wave dynamics are predicted accurately. However, an asymptotic expansion of the model (as opposed to the four-equation model) does not yield the corresponding long-wave equation and thus, although linear predictions are accurate for the investigated conditions, the authors presume the model cannot generally predict the stability threshold. Slightly before Ruyer-Quil & Manneville (2000), Nguyen & Balakotaiah (2000) published a 3-equation second order model derived on the basis of a parabolic velocity profile. The model is shown to predict the linear stability bound accurately over a large Reynolds number range and model predictions of the saturated wave amplitude display very good agreement with experimental data for small values of the Weber number. However, the authors again state that their model does not predict negative wall shear stress.

Scheid *et al.* (2006) remedied the asymptotic deficiency of the two-equation model of Ruyer-Quil & Manneville (2000) by applying a regularization technique to the corresponding four-equation model, obtaining a second order two-equation model based on a 6th-order velocity profile. This model is shown to yield excellent agreement with experimental data and numerical solutions of the full Navier-Stokes equations (by Salamon *et al.* (1994)) both in terms of linear stability and non-linear wave dynamics. Indeed, capillary waves are predicted accurately both in wavelength and amplitude. Most importantly, from the point of view of this thesis, the model predicts backflow in the capillary wave region with velocity profiles agreeing very well with those obtained from direct numerical simulation and displaying a distinctly non parabolic behaviour. Further validation of the model was recently performed by Trifonov (2008) on the basis of direct numerical solutions of the full governing equations. Shortly thereafter, Mudunuri & Balakotaiah (2006) introduced a second order two-equation model on the basis of a parabolic velocity profile, which yields

excellent agreement with experimental film thickness time traces obtained by Nosoko & Miyara (2004). Further, the authors confirm that the model predicts negative wall shear stress in the capillary wave region.

Scheid *et al.* (2006) in their paper also introduce a second order four-equation model for three-dimensional film flow assuming a 6th-order velocity profile (the corresponding equations were derived previously by Ruyer-Quil & Manneville (2000)). They then applied the regularization technique to the four-equation model to obtain a two-equation model for three-dimensional film flow. Agreement between the predictions of this model and the experimental film thickness data obtained by Liu *et al.* (1995) for 3-dimensional films is excellent. Most recently, Trevelyan *et al.* (2007) (see also Ruyer-Quil & Manneville (2005); Scheid *et al.* (2005)) applied Shkadov's integral approach to the energy equation, obtaining a model capable of predicting wave dynamics and interfacial temperature. Thereby, as is the case for the wave dynamics models, the crucial underlying assumption concerns the crosswise temperature profile in the film.

From the foregoing elaborations it is clear that the most promising approach to modelling falling liquid film dynamics is that of multiple-equation models. It has also been established that the assumption of a physically meaningful crosswise velocity profile is crucial to these models. This task is extremely difficult in the important capillary wave region where the velocity field is most complex and an ad hoc approach is bound to fail. For this reason, detailed investigations of transport processes taking place in the capillary wave region (as well as other regions) and their mechanistic elucidation are needed to further drive the development of models capable of predicting the most relevant aspects of falling liquid films.

As a result of the investigations presented in this thesis, it was established that flow separation takes place in the capillary wave region of falling liquid films (see Dietze *et al.* (2008, 2009)), causing a reversal of the flow. This *capillary flow separation* originates at the bounding wall, which directly leads to the conclusion that the velocity profile assumed in multiple-equation models needs to be at least of third order to predict the phenomenon and thereby account for its influence on wave dynamics and scalar transfer. It is herewith

clear that the detailed investigation of flow separation in falling liquid films is of considerable interest to the modelling of their dynamics.

2.3 Liquid phase transport

Having established the state of knowledge with respect to falling film wave dynamics and their modelling, attention in this section is directed toward momentum and scalar transport in the liquid phase. Thereby, the effect exerted on these transport processes by interfacial waves is of particular interest.

2.3.1 Momentum transport

For the simplest case of falling liquid film flow, the primary flow, only transport of streamwise momentum takes place in the liquid phase. Momentum is convected yet maintained in streamwise direction. Streamwise momentum produced by gravitational forces being transported away by crosswise diffusion from the interface to the wall. The resulting streamwise velocity is then given by equation 2.11 which can be rearranged to yield:

$$u_{\text{Nu}}(y) = \frac{g_x \delta_{\text{Nu}}^2}{2 \nu_1} \left[2 \frac{y}{\delta_{\text{Nu}}} - \frac{y^2}{\delta_{\text{Nu}}^2} \right], \quad \delta_{\text{Nu}} = \left[\frac{3 q \nu_1}{g_x} \right]^{\frac{1}{3}}. \quad (2.53)$$

Figure 2.11(a) illustrates the resulting liquid phase streamwise velocity field for an arbitrary regime of vertical film flow ($\text{Re}=10.7$, $\text{Ka}=509$). As stated previously, the developed state of the smooth film evolves over an entry region where the film thickness, starting from the value imposed by the liquid film inlet, asymptotically reaches its final value δ_{Nu} (see e.g. Cerro & Whitaker (1971) and Wilkes & Nedderman (1962)). Over this region the streamwise velocity profile develops from a parabolic shape (usually imposed by a rectangular inlet channel) to the semi-parabolic form shown in figure 2.11(a).

Experimental investigations of the liquid phase velocity field have mainly focused on the streamwise velocity component. An overview of main contributions to the literature, including the investigated flow conditions, is presented in

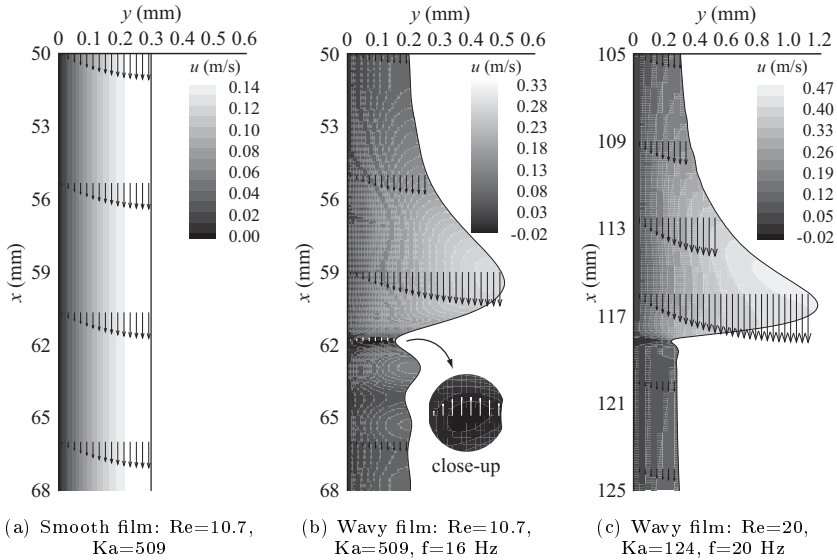


Figure 2.11: Liquid phase velocity field for vertical smooth and wavy films illustrated with contours and crosswise profiles of the streamwise velocity component.

table 2.3. Wilkes & Nedderman (1962), using a stereoscopic Particle Tracking Velocimetry (PTV) technique, measured *streamwise velocity profiles* (meaning crosswise profiles of the streamwise velocity component) in smooth vertically falling liquid films (produced at small Reynolds number values of $Re \approx 0.1$), and confirmed equation 2.53 for these conditions. Cook & Clark (1971), using an improved PTV technique, performed measurements in the smooth inlet region of vertically falling water films at relatively large Reynolds number values and corroborated the conclusion of Wilkes & Nedderman (1962). Later, Mudawar & Houpt (1993a) considered the cylindrical case by performing Laser Doppler Velocimetry (LDV) measurements in falling films, developing on the outside of a vertical tube, at large Reynolds number values ($Re \approx 1000$) and confirmed the

Autors	Re	Ka	Wave inception
Friedman & Miller (1941)	6-375	126-3877	natural
Grimley (1945)	3-89	3012	natural
Brauer (1956)	0.4-40	66-3877	natural
Wilke (1962)	20.5-195	47-4512	natural
Wilkes & Nedderman (1962)	0.07-1.06	2-7	smooth film/natural
Portalski (1964 <i>b</i>)	1-1000	29-3919	natural
Ho & Hummel (1970)	31-700	136-458	natural
Cook & Clark (1971)	75-250	3919	smooth film
Nakoryakov <i>et al.</i> (1977)	5-14.5	195	excited
Semena & Mel'nichuk (1978)	270-1640	3919	natural
Mudawar & Houpt (1993 <i>a</i>)	1435-4997	23.4, 47.4	smooth film
Mudawar & Houpt (1993 <i>b</i>)	209-414	23.4, 47.4	natural
Adomeit & Renz (2000)	27-200	1044.8	natural
Moran <i>et al.</i> (2002)	11-220	20.7	natural
Leefken <i>et al.</i> (2004)	15, 30	117.2	excited
Alekseenko <i>et al.</i> (2007)	-	-	excited rivulets

Table 2.3: List of experimental investigations of the velocity field in falling liquid films. Where liquid properties were not specified, literature values were used instead, assuming a working temperature of 25°C if not specified otherwise.

validity of equation 2.13, which pertains to cylindrical smooth films. As opposed to Wilkes & Nedderman (1962) and Cook & Clark (1971), they ensured the existence of a sufficiently long smooth film by employing working liquids with large kinematic viscosity, leading to large wavelengths and small growth rates for the primary instability (the considered large Reynolds number values also contribute to this effect). As can be deduced from figure 2.6, the critical dimensionless wave number α^* for 2-dimensional waves does not depend strongly on the Kapitza number. As the former is non-dimensionalized with δ_{Nu} , the dimensional wavelength increases drastically with kinematic viscosity.

Although the smooth film velocity distribution (as given by equations 2.11 and 2.13) is of relevance, allowing the validation of velocity measurement techniques and scaling of fluid dynamical quantities in falling liquid films, con-

siderable efforts have been undertaken to elucidate the velocity field in the more frequently encountered wavy film flow. There are two main reasons for this. First, the need to evaluate assumptions (with respect to the liquid phase streamwise velocity profile), underlying multiple-equation models introduced in subsection 2.2.3 and secondly, the desire to clarify the effect of surface waves on liquid phase scalar transport (see subsection 2.3.2). Figures 2.11(b) and 2.11(c) illustrate contours of the streamwise velocity component for two examples of wavy liquid film flow (figure 2.11(b) corresponds to the case of smooth film flow depicted in figure 2.11(a)) along with selected streamwise velocity profiles at different positions in the wave. The underlying data result from the author's own full numerical simulations which will be described in more detail in chapters 3 and 5 (data for figure 2.11(c) were taken from Dietze *et al.* (2006)) and shall serve as a basis for the discussion of the liquid phase velocity field of falling films in this subsection. At first sight, the velocity profiles in figures 2.11(b) and 2.11(c) seem to obey a semi-parabolic function in most regions of the wave. In general, a *semi-parabolic profile* can be parametrized as follows:

$$u(y) = u|_{y=\delta} \left[2\frac{y}{\delta} - \frac{y^2}{\delta^2} \right], \quad (2.54)$$

which corresponds to the *self-similar profile* defined by equation 2.52 and yields a constant value for the ratio of interfacial and mean cross sectional velocity:

$$\frac{u|_{y=\delta}}{\bar{u}} = 1.5, \quad \bar{u} = \frac{1}{\delta} \int_0^{\delta} u(y) dy. \quad (2.55)$$

First velocity measurements in wavy films were conducted with the goal of verifying if the constant ratio in equation 2.55 holds, i.e. if the streamwise velocity profile is semi-parabolic in general. Friedman & Miller (1941), using a dye-tracer, and Brauer (1956), using plastic platelets distributed on the liquid-gas interface, measured the temporally averaged interfacial streamwise velocity as well as the temporally averaged mean cross sectional velocity over a wide range of Reynolds number values for different working liquids. In fact, the

averaged mean cross sectional velocity was not measured directly. Friedman & Miller (1941) approximated it by the ratio of flow rate per unit width and temporally averaged film thickness, while Brauer (1956) approximated it with the relation for smooth film flow in equation 2.12. Both authors established that the ratio of surface velocity to averaged mean cross sectional velocity (or rather its approximation) departs from the value 1.5 at a certain threshold Reynolds number value (which depends on the working liquid and is inferior to the turbulent threshold), converging toward a value of approximately 2.2, and attributed this increase to the effect of surface waves (the same conclusion was drawn by Grimley (1945) from his velocity measurements). Although these authors measured temporally averaged quantities, it can be concluded from their results that the streamwise velocity profile is not semi-parabolic in all regions of the liquid phase for all laminar flow conditions. It should be stated here that Portalski (1964*b*) concluded from his measurements that the ratio of interfacial to mean cross sectional velocity does not deviate considerably from the value 1.5 over the entire range of laminar flow regimes. However, some doubts remain about the validity of the employed measurement procedure.

The first spatially resolved measurements of the streamwise velocity profile were performed by Grimley (1945), Wilkes & Nedderman (1962), Wilke (1962) and Ho & Hummel (1970). Wilke (1962), using a rather intrusive technique (which by his own account significantly distorted his measurement data), actually measured the temporally averaged volume flux profile, which deviates from that of the averaged streamwise velocity for wall distances larger than the minimal film thickness (i.e. for positions that due to the propagation of surface waves do not at all times lie within the liquid phase). The measured profiles are shown to deviate from the smooth film profile in equation 2.53 in the near wall region. Ho & Hummel (1970), using a photochromic dye-tracer technique, measured the temporally averaged streamwise velocity profile for relatively large Reynolds number values ($Re > 100$). They show that measured profiles are parabolic but deviate from the profile of equation 2.53. Later, Semena & Mel'nichuk (1978) confirmed this conclusion by measuring the mean streamwise velocity profile with LDV. Wilkes & Nedderman (1962) measured

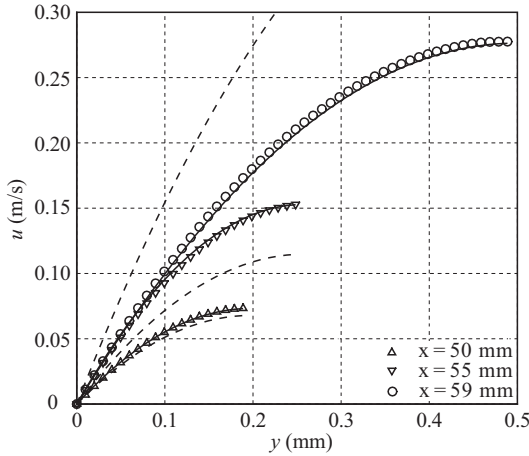


Figure 2.12: Profiles of the streamwise velocity component u at different streamwise positions x , corresponding to figure 2.11(b). Symbols highlight numerical data, solid lines corresponding profiles satisfying $u = u|_{y=\delta} [2y/\delta - (y/\delta)^2]$ and dashed lines corresponding profiles satisfying $u = (g_x \delta^2 / 2\nu_1) [2y/\delta - (y/\delta)^2]$.

instantaneous streamwise velocity profiles but were not able to relate these to specific regions in the wave. However, the authors showed that these profiles deviate from equation 2.53.

In a landmark study, Nakoryakov *et al.* (1977) performed simultaneous streamwise velocity and film thickness measurements in falling liquid films with excited 2-dimensional surface waves, using PTV (similar to Cook & Clark (1971)) and a shadow graph technique respectively. The authors were able to record instantaneous velocity profiles in different regions of a surface wave for flow regimes of varying wave dynamics. Investigated conditions ranged from single-peaked waves to solitary waves with preceding capillary waves. The main results of their article are summarized in figures 2.12 and 2.13, which depict streamwise velocity profiles (highlighted by symbols) at different positions within the wavy

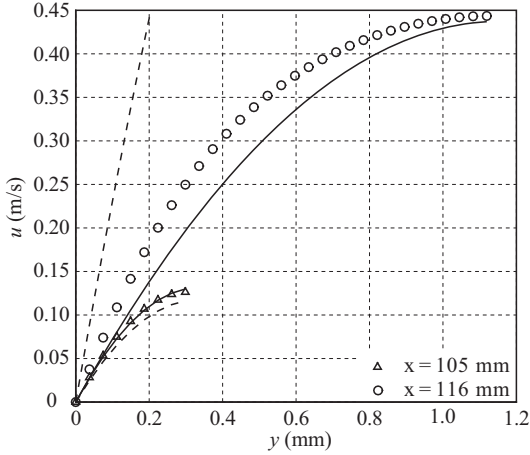


Figure 2.13: Profiles of the streamwise velocity component u at different streamwise positions x , corresponding to figure 2.11(c). Symbols highlight numerical data, solid lines corresponding profiles satisfying $u = u|_{y=\delta} [2y/\delta - (y/\delta)^2]$ and dashed lines corresponding profiles satisfying $u = (g_x \delta^2 / 2\nu_1) [2y/\delta - (y/\delta)^2]$.

liquid films illustrated in figures 2.11(b) and 2.11(c) respectively. In addition, the figures include profiles, satisfying equation 2.54, which are distinguished by solid lines. Figure 2.12 shows that for the wave with smaller maximal to residual (pertaining to the residual layer) film thickness ratio, streamwise velocity profiles are predicted accurately by the semi-parabolic profile of equation 2.54 in the wave peak as well as the wave back and residual layer. In the capillary wave region, the velocity data recorded by Nakoryakov *et al.* (1977) display a large scatter and the authors restricted their analysis to the statement that the streamwise velocity profile is not parabolic there. The cause for this scatter is of course the phenomenon of flow separation at the core of this thesis and consequently, discussion of the velocity field in the capillary wave region shall be deferred to the latter stages of this subsection. For the wave with larger

maximal to residual film thickness ratio, streamwise velocity profiles depicted in figure 2.13 are qualitatively different. In accordance with the results of Nakoryakov *et al.* (1977), the profile in the wave peak is significantly “fuller” than the semi-parabolic profile of equation 2.54. Nakoryakov *et al.* (1977) also established that the profile in the wave back is less “full” than the semi-parabolic profile (which is not shown here in order to avoid plotting too many intersecting lines in figure 2.13). In the residual layer, equation 2.54 is shown to predict the streamwise velocity profile accurately. In addition, Nakoryakov *et al.* (1977) compared their measurement results in this region to a semi-parabolic profile obtained when inserting the local instantaneous film thickness into equation 2.53:

$$u(y) = \frac{g_x \delta^2}{2\nu_1} \left[2\frac{y}{\delta} - \frac{y^2}{\delta^2} \right]. \quad (2.56)$$

Profiles satisfying this equation are also plotted in figures 2.12 and 2.13, using dashed lines. In accordance with Nakoryakov *et al.* (1977) the streamwise velocity profile is shown to agree relatively well with equation 2.56 in the residual layer. However, outside the residual region, equation 2.56 no longer holds. This is of course due to the fact that the underlying physical implication, namely that the flow is locally developed, is only valid in the residual layer, which is characterized by a relatively small streamwise variation of film thickness. In all other regions, fluid elements, due to their inertia, lag the spatio-temporal evolution of film thickness. Wasden & Dukler (1989*b*) showed this mathematically by evaluating the left-hand side (lhs) of the momentum equation for streamwise momentum (i.e. the resulting streamwise inertial “force” per unit volume) normalized with respect to the corresponding gravitational acceleration and evaluated at the interface (where its magnitude is maximal) from the velocity profile given by equation 2.56 and the kinematic condition 2.6[†]:

$$\frac{1}{g_x} \left[\frac{\partial u}{\partial t} + u \frac{\partial u}{\partial x} + v \frac{\partial u}{\partial y} \right]_{y=\delta} = \frac{\partial \delta}{\partial x} \left[\frac{\delta c}{\nu_1} + \frac{g_x \delta^3}{2\nu_1^2} \right] \quad (2.57)$$

From this relation it is clear that the applicability of equation 2.56 is restricted

[†]Wasden & Dukler (1989*b*), as opposed to the treatment here, did not account for non-steady effects.

to waves with small interface inclination (i.e. small values of $\partial\delta/\partial x$), when inertial “forces” are dominated by gravitation. Wasden & Dukler (1989*b*) asserted that equation 2.56 holds for $\mathcal{O}(\partial\delta/\partial x)=10^{-3}$, yet the wave front in figure 2.11(c) has an inclination of $\partial\delta/\partial x\approx 1.5$.

Since the work of Nakoryakov *et al.* (1977), many detailed and mainly numerical investigations have focused on the streamwise velocity profile in wavy liquid films and have confirmed the results illustrated in figures 2.12 and 2.13. Examples of numerical investigations are those of Miyara (1999), Malamataris *et al.* (2002) and Gao *et al.* (2003), while Stuhltrager *et al.* (1995) principally confirmed the same results for falling liquids films formed by condensing water vapour. In addition, Miyara (1999) showed that the temporally averaged velocity profile for wall distances inferior to the minimal film thickness is well approximated by equation 2.53. Finally, experimental confirmation of the contour plot depicted in figure 2.11(c) was provided by Leefken *et al.* (2004), who measured the liquid phase streamwise velocity field with LDV for excited waves of large maximal to residual film thickness ratio.

The studies reported above can be attributed to two main categories. Investigations of technically relevant (and thus complex) film flow regimes with relatively coarse measurement techniques in the earlier works and investigations, using highly resolving optical measurement techniques, which were however applied to films with highly controlled wave dynamics (e.g. two dimensional monochromatically excited waves). There are two experimental studies of the velocity field in falling liquid films that stand out by combining the aspects of complex flow dynamics and highly resolving measurement techniques, namely those of Adomeit & Renz (2000) and Moran *et al.* (2002). Adomeit & Renz (2000) concluded from their Particle Image Velocimetry (PIV) measurements in 3-dimensional falling liquid films that the instantaneous liquid phase velocity profile is semi-parabolic in most regions of the film. They also confirmed substantial deviations of these profiles from equation 2.56 (in accordance with the results of Nakoryakov *et al.* (1977)) except in the residual layer. These results were later corroborated by Moran *et al.* (2002), who in addition found that the mean ratio of interfacial to mean cross sectional streamwise velocity

is very close to the value of 1.5 (resulting from equation 2.54) over the range of investigated flow conditions. The latter conclusion seems to contradict the results of Friedman & Miller (1941) and Brauer (1956), which can be explained by the fact that the encountered wave dynamics in the respective studies were significantly different. Indeed, film thickness time traces measured by Moran *et al.* (2002) show that the interface structure in their experiments was dominated by waves of small maximal to residual film thickness ratio, whereas the regimes investigated by Brauer (1956) displayed values as large as 10 for the average maximal to minimal film thickness ratio.

Concurrently to the studies described above, some investigations of the liquid phase velocity field were performed from a different perspective. These works focused on the elucidation of the transient effect of wave dynamics on the liquid phase momentum transport. Mudawar & Houpt (1993*b*) (using the same setup as Mudawar & Houpt (1993*a*) at considerably lower Reynolds number values) simultaneously measured streamwise velocity and film thickness time traces using LDV and a parallel wire film thickness probe. By evaluating the cross correlation function of these signals the authors were able to determine the effect of surface waves on the streamwise velocity component, and retained two main conclusions. Firstly, that the degree of correlation between the two quantities increases with wall distance and secondly, that increasing residual layer thickness and decreasing dynamic viscosity exert a decoupling effect on the two quantities. Both conclusions can be explained from the point of view of crosswise diffusional momentum transport. As the dynamic viscosity is the transport coefficient in Newton's law of viscosity it scales the crosswise momentum flux and thereby effects the temporal change in momentum. Increasing the residual layer thickness or decreasing wall distance acts to increase the distance over which momentum is to be transported from the interface and thus increases the response time to interfacial fluctuations. In principle, these findings are supported by numerical investigations performed by Stuhlträger *et al.* (1993), who evaluated the root-mean-square (rms) of streamwise velocity time traces in the liquid phase. The authors show that there exists a liquid layer near the wall where velocity fluctuations are negligible, and which is thus almost un-

affected by surface waves. Increasing the wall distance beyond this layer leads to an increase in the degree of correlation of film thickness and streamwise velocity. The authors also show that the rms of the crosswise velocity component is two orders of magnitude smaller than that of the streamwise component. Mudawar & Houpt (1993*b*) also measured the crosswise velocity component (which was the radial component in their case), concluding that its value is negligible compared to the streamwise velocity component. This finding concurs with numerical investigations of inclined liquid films by Malamataris *et al.* (2002). The authors showed that the crosswise variation of liquid phase static pressure is hydrostatic in nature for all regions of the film except the capillary wave region, i.e. that crosswise transport of crosswise momentum is not significant in those regions. In the capillary wave region however, conditions are different and their investigation is the subject of this thesis. For the sake of completeness it should be stated here that the wave dynamics encountered by Mudawar & Houpt (1993*b*) and Stuhlträger *et al.* (1993) did not display significant capillary waves.

In summary, it can be concluded that the locally developed profile defined by equation 2.56 is not able to predict the streamwise velocity distribution in wavy liquid films outside the residual layer. Although the general semi-parabolic profile defined by equation 2.54 and assumed by Shkadov (1967) in his 2-equation model yields a significantly better prediction, deviations still remain in waves with large maximal to residual film thickness ratio.

This discrepancy for large waves is caused by the occurrence of a characteristic phenomenon of liquid phase momentum transport, that fundamentally alters the nature of the velocity field in the wave crest as the maximal to residual film thickness ratio exceeds a certain threshold value, leading to the creation of so called *rolling waves*. A similar term, roll waves, is historically associated with turbulent water flows in man made or natural water courses such as aqueducts. Balmforth & Mandre (2004) provide an overview of the dynamics of these waves as well as a photograph of their occurrence in a laboratory model (see also Dressler (1949) for a picture of naturally occurring roll waves in an open conduit taken from the book of Cornish (1934)). They also

point out (without further specification) that an analogon to these roll waves exists in falling liquid films. The first to specify the phenomenological basis of such waves in conjunction with falling liquid films was Portalski (1964*a*). He employed the term *rolling wave* to designate waves that, when observed with an “imaginary camera” traveling at the same speed, would display streamlines in the shape of a closed eddy. Later, Nakoryakov *et al.* (1976) used the same designation to differentiate waves with large maximal to residual film thickness ratios. As both works note the principle aspects of the phenomenon in question, the same terminology shall be adopted in this thesis.

Figures 2.14(a) to 2.14(c) represent streamlines viewed in a coordinate system moving with wave celerity (i.e. a *wave-fixed reference frame*), as suggested by Portalski (1964*a*), for the waves depicted in figures 2.11(a) to 2.11(c) respectively. Or, in other words, streamlines in figures 2.14(a) to 2.14(c) were determined based on the velocity vector $[u - c, v]^T$. Superimposed arrows illustrate the local flow direction. For the wave with largest maximal to residual film thickness ratio, figure 2.14(c) shows that the scenario of a vortex in the wave crest (envisaged by Portalski (1964*a*)) is indeed correct. Thereby, liquid inside the vortex is “trapped” and recirculated as the wave travels downward (this entrapment was also indirectly suggested by Dukler (1976)). For such a vortex to exist, the interfacial liquid velocity, evaluated in a wall fixed coordinate system, must exceed the wave celerity at some position along the wave. The occurrence of a vortex in the wave-fixed reference frame may be more easily understood when considering the phenomenon from another point of view. Chu & Dukler (1974) and later Brauner & Moalem Maron (1988) contended that conditions in a surface wave could be simulated by moving a wetted bounding wall upward with wave celerity, thus obtaining an interfacial structure that is fixed in space. Technically, the encountered situation would then be one of liquid withdrawal from a reservoir as opposed to a falling liquid film. In this situation, the large wave would represent a cavity into which liquid is conveyed due to the movement of the wall. Based on this picture, it is clear that, depending on the depth of the “cavity” (i.e. the difference between maximal and minimal film thickness) and the withdrawal rate, the flow entering the cavity

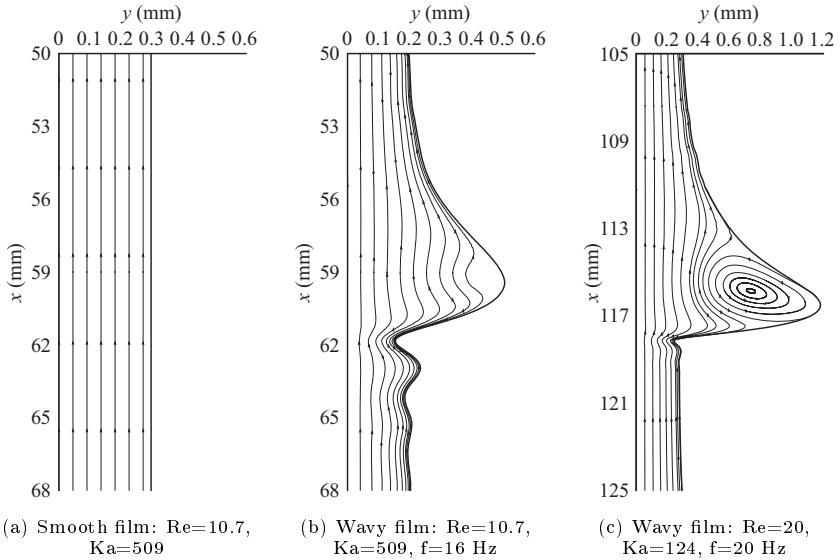


Figure 2.14: Liquid phase streamlines in a coordinate system moving with the respective wave celerity for smooth and wavy films corresponding to figure 2.11 (in subfigure 2.14(a), the same wave celerity as in subfigure 2.14(b) is employed).

may separate, creating a separation vortex.

The concept of flow separation in the wave crest was first introduced by Brauner *et al.* (1987). Based on an analysis of the governing equations at the interface the authors came to the conclusion that for certain flow conditions a characteristic point appears on either side of the wave's maximum. They subsequently showed that these points could either be stagnation points connected by a separation streamline or extremal points, the latter scenario having been refuted by Malamataris *et al.* (2002), who showed that the interfacial velocity varies monotonically with the local film thickness. Brauner & Moalem Maron (1983) had previously supposed the existence of a single upstream stagnation

point and applied laminar withdrawal theory (see Groenveld (1970)) to obtain relations for the residual film thickness δ_{res} and the film thickness δ_{SP} at the stagnation point:

$$\delta_{\text{res}} = 0.52 \left[\frac{c\nu_1}{g} \right]^{\frac{1}{2}}, \quad \delta_{SP} = \left[\frac{2c\nu_1}{g} \right]^{\frac{1}{2}}, \quad (2.58)$$

which quite accurately predict $\delta_{\text{res}}=0.23$ mm and $\delta_{SP}=0.63$ mm for the wave in figure 2.14(c) ($c=0.41$ m/s, $\nu_1=4.7 \cdot 10^{-6}$ m²/s).

Having introduced and explained the phenomenon of rolling waves in falling liquid films, a brief historic overview of different contributions to the proof of its existence is presented here.

Nakoryakov *et al.* (1977) concluded from their velocity measurements in rolling waves (which they defined according to Nakoryakov *et al.* (1976)) that interfacial velocity does not exceed wave celerity at any position along the wave. However, as their data points did not extend sufficiently close to the liquid-gas interface, these are also open to the contrary interpretation. This was later confirmed by Demekhin *et al.* (1987), who solved Shkadov's 2-equation model numerically for one of the said regimes, showing that a vortex in the wave crest is indeed observed in the wave-fixed reference frame[†]. Further contributions to the elucidation of the phenomenon were mainly of numerical nature, since adequately resolved velocity measurements in falling liquid films are extremely difficult.

Moalem Maron *et al.* (1989) and Wasden & Dukler (1989*a,b*) were the first to solve the full Navier-Stokes equations to investigate the phenomenon. They considered the situation as a liquid withdrawal problem, prescribing the wave geometry and moving the wall with wave celerity, directly obtaining the velocity field in the wave-fixed reference frame. Moalem Maron *et al.* (1989) synthesized typical rolling waves with an asymmetric film thickness distribution described by two different sine functions matched at the wave peak. Thereby, the authors arbitrarily prescribed the wall velocity, and thus the wave's celerity, which

[†]Malamataris & Balakotaiah (2008) have recently come to the same conclusion based on a numerical solution of the full Navier-Stokes equations for the same regime.

means that the considered wave dynamics were not necessarily realistic. Later, Jayanti & Hewitt (1997) remedied this deficiency by adapting the wave velocity iteratively until obtaining a periodic streamwise pressure distribution in the wave. Two principle conclusions can be drawn from the work of Moalem Maron *et al.* (1989). Firstly, the authors show that the occurrence of a vortex in the wave-fixed reference frame is governed by the ratio of maximal to residual film thickness. Only when this ratio exceeds a certain threshold value, a vortex develops. The relations in equation 2.58, obtained by Brauner & Moalem Maron (1983) from laminar withdrawal theory, yield the value 2.72 for this threshold, which was corroborated by the numerical experiments of Moalem Maron *et al.* (1989), who show the value to lie between 2.5 and 3.0. Secondly, the authors found that rolling waves develop a second vortex in the wave crest as their base length increases.

Wasden & Dukler (1989*b*) improved the methodology of Moalem Maron *et al.* (1989) by prescribing a realistic wave geometry based on their own film thickness measurements at technically relevant flow conditions[†]. Because wave dynamics under those conditions were not developed (i.e. wave celerity varied along the wave), the authors prescribed a wall velocity profile, which was iteratively adjusted to fulfill both the periodicity of the streamwise pressure distribution and the agreement of numerically and experimentally determined wall shear stress distributions. Thereby, Wasden & Dukler (1989*b*) investigated three different waves of varying maximal to residual film thickness ratio, confirming the finding of Moalem Maron *et al.* (1989) that increasing the ratio increases the size of the vortex in the wave-fixed reference frame. The authors state that due to the resulting recirculation of liquid in the wave crest, rolling waves could be viewed as “lumps of liquid overrunning a slow moving substrate” and carrying most of the liquid mass. The latter assertion was quantitatively verified by Mudawar & Houpt (1993*b*), who determined mass fluxes at different positions in the wave, concluding that rolling waves transport between 40 and 70% of liquid mass. Wasden & Dukler (1989*b*) also communicated some

[†]They also accounted for capillary forces in the normal interfacial boundary condition as opposed to Moalem Maron *et al.* (1989).

observations on the velocity field underneath the recirculation zone, showing that the region near the stagnation points displays large values of the cross-wise velocity component (see figure 2.14(c)). They also demonstrated that the wave trough region is associated with considerable streamwise acceleration of the flow, while the wave crest and the wave back are associated with moderate deceleration[†]. Further, the authors showed that the streamwise velocity profile in rolling waves is well approximated by a third order polynomial, confirming the finding reported earlier in this section that parabolic profiles are inadequate under these conditions. Subsequently, Wasden & Dukler (1989*a*) employed the same methodology as Wasden & Dukler (1989*b*) to investigate binary interactions between different rolling waves (i.e. coalescence and splitting of waves). They showed that such interactions lead to rolling waves with large base length (similar to the ones investigated by Moalem Maron *et al.* (1989)) and multiple peaks displaying multiple vortices in the wave-fixed reference frame. In addition, the authors concluded that, next to the maximal to residual film thickness ratio, the wave shape exerts considerable influence on such multiple (or single) vortices.

More recent numerical studies of rolling waves considered the problem in its full complexity, i.e. the wave geometry was treated implicitly (as variable) and obtained as part of the solution procedure. The first investigation of this kind was published by Miyara (1999). Therein, the author demonstrated the development of a surface wave from small initial interfacial disturbances to a large rolling wave with an internal vortex in the wave-fixed reference frame (subsequently referred to as *moving frame vortex*) for a flow regime with large maximal to residual film thickness ratio. Since then, several other authors have obtained similar results (see e.g. Miyara (2001), Leefken & Renz (2001), Kunugi & Kino (2003), Gao *et al.* (2003), Kunugi *et al.* (2005) and Malamataris & Balakotaiah (2008)). Two more detailed investigations of the phenomenon are those of Miyara (2000) and Trifonov (2008). Miyara (2000) investigated moving frame vortices for a wide range of wave dynamics by systematically varying the governing dimensionless groups Re , We , f^* and Fr . Thereby, nu-

[†]The regimes considered by Wasden & Dukler (1989*b*) did not display capillary waves.

merical data were validated with experimental data of Liu & Gollub (1994). These simulations confirm that the principal quantity influencing the occurrence of a moving frame vortex is the maximal to residual film thickness ratio, which increases with the Reynolds number (increasing the size of the moving frame vortex) and decreases with the Froude and Weber numbers respectively (decreasing the size of the moving frame vortex). Miyara (2000) also made an interesting observation about the influence of the excitation frequency, showing that, for small wave separations (obtained for large values of the excitation frequency) the secondary instability described by Liu *et al.* (1993) sets in, which in turn leads to the intermittent creation and destruction of moving frame vortices in the wave crests[†]. The results of Miyara (2000) were largely confirmed by Trifonov (2008), who added a further insight into regimes of high maximal to residual film thickness ratios. Indeed, the author stated that for large values of Re/Ka (and large wavelengths) his solution procedure failed, which he attributed to the steepening of wave fronts and possibly the subsequent onset of wave breaking and formation of droplets shearing-off from the wave crest. Considering the vorticity inherent in the moving frame vortex, this hypothesis seems quite probable.

The first and up to date only direct experimental proof of a moving frame vortex in the wave crest of rolling waves was recently published by Alekseenko *et al.* (2007) (see table 2.3). The authors performed PIV measurements of the velocity field in a rolling wave developing on the outside of an inclined tube. This situation is more associated with *rivulet flow* than with the flow of a falling liquid film, but the general wave behaviour is similar. Further, Alekseenko *et al.* (2007) showed that the size of the vortex increases with increasing maximal to residual film thickness ratio. Finally, just like Trifonov (2008), the authors invoked the possible significance of the moving frame vortex for the creation of droplets from the wave crest.

With that, characteristics of the liquid phase velocity field have been discussed for all regions of the falling liquid films illustrated in figures 2.11 and

[†]The picture presented by Miyara (2000) is not entirely correct, as he did not take into account that the wave celerity varies along the waves under these conditions.

Autors	Re	Ka	Type of investigation
Kapitza (1948)	-	-	2-equation model
Brauer (1956)	66	3877	experimental
Portalski (1964a)	-	-	2-equation model
Massot <i>et al.</i> (1966)	-	-	2-equation model
Nakoryakov <i>et al.</i> (1977)	12.4	195	experimental
Demekhin <i>et al.</i> (1983)	-	-	boundary layer equations
Demekhin <i>et al.</i> (1987)	12.4	195	boundary layer equations
Salamon <i>et al.</i> (1994)	6.1	528.6	Navier-Stokes
Miyara (1999)	100	2969.8	Navier-Stokes
Adomeit <i>et al.</i> (2000)	13, 16, 50	1044.8	experimental/Navier-Stokes
Leeffen & Renz (2001)	30	-	Navier-Stokes
Malamataris <i>et al.</i> (2002)	19.33	252.3	Navier-Stokes
Tihon <i>et al.</i> (2003)	91	8101	experimental
Tihon (2003)	91	8101	experimental
Kunugi & Kino (2005)	75	3919	Navier-Stokes
Tihon <i>et al.</i> (2006)	13-57	1480	experimental

Table 2.4: List of experimental and numerical investigations pertaining to back-flow in falling liquid films. Where liquid properties were not specified, literature values were used instead, whereby the working temperature was assumed to be 25°C if not specified otherwise.

2.14 except for one, the region of *capillary waves*. Elucidation of the velocity field in this region is precisely the goal of this thesis, and a detailed account of the state of knowledge before the publication of the author's main findings on the subject (see Dietze *et al.* (2008, 2009)) is presented next[†]. To that end, a list of relevant works is presented in table 2.4.

In order to distinguish different subregions of the capillary wave region some appropriate terminology shall be introduced here. Referring to figure 2.11(b), capillary waves shall be numbered in ascending order with increasing stream-wise position relative to the main wave hump to which they belong. Further, the terms *capillary maximum* and *minimum* shall pertain to the points of maximal

[†]Results by other authors that were published later are introduced in section 5 and discussed with respect to the main results of this thesis.

and minimal film thickness in the corresponding capillary wave. As is evident in figure 2.11(b), the streamwise velocity profile at the first capillary minimum exhibits a striking feature. Indeed, the streamwise velocity component there is negative over the entire cross section of the liquid film. This *flow reversal* or *backflow* is nota bene directed opposite to the gravitational acceleration vector as viewed in a *wall-fixed coordinate system*.

The first to conjecture the existence of such backflow in falling liquid films was Kapitza (1948). He solved his 2-equation model (see subsection 2.2.3) analytically, using a harmonic ansatz for the spatio-temporal evolution of film thickness, exploiting that the two model equations in 2.51 can be uncoupled for periodic waves, using the following relation:

$$q^* = c^* [\bar{\delta}^* - \delta^*] + \bar{q}^*, \quad \bar{q}^* = \int_0^1 q^* dx^*, \quad \bar{\delta}^* = \int_0^1 \delta^* dx^* \quad (2.59)$$

between film thickness δ^* and flow rate per unit width q^* . In the above equation, a bar denotes averaging over the wavelength Λ , which was used to non-dimensionalize the streamwise coordinate. Kapitza (1948) evaluated his analytical solution for an exemplary wavy film flow of prescribed mean film thickness $\bar{\delta}^*$ and wavelength Λ , and illustrated the resulting flow field in the film's cross section. This illustration has been reproduced in figure 2.15. Most interestingly, the figure shows the occurrence of backflow at the wave trough. Thereby, the backflow region is bounded by two lines normal to the wall on which the streamwise velocity component vanishes, which suggests that a kind of *cellular pattern* exists at the wave trough. Although the wave dynamics investigated by Kapitza (1948) differ substantially from those in figure 2.11(b), a wave trough such as the one pictured in figure 2.15 is encountered in principle at all capillary minima. A first experimental indication of the validity of Kapitza's conjecture is contained in the work of Brauer (1956). Indeed, Brauer (1956) briefly mentioned[†] that, during his measurements of the interfacial streamwise velocity component (performed by photographically tracking platelets dispersed on the

[†]See his comments regarding figure 35 on page 25.

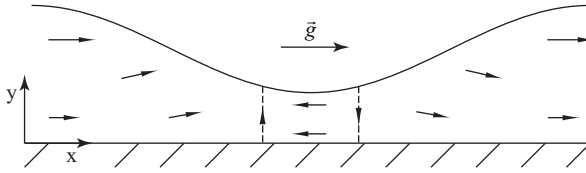


Figure 2.15: Sketch of the flow pattern at the wave trough of a vertically falling liquid film with harmonic surface waves as illustrated by Kapitza (1948) based on an analytical solution of his 2-equation model.

liquid-gas interface), upward motion was observed for intermediate Reynolds number values. Later, Portalski (1964*a*) tried to provide a physical explanation of the back flow phenomenon exhibited by Kapitza's analytical solution, introducing two important terms. Firstly, he stated that “at a fixed point the flow is periodically brought to rest and then reversed by the passage of the wave, so that separation is bound to occur...as in a boundary layer with adverse pressure gradient”. Secondly, he introduced the notion of eddy formation at the wave trough, speculating that the lines of vanishing streamwise velocity component are not normal to the wall but rather “bent forward” in streamwise direction and that the center of an eddy lies on each of these lines. Thereby, the two eddies were supposed to rotate in opposite directions. A continuation of Kapitza's investigations was then provided by Massot *et al.* (1966). The authors, although making some improvements[†] to the 2-equation model used by Kapitza (1948), generally employed the same methodology to analyze the flow field in the region of backflow in greater detail. Most significantly, the authors evaluated the streamwise and crosswise velocity components over the entire cross section and constructed the resulting streamlines, confirming the notion of a cellular pattern in the backflow region as suggested by figure 2.15. Further, the authors introduced a quantitative criterion, requiring that $c^* (\delta_{\max}^* - \bar{\delta}^*) > 1$ for backflow to occur.

Following this first set of investigations on the back flow phenomenon, no

[†]They for instance retained the term $\partial^2 u / \partial x^2$ in the streamwise momentum equation, which was later recommended by Yu *et al.* (1995).

advances in this matter were made roughly for the next twenty years up until the work of Demekhin *et al.* (1983). During that period, the experimental investigations of the liquid phase velocity field by Nakoryakov *et al.* (1977) may have played an important role. Indeed, streamwise velocity data measured by Nakoryakov *et al.* (1977) in the capillary wave region for different wave dynamics exhibit no negative values, which may have led to the conclusion that flow reversal does not occur in falling liquid films. However, these velocity data, as pointed out by the authors themselves, display a significantly larger scatter than data in other regions of the wave. On the one hand, this means that the employed measurement technique displays resolution problems in the capillary wave region caused by the short transition time of capillary waves due to their small wavelength. On the other hand, it can be concluded that the flow field in the capillary wave region undergoes extreme spatio-temporal modifications. Another interesting feature of these velocity data in the capillary wave region is that they seem to indicate a positive curvature at least in some parts of the streamwise velocity profile, which would be opposed to the negative curvature encountered in all other regions of the wave.

As previously mentioned, the next contribution to the elucidation of the back flow phenomenon was provided by Demekhin *et al.* (1983), who numerically solved the first order boundary layer equations 2.40 for a wavy liquid film with relatively small maximal to residual film thickness ratio. Although the computed wave dynamics do not exhibit capillary waves, they are closer to the situation pictured in figure 2.11(b) than the harmonic case considered by Massot *et al.* (1966). In principle, Demekhin *et al.* (1983) confirmed the streamline pattern calculated by Massot *et al.* (1966) for their case, showing the existence of a cellular region of backflow at the wave trough. The authors also show a streamwise velocity profile at a position that appears to lie in the backflow region, and which exhibits a positive curvature at the wall[†]. Further, the authors stated that backflow occurs for $Re^{11/9}Ka^{-1/3} > 1.253^{7/9}$ in their calculations. Subsequently, Demekhin *et al.* (1987) published more detailed

[†]However, there seems to be a contradiction with the streamline pattern, as this profile does not display negative values.

findings concerning the backflow phenomenon by solving the first order boundary layer equations numerically for one of the regimes that were experimentally investigated by Nakoryakov *et al.* (1977) (more precisely, the regime with large maximal to residual film thickness ratio). On the basis of streamwise velocity profiles plotted at different positions, stretching from the wave front to the second capillary minimum, the authors showed that backflow indeed occurs in the capillary wave region. Thereby, velocity profiles at the first and second capillary minimum are parabolic and display positive curvature with negative velocity values over the film's entire cross section. This situation is reversed at the first capillary maximum where the profile displays negative curvature and positive velocity values. Interestingly, while changing its shape from the first capillary maximum to the second capillary minimum, the streamwise velocity profile is shown to develop a point of inflexion associated with a change in near wall curvature. At the corresponding position, only near wall streamwise velocity values are negative. Demekhin *et al.* (1983) stated that, during this streamwise change of the velocity profile, fluid elements are accelerated and decelerated with a magnitude of up to twice the gravitational acceleration. In accordance with Portalski (1964a), the authors hypothesized that backflow is caused by "rapidly moving eddies" in front of the large wave.

Recent investigations pertaining to the backflow phenomenon have been published over the last ten years. These investigations are distinguished by the fact that the falling liquid film flow was considered in its full complexity, either by numerically solving the full Navier-Stokes equations, or by way of sufficiently resolved measurements. Salamon *et al.* (1994) performed numerical simulations of a wavy liquid film with an interfacial structure comparable to that of figure 2.11(b). The authors showed a contour plot of the streamwise velocity field in the liquid phase, confirming the existence of backflow in the capillary wave region (and showing the same characteristic features as the contour plot in figure 2.11(b)). Miyara (1999) conducted a similar numerical investigation focused on a wavy film with larger maximal to residual film thickness ratio and a larger number of capillary waves. His results show that the streamwise velocity profile at the first capillary minimum exhibits negative values over

the film's entire cross section and that it is "fuller" than the profile defined by equation 2.54. Further, the author concluded that the wavy film's interfacial structure influences the near wall flow field. Numerical results similar to those of Miyara (1999) were also obtained by Adomeit *et al.* (2000) and Leefken & Renz (2001). In their work, Adomeit *et al.* (2000) additionally presented very convincing experimental proof of the backflow phenomenon in the form of a photograph (recorded with large exposure time) showing *loop-shaped pathlines* of particles illuminated with a pulsed laser in the capillary wave region. Leefken & Renz (2001) investigated the velocity field in the capillary wave region from a different perspective by evaluating the distribution of the *streamwise wall shear stress* $\tau_{wx} = \mu_1 \partial u / \partial y|_{y=0}$ [†] (subsequently also referred to as *wall shear stress*) from their 2-dimensional numerical data. The authors showed that wall shear stress and film thickness exhibit a correlated streamwise evolution, each capillary extremal value being associated with a corresponding wall shear stress extremum. Further, the wall shear stress distribution exhibits a sign change at several of the first capillary minima, indicating backflow at those positions. A detailed numerical investigation of the streamwise velocity profile in the capillary wave region was performed by Malamataris *et al.* (2002), who came to similar conclusions as Demekhin *et al.* (1987). Indeed, the authors confirmed that the profile develops from a parabolic shape with negative near wall curvature and positive velocity to a profile with positive near wall curvature and negative velocity over a (not precisely specified) stretch of the capillary wave region. During this change in shape, the profile is shown to develop an inflexion point near the wall. These numerical simulations were based on regimes of inclined liquid film flow previously investigated experimentally by Liu *et al.* (1993), and exhibited good agreement with the experimental data in terms of wave dynamics. Further, Malamataris *et al.* (2002) investigated the influence of the excitation frequency on velocity profiles in the capillary wave region. Their results show that reducing the excitation frequency increases the height and separation of main wave humps as well as the number of capillary waves. As a result, the corresponding streamwise velocity profiles in the capillary wave re-

[†]I.e. the streamwise shear stress exerted by the liquid on the wall.

gion depart more significantly from the semi-parabolic form, eventually exhibiting backflow. The authors concluded by stating that the backflow phenomenon “must be considered as a destabilizing event for the film flow”.

An important experimental confirmation of the backflow phenomenon was obtained by Tihon *et al.* (2003). The authors simultaneously measured time traces of the local wall shear rate $\partial u/\partial y|_{y=0}$ (with an electrodiffusion method) and film thickness (with a capacitance method) in an inclined wavy liquid film with relatively large maximal to minimal film thickness ratio and a large number of capillary waves. Indeed, the experimental data exhibit a sign change (from positive to negative) of the wall shear rate at times corresponding to the first two capillary minima[†]. In further accordance with the results of Leefken & Renz (2001), wall shear rate and film thickness time traces were shown to be closely correlated. Later, Tihon (2003) additionally presented photographs of particles in the capillary wave region recorded using a macroscopic lens assembly under the same conditions as in Tihon *et al.* (2003). The authors stated that flow reversal could be discerned from successive pictures, but the evidence does not seem to be clear. Recently, using the same measurement techniques as Tihon *et al.* (2003), a detailed study of wall shear stress in the capillary wave region of inclined wavy liquid films was performed by Tihon *et al.* (2006). The main results of the study are simultaneous time traces of local wall shear stress and film thickness measured at different Reynolds number and excitation frequency values. Based on these parametric studies the authors elucidated the effect of Reynolds number and excitation frequency on the wavelength of capillary waves. This wavelength was shown to decrease with increasing Reynolds number and decreasing excitation frequency, which Tihon *et al.* (2006) attributed to the occurrence of “higher waves that need steeper ripples in order to be stabilized”. This conjecture seems to be supported by the fact (also shown by the authors) that minimal film thickness δ_{\min} and corresponding streamwise velocity $u_{\min} = g\delta_{\min}^2(3\nu_l)^{-1}$ are more adequate scales to describe the observed wave dynamics, suggesting that the capillary wave region

[†]The authors specified a minimal wall shear rate value of $\partial u/\partial y|_{y=0} = -755$ 1/s at the first capillary minimum. The wall shear rate for the corresponding smooth developed film flow is $\partial u_{\text{Nu}}/\partial y|_{y=0} = 3086$ 1/s.

has a considerable effect on the dynamics of large wave humps. The wall shear stress time traces were shown to exhibit the same characteristics as previously observed by Leefken & Renz (2001) and Tihon *et al.* (2003), confirming the existence of backflow at the capillary minima closest to the main wave hump. Further, the authors showed that both the maximal (associated with the main wave hump) and minimal (associated with the first capillary minimum) values of wall shear stress display an extremum in their dependence on the Reynolds number value. The associated decrease in magnitude of these extrema at large Reynolds number values can be attributed to the fact that under these conditions, the ratio of maximal to minimal film thickness increases degressively with the Reynolds number. As a consequence, the relative importance of the residual layer's resistance to diffusional crosswise momentum transport to the wall increases (see also the previous elaborations concerning the results of Mudawar & Houpt (1993*b*)), attenuating the effect of the interfacial structure on the near wall velocity field. Tihon *et al.* (2006) also performed their own numerical simulations, which were shown to compare favorably with experimental data. Finally, the authors, based on their simultaneous film thickness and wall shear stress time traces, confirmed that the streamwise velocity profile defined by equation 2.56 is inadequate. Indeed, this profile yields $\mu_1 \partial u / \partial y|_{y=0} = \rho_1 g \delta$, meaning that the time traces of dimensionless film thickness and wall shear stress (both non-dimensionalized with the respective mean values), would be identical if equation 2.56 were to hold, which is clearly not the case for most of the data presented by Tihon *et al.* (2006). However, the authors showed that a more favorable comparison is obtained for waves with relatively small maximal to residual film thickness ratio, yielding smaller interfacial inclination, which reduces the effect of inertial “forces” as pointed out by Wasden & Dukler (1989*b*). Figure 2.16 depicts streamwise distributions of wall shear stress and the quantity $\rho_1 g \delta$ for the smooth and wavy films pictured in 2.11(a), 2.11(b) and 2.11(c) respectively, illustrating the main findings of Leefken & Renz (2001) and Tihon *et al.* (2006), regarding wall shear stress and its correlation with interfacial topology.

An interesting insight into the complexity of the backflow phenomenon was

recently provided by Kunugi & Kino (2005). The authors, in addition to 2-dimensional numerical simulations similar to those discussed above, also performed the first full numerical simulation of a falling liquid film with 3-dimensional wave dynamics. The results of their 2-dimensional simulations largely confirm previous findings, i.e. flow reversal at the first capillary minima accompanied by sign changes of the wall shear stress, and are shown to be in agreement with the empirical correlations of Nosoko *et al.* (1996). Further, the authors (see also Kunugi *et al.* (2005)) provided the first visualization of the vector field in the cross section of the capillary wave region as obtained from the full Navier-Stokes equations, and in principle confirmed the picture drawn by Kapitza & Kapitza (1949) (see figure 2.15). Thereby, they designate the backflow regions appearing at the first two capillary minima in their simulation as vortices, which they envisage as having an effect on wave dynamics. The most significant contribution of their work are contour plots of film thickness and wall shear stress evaluated from 3-dimensional simulation data. First of all, the calculated 3-dimensional film thickness distribution agrees very well with experimental visualizations published in the book of Alekseenko *et al.* (1994), so that the underlying wave dynamics can be considered realistic. Thereby, the wave topology sufficiently far downstream of the liquid inlet is characterized by 3-dimensional solitary waves, interacting with one another and preceded by capillary waves, which cover a considerable region of the interface. The corresponding wall shear stress distribution in these extensive regions exhibits negative values, showing that the backflow phenomenon plays an important role in the liquid phase momentum transport of falling liquid films under realistic flow conditions. Finally, Kunugi & Kino (2005) discussed the evolution of 2-dimensional waves to 3-dimensional horseshoe-shaped waves from the point of view of the backflow phenomenon. They conjectured that this phenomenon is responsible for the 3-dimensional instability of 2-dimensional waves[†], stating that during this transition the vorticity vector in the back flow region changes from a spanwise orientation toward a streamwise orientation “like a hair-pin

[†]Kunugi & Kino (2005) also considered heat transfer and the temperature dependence of fluid properties, so that thermal effects such as Marangoni-convection must be taken into account when interpreting their results.

vortex motion”. Evidence pointing in this direction is provided in section 5.5 (see subfigure 5.51(b) therein).

In summary, it can be concluded that the velocity field in laminar falling liquid films has been elucidated by various contributions to the literature in all but one sub-region of the liquid phase under wavy conditions, namely the capillary wave region (characterized by length scales of $100\ \mu\text{m}$ and time scales of 1 ms). Some advances concerning this region have also been reported, establishing that extreme changes in the velocity distribution and even backflow can occur there. However, at the onset of investigations documented in this thesis, no physical explanation of this backflow phenomenon neither from the kinematic nor from the dynamic point of view had been proposed. This lack of understanding has led to a relative “negligence” of the phenomenon in falling liquid film research, although all indications point to the possibility of it exerting a great influence on wave dynamics and liquid phase transport. Consequently, the stated goal of this thesis, i.e. the mechanistic elucidation of the backflow phenomenon, is a logical consequence of research conducted on the topic of falling film momentum transport up until now.

Before concluding this review of literature on liquid phase momentum transport, two last topics shall be addressed. First, a more general discussion of the wall shear stress distribution followed by some considerations on turbulence in falling liquid films.

The streamwise wall shear stress $\tau_{wx} = \mu_1 \partial u / \partial y|_{y=0}$, the distribution of which is illustrated in figure 2.16, can be understood as the normal flux of streamwise momentum from the liquid to the wall. Although this quantity is a derivative of the velocity field, its evaluation can nonetheless be useful in itself. For instance, as was discussed above, the wall shear stress allows for the identification of backflow in the capillary wave region. Further, knowledge of the wall shear stress distribution can be useful for the prediction of patterns resulting from material erosion or deposition at the bounding wall (see e.g. Pozrikidis (1988)). Also, due to the analogy between momentum and scalar transport, the wall shear stress distribution can yield more general conclusions regarding transfer between the wall and the liquid film. For smooth falling liquid films

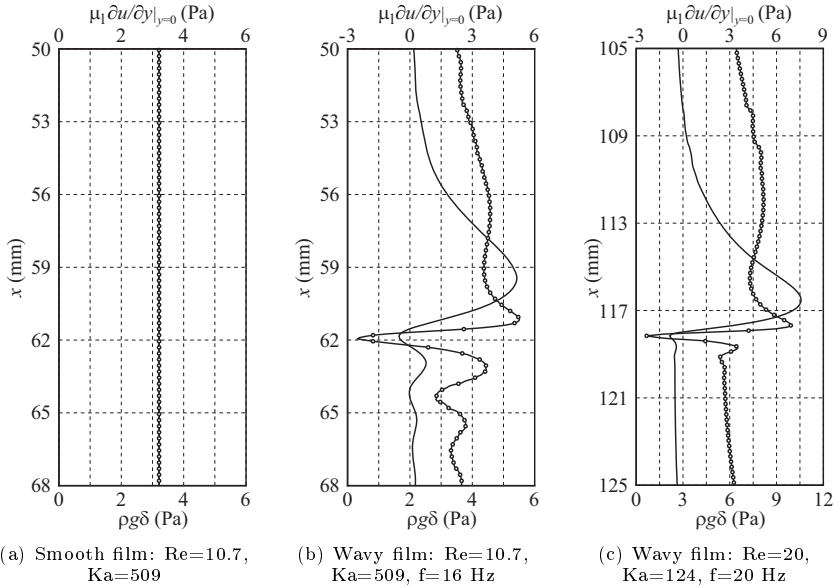


Figure 2.16: Wall shear stress distributions corresponding to figures 2.11(a), 2.11(b) and 2.11(c). Solid lines (bottom ordinate): wall shear stress $\rho_1 g \delta$ obtained from equation 2.56; circles (top ordinate): wall shear stress obtained from numerical simulation.

(see figure 2.16(a)), the wall shear stress follows from equation 2.11 and is given by $\tau_{wx} = \rho_1 g_x \delta N_u$. Brauer (1956), based on his experiments with water, showed that the temporally averaged wall shear stress $\bar{\tau}_{wx}$ in laminar wavy films lies above that value (this was later confirmed by Moran *et al.* (2002), while the results of Alekseenko *et al.* (1973) show a rather good agreement between the two quantities). Further, Brauer's results show that the measured dependence of $\bar{\tau}_{wx}$ on the Reynolds number (over a range of $Re=15-2000$) displays five distinct regions, which he attributed to five different regimes of wavy film flow (see also table 2.5), formulating an empirical wall shear stress correlation for

each one of them.

Since the work of Brauer (1956), several experimental investigations (see Miya *et al.* (1971), Alekseenko *et al.* (1973), Wasden & Dukler (1989 *a, b*), Adomeit & Renz (2000) and Moran *et al.* (2002)) have focused on the temporal correlation of wall shear stress and film thickness (more specifically the quantity $\rho_l g_x \delta$). In principle, the main findings of these investigations are contained in the streamwise distributions[†] presented in figure 2.16 and in the previously discussed works of Leefken & Renz (2001) and Tihon *et al.* (2006). They shall thus be discussed on the basis of figures 2.16(b) and 2.16(c). By comparing the quantities τ_{wx} and $\rho_l g_x \delta$ locally, some of the above mentioned authors sought to deduce the state of acceleration of the liquid film at the considered position. However, integration of the streamwise momentum balance over the thickness of the liquid film (neglecting the contribution of interfacial forces) yields that the substantial derivative of streamwise momentum (per unit wall area) is equal to the difference between the streamwise gravitational force (per unit wall area) $\rho_l g_x \delta$ and the wall shear stress and *streamwise pressure derivative* respectively. Consequently, in order to assert the state of cross sectional acceleration of the liquid film, information about the pressure distribution is needed. To that end, figures 2.17(a), 2.17(b) and 2.17(c), depicting the streamwise distribution of wall pressure, and corresponding to figures 2.16(a), 2.16(b) and 2.16(c) have been included. As mentioned previously, the wall pressure distribution in falling liquid films has been investigated by Malamataris *et al.* (2002), who showed that the crosswise variation of liquid pressure is almost purely hydrostatic (with the exception of the capillary wave region).

As can be deduced from figures 2.16(b) and 2.16(c), the wall shear stress exceeds the quantity $\rho_l g_x \delta$ in the residual layer and the wave back as well as the wave front, while it is inferior in the wave crest. These findings corroborate the results of Wasden & Dukler (1989 *a, b*) and Adomeit & Renz (2000). Moran *et al.* (2002) concluded (without taking into account the effect of pressure forces) that the liquid film is decelerated in the residual layer and the wave back

[†]For locally developed film flow (see equation 2.56) the spatial and temporal evolutions of the two quantities are equivalent.

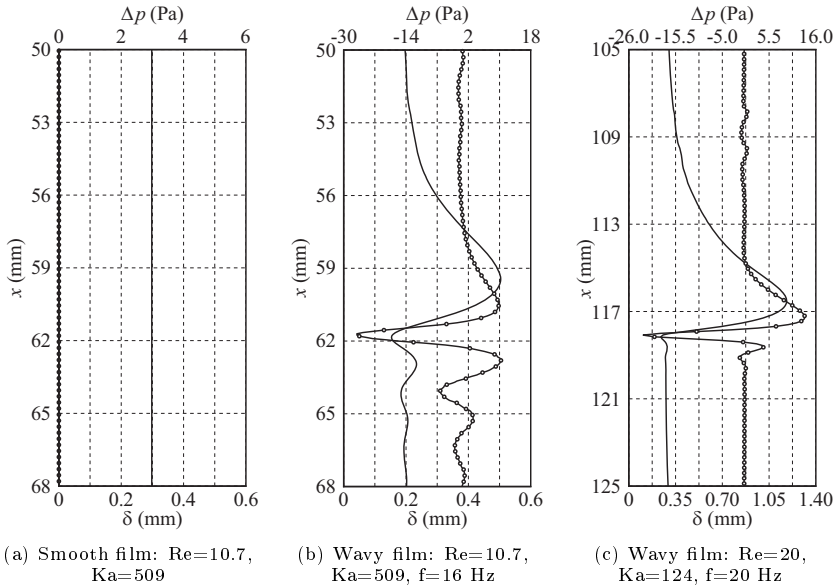


Figure 2.17: Wall pressure distributions, corresponding to figures 2.11(a), 2.11(b) and 2.11(c). Solid lines (bottom ordinate): film thickness; circles (top ordinate): difference between wall pressure and gaseous phase reference pressure $p_r=101325$ Pa.

and is accelerated in the wave crest and the wave front[†]. When taking into account the pressure distribution, one can come to the following conclusions. In the residual layer and the wave back, the streamwise pressure derivative is negligible (see figures 2.17(b) and 2.17(c)). Combined with the fact that $\tau_{wx} > \rho_l g_x \delta$ there, one can conclude that the flow is indeed decelerated. In the wave front, the pressure derivative is very large and negative. Combined with the fact that τ_{wx} and $\rho_l g_x \delta$ do not differ substantially there, one can conclude that the flow is strongly accelerated in the wave front. With respect

[†]The latter assertion however is not entirely consistent with their own line of thought.

to the wave crest, no clear conclusion can be drawn from figures 2.16 and 2.17 without a careful quantitative analysis.

Another characteristic feature of the distributions in figure 2.16 is the occurrence of a peak and subsequent sharp decrease (or “relaxation”) of wall shear stress in the wave front. This was partially confirmed by the respective studies of Alekseenko *et al.* (1973), Wasden & Dukler (1989*a,b*), Adomeit & Renz (2000) and Moran *et al.* (2002). However, some discrepancies between these works are to be noted. Firstly, Moran *et al.* (2002) did not detect the sharp drop in wall shear stress. Secondly, Alekseenko *et al.* (1973) and Adomeit & Renz (2000) measured a wall shear stress peak in the wave back as opposed to the wave front, which at least in the first case may be due to an insufficient dynamical response of the shear stress measurement (as pointed out by Tihon *et al.* (2006)). These discrepancies have not been fully explained and could be due to significantly different wave dynamics investigated in these works, which as mentioned earlier focused on more technically relevant regimes of film flow.

Finally, the wall shear stress measurements of Miya *et al.* (1971), which were conducted in a shear driven horizontal water film, point to another important characteristic property of momentum transfer in liquid films. Indeed, the wall shear stress time trace measured by Miya *et al.* (1971) at $Re=574$ exhibits strong oscillations of high frequency in the wave back and part of the residual layer, indicating the occurrence of turbulence there. However, these oscillations were shown to disappear, as the wall shear stress experiences its sharp decrease in the wave front, indicating the relaminarization of the flow. This is a clear sign that turbulence in falling liquid films is a localized phenomenon, which is strongly influenced by the local wave topology. Miya *et al.* (1971) attributed the relaminarization of the flow to its acceleration in the wave front, citing, amongst others, the work of Kline *et al.* (1967). However, the above considerations concerning the state of acceleration of the flow pertain to the whole cross section of the liquid film, whereas the wall shear stress is a local quantity. As will be shown in this thesis, the dynamics of the capillary wave region, preceding a large wave bear characteristics that could better explain the relaminarization of the flow observed by Miya *et al.* (1971).

With this, focus is now directed toward turbulent momentum transport in falling liquid films, which shall be addressed with a brief overview of relevant literature. The most comprehensive work on this topic is that of Brauer (1956), who used local measurements of the wall-side *heat transfer coefficient* h and the maximal film thickness δ_{\max} , performed for a wide range of working liquids and Reynolds number values, to demarcate the flow regimes of falling liquid films with naturally occurring surface waves. Thereby, limits for the different regimes follow from salient points exhibited by plots of the heat transfer coefficient and maximal film thickness versus the Reynolds number. The resulting Reynolds number limits are listed in table 2.5 along with the corresponding changes in flow dynamics observed or inferred by Brauer (1956), as well as the curve based on which the regime limit was identified. From the point of view of laminar to turbulent flow transition, the salient points of the h - Re -curve are decisive, as they imply a fundamental change in the mechanisms of momentum and scalar transport. Brauer (1956) found two such points, but only considered the one corresponding to the higher Reynolds number value (i.e. $Re=400$) as a transition point, while barely discussing the implications of the other. He thus concluded that falling liquid films are turbulent for $Re>400$. This threshold value was approximatively confirmed by Alekseenko *et al.* (1973) based on their wall shear stress measurement data, which display a salient point between $Re=300$ and $Re=400$.

The salient points of the δ_{\max} - Re -curve delimit changes in wave dynamics, which have in part been previously discussed in section 2.2. The fact that Brauer (1956) observed a threshold Reynolds number value for the onset of harmonic waves is to be attributed to limitations in the film thickness measurement resolution and the test section length, since Brooke Benjamin (1957) later proved that vertically falling liquid films are always unstable to surface perturbations. The second characteristic Reynolds number in table 2.5 pertains to the previously discussed occurrence of solitary waves, which exhibit large maximal to residual film thickness ratios. Brauer (1956) also shows that the streamwise velocity ratio $u|_{y=0} / \bar{u}_{Nu}$ starts to deviate from the value 1.5 at this threshold Reynolds number value, which concurs with the earlier elabora-

No	Re -limit	Salient point	Flow characteristics
1	$0.306 Ka^{3/10}$	δ_{\max} - Re -curve	Occurrence of harmonic waves
2	$0.72 Ka^{3/10}$	δ_{\max} - Re -curve	Occurrence of solitary waves
3	$1.35 Ka^{3/10}$	δ_{\max} - Re -curve	Saturation of streamwise velocity ratio $u _{y=0}/\bar{u}_{Nu}$
4	$0.0181 Ka$	h - Re -curve	No mention of changes in flow characteristics by Brauer (1956)
5	$35.0 Ka^{3/10}$	δ_{\max} - Re -curve	Appearance of parasitic ripples on large waves; saturation of maximal film thickness
6	400	h - Re -curve	Onset of turbulence

Table 2.5: Characteristic Reynolds number values, delimiting regimes of falling liquid film flow according to Brauer (1956).

tions on the change in nature of the streamwise velocity profile as the maximal to residual film thickness ratio increases. The streamwise velocity ratio is then shown to saturate at the third characteristic Reynolds number value. A previously unmentioned change in wave dynamics was observed by Brauer (1956) at $Re=35.0 Ka^{3/10}$, demarcating the occurrence of small *parasitic waves*, that cover the entire wavy interface. Further, at this point, the maximal film thickness is shown to saturate. Brauer (1956) also briefly mentions the occurrence of surge-like waves at $Re>800$ for his measurements with water, but did not attempt to determine a general threshold for this transition.

Later, Ishigai *et al.* (1972) performed experiments similar to those of Brauer (1956) and proposed a different regime classification, which is presented in table 2.6. The deviation regarding the threshold for harmonic waves is to be expected, as no such threshold exists and consequently, measured values depend highly on the employed measurement techniques. Further, Ishigai *et al.* (1972) determined limits of wave dynamics regimes from plots of the *dimensionless* maximal film thickness $\delta_{\max}^* = \delta_{\max}/\delta_{Nu}$ versus the Reynolds number. The δ_{\max}^* - Re -curve exhibits just two salient points as opposed to the δ_{\max} - Re -curve, and accordingly yields one less characteristic Reynolds number value than proposed by Brauer (1956). Based on this, Ishigai *et al.* (1972) differentiated the

2 Falling film dynamics

No	Re -limit	Salient point	Flow characteristics
1	$0.47 Ka^{3/10}$	δ_{\max}^* - Re -curve	Occurrence of harmonic waves
2	$2.2 Ka^{3/10}$	δ_{\max}^* - Re -curve	Onset of stable wavy film flow; saturation of δ_{\max}^* ; onset of wave-induced turbulence
3	75	δ_{\max}^* - Re -curve	Onset of wall-induced turbulence
4	400	see Brauer (1956)	Full wall-induced turbulence

Table 2.6: Characteristic Reynolds number values, delimiting regimes of falling liquid film flow according to Ishigai *et al.* (1972).

following flow regimes. For $0.4 Ka^{3/10} < Re < 2.2 Ka^{3/10}$, the dimensionless maximal film thickness was shown to strongly depend on the Reynolds and Kapitza numbers and the corresponding regime was designated as “first transition region”. The second regime, delimited by $2.2 Ka^{3/10} < Re < 75$, was designated as “stable wavy flow”. In this regime, δ_{\max}^* was shown to be independent of the Reynolds and Kapitza numbers. Further, waves assume a constant amplitude over the length of the employed test section, as opposed to the ensuing third regime ($75 < Re < 400$), where δ_{\max} increases over the entire test section length. This probably indicates the onset of the coarsening dynamics discussed in section 2.2 at $Re=75$.

In addition to the demarcation of wave dynamics regimes, Ishigai *et al.* (1972) investigated the occurrence of turbulence in their work by applying Reynolds’ dye experiment to falling liquid films. By identifying the conditions under which the inserted dye started to exhibit strong lateral dispersion, the authors made the following observations. Turbulent “motions” were shown to appear even in the first wavy regime i.e. for $2.2 Ka^{3/10} < Re < 75$. Therein, turbulent flow conditions were localized and associated with the large waves. These findings thus corroborate the experimental observations of Miya *et al.* (1971). Ishigai *et al.* (1972) conjectured that the generation of turbulence is caused by the “destruction of wave crests”. The authors further hypothesized that, starting at $Re=75$, this wave induced turbulence generation is accompanied by the traditional wall-induced production mechanism, the influence of which was

stated to increase with the Reynolds number. Ishigai *et al.* (1972) concluded by hypothesizing that for $Re > 400$ the production of turbulence in falling liquid films is exclusively wall-induced.

Stirba & Hurt (1955), by way of detailed mass transfer measurements in falling liquid films, determined that turbulence occurs for $Re > 75$, which does not contradict the results of Ishigai *et al.* (1972) and even those of Brauer (1956)[†]. However, the criterion for the transition to turbulence employed by the authors could be misleading. Indeed, transition was assumed to occur once the apparent diffusivity (determined from the measured mass transfer rate on the basis of a smooth film model) deviated from the molecular diffusion coefficient. Such a deviation could also be caused by surface waves without the flow conditions being turbulent. Further, Stirba & Hurt (1955) showed that the apparent diffusivity does not depend on whether interfacial or wall-side mass transfer is considered, deducing that turbulent flow conditions do not vary over the cross section of the film. This could be conceived as a contradiction of the hypothesis by Ishigai *et al.* (1972) that turbulence generation at large Reynolds number values predominantly occurs at the wall.

Having roughly established under which conditions (both in terms of Reynolds number and wave dynamics) turbulence occurs in falling liquid films, the underlying mechanisms shall be addressed here. More specifically, this discussion will focus on the role of surface waves, which has already been implied by the previously evoked observations of Miya *et al.* (1971) and Ishigai *et al.* (1972). An important result in this regard was obtained by Stirba & Hurt (1955), who showed that by adding a *surfactant* (which suppressed surface waves) to a falling liquid film, the onset of turbulence could be delayed to much larger Reynolds number values ($Re = 750$ in their experiments). Although the transitional criterion employed by the authors is somewhat ambiguous, this result is a strong indication that turbulence in wavy falling liquid films is initiated by surface waves.

More systematic investigations of this kind were performed by Brauer (1956),

[†]As listed in table 2.5, Brauer (1956) also found a salient point in this range (i.e. $0.0181 Ka = 70$ for water).

who used the second salient point of his $h-Re$ -curve as a criterion for the onset of turbulence and obtained the following results for a water film. Firstly, he showed that the *transitional Reynolds number*[†] value was not affected by the presence of a tripping wire, which implies that the film would be laminar in the absence of waves. The latter implication was proven by Brauer (1956), by adding a surfactant to the working liquid, which, although not entirely suppressing surface waves, reduced their amplitude. Under these conditions the transitional Reynolds number value was shown to increase to $Re=500$ [‡] in the presence of a tripping wire, whereas in the absence of the wire it increased to $Re=850$. Further, when the initial development of waves was entirely suppressed by the surfactant, turbulence occurred at $Re=1300$ accompanied by the sudden appearance of surface waves. Finally, on the basis of measurements for different working liquids, Brauer (1956) showed that at the onset of turbulence, local wave induced fluctuations, which he characterized with an averaged wave frequency, were identical. In summary, these results indicate that turbulence in falling liquid films is indeed induced by surface waves, and consequently, in accordance with the observations of Miya *et al.* (1971) and Ishigai *et al.* (1972), is intermittent in nature. This intermittency was also observed by Ho & Hummel (1970), who recorded the occasional appearance of eddies in the cross section of the film in their dye-tracer experiments. In addition, the authors proposed some potential explanations for the intermittency. Principally, they identified the residual layer as an inhibitor for the development of turbulence. According to the authors, the small residual film thickness limits streamwise transport of momentum and vorticity and interrupts the turbulence cascade at relatively small eddy sizes, thereby inhibiting the transfer of energy from the main flow to the turbulence carrying vortices. However, the actual mechanism of wave induced turbulence generation has not been elucidated yet. A phenomenological indication was provided by Brauer (1956) (qualitatively) and later by Adomeit & Renz (2000) (quantitatively), who observed the appearance of *turbulent spots* on the surface of large waves.

[†]This term shall refer to the laminar to turbulent transition.

[‡]Interestingly, the critical Reynolds number value for pipe flow $Re_D=2300$ translates to $Re=575$ when introducing the hydraulic diameter of film flow as characteristic length.

Finally, the experimental works of Ueda & Tanaka (1975) and Mudawar & Houpt (1993a) shall be discussed briefly. These investigations are noteworthy in the sense that turbulence was not encountered although measurements were performed at large Reynolds number values (up to $Re=1425$ by Ueda & Tanaka (1975) and up to $Re=1000$ by Mudawar & Houpt (1993a)). Thereby, in both cases, the onset of turbulence or lack thereof was investigated in detail on the basis of velocity fluctuations measured by hot wire anemometry and LDV respectively. In the case of Mudawar & Houpt (1993a) the investigated falling films were smooth due to the use of working liquids with large kinematic viscosity (and small Kapitza number values). Consequently, the authors concluded that the absence of turbulence results from the absence of surface waves, and that turbulence could develop farther downstream. However, these smooth films stayed laminar even in the presence of a tripping wire, which suggests that the transitional Reynolds number for smooth films is also a function of the Kapitza number. Ueda & Tanaka (1975) explained the absence of turbulence in their experiments in a shear driven inclined film by the stabilizing effect of the crosswise component of the gravitational acceleration, which implies an influence of the Froude number as suggested by Freeze *et al.* (2003).

2.3.2 Scalar transport

Having treated falling film wave dynamics and liquid phase momentum transport, a basis has been established to discuss the characteristics of liquid phase *scalar transport*, which is most relevant from a technical standpoint. The term scalar transport refers to the transport of a scalar quantity governed by a *convection-diffusion equation* in the form of 2.21. Examples for such scalars are temperature and the mass fraction of a particular species. Importantly, only *passive scalars*, i.e such that do not affect momentum transport, are considered in this thesis. The overview of scalar transport characteristics, presented in this subsection, will later allow to assess the significance of flow separation in falling liquid films from the perspective of heat and mass transfer. In compliance with section 2.1, formulae shall be developed for the example of heat

transfer with temperature as the transported scalar. Further, the term *scalar transfer* shall be distinguished from the term scalar transport. Scalar transfer designates transport across a material boundary (e.g. a wall surface or the liquid-gas interface), while the term scalar transport shall pertain to diffusional and convective transport in the liquid phase.

Before addressing wavy liquid films, it is useful to establish the characteristics of scalar transport in smooth films. Figure 2.18 depicts two such films for different heat transfer scenarios i.e. wall-side heat transfer and interfacial heat transfer. In both cases, the flow is hydrodynamically and thermally developed, so that velocity profile u_{Nu} and film thickness δ_{Nu} are given by the definitions in 2.11. Introducing a dimensionless temperature Θ^* :

$$\Theta^* = \frac{T - T_d}{T_m - T_d}, \quad T_m = \frac{\int_0^{\delta_{Nu}} \rho_1 c_1 u_{Nu} T dy}{\int_0^{\delta_{Nu}} \rho_1 c_1 u_{Nu} dy}, \quad (2.60)$$

where T_m designates the mean (or bulk) liquid temperature and T_d the temperature at the diabatic boundary, the condition of thermally developed flow can be expressed as $\partial\Theta^*/\partial x=0$ or in terms of the heat transfer coefficient h^\dagger as $\partial h/\partial x=0$. Under these *fully developed* conditions and assuming that stream-wise diffusive transport is negligible, the liquid phase energy equation 2.21 can be simplified to yield:

$$\left[\frac{3}{2}y^{*2} - 3y^* \right] Nu = \frac{\partial^2 \Theta^*}{\partial y^{*2}} \quad (2.61)$$

for the case of a constant heat flux (or Neumann) condition at the diabatic boundary, and:

$$\left[\frac{3}{2}y^{*2} - 3y^* \right] Nu \Theta^* = \frac{\partial^2 \Theta^*}{\partial y^{*2}} \quad (2.62)$$

for the case of a constant temperature (or Dirichlet) condition at the dia-

[†]If not otherwise specified, h is to be considered as the ratio between the local heat flux at the diabatic boundary and the difference between boundary temperature T_d and mean temperature T_m .

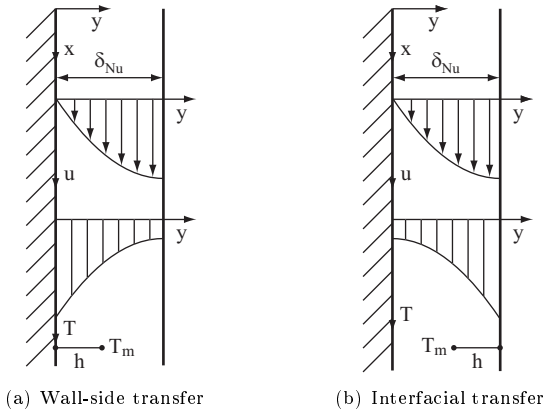


Figure 2.18: Qualitative velocity and temperature profiles in a smooth hydrodynamically and thermally developed film for wall-side and interfacial transfer.

batic boundary. The above equations can be solved for the *Nusselt number* $Nu = h \delta_{Nu} / k_l$ and the dimensionless temperature Θ^* , assuming that the opposing crosswise boundary is adiabatic, i.e. with the following boundary conditions:

$$\left. \frac{\partial \Theta^*}{\partial y^*} \right|_{y^*=0} = -Nu, \quad \left. \frac{\partial \Theta^*}{\partial y^*} \right|_{y^*=1} = 0 \quad (2.63)$$

for the case of wall-side transfer, and:

$$\left. \frac{\partial \Theta^*}{\partial y^*} \right|_{y^*=0} = 0, \quad \left. \frac{\partial \Theta^*}{\partial y^*} \right|_{y^*=1} = -Nu \quad (2.64)$$

for the case of interfacial transfer. Results for the four different scenarios are summarized in table 2.7. For the constant heat flux boundary condition the boundary value problem given by equations 2.61 and 2.63 can be solved analytically, and the exact Nusselt number and temperature profile are given in table 2.7 for wall-side and interfacial transfer respectively. By contrast, no closed form solution has been obtained for the case of a constant temperature bound-

	Wall-side transfer	Interfacial transfer
Dirichlet	$Nu=1.88$ (Kays (1966))	$Nu=3.41$ (Brauer (1971))
Neumann	$Nu=35/17$	$Nu=140/33$
	$\Theta^*=Nu \left[\frac{1}{8}y^{*4} - \frac{1}{2}y^{*3} + y^* \right]$	$\Theta^*=Nu \left[\frac{1}{8}y^{*4} - \frac{1}{2}y^{*3} + \frac{3}{8} \right]$

Table 2.7: Liquid phase Nusselt number and temperature profile, corresponding to figures 2.18(a) and 2.18(b) for conditions of constant temperature (Dirichlet) or constant heat flux (Neumann) at the respective diabatic boundary.

ary condition, although several authors have derived approximate solutions, using iterative methods or series expansions for the dimensionless temperature (see e.g. Nusselt (1923), Kays (1966) and Limberg (1973) regarding wall-side transfer and Brauer (1971) regarding interfacial transfer[†]). For this case, only the (approximate) Nusselt number values are listed in table 2.7 for wall-side and interfacial transfer respectively, as the (approximate) solutions for the temperature profile cannot be written in closed form or are too cumbersome. Nusselt (1923) solved the energy equation without the assumption of thermally developed flow, using an iterative method, and obtained the following approximate relation for the Nusselt number averaged over a considered transfer length x :

$$\overline{Nu}|_x = \frac{1}{x} \int_0^x Nu(\tilde{x}) d\tilde{x} \approx 1.88 + 0.0942 b, \quad b = Re Pr \frac{\delta_{Nu}}{x}. \quad (2.65)$$

This relation was stated to hold for $b < 1/0.15$ and, for thermally developed flow ($b \rightarrow 0$), converges toward the value 1.88 (see table 2.7). Brauer (1971) (see also Emmert & Pigford (1954)) derived a similar relation for the case of interfacial mass transfer with constant interfacial mass fraction, which can be reformulated for the corresponding case of heat transfer to yield:

$$\overline{Nu}|_x \approx 3.41 + \frac{0.276 b^{-1.2}}{1 + 0.2 b^{-0.7}}. \quad (2.66)$$

[†]The solutions obtained by Nusselt (1923), Brauer (1971) and Limberg (1973) are not subject to the assumption of thermally developed flow and thus also describe the streamwise development of Θ^* and/or Nu .

For thermally developed flow ($b \rightarrow 0$), the above relation converges toward the value 3.41 (see table 2.7), while in the limit of a vanishing boundary layer ($b \rightarrow \infty$) it tends toward $\overline{Nu}|_x = (6b/\pi)^{1/2}$. The latter result was obtained by Higbie (1935), by considering the film as a semi-infinite layer traveling with the interfacial velocity. It is clear from table 2.7 that the Nusselt number value is larger for interfacial transfer compared to wall-side transfer and larger for the constant heat flux boundary condition compared to the constant temperature boundary condition.

The discussion of scalar transport in *wavy* liquid films shall be conducted in two steps. First, a basis of evidence concerning the wave effect on scalar *transfer* shall be established, before discussing the underlying liquid phase scalar *transport* mechanisms.

Reviews of early investigations concerning wall-side scalar transfer can be found in the article by Seban & Faghri (1978) and the monograph by Alekseenko *et al.* (1994). Wilke (1962) published the first rigorous investigations of wall-side heat transfer to wavy liquid films, considering laminar and turbulent flow regimes for different working liquids under the condition of constant wall temperature. By measuring the streamwise evolution of the temporally averaged heat transfer coefficient \bar{h} , he was able to show that a drastic increase occurs at the onset of surface waves, after which the flow is *thermally developed*, i.e. \bar{h} assumes a constant value. As a result of this increase, the heat transfer coefficient is approximatively doubled under laminar flow conditions and tripled under turbulent conditions. Further, Wilke (1962) established that the temporally averaged Nusselt number \overline{Nu}_∞ in the thermally developed region departs from the value 1.88 for smooth films as the Reynolds number exceeds a threshold value, which itself decreases with increasing Prandtl number. Above this threshold, \overline{Nu}_∞ was shown to increase with $Re^{8/15}$ in the laminar range and with $Re^{6/5}$ in the turbulent range (i.e. for $Re > 400$). Similar results to those of Wilke (1962) were obtained by Miyara (1999), who numerically simulated liquid films developing from condensing steam. The author showed that the temporally averaged Nusselt number begins to deviate from the smooth

film solution of Nusselt (1916)[†] at a certain streamwise position in the wavy region. This position was shown to move downstream with increasing Prandtl number. Wilke (1962) made a similar observation based on his experiments, showing that, for large Prandtl number values, the streamwise evolution of the temporally averaged Nusselt number \overline{Nu} followed equation 2.65 for smooth films even though waves were present. This effect of increasing Prandtl number values can be attributed to a decrease in boundary layer thickness. As is well established in heat and mass transfer, the thickness of boundary layers decreases with increasing Prandtl, Schmidt and Reynolds number values[‡].

Following initial departure from the smooth film solution, the Nusselt number increased in streamwise direction toward an asymptotic limit which itself increased with the Prandtl number. For large Prandtl number values this limit exceeded the corresponding smooth film Nusselt number by roughly 50%.

On the basis of measurements in a horizontal shear driven film, Frisk & Davis (1972) established the influence of surface waves on wall-side heat transfer very clearly. In their case, the film was hydrodynamically developed at the start of the heating section, which imposed a condition of constant wall heat flux. Results showed that films with large surface waves assumed a thermally developed state at short distances from the start of the heating section (confirming similar observations by Wilke (1962)). Indeed, by comparing the measured streamwise distribution of \overline{Nu} with an analytical solution for smooth films, the thermal entry length for the wavy films was shown to be substantially shorter. Moreover, \overline{Nu}_∞ reached values approximatively twice as large as the value 2.06 for smooth films. Most interestingly, the authors artificially generated smooth films at the same operating conditions as corresponding wavy films by adding a surfactant to the working liquid. Before introducing their results, a brief discussion of the effect of surfactants on film instability is in order.

Indeed, considering that surfactants generally reduce surface tension, the stability analysis results presented in figure 2.4 would suggest that their ad-

[†]Note that reference is made to the earlier work of Nusselt, which treated film condensation.

[‡]Wilke (1962) confirmed this, at least in regard to the Reynolds number, through measurements of the temporally averaged liquid phase temperature profile.

dition to a liquid film has a destabilizing effect. However, Blyth & Pozrikidis (2004) and Pereira & Kalliadasis (2008), on the basis of linear stability analysis accounting for surfactant transport at the liquid-gas interface, showed that the addition of surfactants increases the critical Reynolds number for the onset of surface waves. They explained this effect by variations in the interfacial surfactant concentration, which would arise due to surface waves, in turn causing soluto-capillary or Marangoni-convection believed to stabilize the film.

Getting back to the work of Frisk & Davis (1972), experimental data for their artificially generated smooth films were shown to follow the analytical relation for \overline{Nu} closely. As the only difference between the two sets of experiments was the presence or absence of surface waves, the observed substantial increase of \overline{Nu}_∞ can be irrefutably attributed to the wavy nature of the film. Further, Frisk & Davis (1972) established that small parasitic waves, covering the already wavy interface, had a negligible effect on wall-side heat transfer. Finally, the authors mentioned the potential significance of “turbulent eddies that precede the wave crests” for the wave induced intensification of heat transfer. It will be established in this thesis that the phenomenon of flow separation in falling liquid films, which, although being laminar, fits the above description quite well, bears such a significance.

Comprehensive measurements of the temporally and spatially averaged wall-side *mass transfer coefficient* \bar{h}_m^\dagger were performed by Oliver & Atherinos (1968) for laminar liquid films developing on an inclined wall of dissolving material. This configuration led to a condition of constant wall mass fraction for the transferred component. For a wide range of wavy operating conditions (of varying Reynolds and Froude number values), the authors found that \bar{h}_m could be predicted by an analytical smooth film relation obtained by assuming a linear velocity profile in the convection-diffusion equation (see L ev eque (1928)). They explained this apparent contradiction to heat transfer data, i.e. the absence of a wave effect, by the fact that mass fraction boundary layers are generally substantially thinner than temperature boundary layers. This is owed

[†]Note that the unit of \bar{h}_m is $\text{kg}/(\text{m}^2 \text{s})$.

to significantly smaller values of the *diffusion coefficient* D^\dagger compared to the *thermal diffusivity* α_1 , the ratio between mass and temperature boundary layer thickness scaling with D/α_1 . Consequently, the authors concluded that the employed measurement section was too short for the growing boundary layer to be penetrated by wave induced fluctuations. Chand & Rosson (1965) confirmed the validity of this conclusion with temporally resolved measurements of the wall heat flux in the thermally developing region of a wavy film. They showed that increasing the mean wall heat flux, and thus the local boundary layer thickness, without altering the wave dynamics led to an amplitude increase of the instantaneous wall heat flux oscillation. The results by Oliver & Atherinos (1968) largely confirm the previously published findings of Iribarne *et al.* (1967), who performed similar mass transfer measurements for vertically falling liquid films. However, Iribarne *et al.* (1967) additionally investigated the effect of the Schmidt number $Sc=\nu_1/D$ on the *Sherwood number* $Sh=\bar{h}_m \delta_{Nu}/(\rho_1 D)$ by using different working liquids. Although their experimental data for the temporally and spatially (see corresponding smooth film Nusselt number definition in equation 2.65) averaged Sherwood number $\overline{Sh}|_x$ agree well with the L ev eque-type smooth film solution at large Schmidt number values for both laminar and turbulent flow conditions, deviations were observed at lower values. Indeed, at intermediate values of Sc , mass transfer data for turbulent flow conditions increased in comparison to the smooth film solution, and at even lower values this also occurred for laminar conditions. This influence of the Schmidt number conceivably emanates from its effect on the boundary layer thickness.

Although early investigations conclusively showed a substantial wave-induced increase of the temporally averaged wall-side heat (or mass) transfer coefficient, they did not provide much insight into the nature of this wave effect. Some progress was made in a series of experimental investigations through the temporally resolved simultaneous measurement of film thickness and wall-side transfer coefficient. Brauner & Moalem Maron (1982) measured the local instantaneous film thickness and wall-side mass transfer coefficient h_m for inclined liquid films

[†]Note that the unit of D is m^2/s .

in a dissolution experiment. Time traces in the fully developed[†] region of the flow were shown to be highly correlated, mass transfer coefficient data slightly lagging film thickness data. The maximal mass transfer coefficient value was thus attained in the wave back. These observations were later confirmed by measurements of the wall-side heat transfer coefficient in vertically falling liquid films under laminar (see Al-Sibai *et al.* (2003)) and turbulent flow conditions (see Lyu & Mudawar (1991*a*)). Further, the experimental data of Brauner & Moalem Maron (1982) further showed that h_m was modulated immediately at the onset of large surface waves, while short wavelength parasitic waves, superimposed on the already wavy interface, had a negligible effect. The former observation was later clearly confirmed by full numerical heat transfer simulations of Kunugi & Kino (2005), while the relative insignificance of parasitic waves was also concluded by Ganchev & Trishin (1987), who performed simultaneous measurements of instantaneous wall temperature and film thickness in films heated with a constant wall heat flux. Their data showed that the frequency spectrum of film thickness time traces extended toward significantly greater frequencies compared to that of corresponding wall temperature time traces.

As Brauner & Moalem Maron (1982) did not calibrate their measurement technique, no absolute information about h_m was obtained. However, they were able to evaluate relative quantities such as the rms of h_m related to the temporally averaged value \bar{h}_m . The dependence of this ratio on the streamwise position and the Reynolds number was investigated for a wide range of flow regimes. The ratio was shown to increase in streamwise direction, attaining constant values of 20% for laminar conditions and 35% for turbulent conditions in the fully developed flow. The authors explained this spatial evolution by the concurring streamwise development of surface waves, including the coarsening dynamics discussed in section 2.2, and the simultaneous downstream growth of the mass fraction boundary layer. The ratio $\text{rms}(h_m)/\bar{h}_m$ was also shown to increase with the Reynolds number value, which the authors

[†]In the non-steady case, “fully developed” signifies that the temporally averaged transfer coefficient is spatially independent.

attributed to an increase in wave amplitude. However, the rate of increase diminishes at large Reynolds number values (up to $Re=860$), possibly resulting from the saturation of wave amplitude. Heat transfer measurements by Lyu & Mudawar (1991*a*) show that, at even larger Reynolds number values ($Re \geq 3000$), the ratio $\text{rms}(h)/\bar{h}$ diminishes with Re and converged toward a constant value, which the authors attributed to increasing “levels of turbulence mixing”. Experiments by Ganchev & Trishin (1987), also conducted under turbulent conditions, yielded similar results, showing the rms of wall temperature to decrease with the Reynolds number. Thereby, for waves of saturated amplitude, the Reynolds number determines the thickness of the residual layer, which, as stated earlier (see Mudawar & Houpt (1993*b*)), represents a resistance to crosswise momentum transport and dampens the effect of wave-induced fluctuations on near-wall conditions (see also Lyu & Mudawar (1991*b*)). The consequences for wall-side heat transfer were established by Ganchev & Trishin (1987), who in addition to wall temperature and film thickness also measured the instantaneous liquid temperature at a constant crosswise position in the film. Their data shows that the amplitude of wall temperature fluctuations is significantly lower than that of temperature fluctuations in the film.

Detailed investigations of the instantaneous wall-side heat transfer coefficient were performed by Al-Sibai *et al.* (2002). The authors used a resistively heated thin constantan foil, along the surface of which a laminar vertically falling liquid film developed, to impose a condition of constant wall heat flux. The spatio-temporal distribution of wall temperature was measured with an infrared camera, collecting radiation from the rear side of the foil, which was dyed black. First of all, Al-Sibai *et al.* (2002) confirmed the findings of the previously discussed works, concerning the temporally averaged Nusselt number. Their results show that \overline{Nu} increases with streamwise position and Reynolds number and attains values twice as large as the corresponding smooth film Nusselt number ($Nu=2.06$) in the fully developed region of the flow. In addition, the authors quantified the Prandtl number influence on the Nusselt number in both the developing and developed region of the flow, by performing experiments with different working liquids. In the fully developed region, the ratio

between the temporally averaged Nusselt number for wavy film flow and the corresponding value for smooth film flow increases with the Prandtl number. On the basis of Nusselt number time traces obtained from numerical simulations for three different Prandtl number values (at a constant Reynolds number value) and evaluated in the developed region of the flow, the authors were able to elucidate the cause for this increase. While the three different time traces exhibit equivalent maximal values for Nu , which were periodically attained as waves passed the considered position, minimal values, and consequently the temporal average, increase with the Prandtl number. Since the wave dynamics were identical in the three cases and the flow was fully developed, barring the influence of boundary layer evolution, the authors attributed this effect to the scaling of liquid phase convective transport by the Prandtl number. Indeed, as can be deduced from the dimensionless energy equation in 2.21, the product $Re Pr$, which corresponds to the *Péclet number*, scales the convective transport terms. Consequently, the importance of liquid phase convective transport and with it the effect of wave-induced velocity fluctuations increases with the Prandtl number[†]. Unfortunately, Al-Sibai *et al.* (2002) did not simultaneously measure film thickness time traces so that it was not possible to discern which part of the wave gains influence as the Prandtl number increases. The authors merely stated that the investigated liquid films were covered by 3-dimensional waves over most of the heated section with the exception of a short 2-dimensional region where the flow was not thermally developed. In this region, Al-Sibai *et al.* (2002) found the Prandtl number to exert a different influence on wall-side heat transfer. Indeed, Nusselt number time traces measured at a constant streamwise position for different working liquids exhibit larger fluctuations with decreasing Prandtl number, which is to be attributed to an increase in boundary layer thickness (see also Chand & Rosson (1965)). It should be mentioned here that none of the regimes investigated in the works of Brauner & Moalem Maron (1982), Lyu & Mudawar (1991a) and Al-Sibai *et al.* (2002, 2003) displayed significant capillary waves in front of large wave humps.

[†]This argument was previously presented by Wilke (1962) and also explains his observation that the threshold Reynolds number value for wave induced intensification of wall-side heat transfer decreases with increasing Prandtl number.

As will be established subsequently, the presence of such waves significantly alters the behaviour of wall-side scalar transfer.

The characteristics of wall-side heat transfer in 2-dimensional falling liquid films with pronounced capillary waves have been elucidated only recently, by way of full numerical simulations (Adomeit *et al.* (2000) and Kunugi & Kino (2005)) and detailed experiments (Schagen *et al.* (2006)). Adomeit *et al.* (2000) computed streamwise distributions of instantaneous film thickness and wall-side heat transfer coefficient at different times in the evolution of a surface wave, consisting of a large wave hump and several preceding capillary waves. The heat transfer coefficient h was shown to exhibit a global maximum at the first capillary minimum and a global minimum in the large wave. Moreover, all capillary waves were associated with local heat transfer coefficient minima and maxima, corresponding to respective capillary maxima and minima, while no variation of h was observed in the residual layer. Similar numerical results were obtained by Miyara (2001) for films developing as a result of steam condensation. Importantly, Adomeit *et al.* (2000) showed that this modulation of h depends highly on the Prandtl number. At very low Prandtl number values, h varies almost inversely with the film thickness. Consequently, the global minimum of h coincides with the wave crest, and is approximately five times smaller than the maximum. With increasing Prandtl number, the ratio of maximal to minimal heat transfer coefficient decreases, while the position of the global minimum moves upstream toward the wave back. Thereby, the maximal streamwise velocity at the interface was shown to slightly exceed the wave celerity, meaning that a moving frame vortex is present in the large wave hump. To illustrate the findings by Adomeit *et al.* (2000), a selection of the author's own simulation data for the case of wall-side heat transfer and constant wall temperature is depicted in figure 2.19. Pictured are simultaneous time traces of the wall-side Nusselt number[†] as well as the film thickness for films corresponding to subfigures 2.11(b) and 2.11(c). Subfigures 2.19(b) and 2.19(c) display the influence of the Prandtl number for one of the flow

[†] Nu was evaluated with the difference between wall and instantaneous mean (see equation 2.60) temperature, while Adomeit *et al.* (2000) used the temperature difference between wall and interface.

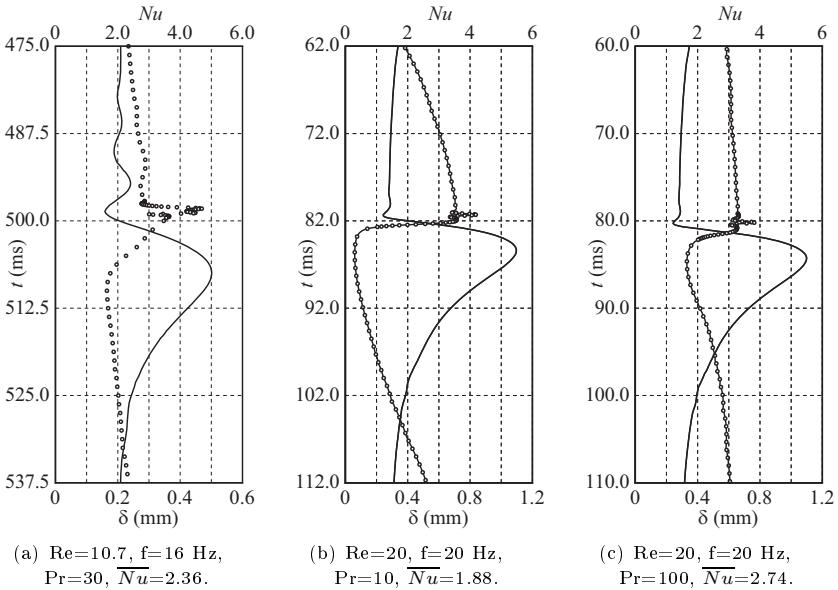


Figure 2.19: Nusselt number time traces for wall-side heat transfer and constant wall temperature, corresponding to figures 2.11(b) and 2.11(c). Solid lines (bottom ordinate): film thickness; circles (top ordinate): Nusselt number.

regimes. It is important to note that Adomeit *et al.* (2000) applied periodic boundary conditions for the temperature field in their numerical simulations, which is incorrect. Nonetheless, their results regarding the heat transfer coefficient were qualitatively confirmed by the measurements of Schagen *et al.* (2006), who used a Laser Induced Luminescence technique to measure the instantaneous liquid phase temperature profile as well as the film thickness, and also found a heat transfer coefficient maximum at the first capillary minimum. However, spatial temperature information was obtained indirectly through the solution of an inverse problem based on the assumption of a parabolic liquid

phase velocity profile without accounting for the possibility of backflow in the capillary wave region. Recently, Kunugi & Kino (2005) (see also Kunugi & Kino (2003); Kunugi *et al.* (2005)), by way of full numerical simulations of the Navier-Stokes equations for a vertically falling water film, confirmed the existence of a heat transfer coefficient maximum at the first capillary minimum unambiguously. In this region, the simulation data exhibit a roughly twofold increase in the Nusselt number, which was defined based on the temperature difference between wall and interface. Interestingly, different results were obtained depending on the nature of the diabatic boundary condition (constant wall heat flux or constant wall temperature), which the authors attributed to effects of coupled heat and momentum transport e.g. thermo-capillary effects. Indeed, capillary waves were shown to be less pronounced for the constant wall temperature condition, which resulted in a lower maximal to minimal Nusselt number ratio (approximately 1.8) in the fully developed region of the flow, the other wave characteristics remaining largely unchanged. As mentioned previously, Kunugi & Kino (2005) also reported results of a 3-dimensional numerical simulation, displaying a complex wave pattern and associated wall shear stress distribution. Heat transfer data for this case show that the wall-side heat transfer coefficient is strongly correlated with film thickness and wall shear stress data and attains maximal values wherever capillary waves are present.

The findings reported above indicate that the region of capillary waves strongly influences wall-side scalar transfer in falling liquid films. It is also reasonable to assume that the previously discussed occurrence of backflow in this region could be responsible for the drastic increase of the wall-side heat transfer coefficient observed by Adomeit *et al.* (2000), Kunugi & Kino (2005) and Schagen *et al.* (2006). Indeed, it will be shown in this thesis (see section 5.3) that the phenomenon of flow separation in the capillary wave region (which causes the backflow) provides a physical explanation for these observations.

Although only wall-side scalar transfer is explicitly considered in this thesis, a brief discussion of interfacial transfer in wavy liquid films is presented next. As the difference between these cases is simply a matter of boundary conditions, the principle characteristics established above must also hold for interfacial

transfer. However, in the latter case, the diabatic boundary coincides with the interface, which is the origin of the film's waviness. Consequently, the wave-induced intensification of scalar transfer is conceivably stronger for this scenario, which has been confirmed by different experimental investigations. Concerning the capillary wave region, a mechanistic explanation for this difference between interfacial and wall-side transfer shall be provided in this thesis (see section 5.3). It is with this in mind that the ensuing literature review was conducted.

An excellent overview of early investigations was summarized by Seban & Faghri (1978) and Henstock & Hanratty (1979) (see also the book of Alekseenko *et al.* (1994)). Seban & Faghri (1978) compared measurement results of different experimentalists for the temporally and spatially averaged Sherwood number $\overline{\overline{Sh}}|_x$ with a smooth film relation similar to equation 2.66, showing that $\overline{\overline{Sh}}|_x$ is three (data of Emmert & Pigford (1954)) to four (data of Kamei & Oishi (1956)) times larger in wavy films, independently of the boundary layer's state of development (characterized by the parameter $b = Re Sc \delta_{Nu}/x$). In contrast, as was established earlier, the temporally averaged wall-side Nusselt number follows the corresponding smooth film relation closely even in the wavy region of a film, if the boundary layer thickness is sufficiently small and thus confined to a layer hydrodynamically unaffected by waves. Further, as reported previously, in the wave-affected region of the flow, the wall-side Nusselt number increase compared to the corresponding smooth film solution was roughly 100%, which is lower than the 200-300% increase reported by Seban & Faghri (1978) for interfacial transfer. The review of Seban & Faghri (1978) also enables a comparison of temporally averaged Nusselt (or Sherwood) numbers for the two transfer scenarios in the fully developed region of the flow. Indeed, the authors correlated experimental data of Kamei & Oishi (1956) for the temporally averaged Sherwood number $\overline{\overline{Sh}}_\infty$ in terms of the Reynolds and Schmidt numbers, yielding the same power for Re as in the Nusselt number correlation of Wilke (1962) for wall-side transfer. When relating these two correlations, one obtains a factor of roughly 1.26 for the ratio between interfacial and wall-side Nusselt (or Sherwood) number, which is inferior to the corresponding ratio obtained for

smooth film flow (see table 2.7). Later, Henstock & Hanratty (1979) proposed a more general relation for the interfacial Sherwood number by correlating the experimental data of nine different authors. Their results show that data by Kamei & Oishi (1956) were systematically larger than data of other workers and thus represent an upper bound.

More recent investigations have focused on elucidating the influence of different control parameters, such as wave frequency, Reynolds number, transfer length and inclination angle on the wave-induced intensification of interfacial scalar transfer, in order to identify optimal regimes of operation for technical apparatuses. An excellent example of such investigations is that of Rastaturin *et al.* (2006). The authors investigated the influence of the frequency of excited surface waves on the temporally and spatially averaged Sherwood number $\overline{Sh}|_x$ by way of 2-dimensional numerical simulations. With increasing frequency, as the wave dynamics change from solitary waves with preceding capillary waves to multi-peaked interacting waves and finally to harmonic waves, the Sherwood number exhibits a local maximum in each of these three regions, while the global maximum occurs for the solitary wave regime. By comparing these results with their own computations for naturally arising waves (see Demekhin *et al.* (2007)), the authors showed that mass transfer could be significantly enhanced through the imposition of controlled monochromatic disturbances. This frequency dependence, at least for the region of solitary waves, was also observed experimentally by Nakoryakov *et al.* (1982) and Yoshimura *et al.* (1996), who provided a physical explanation. These authors contended that an increase in frequency in the range of low values, while increasing the number of waves covering the transfer section, does not cause solitary waves to change significantly in shape. Consequently, the wave induced transfer intensification, and with it $\overline{Sh}|_x$, increases. At large frequency values, neighbouring waves constrain each other, reducing their respective amplitudes and consequently their effect on liquid phase transport, and cause $\overline{Sh}|_x$ to decrease with frequency (Nakoryakov *et al.* (1982) also cited this effect to explain, why their measured Sherwood number values are lower for 3-dimensional waves compared to 2-dimensional waves excited at the same frequency). As both effects are countercurrent, a

maximum is established at intermediate frequency values. Yoshimura *et al.* (1996) showed that this maximum moves toward higher frequency values with increasing Reynolds number. Further, the maximal value of $\overline{Sh}|_x$ related to the corresponding value for smooth film flow was shown to increase with the Reynolds number, attaining an asymptotic limit of roughly 2.5. Nakoryakov *et al.* (1982) and Oliver & Atherinos (1968) had earlier come to similar conclusions, and Oliver & Atherinos (1968) remarked that the observed saturation sets in when the Weber number exceeds unity. Park & Nosoko (2003) measured $\overline{Sh}|_x$ in falling liquid films with naturally arising surface waves over a wide range of Reynolds number values, observing the same wave-induced increase of mass transfer as in the previously mentioned studies. Further, their results exhibit salient points of the $\overline{Sh}|_x-Re$ relation at $Re=400$, i.e. at the onset of turbulence, and at $Re=40$, which coincides with the “disintegration” of 2-dimensional waves into 3-dimensional structures.

Alekseenko *et al.* (1996) found that, similar to the influence of wave frequency, an optimum (in terms of $\overline{Sh}|_x$) exists for the length of the transfer section, while Oliver & Atherinos (1968) showed that the wave-induced intensification of interfacial transfer increases with the inclination angle. Oliver & Atherinos (1968) also demonstrated that artificially imposed parasitic waves, covering the already wavy interface, have no effect on the Sherwood number. For highly turbulent wavy films, Freeze *et al.* (2003) came to the opposing conclusion, establishing that small scale parasitic waves attenuate the stabilizing effect of surface tension on turbulence near the interface. This process was shown to intensify with increasing inclination angle.

The only temporally resolved experimental investigations of interfacial scalar transfer in wavy liquid films are those of Stainthorp & Wild (1967), Wolff & Hanratty (1994) and Schagen & Modigell (2005). Stainthorp & Wild (1967), using an optical measurement technique, determined the instantaneous film thickness and mean (or bulk) liquid phase mass fraction of the transferred component. Time traces of these two quantities were shown to be highly correlated, the mean mass fraction’s maximum slightly lagging the wave crests near the liquid inlet and leading them further downstream. Schagen & Modigell (2005),

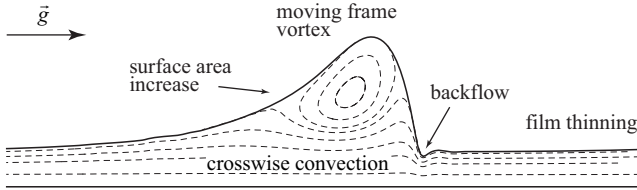


Figure 2.20: Sketch of possible mechanisms for the intensification of scalar transport in wavy falling liquid films.

using the previously mentioned Luminescence technique, simultaneously measured instantaneous mass fraction profiles as well as the local film thickness and found that the interfacial mass flux is highest in the capillary wave region compared to the wave crest and wave back. The investigations of Wolff & Harratty (1994), who also measured instantaneous mass fraction profiles using a LIF technique without measuring the film thickness, had previously shown a substantial temporal variation of the interfacial mass flux in wavy films. For the case of film condensation, which is characterized by both interfacial and wall-side heat transfer, Miyara (2001) numerically showed that the interfacial heat transfer coefficient is modulated by waves in a much stronger fashion than is the case for the corresponding wall-side coefficient.

To conclude this chapter, an overview of literature, concerning liquid phase transport mechanisms at the origin of the above established wave-induced scalar transfer intensification, is provided next. Different possible mechanisms of this sort have been proposed thus far, and are illustrated by means of a typical solitary rolling wave in figure 2.20. The first of these mechanisms pertains to the wave-induced increase in interfacial area, which could be conceived to augment interfacial scalar flow similarly to the effect of a fin. However, Portalski & Clegg (1971), through careful film thickness measurements, established that the interfacial area increase caused by waves is only of the order of 1%, thus refuting the significance of this effect for scalar transfer in falling liquid films.

For the case of liquid films developing from condensing steam (or evaporating

liquid films for that matter), i.e. with constant temperature conditions at both the wall and the interface, the so called *film thinning effect* has been evoked by a series of authors. Due to these boundary conditions, streamwise temperature changes are largely suppressed, leaving only crosswise convective transport to distort an otherwise linear liquid phase temperature profile. Consequently, the *smooth film* Nusselt number, based on the temperature difference across the film, is unity, i.e. heat is transported by pure conduction from the wall through the film and into the gaseous phase. For small Prandtl number values (or, more generally, small Péclet number values) the crosswise conduction term in the energy equation dominates, yielding linear instantaneous temperature profiles also in wavy films (see the numerical simulations of Adomeit *et al.* (2000)). Under such conditions, the temporally averaged Nusselt number satisfies $\overline{Nu} = \overline{\delta_{Nu}}/\delta$, which, depending on the wave shape, may deviate significantly from unity. In fact, as the average of the reciprocal value of a given quantity is generally smaller than the reciprocal of that quantity's average, and as the mean film thickness tends to the smooth film thickness δ_{Nu} , $\overline{\delta_{Nu}}/\delta$ is generally larger than unity. This conductive-kinematic intensification of heat transfer in wavy liquid films is termed the film thinning effect.

Jayanti & Hewitt (1997) performed a detailed analysis of this effect by numerically solving the Navier-Stokes and energy equations for predefined wave shapes as explained in subsection 2.3.1 for a liquid with $Pr=1$. For all investigated cases the instantaneous heat transfer coefficient closely follows $h = k_1/\delta$, indicating linear temperature profiles. For harmonic and distorted harmonic wave shapes, the authors showed that \overline{Nu} increases with distortion (only slightly) and wave amplitude, attaining values roughly 25% larger than unity. The strongest film thinning effect (an increase in \overline{Nu} of roughly 35% over unity) was observed for rolling waves, which, as stated earlier, transport most of the liquid and thereby leave behind long stretches of thin residual layer. Although these rolling waves were shown to slightly distort the temperature field, pointing to the significance of convective transport, this contribution is small compared to the film thinning effect.

For larger Péclet number values, Faghri & Seban (1985) (using a different

numerical approach) had previously shown that $\overline{\delta_{Nu}/\delta}$ accounts for only a part of the wave-induced increase of interfacial and wall-side mean Nusselt numbers. The rest was attributed to convective transport. Indeed, for their largest Péclet number value, the Nusselt number maximum was observed in the wave hump and the minimum in the wave trough. Further, interfacial transfer was shown to be affected more strongly by waves than wall-side transfer. Both of these observations not being compatible with pure crosswise conduction. The authors also discarded the effect of streamwise conduction caused by wave-induced streamwise temperature gradients based on a solution of the 2-dimensional Fourier equation in the liquid phase. Nusselt number values derived from these data closely agree with those obtained under the assumption of pure crosswise conduction[†]. Finally, the authors showed \overline{Nu} to be strongly influenced by wave amplitude, attaining values of up to 1.75 as a result of the combined effects of film thinning and convection.

A thorough numerical investigation of the respective relevance of these two effects was performed by Miyara (1999). The author simulated condensate films of varying Prandtl number and found that for low values ($Pr \leq 1$) the temporally averaged wall-side Nusselt number closely follows $\overline{Nu} = \overline{\delta_{Nu}/\delta}$, exceeding unity by roughly 37% (see also Stuhlträger *et al.* (1995) and Miyara (2001)). As the Prandtl number is increased ($10 \leq Pr \leq 100$), \overline{Nu} attains values of approximately 1.56, while $\overline{\delta_{Nu}/\delta}$ stays unchanged. Temperature contours under these conditions were shown to be distorted in the wave hump (Stuhlträger *et al.* (1995) and later Adomeit *et al.* (2000) showed that temperature profiles deviate from a linear shape in the wave hump), pointing to the relevance of convection, while, at low Prandtl number values, isothermal lines closely follow the wave shape (indicating linear temperature profiles). Miyara (1999) concluded from his investigations that, at small Prandtl number (or, more generally, Péclet number) values, the film thinning effect is dominant, while for larger values it is accompanied by a mechanism of wave-induced convective transport intensification. As stated earlier, this influence of the Prandtl (or Péclet) number

[†]Later, Roberts & Chang (2000) modelled the wave induced streamwise conduction effect by likening it to *Arís-Taylor dispersion* and also found it to be weak.

follows from its scaling property of convective terms in the energy equation. Later, these results, were also obtained by Leefken & Renz (2001), using a different numerical approach.

The convective effect of the wave hump is evident in the previously discussed temporally resolved wall-side Nusselt number data obtained numerically by Adomeit *et al.* (2000) and Al-Sibai *et al.* (2002) (see also Leefken & Renz (2001)). Indeed, both authors showed the minimal value of Nu , which was attained in the wave hump, to increase with the Péclet number. Adomeit *et al.* (2000) quantified the convection effect by evaluating the streamwise distribution of $h \delta/k_1$. This quantity was shown to exhibit a global maximum (with a value of roughly 2 for a Péclet number value of 50) in the wave hump and several local maxima (also in excess of unity) associated with respective capillary maxima, pointing to the significance of convective transport (compared to the film thinning effect) in these regions. Later, Leefken & Renz (2001) showed that the global maximum of $h \delta/k_1$ decreases significantly with the Péclet number, while the local maxima in the capillary wave region are less affected. It should be stated that in the investigations by Miyara (1999), Adomeit *et al.* (2000) and Leefken & Renz (2001) surface waves exhibit a moving frame vortex in the main wave hump.

Although the above elaborations establish the significance of liquid phase convective transport for the wave-induced intensification of scalar transfer, as well as identify regions of the wavy film where this contribution is important (i.e. the main wave hump and the capillary wave region), the actual transport mechanisms responsible for this effect have not been discussed. In principle, three such mechanisms have been distinguished in the literature. Firstly, *cross-wise convective transport* induced by the variation of film thickness. Secondly, mixing in the wave hump caused by a *moving frame vortex*, and thirdly an effect resulting from the existence of *backflow* in the capillary wave region.

Intensification due to crosswise convective transport refers to Prandtl's well established mixing length concept, which states that diffusive transport can be effectively (or apparently) augmented by velocity oscillations superimposed on the mean flow. In essence these fluctuations cause fluid elements to make

excursions into regions of different temperature where they heat up or cool down before returning to their region of origin, thus completing (convective) transport on a smaller scale than the mean flow but on a larger scale than the diffusion process. This contribution can be described with an effective thermal diffusivity given by $\alpha_{\text{eff}} = \hat{v} l$, where \hat{v} and l designate the characteristic mixing velocity and mixing length respectively. Arguably, in falling liquid films, it is in crosswise direction that this effect is most significant, as crosswise temperature gradients are significantly larger than streamwise gradients and due to the fact that, in streamwise direction, convection by the mean flow dominates all other transport mechanisms. Thereby, the crosswise convective transport under consideration here is caused by wave-induced fluctuations of the crosswise velocity component. The potential relevance of this effect was demonstrated by O'Brien (1967), who, for a modelled wave, showed that the wall heat flux is increased by 100% at large Péclet number values, due to crosswise convective transport.

Wasden & Dukler (1990) approximated the near wall crosswise velocity component by $v \approx -0.5 y^2 \mu_1 \partial \tau_{wx} / \partial x$, relating it to the streamwise derivative of wall shear stress. Consequently, crosswise velocity fluctuations, and thereby the crosswise convection effect, are concomitant with fluctuations in wall shear stress. This explains the previously discussed correlation between wall shear stress and wall-side heat transfer coefficient observed by Kunugi & Kino (2005), which is evident when comparing figures 2.16 and 2.19 (see also Leefken & Renz (2001)). Wasden & Dukler (1990) singled out the region near the front stagnation point in a rolling wave as exhibiting strong crosswise convective transport (which is evident from the streamlines in subfigure 2.14(c)). This effect is clear in their simulations of interfacial mass transfer as the scalar field is significantly distorted in this region (to be precise, the region near the stagnation point is characterized by smaller gradients of the transported scalar than in the surrounding regions) and the local interfacial mass flux is maximal. A similar yet weaker effect was observed at the back stagnation point. Lyu & Mudawar (1991*b*) confirmed these results with highly resolved measurements of the liquid phase temperature field, showing “temperature excursions” in the

regions where the moving frame stagnation points were suspected. Further, the authors observed strong temperature fluctuations in the residual layer, which are correlated with corresponding film thickness fluctuations. Oliver & Atherinos (1968) provided a direct experimental proof of the significance of crosswise convective transport in the liquid phase by observing the spread of dye inserted at different wall distances. Indeed, the dye, when injected close to the wall, stayed confined to a narrow trace in streamwise direction, while, when injected further from the wall, it spread considerably in crosswise direction.

Some experimentalists have tried to measure the distribution of the effective diffusivity, resulting from crosswise convective transport, directly. Wilke (1962) determined mean profiles of the effective thermal diffusivity from his temperature measurements, showing α_{eff} to exhibit a maximum inside the residual layer and to vanish at the wall. Further, the magnitude of α_{eff} was shown to be up to four times larger than the corresponding molecular value and to depend on the Reynolds and Prandtl numbers. Jepsen *et al.* (1966) came to similar conclusions for the case of interfacial mass transfer. Later, Schagen & Modigell (2005) and Schagen *et al.* (2006) evaluated instantaneous profiles of the effective diffusivity for wall-side heat transfer and interfacial mass transfer, showing these to exhibit maxima at a wall distance of roughly half the local film thickness in all regions of the wave. Finally, Adomeit *et al.* (2000) and Leefken & Renz (2001) also evoked the effect of crosswise convective transport to explain their simulated distributions of the wall-side Nusselt number without elaborating its contribution in detail.

The contribution of moving frame vortices to the intensification of scalar transport has been more rigorously investigated from the perspective of interfacial mass transfer, as due to the greater proximity of the phenomenon to the interface its effect is stronger in this case. Dukler (1976) was the first to conjecture a mixing action inside large wave humps, causing the homogenization of a transferred component's mass fraction there. This conception was later validated, based on numerical simulations, by Wasden & Dukler (1990), who showed that this mixing action is performed by a moving frame vortex developing in rolling waves. Dukler (1976) also proposed a mechanism for the

intensification of interfacial mass transfer by these well mixed wave humps. He designated this mechanism as one of renewal, echoing a previous conjecture by Dankwerts (1951) (see also Banerjee *et al.* (1967)). A detailed description of the mechanism was later provided by Yoshimura *et al.* (1996), who termed it *surface renewal mechanism*. The surface renewal mechanism is based on the conception that a large wave passing over a residual film interrupts the growth of the interfacial boundary layer developing in that film, the liquid of which is engulfed by the mixing action of the wave hump. After passage of the wave, a “fresh” (in terms of the homogeneity of the mass fraction distribution) residual film is left behind, which subsequently re-initiates the development of a boundary layer. Due to the intermittent interruption of boundary layer growth by large wave humps, the mean boundary layer thickness is considerably reduced, leading to large Sherwood number values. Dukler (1976), in his conception assumed that the liquid engulfed by the wave hump would be fully mixed in a large mixing zone in the wave hump similar to the moving frame vortex later observed by Wasden & Dukler (1990). However, the streamlines of such a moving frame vortex (see e.g. figure 2.20) are closed and thus always contain the same liquid. Consequently, the evoked mixing action must be provided by the crosswise transport mechanisms discussed earlier. In such a case it is conceivable that liquid left behind by a large wave is not fully mixed but rather exhibits a “relaxed” boundary layer near the interface. Yoshimura *et al.* (1996) introduced the concept of successive convoluted boundary layers to describe this effect. According to Roberts & Chang (2000) however, the mixing action of rolling waves is considerably increased if moving frame vortices are subject to intermittent disintegration and redevelopment due to wave coalescence events (see Miyara (2000)). Under such conditions liquid in the moving frame vortex is intermittently shed after having been mixed and “new” liquid from the residual film is entrapped anew as the vortex redevelops. The moving frame vortex then acts as a well mixed buffer reservoir. As stated by Roberts & Chang (2000), the surface renewal mechanism is not restricted to rolling waves, as waves without a moving frame vortex also “relax” the boundary layer of the engulfed liquid due to the crosswise convective transport arising from its “expansion” into the

wave hump (to be understood in a moving frame of reference).

In addition to the surface renewal mechanism, interfacial transfer to a rolling wave hump is also directly enhanced by the recirculation there. As established by Bontozoglou (1998) and Roberts & Chang (2000), the growth of the interfacial boundary layer in the wave hump is limited by the moving frame vortex, which “sucks” enriched liquid from the front stagnation point and recirculates it. As this liquid is recirculated, the transferred component diffuses into the vortex core and the near wall region to the other side, thereby being “refreshed” before it attains the interface again in the wave back. This mixing mechanism stays significant until the moving frame vortex is saturated. An excellent overview of the two intensification mechanisms of the moving frame vortex is provided by Rastaturin *et al.* (2006).

Miyara (1999) investigated the effect of moving frame vortices from the point of view of wall-side heat transfer in a condensate film. The author, in agreement with the previously discussed investigations, observed that, for large Prandtl number values, such vortices mix the liquid confined in the wave hump, causing the homogenization of the temperature field within this region (at small Prandtl number values, no such effect was observed, the isothermal lines following the wave shape closely). Thereby, with increasing Prandtl number, this almost isothermal region was shown to expand beyond the actual vortex in the direction of the wall thus establishing a near wall boundary layer. The author concluded that the accompanying increase in the near wall crosswise temperature derivative is responsible for the intensification of wall-side scalar transfer beneath the wave. This effect of moving frame vortices was later confirmed by Adomeit *et al.* (2000), Leefken & Renz (2001) and Kunugi & Kino (2003), as opposed to Jayanti & Hewitt (1997), who observed only a comparatively small mixing action. This however was due to the small Prandtl number value considered in the latter study.

Only a few investigations have considered the effect of backflow in the capillary wave region on scalar transfer. Portalski (1964*a*) conjectured that the cellular pattern in the backflow region he obtained from Kapitza’s two equation model caused “vigorous bulk mixing” and ensured “fast surface renewal”.

This scenario was also proposed by Banerjee *et al.* (1967) and later Kunugi & Kino (2005) and Kunugi *et al.* (2005). In this thesis (see section 5.3), a mechanistic understanding of the effect of backflow on liquid phase scalar transport shall be developed, explaining the substantial increase of transfer coefficients in the capillary wave region observed by several authors (see e.g. Adomeit *et al.* (2000) and Kunugi & Kino (2005)). Further, this understanding will allow to explain the difference in effects on wall-side and interfacial transfer and, by extension, will shed light on some of the transport mechanisms in the wave hump. Oliver & Atherinos (1968) inferred from dye tracer experiments that, under 3-dimensional flow conditions, “corkscrew” type vortices cause lateral mixing in the film and could help to explain the wave induced transfer intensification. The authors estimated these vortices to lie within the main wave hump and did not specify if they were to be viewed in a moving frame of reference or not. As will be shown in this thesis, such vortices indeed develop in the capillary wave region of 3-dimensional falling liquid films, causing both backflow and strong spanwise convective transport (see section 5.5).

A discussion of liquid phase scalar transport would not be complete without mentioning the effect of turbulence. Concerning this topic, the reader is referred to the works of Banerjee *et al.* (1968), Ueda & Tanaka (1975), Lyu & Mudawar (1991a) and Freeze *et al.* (2003) on the subject.

Summarizing this review of relevant literature, it can be stated that the elucidation of the backflow phenomenon occurring in the capillary wave region is an important step toward completing the understanding of falling liquid films. It has been shown that the backflow phenomenon, barring turbulence, up until now has remained the only unexplained and unaccounted for aspect of the liquid phase velocity field. Further, it has been shown that the characteristics of this phenomenon are potentially critical to the development of multi equation models. Further, it is conceivable that backflow could be connected to the secondary instability of surface waves. Finally, the potential significance of the phenomenon in the context of wave-induced intensification of liquid phase scalar transport has been established. All these points warrant a detailed fluid mechanical investigation of the backflow phenomenon in falling liquid films.

3 Numerical simulation using the Volume of Fluid method

In the context of this thesis, numerical simulations have been performed in order to gain insight into the dynamics of the flow in the falling film's capillary wave region. In combination with experiments, which will be discussed in chapter 4, these simulations directly contributed to the elucidation of physical mechanisms. Consequently, great care had to be taken to ensure their accuracy and capacity to resolve the relevant phenomena. In this context, it is the goal of this chapter to establish the employed numerical methodology as well as to demonstrate its validity. Thereby, emphasis will be placed on the numerical methods used to account for the multiphase character of the falling film flow. These will be presented first (section 3.1). Subsequently, a detailed account of all relevant numerical settings for the investigated flow conditions will be rendered (section 3.2). Finally, the consistency of the employed methods shall be demonstrated on the basis of analytically tractable test cases and through the comparison with own experimental data obtained for falling liquid films (section 3.3).

The Navier-Stokes equations as well as the energy equation were solved numerically for both the liquid and gaseous phase with the approach of Patankar (1980) based on the *Finite Volume method* of spatial discretization and using a non-staggered grid with all variables defined at cell centers. Two computational Fluid Dynamics (CFD) codes implementing these methods were employed, namely FLUENT (version 6.3.26) for 2-dimensional simulations and OpenFOAM (version 1.5) for one 3-dimensional simulation, using a *periodic boundary condition*, which was not applicable in the first code.

3.1 Employed numerical multiphase methods

Since the general finite volume based procedure for the numerical solution of the Navier-Stokes equations as well as additional scalar transport equations is well established, a detailed account of numerical details is forgone here. Instead, the employed conceptual approach for the numerical tractation of multiple incompressible fluid phases, respectively governed by the Navier-Stokes equations, will be presented in this section. An exhaustive overview of different approaches can be found in the book of Prosperetti & Tryggvason (2007).

Before introducing the employed numerical methods, a brief discussion regarding the application of the Finite Volume approach to computational domains containing fluid interfaces is provided first. Indeed, when integrating the differential equations governing the flow over a computational cell, as is done in the context of the finite volume approach, some special considerations are necessary in the presence of fluid interfaces, as illustrated in figure 3.1. First, the effect of surface tension must be accounted for and second, the jump of fluid properties across the interface.

Since the effect of surface tension is not accounted for in the Navier-Stokes equations, the spatially discretized form of momentum conservation is obtained by directly applying Newton's second axiom to the mass of fluid contained in the finite control volume sketched in figure 3.1, which contains material of two different phases at the considered point in time and can be conceived as a computational cell. This yields:

$$\frac{d(\Delta P_i)}{dt} = \int_0^{\Delta V} (\rho g_i) dV + \int_0^{\Delta A} S_{ji} n_j dA + \int_0^{\Delta s} \varepsilon_{ijk} \sigma n_j ds_k, \quad (3.1)$$

where ΔV and ΔA designate the total volume and surface area of the control volume. The right-hand side of equation 3.1 formulates the contributions of volume, surface and line forces to the integral momentum balance. Thereby, the effect of surface tension enters in the form of a line integral (last term on the right-hand side) evaluated along the closed intersection line of length Δs

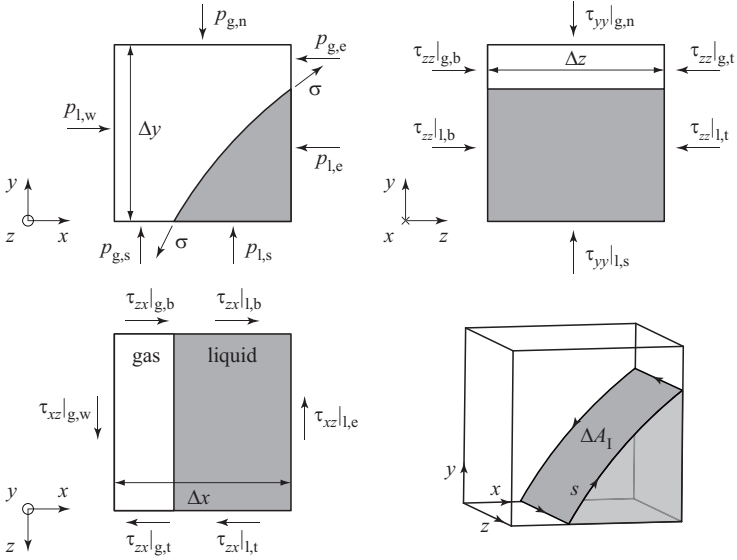


Figure 3.1: Finite control volume containing a portion of the gas-liquid interface. Arrows highlight different contributions to the integral momentum balance. The letters n, s, e, w, b and t pertain to different control volume faces (see Patankar (1980)), while the liquid and gaseous phase are differentiated by l and g respectively.

between the interface and the control volume's outer surface, which is highlighted in the bottom right view of figure 3.1 and parametrized by the coordinate s . In the integrand of the line integral, ε_{ijk} is the Levi-Civita permutation tensor and n_i the normal interfacial unit vector defined by equation 2.2. The line integral yields the total tensile force acting on that part of the interface, which is contained in the control volume. This becomes clear when writing the integral in vector notation instead of Einstein's notation:

$$\int_0^{\Delta s} \varepsilon_{ijk} \sigma n_j ds_k = \int_0^{\Delta s} \vec{ds} \times \sigma \vec{n}. \quad (3.2)$$

The left-hand side of equation 3.1 constitutes the substantial temporal derivative of the components of momentum ΔP_i owned by the mass Δm contained in the control volume. It can be reformulated as a volume integral, yielding:

$$\frac{d(\Delta P_i)}{dt} = \frac{d}{dt} \int_0^{\Delta V} (\rho u_i) dV = \frac{\partial}{\partial t} \int_0^{\Delta V} (\rho u_i) dV + \int_0^{\Delta A} (\rho u_i u_j n_j) dA, \quad (3.3)$$

where the substantial derivative was expressed in terms of the respective partial derivatives and Gauss's divergence theorem was applied to obtain the surface integral (last term on the right-hand side).

Assuming that all quantities remain constant in each of the respective phase volumes contained in the control volume, the integrals in equations 3.1 and 3.3 can be expressed in terms of the center (subscript P) and face (subscripts n, e, s, w, t and b) values of these quantities, yielding the discretized momentum balance. For the x-component of momentum this yields the following equation[†]:

$$\begin{aligned} & \frac{\partial}{\partial t} (u_P \bar{\rho}_P) + \frac{1}{\Delta x} \sum_{k=w}^e \varepsilon_{ek} \hat{\rho}_k u_k^2 + \frac{1}{\Delta y} \sum_{k=s}^n \varepsilon_{nk} \hat{\rho}_k v_k u_k = \bar{\rho}_P g_x + \\ & \frac{1}{\Delta x} \sum_{k=w}^e [\phi_{1,k} p_{1,k} + \phi_{g,k} p_{g,k}] - \frac{1}{\Delta x} \sum_{k=w}^e \varepsilon_{wk} \left[\phi_{1,k} \mu_1 \frac{\partial u_1}{\partial x} \Big|_k + \phi_{g,k} \mu_g \frac{\partial u_g}{\partial x} \Big|_k \right] - \\ & \frac{1}{\Delta y} \sum_{k=s}^n \varepsilon_{nk} \left[\phi_{1,k} \mu_1 \frac{\partial u_1}{\partial y} \Big|_k + \phi_{g,k} \mu_g \frac{\partial u_g}{\partial y} \Big|_k \right] + \frac{1}{\Delta x \Delta y \Delta z} \int_0^{\Delta s} \varepsilon_{ijk} \sigma n_j ds_k, \end{aligned} \quad (3.4)$$

where the volume and area fractions φ and ϕ of the respective phases have been introduced along with the volume and area averaged densities $\bar{\rho}$ and $\hat{\rho}$:

$$\bar{\rho} = (\rho_1 \varphi_1 + \rho_g \varphi_g), \quad \hat{\rho} = (\rho_1 \phi_1 + \rho_g \phi_g) \quad (3.5)$$

and all terms have been divided by $\Delta x \Delta y \Delta z$. The operator ε_{ij} ($\varepsilon_{ij} = 1$ for $i = j$ and $\varepsilon_{ij} = -1$ for $i \neq j$) was introduced to avoid writing out all terms in

[†] Assuming a 2-dimensional velocity field.

the above equation and the subscripts l and g pertain to the liquid and gaseous phase respectively.

The left-hand side of equation 3.4 assumes a form, which deviates from that obtained for single-phase flow *only* by the appearance of volume and area averaged densities. This is due to the fact that velocity components are continuous across the interface. The same holds for the gravitational term. However, the formulation of surface forces (i.e. pressure and shear forces) necessitates a distinction between the respective contributions of the liquid and gaseous phase, as they are discontinuous across the interface, leading to the more complicated second, third and fourth terms on the right-hand side of equation 3.4. The surface tension term has not been discretized at this stage and will be addressed later.

The above elaborations concerning the x-momentum balance also apply to momentum balances in all other directions as well as, in principle, to the energy balance. Meanwhile, the total mass balance is given in differential form by:

$$\frac{\partial \bar{\rho}}{\partial t} + \frac{\partial (u_i \bar{\rho})}{\partial x_i} = 0. \quad (3.6)$$

3.1.1 The Volume of Fluid method

The relatively simple way in which the flow's multiphase character is accounted for by the left-hand side terms of equation 3.4, suggests modelling the different phases by a single fluid governed by an appropriately modified set of transport equations. This *single-fluid* approach is the common basis for a class of numerical methods enabling the simulation of multiphase flows. Prosperetti & Tryggvason (2007) provide a general overview of such methods and designate them as *Immersed Boundary methods*. The *Volume of Fluid method*, which was employed in this thesis, is part of this class. A helpful succinct description of the method can be found in the paper of Gao *et al.* (2003), who applied it to the simulation of falling liquid films in much the same way as was done in this thesis. The same holds for the investigations of Kunugi & Kino (2003) (see also Kunugi & Kino (2005) and Kunugi *et al.* (2005)). For completeness, it should

be mentioned that a series of numerical investigations of falling liquid films have been performed, using various other methods including other methods of discretization. The earliest simulations of falling liquid films were performed by Wasden & Dukler (1989 *a*), Wasden & Dukler (1989 *b*) and Moalem Maron *et al.* (1989) based on a prescription of the interface shape and using the finite difference approach of discretization. Later, using the same discretization approach, simulations incorporating the implicit computation of the interface were performed by Stuhltrager *et al.* (1993), Miyara (1999), Miyara (2001) and Miyara (2000). The finite element methodology has also been widely applied to falling film simulations, using different methods for the computation of phase distribution and interfacial coupling conditions. See e.g. Ho & Patera (1990), Bach & Villadsen (1984), Kheshgi & Scriven (1987), Moalem Maron *et al.* (1989), Malamataris & Papanastasiou (1991), Salamon *et al.* (1994), Ramaswamy *et al.* (1996), Malamataris & Bontozoglou (1999), Malamataris *et al.* (2002), Tihon *et al.* (2006) and Trifonov (2008).

The modified single-fluid momentum, continuity and energy equations, which are solved in the context of the Volume of Fluid method, are given by:

$$\begin{aligned} \frac{\partial(\bar{\rho} u_i)}{\partial t} + \frac{\partial}{\partial x}(\bar{\rho} u_i u_i) &= -\frac{\partial p}{\partial x_i} + \frac{\partial}{\partial x_i} \left(\bar{\mu} \frac{\partial u_i}{\partial x_j} \right) + \bar{\rho} g_i + F_{\sigma i}''' \\ \frac{\partial u_i}{\partial x_i} &= 0, \quad \frac{\partial}{\partial t}(\bar{\rho} \bar{c} T) + \frac{\partial}{\partial x_j}(\bar{\rho} \bar{c} u_j T) = \frac{\partial}{\partial x_j} \left(\bar{k} \frac{\partial T}{\partial x_j} \right), \end{aligned} \tag{3.7}$$

where fluid properties of the single fluid are obtained through volume averaging of respective phase properties i.e.:

$$\begin{aligned} \bar{\rho} &= (\rho_l \varphi + \rho_g (1 - \varphi)), \quad \bar{\mu} = (\mu_l \varphi + \mu_g (1 - \varphi)), \\ \bar{c} &= (c_l \varphi + c_g (1 - \varphi)), \quad \bar{k} = (k_l \varphi + k_g (1 - \varphi)). \end{aligned} \tag{3.8}$$

In the above equations, as well as in all subsequent elaborations, the case of two immiscible fluid phases (one liquid and one gaseous) is considered, so that volume fractions of the respective phases are related by $\varphi_l + \varphi_g = 1$.

Consequently, the properties of the single-fluid can be parametrized by a single volume fraction φ which was chosen as that of the liquid phase $\varphi = \varphi_1$.

Next to the appearance of averaged fluid properties, the Navier-Stokes equations in 3.7 further deviate from their single-phase form by the inclusion of a volume force $F''_{\sigma i}$, modelling the effect of surface tension. This term will be discussed later in greater detail.

Integrating the equations in 3.7 over the finite control volume sketched in figure 3.1 then yields the discretized transport equations for the single-fluid approach. The discretized x-momentum balance for example takes the form:

$$\begin{aligned} \frac{\partial}{\partial t} (u_P \bar{\rho}_P) + \frac{1}{\Delta x} \sum_{k=w}^e \varepsilon_{ek} \bar{\rho}_k u_k^2 + \frac{1}{\Delta y} \sum_{k=s}^n \varepsilon_{nk} \bar{\rho}_k v_k u_k = \bar{\rho}_P g_x + \\ \frac{1}{\Delta x} \sum_{k=w}^e p_k - \frac{1}{\Delta x} \sum_{k=w}^e \varepsilon_{wk} \bar{\mu}_k \left. \frac{\partial u}{\partial x} \right|_k - \frac{1}{\Delta y} \sum_{k=s}^n \varepsilon_{nk} \bar{\mu}_k \left. \frac{\partial u}{\partial y} \right|_k + F''_{\sigma x}, \end{aligned} \quad (3.9)$$

which can directly be compared with equation 3.4. From this, it is clear that the left-hand side of equation 3.4 is well modelled by the single-fluid approach (assuming that the volume fraction at a given cell face φ_k is a good estimator of the corresponding area fraction ϕ_k there). However, the interfacial jump of surface forces cannot be resolved in a numerical implementation of the single-fluid approach, as it occurs inside a single cell. Consequently, the contribution of surface forces to the integral momentum balance is smoothed over the respective cell faces. Finally, since the formulation of $F''_{\sigma i}$ has not been specified, no assessment of its accuracy can be made at this stage. It should also be noted that the single-fluid continuity equation in 3.7 imposes a divergence-free velocity field also for cells containing part of the interface as opposed to the exact multiphase mass balance given by equation 3.6.

Compared to the Finite Volume based numerical simulation of single phase flows, the Volume of Fluid method introduces one main complication i.e. the necessity to compute the spatio-temporal evolution of the volume fraction φ . This volume fraction represents a differentiator between phases. In the liquid

phase, $\varphi=1$ and the governing equations for the pure liquid are recovered and vice versa in the gaseous phase where $\varphi=0$. In a spatially discretized domain, φ can assume values between 0 and 1, thus identifying cells containing both liquid and gas i.e. *interfacial cells*. In these cells, the governing equations of the single-fluid lead to the more or less accurate application of a multiphase momentum balance (compare equations 3.9 and 3.4), which is equivalent to applying the interfacial coupling conditions introduced in section 2.1 (see equations 2.4 there). As will be shown later, the effect of surface tension, which is modeled by way of the volume force F_σ''' , is also selectively applied to interfacial cells.

Consequently, the accurate computation of the volume fraction field is the paramount task in the context of the Volume of Fluid method. It is also the primary differentiator for different Volume of Fluid based approaches developed over the years. The most cited contribution in this context is the landmark paper by Hirt & Nichols (1981), who introduced the term Volume of Fluid or VOF method. The authors derived a differential equation, governing the transport of φ , from a phase-specific mass balance. For the case of fluids with constant density, this yields:

$$\frac{\partial \varphi}{\partial t} + \frac{\partial (u_i \varphi)}{\partial x_i} = 0. \quad (3.10)$$

Note that the equation is written in its conservative form here and that, due to the immiscibility of the two fluids, no diffusional transport needs to be considered. The numerical solution of equation 3.10 is not as straight forward as it may seem, and will be treated in the next subsection.

3.1.2 Interface reconstruction

When applying conventional Finite Volume based methodology for the numerical solution of equation 3.10, the spatio-temporal propagation of the volume fraction φ may be considerably overestimated, which, in multi-dimensional cases, leads to the creation of *flotsam* i.e. detached regions of a considered phase. To illustrate this specificity, a simple example of one-dimensional uniform convection (i.e. as the result of a one-dimensional uniform velocity field)

of φ is considered here[†]. Under these conditions, equation 3.10 reduces to:

$$\frac{\partial \varphi}{\partial t} + u \frac{\partial \varphi}{\partial x} = 0. \quad (3.11)$$

Integrating it over a control volume and one time step (using a first-order *upwind* approximation for the face values of φ and an explicit formulation of time dependence) yields the following relation for updating the volume fraction in a given cell:

$$\varphi_{\text{P}}^{i+1} = \varphi_{\text{P}}^i + \frac{u \Delta t}{\Delta x} (\varphi_{\text{W}}^i - \varphi_{\text{P}}^i). \quad (3.12)$$

Here, the subscript P refers to the considered cell and subscripts W and E designate its west and east neighbours, whereas the superscript refers to the considered time step. The advancement of the numerical solution over one time step is illustrated in figure 3.2, assuming for convenience $u \Delta t / \Delta x = 0.5$. The figure's middle sequence shows the exact phase distribution in a continuum. The top sequence depicts the phase distribution obtained when discretizing the continuum, and the exact distribution defined thereon, with finite volumes. Through this step, the sharpness of the interface is lost and liquid is redistributed over the entire cell. The bottom sequence depicts the phase distribution as obtained from the numerical solution given by equation 3.12. As is evident in the phase distributions at time step $i + 1$ (on the right hand side of figure 3.2), the numerical solution propagates liquid too far downstream. The cause for this artificial transport is the incapacity of conventional discretization schemes to resolve the phase distribution within a cell. Consequently, special schemes accounting for the multiphase character of the flow are necessary in order to numerically solve equation 3.10.

Among the first to propose such a scheme were Hirt & Nichols (1981), who introduced the *Donor-Acceptor method*[‡]. The basic idea of the method consists of reconstructing the interface within an interfacial cell and using this information to compute phase-specific fluxes at the cell faces. Hirt & Nichols (1981)

[†]This example was taken from Prosperetti & Tryggvason (2007).

[‡]See also the Simple Line Interface Calculation (SLIC) method of Noh & Woodward (1976).

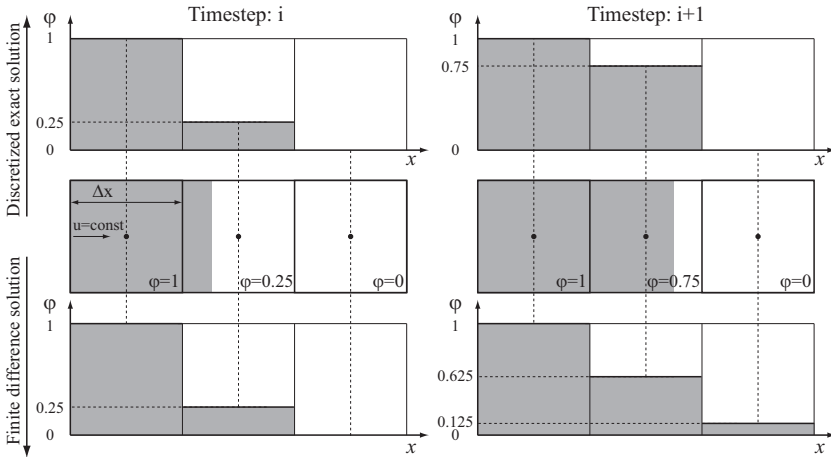


Figure 3.2: One-dimensional uniform convection of the liquid volume fraction φ between time steps i and $i + 1$. Middle sequence: exact phase distribution in a continuum; top sequence: finite volume spatial discretization of exact phase distribution; bottom sequence: explicit numerical solution of equation 3.10 using upwind discretization.

reconstructed the interface within computational cells using line segments (or plane segments in the 3-dimensional case) that could be oriented parallel to either of the cell faces, depending on the total volume fraction of the considered cell and of its neighbours. The Donor Acceptor method was subsequently improved upon by Youngs (1982), who dropped the constraint of line segments having to be parallel to a cell face, instead allowing them to be arbitrarily oriented within a considered cell. This method was employed for the numerical simulations in this thesis[†] and will be briefly described next.

Figure 3.3 shows a row of interfacial cells, containing part of an interface and exhibiting different volume fraction values, as highlighted by the gray areas. For the sake of simplicity, the problem shall be considered as 2-dimensional

[†]With the exception of the 3-dimensional simulation (see section 5.5) using OpenFOAM, which relied on a different method also employed by Rusche (2002).

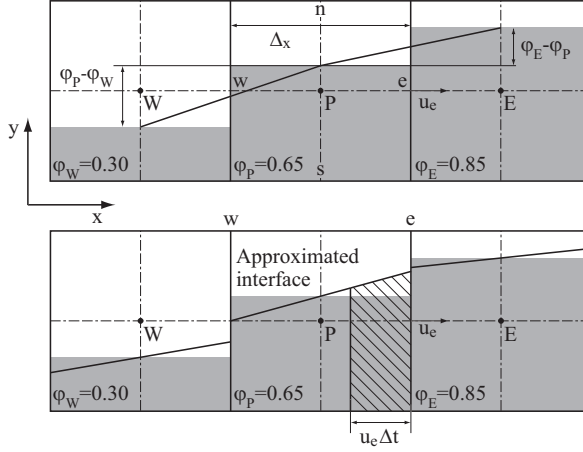


Figure 3.3: Interface reconstruction and computation of volume fluxes at cell faces according to Youngs (1982).

in the sense that no variations take place in the third coordinate. Integrating equation 3.10 over the central cell in figure 3.3 and over one time step introduces the volume fluxes of liquid crossing the respective cell faces:

$$\frac{\varphi^{i+1} - \varphi^i}{\Delta t} + \frac{(u\varphi)_e^i - (u\varphi)_w^i}{\Delta x} + \frac{(v\varphi)_n^i - (v\varphi)_s^i}{\Delta y} = 0. \quad (3.13)$$

Using an explicit formulation of time dependence, then yields the following expression for updating the central cell's volume fraction φ_P :

$$\varphi_P^{i+1} = \varphi_P^i + \frac{\Delta t}{\Delta x} \left[(u\varphi)_e^i - (u\varphi)_w^i \right] + \frac{\Delta t}{\Delta y} \left[(v\varphi)_n^i - (v\varphi)_s^i \right], \quad (3.14)$$

where the face fluxes have yet to be formulated. Before doing so, another specificity of Youngs' method needs to be mentioned. In practice, the iterative procedure defined by equation 3.14 is split into two substeps performed within one time step. In the first substep, the volume fraction is convected only in

x-direction (or in y-direction), yielding an intermediate volume fraction φ_P^+ :

$$\varphi_P^+ = \varphi_P^i + \frac{\Delta t}{\Delta x} \left[(u\varphi)_e^i - (u\varphi)_w^i \right], \quad (3.15)$$

which is then convected in y-direction (or in x-direction) in the second substep according to:

$$\varphi_P^{i+1} = \varphi_P^+ + \frac{\Delta t}{\Delta y} \left[(v\varphi)_n^+ - (v\varphi)_s^+ \right]. \quad (3.16)$$

Thereby, the order in which these unidirectional substeps are performed is alternated between successive time steps (see Puckett *et al.* (1997)).

Without loss of generality, the computation of the face fluxes shall be explained representatively for the volume flux $(u\varphi)_e$ in equation 3.15, which crosses the east face of the central cell in figure 3.3. The procedure is performed in two steps. First, the interface within the considered cell is approximated by a line segment (see bottom sequence of figure 3.3). This line has only its slope as a degree of freedom as its vertical position is fixed by the total volume fraction φ_P of the cell. Indeed, the area underneath the line must correspond to the gray area in the cell. The determination of the line's slope is illustrated in the top sequence of figure 3.3. First, a first order central difference estimate of the volume fraction's spatial derivative at the west and east faces is computed:

$$\left. \frac{\partial \varphi}{\partial x} \right|_w = \frac{\varphi_P - \varphi_W}{\Delta x}, \quad \left. \frac{\partial \varphi}{\partial x} \right|_e = \frac{\varphi_E - \varphi_P}{\Delta x}. \quad (3.17)$$

The slope of the interface segment in the considered cell $\partial\varphi/\partial x|_P$ is then computed from a weighted sum of these derivatives:

$$\left. \frac{\partial \varphi}{\partial x} \right|_P = \left(\frac{2 - u_e \Delta t / \Delta x}{3} \right) \left. \frac{\partial \varphi}{\partial x} \right|_w + \left(\frac{1 + u_e \Delta t / \Delta x}{3} \right) \left. \frac{\partial \varphi}{\partial x} \right|_e. \quad (3.18)$$

Thereby, $u_e \Delta t / \Delta x$ estimates the translation of the interface during the time step in relation to the total cell width and scales the influence of the west and east neighbours of the cell.

Based on this approximated interface shape within the considered cell, the face fluxes can be computed. Therefore, the interface is assumed to translate by

a distance of $u_e \Delta t$ in x-direction, convecting the entire volume corresponding to the shaded area highlighted in figure 3.3 into the eastern neighbouring cell. This area corresponds to the volume flux $(u \varphi)_e^i$ multiplied with the time step Δt and can be determined by geometric considerations, thus yielding:

$$\Delta t (u \varphi)_e^i = \Delta t u_e \left[\varphi_P^i + \frac{1}{2} (\Delta x - u_e \Delta t) \left. \frac{\partial \varphi}{\partial x} \right|_P \right]. \quad (3.19)$$

Equation 3.19 constitutes the principal step in the computation of face fluxes in the context of Youngs' method. Further measures need to be taken to prevent cells from shedding more liquid than they contain or receiving more liquid than they can hold. This is done through the use of bounding procedures detailed by Youngs (1982). Finally, since the work of Youngs (1982), a series of improvements have been made to his method, without changing the general idea. A review of modern developments concerning interface reconstruction and face flux computation was recently conducted by Scardovelli & Zaleski (1999).

3.1.3 The Continuum Surface Force method

To complete the description of numerical methods for the simulation of multiphase flows employed in this thesis, the computation of the effect of surface tension will be addressed here. Tensile forces enter the momentum balance formulated in equation 3.1 in the form of a line integral along the intersection line between the interface and the outer surface of a computational cell, as illustrated in figure 3.1 (bottom right view). Brackbill *et al.* (1992) first proposed to model this contribution with a volume force in the single-fluid Navier-Stokes equations, as introduced in equation 3.7. Their method, designated as *Continuum Surface Force* or CSF method, was employed in this thesis and will be outlined next.

The line integral in equation 3.1 can be reformulated as a surface integral over the interfacial area ΔA_I contained in the computational cell of figure 3.1

using an alternate form of the curl theorem (see Kaplan (1991)):

$$\int_0^{\Delta s} \vec{ds} \times \sigma \vec{n} = \int_0^{\Delta A_I} F''_{\sigma i} dA, \quad F''_{\sigma i} = (\vec{n} \times \vec{\nabla}) \times \sigma \vec{n}, \quad (3.20)$$

where $F''_{\sigma i}$ designates the resulting tensile force per unit surface area. Using differential geometry detailed in Brackbill *et al.* (1992), $F''_{\sigma i}$ can be reformulated to yield:

$$F''_{\sigma i} = -\sigma \vec{n} (\vec{\nabla} \cdot \vec{n}), \quad (3.21)$$

assuming constant surface tension. Next, the surface integral in equation 3.20 can be expressed in terms of a volume integral over the total volume ΔV of a computational cell by introducing the delta function $\hat{\delta}$, which is zero everywhere but at the interface:

$$\int_0^{\Delta A_I} F''_{\sigma i} dA = \int_0^{\Delta V} \left(F''_{\sigma i} \hat{\delta}(\hat{n}) \right) dV, \quad \hat{n} = \vec{n}_\perp \cdot (\vec{x} - \vec{x}_\perp). \quad (3.22)$$

Here, the symbol \perp refers to the interfacial point obtained by normal projection of the considered point \vec{x} onto the interface and \hat{n} designates the projected normal distance to the interface. According to Brackbill *et al.* (1992), the delta function can be expressed in terms of the gradient of the volume fraction:

$$\vec{n} \hat{\delta}(\hat{n}) = \vec{\nabla} \varphi. \quad (3.23)$$

With this, the following formulation for the total tensile force in equation 3.1 is obtained:

$$\int_0^{\Delta s} \vec{ds} \times \sigma \vec{n} = \int_0^{\Delta A_I} F''_{\sigma i} dA = \int_0^{\Delta V} \tilde{F}'''_{\sigma i} dV, \quad \tilde{F}'''_{\sigma i} = \sigma \kappa (\vec{\nabla} \varphi), \quad \kappa = -\vec{\nabla} \cdot \vec{n}, \quad (3.24)$$

where the interface curvature κ has been introduced. The total tensile force acting on a finite interface segment contained in a computational cell can thus be exactly expressed in terms of an integral over the cell's volume. The inte-

grand $\tilde{F}_{\sigma i}'''$ is then a volume specific force and an adequate choice for the term $F_{\sigma i}'''$, modelling the effect of surface tension in the single-fluid Navier-Stokes equations written in 3.7. In practice, in order for the surface tension term to be explicitly independent of the local density level in a mass specific formulation of the single-fluid Navier-stokes equations, $\tilde{F}_{\sigma i}'''$ is scaled with a density ratio to obtain $F_{\sigma i}'''$:

$$F_{\sigma i}''' = \tilde{F}_{\sigma i}''' \frac{\bar{\rho}}{0.5(\rho_l + \rho_g)} = -\sigma (\vec{\nabla} \cdot \vec{n}) (\vec{\nabla} \varphi) \frac{\bar{\rho}}{0.5(\rho_l + \rho_g)}. \quad (3.25)$$

To enable the determination of $F_{\sigma i}'''$ in the context of a numerical solution, a relation for the computation of the unit normal vector \vec{n} remains to be specified. Brackbill *et al.* (1992) related \vec{n} to the gradient of the volume fraction, obtaining:

$$\vec{n} = \frac{\vec{\nabla} \varphi}{|\vec{\nabla} \varphi|}. \quad (3.26)$$

From equation 3.25 it is clear that the surface tension term $F_{\sigma i}'''$ as defined by equations 3.25 and 3.26 is selectively applied to interfacial cells (i.e., where $\vec{\nabla} \varphi \neq 0$). A description of its numerical discretization is forgone here and the reader is instead referred to the detailed account by Brackbill *et al.* (1992).

In summary, the contribution of tensile forces to the momentum balance for a finite volume containing multiple phases can be exactly computed using equations 3.25 and 3.26. However, the relations in equation 3.24, used to derive these equations, hold exactly only if the interface is sharp and the volume fraction φ experiences an interfacial jump. In the context of the Finite Volume based numerical application of the VOF method, φ does not change discontinuously from one phase to another, assuming values between 0 and 1 in interfacial cells. Consequently, 3.25 provides only a numerical approximation of the total tensile force per unit volume acting on the interface segment in a given interfacial cell. Nonetheless, this approximation converges toward the exact relation with decreasing cell size.

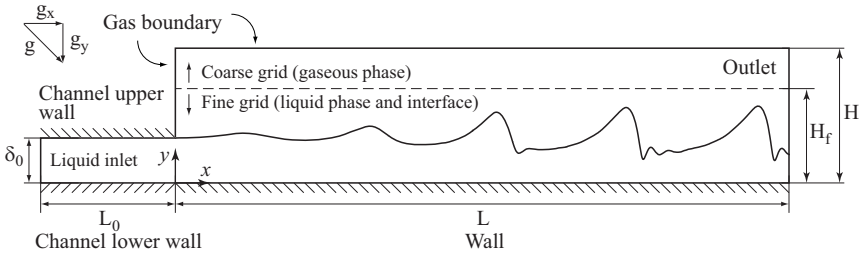


Figure 3.4: Sketch of the computational domain employed for the simulation of 2-dimensional falling liquid films.

3.2 Specification of performed numerical simulations

This section renders an account of the principal settings, specifying the numerical simulations of falling liquid films performed in this thesis. First, the spatial approximation of the falling film flow will be addressed by demarcating the computational domains and defining the associated grid topologies, followed by a description of the boundary conditions numerically imposed on the boundaries of the grid. Subsequently, principal numerical settings pertaining to the iterative solution of the governing equations will be specified, such as the employed algorithm and *discretization schemes*. Finally, all simulations performed in the context of this thesis will be quantified in terms of the simulated physical conditions i.e. operating conditions and fluid properties, as well as in terms of the imposed spatial and temporal resolution.

3.2.1 Computational domain and grid topology

In this thesis, 2-dimensional simulations as well as one 3-dimensional simulation were performed. A typical computational domain used for the simulation of 2-dimensional falling liquid films is sketched in figure 3.4. Liquid enters the domain from the left through an inlet channel bounded by two parallel walls. Within the inlet channel, the flow consists of only the liquid phase, and repro-

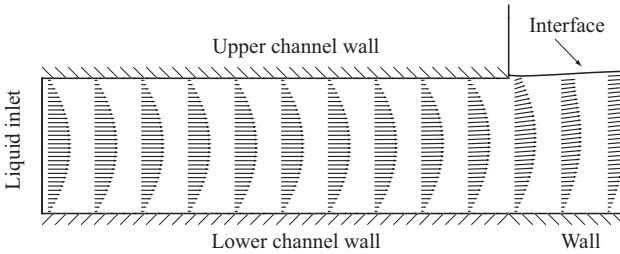


Figure 3.5: Evolution of the streamwise velocity profile within the inlet channel of the computational domain pictured in figure 3.4.

duces the inlet configuration of the employed experimental test sections, which will be described in chapter 4. In the experiments, the inlet channel length was sufficient to ensure that the streamwise velocity profile reached the shape for fully developed channel flow before evolving toward the semi-parabolic shape associated with falling liquid films, while approaching the start of the two-phase region at $x=0$. Accordingly, the portion of the inlet channel, included in the computational domain, was chosen such that a streamwise velocity profile of fully developed channel flow could be assumed at the inlet. In other words, as illustrated in figure 3.5, the channel length L_0 was set to be longer than the upstream region of influence of the single- to two-phase flow transition. Meanwhile, the channel height δ_0 for the numerical simulations was set according to experimental conditions.

After leaving the inlet channel at $x=0$, the liquid enters the 2-phase region of the computational domain, which is separated into two portions with different grid resolution. In the top portion, which contains only gas at all times, a coarser spatial resolution was chosen, as length scales in the gaseous phase are larger. In the bottom part of the grid (as well as in the inlet channel), which contains the liquid film, including all interfacial cells, a significantly finer resolution was chosen in order to ensure accurate computation of the interface and resolution of all relevant scales of the liquid phase velocity field. The resulting cell geometries in these respective regions are illustrated in figure 3.6,

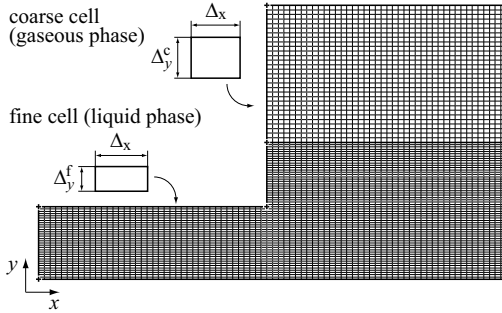


Figure 3.6: Close-up of the computational grid near the liquid inlet, showing the different cell geometries employed for the gaseous and liquid phase regions respectively.

displaying a close-up of the inlet. As is discernible from the figure, rectangular computational cells were employed, which were organized in a *structured grid*.

The two-phase region of the computational domain is bounded on the liquid side by a wall, along which the liquid film develops, and on the gaseous side by a boundary permitting fluid to pass through. This boundary is removed sufficiently from the interface in order to minimize the wave-induced disturbance of the gas flow there, allowing for the definition of adequate boundary conditions. The length L of the two-phase region is chosen such that surface waves are enabled to fully develop within the domain. Further, an additional buffer zone of approximately one wavelength is included in order to separate the film's region of interest from the outlet boundary, through which the liquid film leaves the computational domain, and which is also permeable for the gaseous phase. A discussion of the outlet boundary condition and its upstream effect will be provided later (see subsections 3.2.4 and 3.3.3).

As opposed to the 2-dimensional simulations, the performed 3-dimensional simulation does not represent the complete spatial evolution of the liquid film, as this would have been associated with a prohibitive computational cost in the context of this thesis. As an alternative, the computational domain was

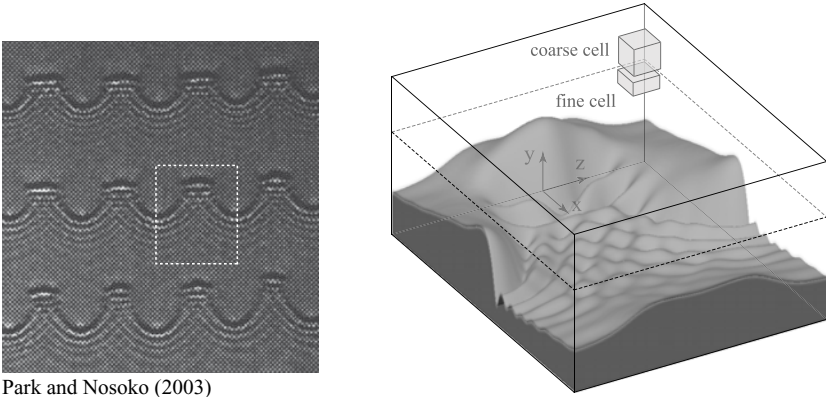


Figure 3.7: Computational domain employed for the 3-dimensional simulation. Left: shadowgraph of a vertically falling liquid film with 3-dimensional surface waves (taken from Park & Nosoko (2003)), demarcating the periodic wave segment included in the computational domain. Right: computational domain showing the calculated wave topology and cell geometries (cells are not drawn to scale).

restricted to one segment of a periodic 3-dimensional wave pattern, as illustrated in figure 3.7. As a consequence, the 3-dimensional investigation was restricted to the developed state of the investigated waves. The length L and width W of the domain were accordingly set to the streamwise and spanwise wave separation, which were obtained from experiments.

Liquid and gas enter and leave the computational domain, pictured in figure 3.7, through boundaries permeable for both phases. Thereby, as will be detailed later, inlet and outlet are coupled through a periodic boundary condition, imposing streamwise periodicity. In physical terms, this implies that fluid, leaving the computational domain through the outlet, simultaneously re-enters it through the inlet as if it were flowing in a closed loop.

In y -direction, the computational domain is bounded by a wall on the liquid side and a permeable boundary on the gaseous side, and, in z -direction, by

boundaries rendered impermeable through the application of *symmetric boundary conditions*, imposing spanwise symmetry. Indeed, through the previously mentioned choice of W these boundaries correspond to planes of symmetry of the investigated 3-dimensional periodic wave pattern if the latter is centered in the computational domain (see left-hand side of figure 3.7). Finally, as in the 2-dimensional case, the 3-dimensional structured grid is partitioned into a finely resolved region, which includes the entire liquid phase, and a region of coarser spatial resolution, containing only gas. In all 2-dimensional simulations as well as in the 3-dimensional simulation, computational cells at the computational domain's boundaries were positioned such that their faces coincided with the respective boundaries.

3.2.2 Discretization of governing equations

The differential equations, governing the falling liquid film flow in the context of the performed numerical simulations, are given by 3.7 and 3.10. To obtain the discretized algebraic form, required for their iterative solution, using the numerical algorithms detailed in subsection 3.2.3, all governing equations are integrated in time over one time-step Δt and in space over the same computational cell such as the one pictured in figure 3.3, surrounding the point P. Consequently, all variables computed during the numerical solution i.e. velocity components, static pressure, volume fraction and temperature are solved for at the cell centers P, so that the grids presented in subsection 3.2.1 are *non-staggered* or *colocated*. For the temporal integration, integrands are assumed to immediately adopt their final value at the onset of a new time step, leading to a fully implicit formulation. With these definitions, for the 2-dimensional case, the discretized transport equation for x-momentum (the equation for y-

momentum is omitted for the sake of brevity) is[†]:

$$\begin{aligned}
 & \Delta t^{-1} \left[(\bar{\rho} u)_P^i - (\bar{\rho} u)_P^{i-1} \right] + \\
 & \Delta x^{-1} \left[\underbrace{(\bar{\rho} u)_e}_{\text{Rhie-Chow interpolation}} \underbrace{u_e}_{\text{1st order upwind}} - (\bar{\rho} u)_w u_w \right]^i + \Delta y^{-1} [(\bar{\rho} v)_n u_n - (\bar{\rho} v)_s u_s]^i = \\
 & - \underbrace{\partial p / \partial x|_P^i}_{\text{PRESTO}} + \Delta x^{-1} [\bar{\mu}_e \underbrace{\partial u / \partial x|_e}_{\text{1st order central difference}} - \bar{\mu}_w \partial u / \partial x|_w]^i + \\
 & \Delta y^{-1} [\bar{\mu}_n \partial u / \partial y|_n - \bar{\mu}_s \partial u / \partial y|_s]^i + [(\bar{\rho} g_x)_P + F''_{\sigma x}|_P]^i,
 \end{aligned} \tag{3.27}$$

where the superscript i refers to the time-step, and the spatial interpolation schemes employed to evaluate face values as a function of values stored at cell centers are specified beneath representative terms they pertain to[‡]. As the employed numerical algorithms are based on a colocated storage strategy, special attention needs to be paid to the task of interpolation in order to avoid the decoupling of cell velocity and cell pressure pointed out by Patankar (1980) (see also Date (2005) for an in depth discussion). Accordingly, the *Rhie-Chow interpolation* procedure (see Rhie & Chow (1983)) was employed to determine the face values of velocity components featuring in respective face fluxes. The face value of the streamwise velocity component on the eastern face u_e is consequently given by:

$$\begin{aligned}
 u_e = & (\alpha_P u_P + \alpha_E u_E) + [(\alpha_E / a_P|_E) \underbrace{\partial p / \partial x|_E}_{\text{1st order central difference}} + \\
 & (\alpha_P / a_P|_P) \partial p / \partial x|_P - (\alpha_E / a_P|_E + \alpha_P / a_P|_P) \underbrace{\partial p / \partial x|_e}_{\text{1st order central difference}}],
 \end{aligned} \tag{3.28}$$

[†]After integration of the different terms in the differential x-momentum equation over time and space, the final form of equation 3.27 was obtained by subsequently dividing through $\Delta t \Delta x \Delta y$.

[‡]The PRESTO scheme is an undisclosed method implemented in the CFD code FLUENT.

where the weighting factors α_P and α_E were introduced:

$$\alpha_P = 1 - \alpha_E = \frac{a_P|_P}{a_P|_P + a_P|_E}, \quad (3.29)$$

and $a_P|_P$ and $a_P|_E$ are coefficients appearing in the final form of the discretized x-momentum equation after application of the interpolation schemes to equation 3.27:

$$(a_P|_P u_P)^i = \left(\sum_{K=NESW} a_K|_P u_K \right)^i - \partial p / \partial x|_P^i - b|_P^i. \quad (3.30)$$

This has led to the introduction of the term *momentum-weighted interpolation* to designate the relation given by equation 3.28. The second subscript of the coefficient $a_K|_P$ refers to the computational cell, over which the spatial integration is performed (in this case P), while the first subscript designates the considered neighbouring cell[†]. It is important to note that the coefficients $a_K|_P$, on the right-hand side of equation 3.30, depend on the velocity components u_w^i , u_e^i , v_s^i and u_n^i on the cell faces. A derivation of equation 3.28 for the case $\alpha_P = \alpha_E = 0.5$ can be found in Miller & Schmidt (1988). All other interpolation schemes applied to equation 3.27 are standard and thus not explicitly written here (see e.g. Patankar (1980) for definitions).

The discretized forms of the continuity equation as well as the transport equation for the volume fraction φ (equation 3.10) are:

$$\begin{aligned} & \underbrace{[u_e - u_w]}_{\text{Rhie-Chow interpolation}}^i \Delta y + [u_n - u_s]^i \Delta x = 0, \\ & \Delta t^{-1} [\varphi_P^i - \varphi_P^{i-1}] + \Delta x^{-1} \underbrace{[(u\varphi)_e]}_{\text{Youngs' method}} - (u\varphi)_w^i + \Delta y^{-1} \underbrace{[(v\varphi)_n]}_{\text{Youngs' method}} - (v\varphi)_s^i = 0. \end{aligned} \quad (3.31)$$

Although the continuity equation is not solved directly by the employed nu-

[†]Consequently, $a_P|_E$ would appear in the formulation of equation 3.30 for the eastern cell, which is not included here.

merical algorithms it is nonetheless needed for derivation purposes as will be established in subsection 3.2.3. The computation of face fluxes in the discretized form of equation 3.10 (second equation in 3.31) was addressed in subsection 3.1.2, while describing Youngs' method of interface reconstruction.

The discretized form of the energy equation is given by:

$$\begin{aligned}
 & \Delta t^{-1}[(\bar{\rho} \bar{c} T)_P^i - (\bar{\rho} \bar{c} T)_P^{i-1}] + \\
 & \Delta x^{-1} [\underbrace{(\bar{\rho} u)_e}_{\text{Rhie-Chow interpolation}} \bar{c}_e \underbrace{T_e}_{\text{1st order upwind}} - (\bar{\rho} u)_w \bar{c}_w T_w]^i + \Delta y^{-1} [(\bar{\rho} v)_n \bar{c}_n T_n - (\bar{\rho} v)_s \bar{c}_s T_s]^i = \\
 & \Delta x^{-1} [\bar{k}_e \underbrace{\partial T / \partial x|_e}_{\text{1st order central difference}} - \bar{k}_w \partial T / \partial x|_w]^i + \Delta y^{-1} [\bar{k}_n \partial T / \partial y|_n - \bar{k}_s \partial T / \partial y|_s]^i.
 \end{aligned} \tag{3.32}$$

Application of the respective interpolation schemes to equation 3.32 then yields the final form of the discretized energy equation, in analogy to equation 3.30:

$$(\tilde{a}_P|_P T_P)^i = \left(\sum_{K=\text{NESW}} \tilde{a}_K|_P T_K \right)^i - \tilde{b}|_P^i \tag{3.33}$$

The final discretized form of the continuity equation is not needed, whereas that of the volume fraction transport equation is given by the fractional formulations 3.15 and 3.16.

3.2.3 Numerical algorithms

Having addressed the spatial discretization of physical space as well as the spatio-temporal discretization of the governing equations, the employed algorithms for the iterative numerical solution of the latter will be specified in this subsection. For both the 2-dimensional and 3-dimensional simulations, the PISO (Pressure Implicit Split Operator) algorithm introduced by Issa (1985) was employed for the numerical solution of the coupled system represented by equations 3.15, 3.16, 3.30, 3.33 as well as the discretized continuity equation.

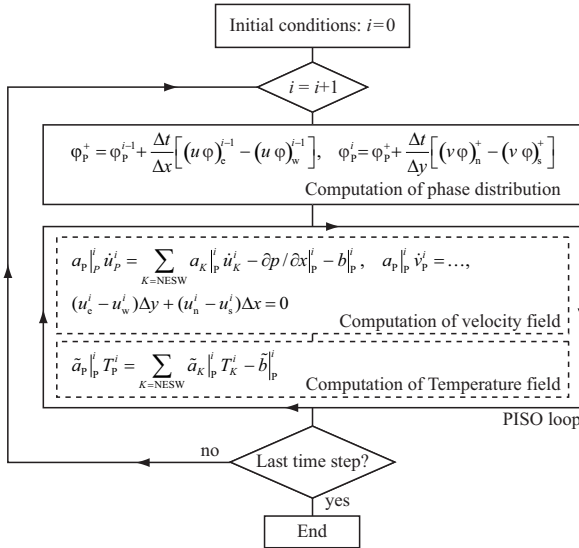


Figure 3.8: Flowchart of the numerical algorithm for the computation of phase distribution, velocity and temperature as implemented in the CFD code (FLUENT) employed for 2-dimensional simulations.

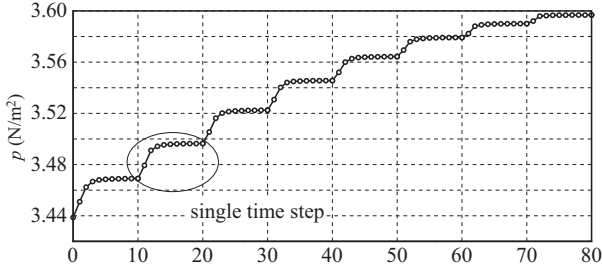
Figures 3.8 and 3.9 represent flow charts of the iterative solution process as implemented in the CFD code FLUENT employed for 2-dimensional simulations[†]. Figure 3.8 depicts the full iterative loop for the time-resolved computation of volume fraction, velocity and temperature. Thereby, as discussed in subsection 3.1.2, the volume fraction distribution is computed in an explicit manner based on data from the previous time step. The velocity and temperature fields are computed in an implicit manner in the so called PISO loop, where momentum, continuity and energy equations are solved iteratively. The inner workings of the PISO loop are illustrated by the flow chart in figure 3.9, where the solution step for the energy equation has been omitted for the sake of brevity. The

[†]As stated earlier, the procedure for the OpenFOAM CFD code used for 3-dimensional simulations is similar.

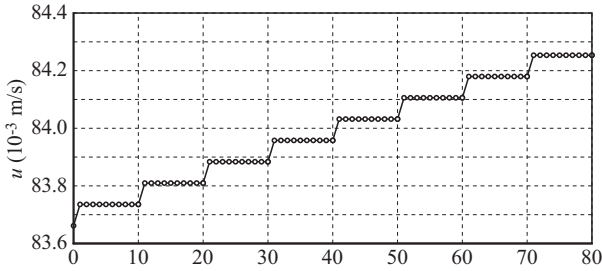
chart thus illustrates the coupled iterative solution of the Navier-Stokes and continuity equations using the PISO procedure.

The procedure basically consists of a predictor step in which the discretized implicit momentum equations are solved iteratively using the pressure distribution from the previous time step and two corrector steps, which determine better estimates of pressure and velocity by enforcing the condition of a divergence free velocity field called for by the continuity equation. Thereby, the pressure correction (see fifth and ninth box of the flow chart in figure 3.9) is determined by solving the implicit *pressure correction equation* obtained from the discretized form of the continuity equation using momentum-weighted Rhie-Chow interpolation for the formulation of face fluxes. The velocity corrections are obtained from the momentum equations using the corrected pressure field. Thereby an explicit formulation is employed in the sense that uncorrected neighbouring velocity components are used in the first term on the right-hand side of the discretized momentum equation. In the 2-dimensional simulations (using FLUENT), the predictor step and the two corrector steps were iteratively applied within a time step until velocity and pressure estimates converged to a predefined degree. For an exemplary 2-dimensional simulation, the convergence history for static pressure as well as streamwise and crosswise velocity components is illustrated in figure 3.10. Variables displayed in these graphs were evaluated at one point in the liquid phase of a developed wavy falling liquid film over the span of eight time steps. The number of PISO loop iterations within a time step was set to a fixed value (in this case 10), which was determined for each performed simulation based on the convergence history of the residuals of the discretized momentum and continuity equations. For the 3-dimensional simulations (using OpenFOAM), the predictor-corrector sequence in figure 3.9 was performed only once for each time step in order to reduce computational burden.

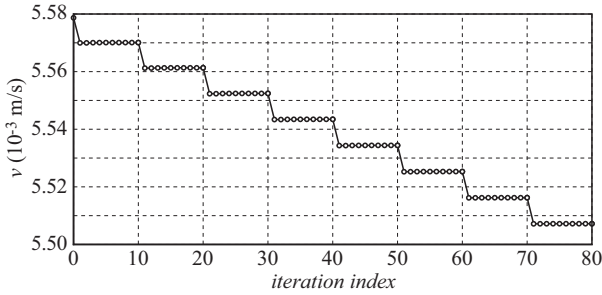
3.2 Specification of performed numerical simulations



(a) Static pressure



(b) Streamwise velocity



(c) Crosswise velocity

Figure 3.10: Exemplary convergence history of static pressure as well as streamwise and crosswise velocity components at one point in the liquid phase of a wavy film for the PISO algorithm employed for 2-dimensional simulations. In this case, exactly 10 iterations were performed for each time step.

3.2.4 Initial and boundary conditions

2-dimensional simulations

For the 2-dimensional simulations, the initial state of the falling liquid film was set to the corresponding primary flow given by equations in 2.11. The streamwise velocity profile in the single-phase flow within the inlet channel was defined to evolve from a fully-parabolic shape, corresponding to fully developed channel flow (with vanishing streamwise pressure gradient), at the liquid inlet to the semi-parabolic shape associated with smooth film flow at the inlet to the two-phase region. The crosswise velocity component was initially set to zero in the entire domain. In terms of a continuum physical description and with reference to figure 3.4, the initial conditions then are:

$$\begin{aligned}
 x \leq 0 & \left\{ \begin{array}{l} u(x,y,t=0) = [u_F(y) - u_C(y)]x/L_0 + u_F(y) \\ v(x,y,t=0) = 0, \quad p(x,y,t=0) = p_\infty, \quad T(x,y,t=0) = T_0 \end{array} \right. \\
 x > 0 & \left\{ \begin{array}{l} \delta(x,t=0) = \delta_{Nu}, \quad u(x,y,t=0) = \begin{cases} u_F(y) & y \leq \delta_{Nu} \\ 0 & y > \delta_{Nu} \end{cases} \\ v(x,y,t=0) = 0, \quad p(x,y,t=0) = p_\infty, \quad T(x,y,t=0) = T_0 \end{array} \right. \quad (3.34)
 \end{aligned}$$

where the semi-parabolic and parabolic profiles $u_F(y)$ and $u_C(y)$ [†] are defined as follows:

$$u_F(y) = \frac{\delta_{Nu}^2 g_x}{\nu_1} \left(\frac{y}{\delta_{Nu}} - \frac{1}{2} \frac{y^2}{\delta_{Nu}^2} \right), \quad u_C(y) = \frac{6 Re \nu_1}{\delta_0} \left(\frac{y}{\delta_0} - \frac{y^2}{\delta_0^2} \right). \quad (3.35)$$

Application of these conditions to all cells (more specifically, cell centers indexed with the letter P) contained in the spatially discretized computational domain

[†]The subscript C refers to the inlet *channel* and F to the smooth *film* flow.

represented in figures 3.4 and 3.6 for $i=0$ yields:

$$\begin{aligned}
 x_P \leq 0 & \left\{ \begin{array}{l} \varphi_P^0 = 1, \quad p_P^0 = p_\infty, \quad T_P^0 = T_0 \\ u_P^0 = \left[u_F|_{y_P} - u_C|_{y_P} \right] x_P/L_0 + u_F|_{y_P}, \quad v_P^0 = 0 \end{array} \right. \\
 x_P > 0 & \left\{ \begin{array}{l} p_P^0 = p_\infty, \quad T_P^0 = T_0, \quad y_P \geq \delta_{Nu} + \frac{\Delta y_f}{2} \left\{ \begin{array}{l} \varphi_P^0 = 0 \\ u_P^0, v_P^0 = 0 \end{array} \right. \\ y_P \leq \delta_{Nu} - \frac{\Delta y_f}{2} \left\{ \begin{array}{l} \varphi_P^0 = 1 \\ u_P^0 = u_F|_{y_P}, \quad v_P^0 = 0 \end{array} \right. \\ y_P < \delta_{Nu} + \frac{\Delta y_f}{2} \left\{ \begin{array}{l} \varphi_P^0 = 0.5 - \frac{y_P - \delta_{Nu}}{\Delta y_f}, \quad v_P^0 = 0 \\ u_P^0 = u_F|_{y_P} \end{array} \right. \\ y_P > \delta_{Nu} - \frac{\Delta y_f}{2} \left\{ \begin{array}{l} \varphi_P^0 = 0.5 + \frac{y_P - \delta_{Nu}}{\Delta y_f}, \quad v_P^0 = 0 \\ u_P^0 = u_F|_{y_P} \end{array} \right. \end{array} \right. \quad (3.36)
 \end{aligned}$$

In order to compute the implicit steps of the PISO algorithm described in figures 3.8 and 3.9, i.e. to iteratively solve the discretized momentum, pressure correction and energy equations as well as the volume fraction transport equations, boundary conditions need to be defined on the entire border of the computational domain for the corresponding transported quantities. As stated earlier, all boundaries of the domain coincide with cell faces so that the prescribed boundary conditions define face values of dependent variables or their face fluxes. Boundary conditions for velocity components, static pressure, temperature as well as volume fraction for the 2-dimensional case are summarized in figure 3.11 and are detailed below. For the sake of brevity, only the discretized form of the boundary conditions is given.

At the liquid inlet, the streamwise velocity profile is prescribed at each time step t^i , and the crosswise velocity component set to zero. The temporally averaged profile corresponds to that of fully developed channel flow given by $u_C(y)$ in equation 3.35, onto which a harmonic and monochromatic (in time) disturbance of amplitude ε_0 and frequency f is superimposed. With this disturbance, the generation of monochromatic surface waves, as realized in the experimental investigations, was reproduced. With reference to figure 3.4, the discretized liquid inlet boundary conditions employed in the context of two-dimensional simulations and applied to the west face of the corresponding boundary cells

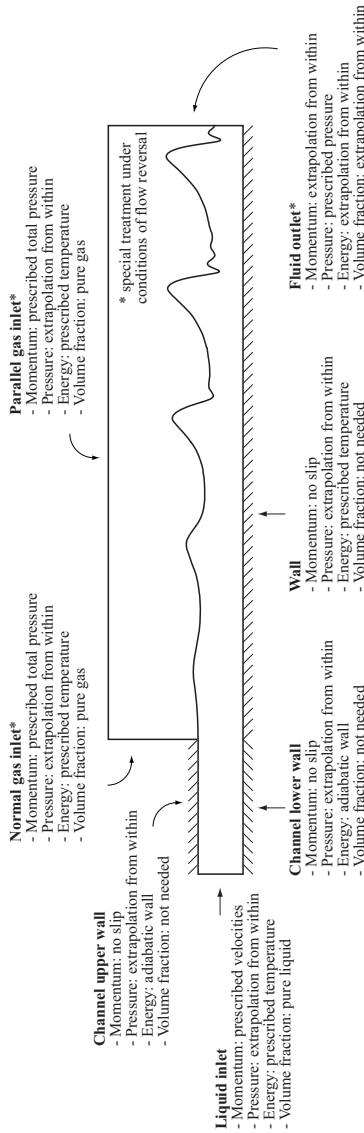


Figure 3.11: Boundary conditions for the numerical solution of the momentum (predictor), pressure correction, energy and volume fraction equations for simulations on the computational domain in figures 3.4 and 3.6. The gas inlet boundaries as well as the fluid outlet boundary are treated in a special way based on the occurrence or not of flow reversal.

at each time step t^i are:

$$\begin{array}{l}
 \text{Liquid inlet} \\
 x_P = -L_0 + \Delta x/2 \\
 \Delta y_f/2 \leq y_P \leq \delta_0 - \Delta y_f/2
 \end{array}
 \left\{ \begin{array}{l}
 u_w^i = u_C|_{y_P} \left[1 + \varepsilon_0 \sin(2\pi f t^i) \right] \\
 v_w^i = 0, \quad p_w^i = p_P^i \\
 T_w^i = T_0, \quad \varphi_w^i = 1
 \end{array} \right. \quad (3.37)$$

Note that, as the west face velocity is given, the Rhie-Chow interpolation does not have to be employed there for the discretization of the continuity equation and consequently, no information about the west face pressure derivative is needed to solve the pressure correction equation. However, the west face pressure is needed for the solution of the predictor equation and is obtained by equating it to the pressure at the adjacent cell center. The streamwise velocity derivatives at the west face, which appear in the viscous terms of the discretized momentum equations are evaluated through finite difference approximation using face and center values of the corresponding variable. The same procedure is applied for the streamwise temperature derivative. The liquid volume flux through the west face is computed with the prescribed face values of velocity and volume fraction $u_w \phi_w$, which means that ϕ_w does not need to be specified at wall boundaries. The above considerations were also applied for all comparable boundaries of the computational domain, for which they will not be further commented. The boundary conditions at the upper and lower channel walls as well as those at the wall, bounding the two-phase region, are straightforward and given by:

$$\begin{array}{l}
 \text{Channel upper wall} \\
 -L_0 + \Delta x/2 \leq x_P \leq 0 \\
 y_P = \delta_0 - \Delta y_f/2
 \end{array}
 \left\{ \begin{array}{l}
 u_n^i = v_n^i = 0, \quad \partial T / \partial y|_n^i = 0
 \end{array} \right. \quad (3.38)$$

$$\begin{array}{l}
 \text{Channel lower wall} \\
 -L_0 + \Delta x/2 \leq x_P \leq 0 \\
 y_P = \Delta y_f/2
 \end{array}
 \left\{ \begin{array}{l}
 u_s^i = v_s^i = 0, \quad T_s^i = T_w
 \end{array} \right. \quad (3.39)$$

$$\left. \begin{array}{l} \text{Wall} \\ \Delta x/2 \leq x_P \leq L - \Delta x/2 \\ y_P = \Delta y_f/2 \end{array} \right\} u_s^i = v_s^i = 0, \quad T_s^i = T_w. \quad (3.40)$$

Boundary conditions at the respective sections of the gas inlet involve an assumption regarding the gas flow outside the computational domain. The flow in that region is assumed to be non-viscous and thus satisfies the *Bernoulli equation*. By prescribing a far-field static pressure p_∞ (under the assumption of a quiescent atmosphere) the latter then constitutes a relation between velocity magnitude and static pressure at the boundary. In addition, the flow is prescribed to be normal to the considered boundary. This yields the following boundary conditions:

$$\left. \begin{array}{l} \text{Normal gas inlet} \\ y_P \geq \delta_0 + \Delta y_f/2 \\ y_P \leq H - \Delta y_c/2 \\ x_P = \Delta x/2 \end{array} \right\} \left\{ \begin{array}{l} u_w^i = \left(2p_\infty/\rho_g - 2p_w^i/\rho_g\right)^{\frac{1}{2}} \\ v_w^i = 0, \quad p_w^i = p_P^i \\ T_w^i = T_0, \quad \varphi_w^i = 0 \end{array} \right\} u_w^i \geq 0 \quad (3.41)$$

$$\left\{ \begin{array}{l} u_w^i = v_P^i, \quad v_w^i = 0 \\ p_w^i = p_\infty, \quad T_w^i = T_0 \\ \varphi_w^i = 0 \end{array} \right\} u_w^i < 0$$

$$\left. \begin{array}{l} \text{Parallel gas inlet} \\ \Delta x/2 \leq x_P \leq L - \Delta x/2 \\ y_P = H - \Delta y_c/2 \end{array} \right\} \left\{ \begin{array}{l} u_n^i = 0, \quad v_n^i = \left(2p_\infty/\rho_g - 2p_n^i/\rho_g\right)^{\frac{1}{2}} \\ p_n^i = p_P^i, \quad T_n^i = T_0, \quad \varphi_n^i = 0 \end{array} \right\} v_n^i \geq 0 \quad (3.42)$$

$$\left\{ \begin{array}{l} u_n^i = 0, \quad v_n^i = v_P^i, \quad p_n^i = p_\infty \\ T_n^i = T_0, \quad \varphi_n^i = 0 \end{array} \right\} v_n^i < 0$$

In the above definitions, a distinction was made depending on the direction of the gas flow through the respective inlet boundaries. For the case of inflow, the face pressure is extrapolated from within the domain, setting it to the pressure value at the adjacent cell center while for the case of outflow the normal velocity component is extrapolated in this manner and the face pressure set to the far-field pressure p_∞ .

Finally, the boundary conditions at the fluid outlet are as follows:

$$\left. \begin{array}{l} \text{Fluid outlet} \\ x_P = L - \Delta x/2 \\ \Delta y_t/2 \leq y_P \leq H - \Delta y_c/2 \end{array} \right\} \begin{cases} \left. \begin{array}{l} u_e^i = u_P^i, \quad v_e^i = v_P^i, \quad p_e^i = p_\infty \\ T_e^i = T_P^i, \quad \varphi_e^i = \varphi_P^i \end{array} \right\} u_e^i \geq 0 \\ \left. \begin{array}{l} u_e^i = u_P^i, \quad v_e^i = v_P^i, \quad T_e^i = T_P^i \\ p_e^i = p_\infty - \left(u_P^{i2} + v_P^{i2} \right) \bar{\rho}_e^i/2 \end{array} \right\} u_e^i < 0 \\ \varphi_e^i = \begin{cases} 1 & \varphi_P^i > 0 \\ 0 & \varphi_P^i \leq 0 \end{cases} \end{cases} \quad (3.43)$$

Here, as for the gas inlet boundaries, a distinction is made depending on the direction of the flow through the boundary. Specifically, the volume fraction in case of backflow is prescribed depending on the corresponding value at the adjacent cell center. This option is not included in the standard formulation of the FLUENT code and was added in the form of a so called *user defined function*. It was found that, although its implementation is fairly straightforward, the phase-specific prescription of the backflow volume fraction was essential. Indeed, as will be shown in later chapters, the performed simulations display a substantial region of backflow in the capillary wave region (which is exactly the phenomenon under consideration in this thesis), which in some cases extends over the entire film thickness. In such cases the total volume flux over the outlet boundary becomes negative (when a capillary wave reaches the fluid outlet) and, in the absence of a phase-specific accounting of backflow (in particular in terms of the volume fraction), a single-phase flow would re-enter the computational domain over the entire height of the outlet boundary, causing an unphysical phase distribution.

3-dimensional simulation

Initial conditions bear a more significant influence on the 3-dimensional simulation, since, most importantly, they define the volume of liquid contained in the computational domain. Due to the periodic boundary condition in stream-wise direction and the symmetric conditions in spanwise direction this volume remains constant over the course of the non-steady numerical solution. Conse-

quently, the initial liquid volume $V_{l,0}$ defines the Reynolds number value of the considered simulation case. This value can be obtained by considering the film thickness of a smooth liquid film of the same volume entirely contained in the computational domain. Then, using the relation for the film thickness of the primary flow and with reference to figure 3.7, the Reynolds number is given by:

$$Re = \frac{\delta_{Nu}^3 g_x}{3 \nu_1^2}, \quad \delta_{Nu} = \frac{V_{l,0}}{W L H}, \quad V_{l,0} = \int_{-W}^W \int_{-L}^L \delta(x,z,t=0) dx dz. \quad (3.44)$$

For the initial film thickness distribution $\delta^0(x,z)$, a biharmonic (in x- and z-direction) spatial variation was imposed, with both the streamwise and spanwise wavelengths equaling the corresponding domain dimensions, i.e. $\Lambda_x = L$ and $\Lambda_z = W$:

$$\delta^0(x,z) = \delta_{Nu} (1 + \varepsilon_0^x \cos(2\pi x/\Lambda_x) + \varepsilon_0^z \cos(2\pi z/\Lambda_z)). \quad (3.45)$$

The relative amplitudes of the streamwise and spanwise disturbances are designated with ε_0^x and ε_0^z respectively. For the performed 3-dimensional simulation both amplitudes were set equal, i.e. $\varepsilon_0^x = \varepsilon_0^z = \varepsilon_0$. Based on this phase distribution, the remaining initial conditions in terms of a continuum physical description are:

$$u(x,y,z,t=0) = \begin{cases} 0 & y > \delta^0(x,z) \\ \frac{\delta^{0,2} g_x}{\nu_1} \left(\frac{y}{\delta^0} - \frac{1}{2} \frac{y^2}{\delta^{0,2}} \right) & y \leq \delta^0(x,z) \end{cases} \quad (3.46)$$

$$v(x,y,z,t=0) = w(x,y,z,t=0) = 0, \quad p(x,y,z,t=0) = p_\infty.$$

Here, a locally semi-parabolic streamwise velocity profile was prescribed in the liquid phase, using the relation for developed film flow and the local film thickness $\delta^0(x,z)$. Thus, the discretized initial conditions are given by:

$$y_P \geq \delta^0|_{x_P, z_P} + \frac{\Delta y_f}{2} \begin{cases} u_P^0 = v_P^0 = w_P^0 = 0 \\ p_P^0 = p_\infty, \quad \varphi_P^0 = 0 \end{cases} \quad (3.47)$$

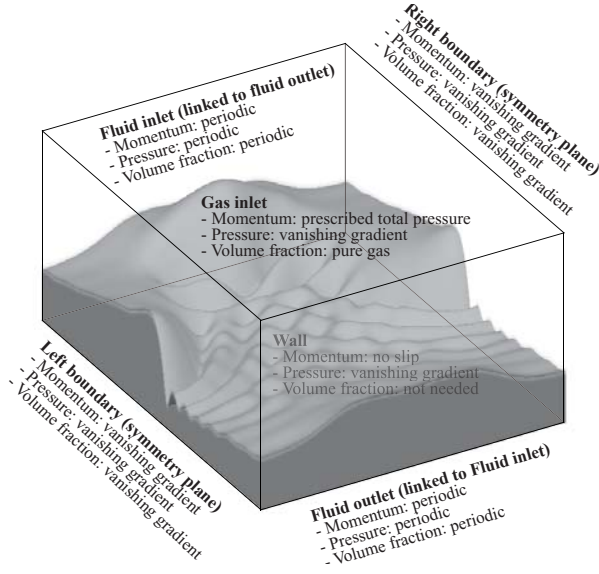


Figure 3.12: Boundary conditions for the numerical solution of the momentum (predictor), pressure correction, energy and volume fraction equations in the context of the 3-dimensional simulation on the computational domain pictured in figure 3.7.

$$y_P \leq \delta^0|_{x_P, z_P} - \frac{\Delta y_f}{2} \left\{ \begin{array}{l} u_P^0 = \frac{g_x \delta^{02}|_{x_P, z_P}}{\nu_1} \left[\frac{y_P}{\delta^0|_{x_P, z_P}} - \frac{1}{2} \frac{y_P^2}{\delta^{02}|_{x_P, z_P}} \right] \\ v_P^0 = w_P^0 = 0, \quad p_P^0 = p_\infty, \quad \varphi_P^0 = 1 \end{array} \right. \quad (3.48)$$

$$y_P > \delta^0|_{x_P, z_P} - \frac{\Delta y_f}{2} \left\{ \begin{array}{l} u_P^0 = \frac{g_x \delta^{02}|_{x_P, z_P}}{\nu_1} \left[\frac{y_P}{\delta^0|_{x_P, z_P}} - \frac{1}{2} \frac{y_P^2}{\delta^{02}|_{x_P, z_P}} \right] \\ v_P^0 = w_P^0 = 0, \quad p_P^0 = p_\infty \\ \varphi_P^0 = 0.5 - \left(y_P - \delta^0|_{x_P, z_P} \right) / \Delta y_f \end{array} \right. \quad (3.49)$$

Boundary conditions for the 3-dimensional simulation are summarized in figure 3.12 and specified below. At the fluid inlet and outlet boundaries, which are

linked through a condition of streamwise periodicity, face values of respective variables are prescribed to match, yielding the following discretized boundary conditions:

$$\begin{array}{l}
 \text{Fluid inlet/outlet} \\
 \Delta y_f/2 \leq y_P \leq H - \Delta y_c/2 \\
 z_P \leq (W - \Delta z)/2 \\
 z_P \geq (-W + \Delta z)/2
 \end{array}
 \left\{ \begin{array}{l}
 u_e^i \Big|_{x_P=L-\Delta x/2} = u_w^i \Big|_{x_P=\Delta x/2} \\
 v_e^i \Big|_{x_P=L-\Delta x/2} = v_w^i \Big|_{x_P=\Delta x/2} \\
 w_e^i \Big|_{x_P=L-\Delta x/2} = w_w^i \Big|_{x_P=\Delta x/2} \\
 p_e^i \Big|_{x_P=L-\Delta x/2} = p_w^i \Big|_{x_P=\Delta x/2}
 \end{array} \right. \quad (3.50)$$

At the spanwise boundaries of the domain, which are planes of symmetry, face values are equated to corresponding values at adjacent cell centers, leading all normal derivatives to vanish, and the normal velocity component is set to zero:

$$\begin{array}{l}
 \text{Symmetry planes} \\
 \Delta x/2 \leq x_P \leq L - \Delta x/2 \\
 \Delta y_f/2 \leq y_P \leq H - \Delta y_c/2
 \end{array}
 \left\{ \begin{array}{l}
 u_t^i = u_P^i, \quad v_t^i = v_P^i \\
 w_t^i = 0, \quad p_t^i = p_P^i \\
 u_b^i = u_P^i, \quad v_b^i = v_P^i \\
 w_b^i = 0, \quad p_b^i = p_P^i
 \end{array} \right\}
 \begin{array}{l}
 z_P=(W-\Delta z)/2 \\
 z_P=(-W+\Delta z)/2
 \end{array} \quad (3.51)$$

Finally, the discretized boundary conditions at the wall and the gas inlet are similar to their counterparts in the 2-dimensional case. Consequently, boundary conditions at the wall are given by:

$$\begin{array}{l}
 \text{Wall} \\
 \Delta x/2 \leq x_P \leq L - \Delta x/2 \\
 y_P = \Delta y_f/2 \\
 (-W + \Delta z)/2 \leq z_P \leq (W - \Delta z)/2
 \end{array}
 \left\{ \begin{array}{l}
 u_s^i = v_s^i = w_s^i = 0 \\
 p_s^i = p_P^i
 \end{array} \right. \quad (3.52)$$

and boundary conditions at the gas inlet by:

$$\begin{array}{l}
 \text{Gas inlet} \\
 \Delta x/2 \leq x_P \leq L - \Delta x/2 \\
 y_P = H - \Delta y_c/2 \\
 (-W + \Delta z)/2 \leq z_P \leq (W - \Delta z)/2
 \end{array}
 \left\{ \begin{array}{l}
 u_n^i = w_n^i = 0 \\
 v_n^i = \left(2p_\infty / \rho_g - 2p_n^i / \rho_g \right)^{\frac{1}{2}} \\
 p_n^i = p_P^i, \quad \varphi_n^i = 0
 \end{array} \right. \quad (3.53)$$

Case	Dim.	Re	Ka	We	Fr	φ (deg)	f (1/s)	ε_0 (%)
1	2D	15.6	133.6	2.0	1.9	35	15.0	0.024
2	2D	21.4	139.8	1.2	2.2	35	24.0	40
3	2D	21.4	139.8	1.2	2.2	35	17.7	40
4	2D	21.4	139.8	1.2	2.2	35	11.3	40
5	2D	8.6	509.5	20.3	∞	90	16.0	40
6	2D	10.7	509.5	14.1	∞	90	16.0	40
7	2D	12.9	509.5	10.3	∞	90	16.0	40
8	2D	15.0	509.5	8.0	∞	90	16.0	40
9	2D	10.7	509.5	14.1	∞	90	20.0	40
10	2D	10.7	509.5	14.1	∞	90	18.0	40
11	3D	59.3	3940.2	6.3	∞	90	-	25

Table 3.1: Parameters quantifying the flow regimes for the performed 2- and 3-dimensional numerical simulations of falling liquid films.

3.2.5 Quantification of simulated cases

This subsection succinctly documents all relevant quantifiable settings for the falling film simulations performed in this thesis. More specifically, all parameters that have been introduced in previous subsections, such as parameters pertaining to the grid topology and parameters specifying initial and boundary conditions as well as liquid properties and dimensionless groups are quantified. This information is presented in tables 3.1 to 3.5.

Values for the characteristic dimensionless groups introduced in section 2.1 as well as other parameters characterizing the simulated film flow regimes are quantified in table 3.1. According to this, the performed simulations can be attributed to five categories. Case 1 reproduces experimental conditions realized in an inclined test setup, which will be presented in subsection 4.1.2. For this case, the inlet disturbance amplitude ε_0 was chosen such that the wave evolution from inlet to fully developed state matched experimental observations (see figure 3.19(b)). On this basis, the spatio-temporal development of the capillary flow separation phenomenon (which is central to this thesis) from its initiation to its developed state was elucidated.

Case	ν_1 ($10^{-6}\text{m}^2/\text{s}$)	σ (N/m)	ρ_l (kg/m^3)
1	5.70	0.0220	909.3
2-4	5.21	0.0204	908.5
5-10	2.85	0.0484	1098.3
11	0.89	0.0720	997.1

Table 3.2: Liquid properties for the performed 2- and 3-dimensional numerical simulations of falling liquid films.

Case	δ_0 (μm)	L_0 (mm)	L (mm)	H (mm)	H_f (mm)
1	635	2	220	2.40	1.20
2	635	2	80	2.40	1.40
3	635	2	80	2.40	1.40
4	676	2	220	1.90	1.60
5	277	10	80	1.30	0.80
6	298	10	80	1.30	0.80
7	317	10	80	1.30	0.80
8	334	10	80	1.30	0.80
9	298	10	80	1.30	0.80
10	298	10	80	1.30	0.80
11	$W=20$ mm		25	0.91	0.59

Table 3.3: Dimensions of the computational domain for the performed 2- and 3-dimensional numerical simulations of falling liquid films.

The next set of investigations (cases 2-4) aimed to investigate the influence of wave frequency f on the capillary flow separation. These simulations also reproduce experimental conditions realized in the inclined test setup, yet ε_0 was set to a significantly higher value in order to achieve wave development at an earlier stage and thus reduce the length of the computational domain and with it the computational burden. Consequently, only the fully developed state of the flow separation phenomenon was considered. Cases 5-10 reproduce conditions, which were realized in a vertical optical test setup (see subsection 4.1.1), specifically designed for the measurement of the liquid phase velocity field. Under these conditions, the effect of the Reynolds number (cases 5-8) and

3.2 Specification of performed numerical simulations

Case	Δx (μm)	Δy_f (μm)	Δy_c (μm)	Δz (μm)	Δt (μs)
1-10	50	20	40	-	5
11	60	16	32	60	5

Table 3.4: Spatio-temporal discretization for the performed 2- and 3-dimensional numerical simulations of falling liquid films.

Case	k_l (W/(mK))	c_l (J/(kgK))	Pr	T_w (K)	T_0 (K)
1	0.12	1540.0	66.5	350	300
8	0.24	2349.9	30.6	350	300

Table 3.5: Thermal liquid properties and boundary conditions for the 2-dimensional heat transfer simulations.

the excitation frequency (cases 6, 9 and 10) on the fully developed capillary flow separation was clarified.

The last simulation (case 11) is of 3-dimensional character and reproduces flow conditions investigated by Park & Nosoko (2003)[†] experimentally (see figure 3.7) and by Scheid *et al.* (2006) using a multiple-equation model. On this basis, the occurrence of the capillary flow separation under 3-dimensional wave dynamics was elucidated. In this case, $\varepsilon_0 = \varepsilon_0^x = \varepsilon_0^y$ and thus quantifies the relative amplitudes of the initial biharmonic disturbance of the liquid film, as introduced in subsection 3.2.4. The value of ε_0 was chosen to be relatively large in order to reduce the computation time needed to obtain fully developed waves.

The liquid properties employed for the simulation cases listed in table 3.1 are summarized in table 3.2. For all 2-dimensional cases, these were obtained from liquid property measurements for the working liquids employed in the experiments, which will be discussed in chapter 4. For the 3-dimensional case, water properties were obtained from the literature[‡] and evaluated at a temperature of $T=25^\circ\text{C}$. For all simulations, the gaseous phase consisted of air, the properties

[†]See figure 7(d) there.

[‡]The density was obtained from Nakanishi *et al.* (1966), dynamic viscosity from Mazurkiewicz & Tomasik (1990) and surface tension from Vázquez *et al.* (1995).

of which were evaluated at a temperature of 25°C and at the far field static pressure $p_\infty=101325 \text{ N/m}^2$, i.e. $\rho_g = 1.2 \text{ kg/m}^3$ and $\nu_g = 1.5 \cdot 10^{-6} \text{ m}^2/\text{s}$.

Dimensions of the computational domain for the respective simulations are given in table 3.3. The latter were chosen based on experimental data in order to ensure that full development of surface waves took place within the length of the computational domain and the height of the finely resolved section of the grid for all cases. For the 3-dimensional simulation, the length and width of the domain were set to the streamwise and spanwise wavelengths $\Lambda_x=25 \text{ mm}$ and $\Lambda_z=20 \text{ mm}$, which were obtained from the previously mentioned publication of Park & Nosoko (2003).

Table 3.4 lists the spatial and temporal discretization increments for the 11 simulation cases. For all 2-dimensional simulations, the same values for Δx , Δy_f and Δy_c were employed, as the length and time scales of the capillary flow separation did not vary significantly over the investigated parameter space. The adequacy of the employed spatio-temporal discretization will be demonstrated in subsection 3.3 by way of a grid dependence analysis.

In order to investigate the influence of the capillary flow separation on scalar transfer, the simulation of heat transfer from the wall to the liquid film was additionally simulated for cases 1 and 8. No temperature dependence of liquid properties was considered so that the solution of the Navier-Stokes equations remained uncoupled from the solution of the energy equation. Additional parameters specifying heat transfer conditions, such as thermal liquid properties and boundary conditions are given in table 3.5. For the gaseous phase, the thermal fluid properties $k_g=0.024 \text{ W/mK}$ and $c_{p,g}=1006 \text{ J/kgK}$ were employed.

3.3 Consistency tests

In order to establish the soundness of data obtained from the numerical simulations specified in subsection 3.2.5 a series of consistency tests centered on various known weak points of the employed numerical methodology will be presented in this section. The tests were conducted for two of the simulation

	Case 1			Case 8		
	coarse	reference	fine	coarse	reference	fine
Δx (μm)	100	50	25	100	50	25
Δy_f (μm)	40	20	10	40	20	10
Δy_c (μm)	80	40	20	80	40	20
Δt (μs)	10	5	2.5	10	5	2.5
L (mm)	60	60	60	160	160	160

Table 3.6: Spatio-temporal discretization for the grid dependence analysis of cases 1 and 8. The relative inlet perturbation ε_0 was set to 40% for all variants.

cases listed in table 3.1, namely cases 1 and 8, which are representative of the two main groups of 2-dimensional simulations, representing inclined and vertical flow conditions respectively. First, a grid dependence analysis will be performed, showing the adequacy of the chosen spatio-temporal discretization. Next, the significance of spurious currents, appearing at the interface due to numerical errors in the representation of tensile forces, will be investigated on the basis of two test cases generally employed in the literature. First, the simulation of a static bubble, which allows for the direct quantification of the spurious velocity magnitude and second, the simulation of a horizontal capillary wave for which an analytical solution exists, and which reproduces the conditions encountered in the capillary wave region of falling liquid films quite closely. Then, the influence of the fluid outlet boundary condition on upstream flow dynamics will be investigated in order to assess if its, more or less arbitrary, character significantly distorts results. Finally, simulation data for all cases will be compared to own experimental data (in the 3-dimensional case, the data of Park & Nosoko (2003) will be employed).

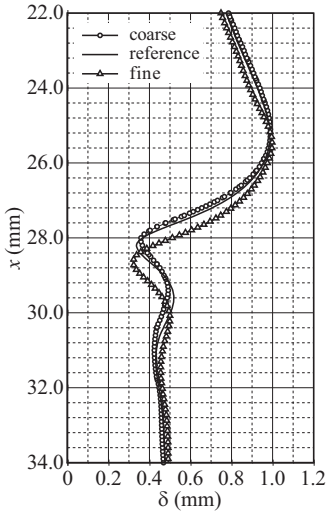
3.3.1 Grid dependence analysis

Table 3.6 summarizes the spatio-temporal discretization increments employed for the grid dependence analysis of simulation cases 1 and 8. For both cases, three different discretization variants were investigated. The finally employed

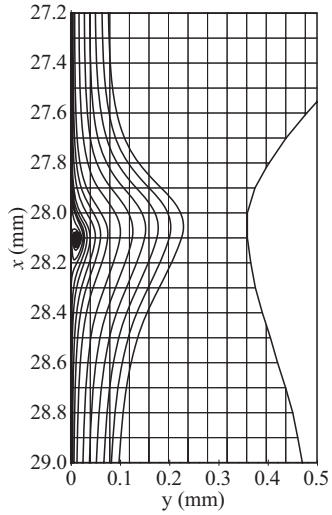
discretization (or *reference discretization*), a coarser variant, with increments twice as large as for the reference case, and a finer variant, with increments half as large as for the reference case. Results are illustrated in figures 3.13 (case 1) and 3.14 (case 8).

As mentioned in subsection 3.2.5, numerical results from simulation case 1 will be used in chapter 5 to investigate the spatio-temporal evolution of the capillary flow separation phenomenon. Consequently, the grid dependence analysis for this case was performed in the developing region, while using a short grid and a large perturbation amplitude $\varepsilon_0=40\%$ to reduce computational burden. Accordingly, figure 3.13(a) depicts film thickness distributions for the 3 resolution variants evaluated at the same time $t=0.193750$ s at a position within the developing region of surface waves. With the exception of a small translational shift, the wave topology for the reference and fine variants is in good agreement both in the wave hump and the capillary wave region. This is also the case for the liquid phase streamline pattern at the first capillary minimum, which shows the *Capillary Separation Eddy* or CSE at the center of investigations in this thesis (see chapter 5). Meanwhile, the size of the CSE is significantly underestimated by the coarse resolution variant.

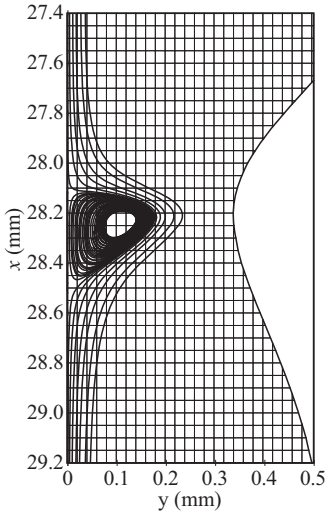
Figure 3.14 depicts results of the grid dependence analysis for case 8. Before discussing these, a few preliminary remarks are in order. First, as documented in table 3.6, simulations for the different resolution variants were performed on a relatively long grid (i.e. $L=160$ mm). This was necessary due to the fact that, for the fine resolution variant, surface waves did not attain their developed state within the domain length specified for case 8 in table 3.3 (i.e. $L=80$ mm). Further, due to the use of a longer grid, respective simulations had to be performed over a longer time span in order to ensure independence from the initial condition. This in turn led to a larger shift (between the respective resolution variants) in the streamwise position of the wave designated for comparison. Consequently, in order to facilitate the plotting of film thickness distributions in one graph, respective simulations were conducted until the considered wave reached a fixed streamwise position. Numerical data depicted in figure 3.14 are thus associated with different time points for the coarse ($t=0.674500$ s),



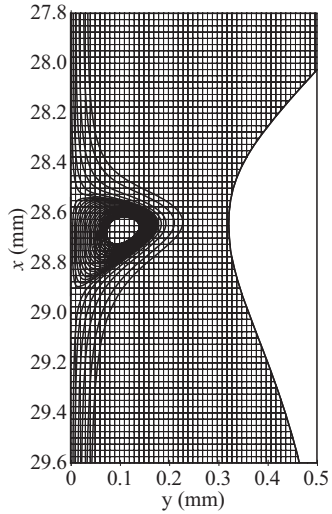
(a) Film thickness time traces



(b) Coarse discretization

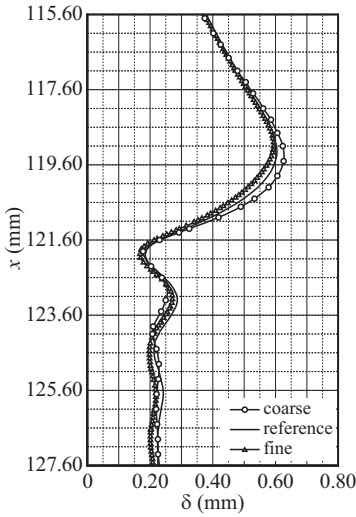


(c) Reference discretization

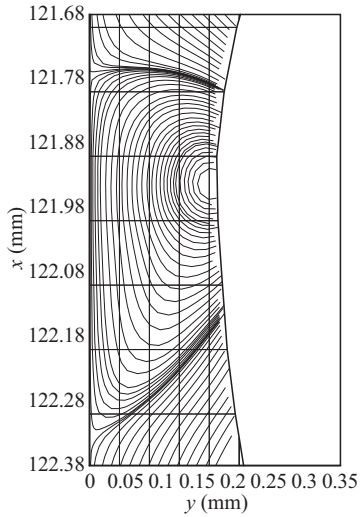


(d) Fine discretization

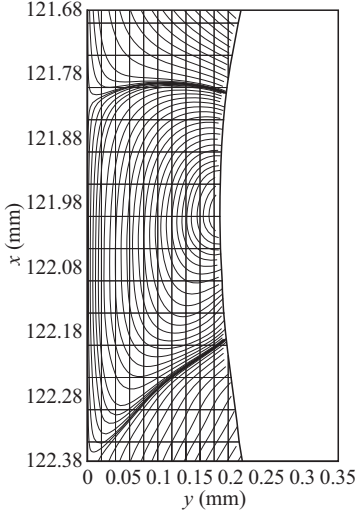
Figure 3.13: Grid dependence analysis for case 1 (see table 3.6).



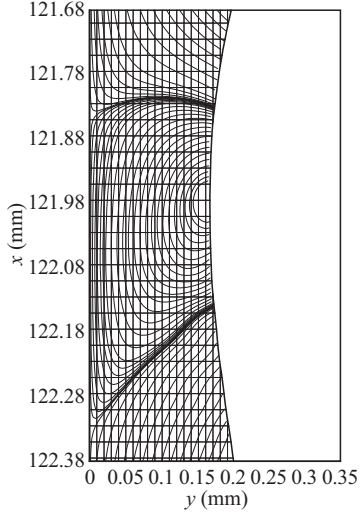
(a) Film thickness time traces



(b) Coarse discretization



(c) Reference discretization



(d) Fine discretization

Figure 3.14: Grid dependence analysis for case 8 (see table 3.6).

reference ($t=0.676000$ s) and fine ($t=0.657925$ s) resolution variant respectively.

In terms of the film thickness distribution, subfigure 3.14(a) exhibits good agreement between the different resolution variants. Meanwhile, streamline patterns in subfigures 3.13(b) to 3.13(d) show that the coarse variant, as opposed to the other variants, does not resolve the shape of the CSE sufficiently, while a small difference in CSE size is discernible between the reference and fine resolution variant. Finally, as will become evident later, the size of the CSE predicted by simulation case 8 using the settings in table 3.3 (see subfigure 5.5(a) in subsection 5.1.2) lies between that of subfigures 3.14(c) and 3.13(d). This is to be attributed to the fact that surface waves computed on the longer computational domain developed slight streamwise oscillations of wave topology, resulting from the secondary instability discussed in subsection 2.2.2, which did not occur in the simulation on the shorter grid. Nonetheless, figures 3.14(c), 3.13(d) and 5.5(a) do not exhibit significant differences.

In summary, it can thus be concluded that the employed discretization increments for the 2-dimensional simulation cases specified in table 3.4 are adequate to resolve the flow separation phenomenon accurately.

3.3.2 Interfacial spurious currents

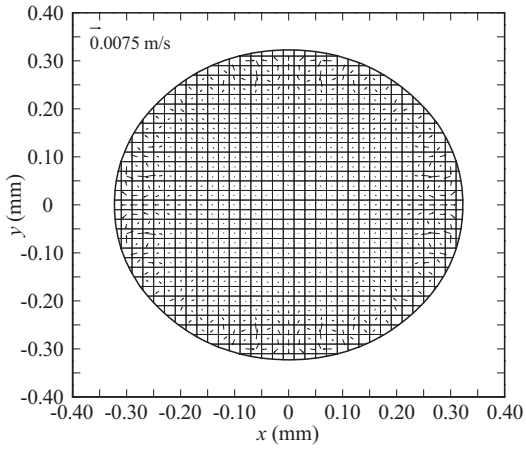
A well documented (see e.g. Lafaurie *et al.* (1994)) problem of the combined VOF-CSF method, stemming from the numerical discretization of equation 3.25 (which formulates the volume specific total tensile force $F''''_{\sigma i}$), is the appearance of small scale erroneous or *parasitic velocities*, also designated as *spurious currents*, near the interface. As pointed out by Jamet *et al.* (2002) the main complication in equation 3.25 is the fact that the volume fraction φ needs to be differentiated twice, which in a numerical implementation (using central difference discretization) introduces a large truncation error. Many attempts have been directed at reducing the magnitude of such spurious currents using different methods (see e.g. Jamet *et al.* (2002) and Renardy & Renardy (2002)) without providing a final cure. From a physical standpoint, the spurious currents arise from the unsmooth representation of the liquid-gas interface

due to the spatial discretization imposed by the numerical approach. This unsmoothness (coupled with the previously mentioned truncation errors) induces an oscillating normal tensile force which in turn leads to an oscillating pressure field. This pressure oscillation then drives the spurious currents.

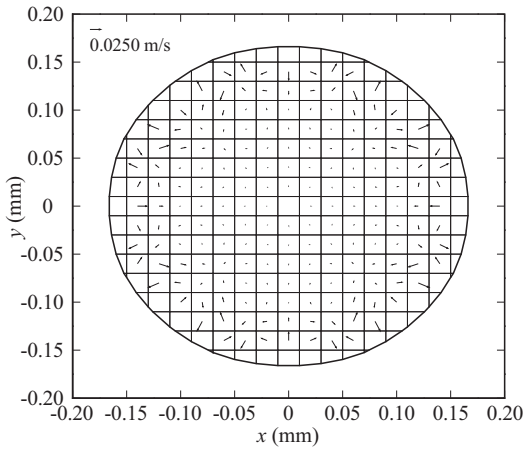
In order to assess the effect of spurious currents on the simulations performed in this thesis, two well known test cases were computed using the liquid properties and discretization increments employed for simulation cases 1 and 8 respectively (see tables 3.2 and 3.4). The first test case represents a liquid droplet in a quiescent gaseous atmosphere in the absence of gravity and external flow. The exact solution for the velocity field in this case is trivial i.e. $u=v=0$. Thus, computed velocity components offer a direct estimator of the spurious currents. The second case represents the decay of a harmonic capillary wave in a horizontal liquid layer as previously illustrated in figure 2.2. An analytical solution for the temporal evolution of the film thickness was derived for this situation by Prosperetti (1981). This test case represents the conditions in the capillary wave region of falling liquid films quite closely.

Static drop The static drop simulations were performed on a quadratic domain with edge length 1.3 mm^\dagger . On the four edges of the domain, the same boundary condition as for the gas inlet in the falling film simulations (cases 1 and 8) was imposed. Although the static drop problem is steady by definition the same non-steady solution procedure as for the falling film simulations was employed. Results showed that, after a period with oscillations induced by spurious currents, the computed solutions attained a steady state. As initial condition, a zero velocity field and a phase-wise constant pressure field, satisfying Laplace's law for the interfacial pressure jump, was prescribed. The initial diameter of the drop was set to the value of the corresponding primary film flow's film thickness δ_{Nu} . Velocity vectors in the liquid drop for the respective test cases, pertaining to cases 1 and 8, are pictured in figure 3.15. The reference vector in the upper left corner of the subfigures represents the respective

[†]Accordingly, quadratic computational cells of edge length Δy_f were employed for static drop simulations.



(a) Case 1



(b) Case 8

Figure 3.15: Static drop test case simulations using liquid properties and discretization increments for cases 1 and 8 (see tables 3.2 and 3.4).

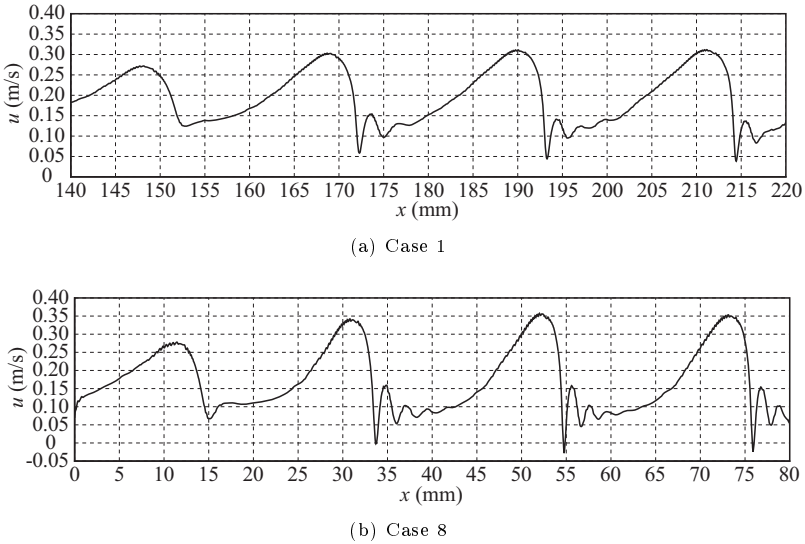


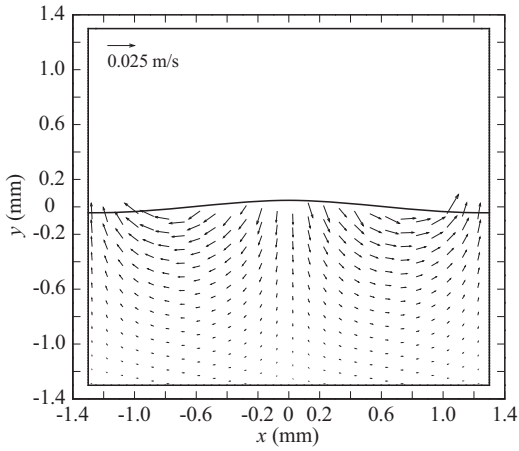
Figure 3.16: Instantaneous interfacial streamwise velocity distribution for cases 1 and 8 (see table 3.1), showing small oscillations due to spurious currents.

maximal velocity magnitude encountered inside the drop. For case 1 this value ($|\vec{v}|_{\max}^{\text{SP}}=0.0075$ m/s) is much smaller than for case 8 ($|\vec{v}|_{\max}^{\text{SP}}=0.025$ m/s), which is due to both the higher surface tension and smaller drop diameter in the latter case. Indeed, according to equation 3.25, surface tension scales the effect of truncation error, while the drop diameter determines the relative spatial resolution for a given grid. In both cases, the magnitude of spurious velocities is significantly smaller than the mean streamwise velocity for the corresponding primary film flow i.e. $u_{\text{Nu}}=0.14$ m/s for case 1 and $u_{\text{Nu}}=0.13$ m/s for case 8. For case 1 the ratio is approximately one order of magnitude. Since the dynamical analysis of the capillary flow separation will be introduced on the basis of this case it is noteworthy that spurious currents play no appreciable role.

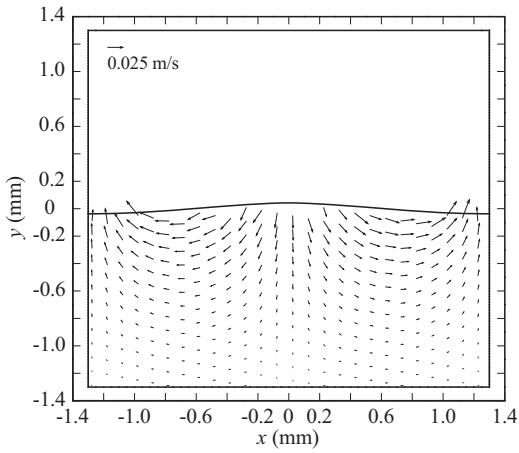
In order to assess the significance of the spurious currents for the corresponding falling film simulations in greater detail, interfacial streamwise velocity distributions for cases 1 and 8 are pictured in figure 3.16. In these distributions, the effect of spurious currents is evidenced by small scale oscillations superimposed on the wave induced modulation of interfacial velocity. Notably, the oscillations are mostly localized at the top of the wave back (near the wave crest) and absent from the region of the first capillary minimum, which is of most interest in this thesis. Further, their amplitude is negligible compared to the magnitude of local streamwise velocity.

Horizontal capillary wave The horizontal capillary wave test case (see figure 2.2) represents conditions in the capillary wave region of falling liquid films more closely than the static drop test case and enables an estimate of the effect of spurious currents on wave dynamics. Two such simulations were performed, using liquid properties and discretization increments for cases 1 and 8 as specified in tables 3.2 and 3.4. Computations were performed on a square 2-dimensional domain of edge length 2.6 mm, which approximately corresponds to the wavelength of the first capillary wave for cases 1 and 8 (see figures 3.20(a) and 3.21(d)). Conditions of symmetry were applied to all boundaries of the domain, while the initial interface distribution was prescribed with a cosine function centered (in both directions) in the domain, using the domain width as wavelength. The initial velocity components were set to zero in the entire domain while the initial pressure was constant in the gaseous phase, with the local interfacial pressure jump satisfying Laplace's law and no pressure variation in vertical direction. Using these settings, the temporal evolution of a single capillary wave was computed.

Figures 3.17(a) and 3.17(b) show liquid phase velocity vector fields at a given point in time for the two test cases pertaining to cases 1 and 8 respectively. These clearly show the capillary-induced flow from the wave crest to the wave trough previously indicated in figure 2.2. Figures 3.18(a) and 3.18(b) depict corresponding film thickness time traces evaluated at the center of the computational domain. For comparison, film thickness time traces obtained from

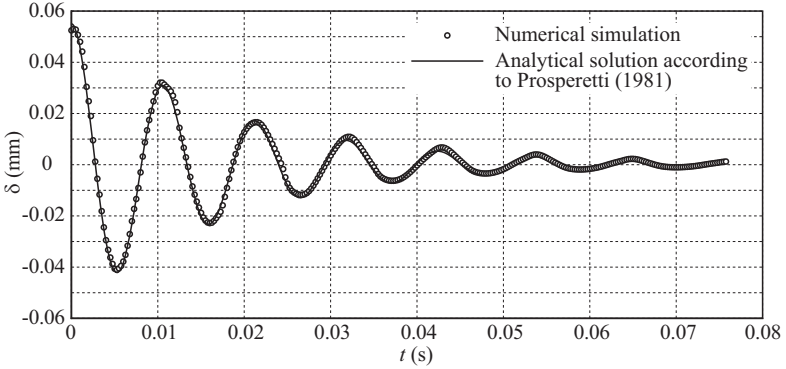


(a) Case 1

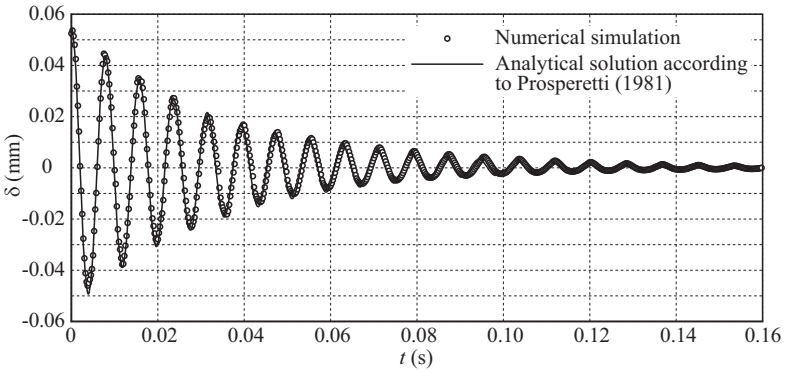


(b) Case 8

Figure 3.17: Horizontal capillary wave test case simulations corresponding to cases 1 and 8 (see tables 3.2 and 3.4).



(a) Case 1



(b) Case 8

Figure 3.18: Comparison of numerical and analytical film thickness time traces for the horizontal capillary wave test cases, pertaining to cases 1 and 8 (see tables 3.2 and 3.4).

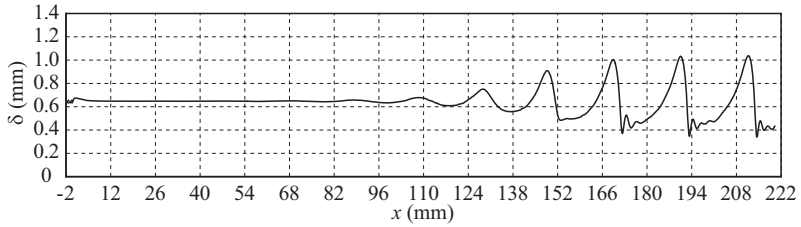
the analytical solution of Prosperetti (1981)[†] are also plotted. Results show good agreement between the numerical and analytical solutions, leading to the conclusion that the spurious currents do not effect capillary wave dynamics.

In summary, the following conclusions with respect to spurious currents can be drawn from the two test cases. First, the magnitude of spurious velocities is significantly smaller than the characteristic streamwise velocity of the respective film flows. Second, their effect on interfacial velocity is absent in the region of the first capillary wave. And finally, their effect on capillary wave dynamics is negligible. In addition, the capillary flow separation, as will be established in subsection 5.1.1, originates at the bounding wall, where spurious currents have no effect.

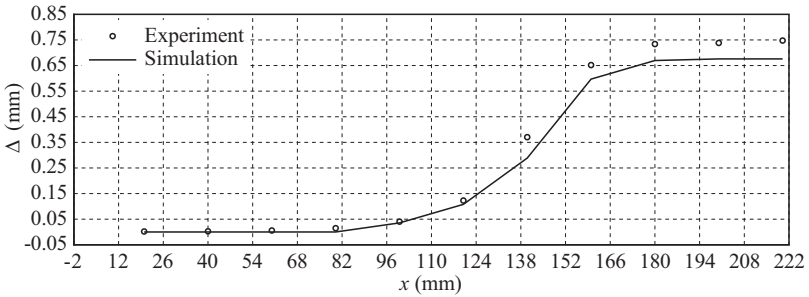
3.3.3 Outlet boundary condition

As the outlet boundary of the computational domain for the performed 2-dimensional simulations truncates the falling liquid film at an arbitrary downstream position, no explicit information about the flow variables is obtainable there, necessitating the definition of a more or less arbitrary boundary condition (see section 3.2.4). Due to the arbitrary character of this condition, it is conceivable that the latter may influence the upstream evolution of the falling liquid film in an unrealistic manner. In order to disprove this hypothesis, film thickness distributions for all 2-dimensional cases are plotted in figures 3.19 to 3.22 over the entire length of the computational domain. These distributions show that no significant change in wave topology takes place as fully developed waves approach and exit the outlet boundary. This proves the absence of a strong and localized upstream effect by the outlet condition. However, it does not exclude a smooth effect distributed over the entire upstream region, and influencing the amplitude and shape of developed waves. The latter hypothesis can be assessed by comparing simulated film thickness data for fully developed waves with corresponding experimental data, which will be done in

[†] Prosperetti's analytical solution is formulated in the complex variable domain and was transformed numerically to the time domain with the method of de Hoog *et al.* (1982) using the program written by Hollenbeck (1998).



(a) Simulated instantaneous film thickness distribution

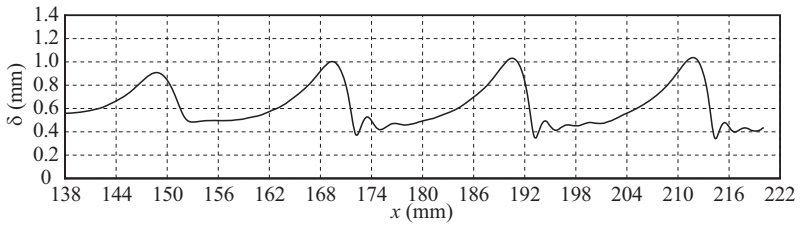
(b) Simulated and measured wave amplitude $\Delta = \delta_{\max} - \delta_{\min}$ Figure 3.19: Streamwise wave evolution for case 1: $Re=15.6$, $f=15.0$ Hz.

the next and last subsection. Anticipating the result of this comparison, it can be stated that in the context of this thesis no special treatment of the outlet boundary condition, as performed by Malamataris & Papanastasiou (1991), Papanastasiou *et al.* (1992) and Stuhlträger *et al.* (1993), was necessary.

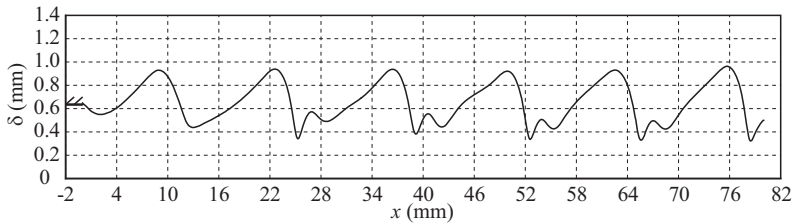
3.3.4 Comparison with experimental data

The most straightforward way to assess the accuracy of the performed numerical simulations is through direct comparison with experimental data. Consequently, figures 3.23 to 3.26 compare simulated film thickness time traces (evaluated in the fully developed region of the flow) for all 2-dimensional simulations

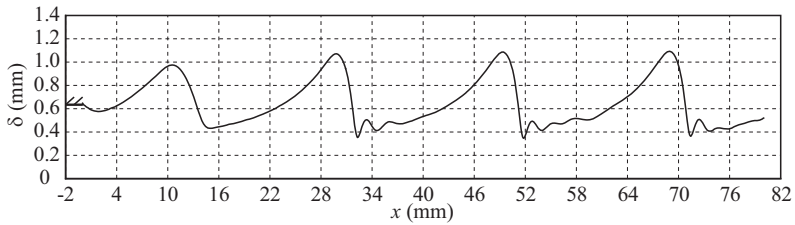
3 Numerical simulation using the Volume of Fluid method



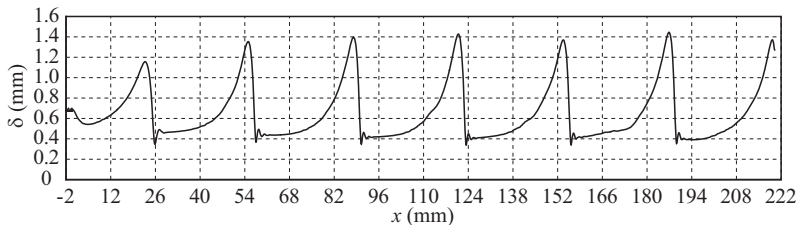
(a) Case 1: $Re=15.6$, $f=15.0$ Hz



(b) Case 2: $Re=21.4$, $f=24.0$ Hz



(c) Case 3: $Re=21.4$, $f=17.7$ Hz



(d) Case 4: $Re=21.4$, $f=11.3$ Hz

Figure 3.20: Computed instantaneous film thickness distributions for cases 1-4.

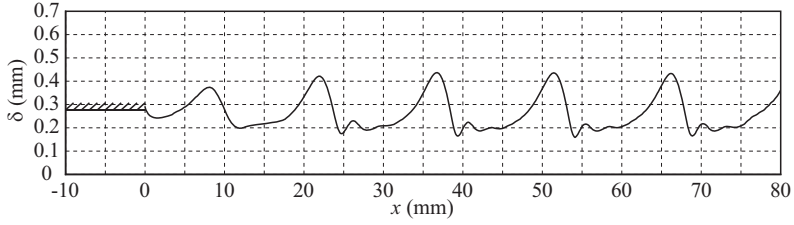
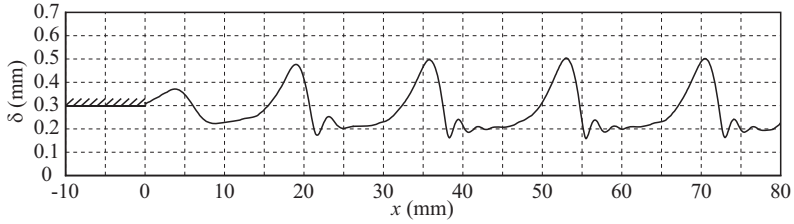
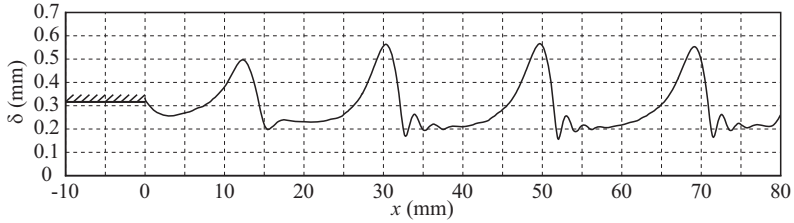
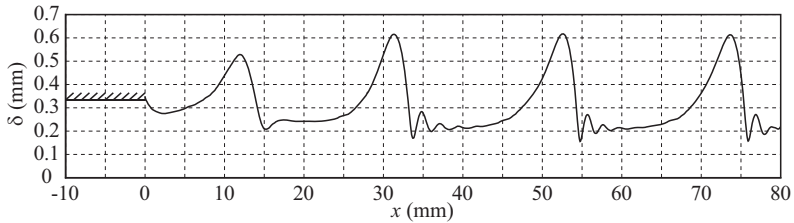
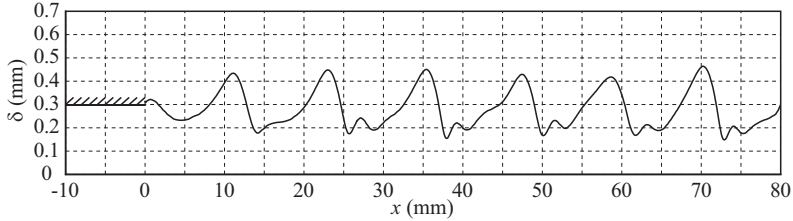
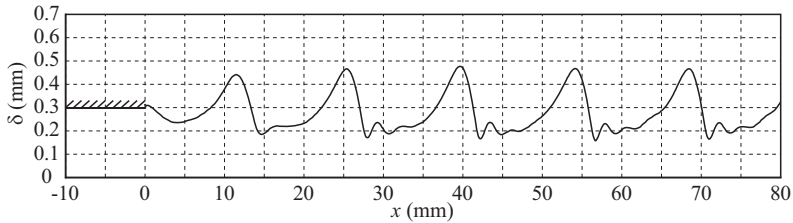
(a) Case 5: $Re=8.6$, $f=16.0$ Hz(b) Case 6: $Re=10.7$, $f=16.0$ Hz(c) Case 7: $Re=12.9$, $f=16.0$ Hz(d) Case 8: $Re=15.0$, $f=16.0$ Hz

Figure 3.21: Computed instantaneous film thickness distributions for cases 5-8.



(a) Case 9: $Re=10.7$, $f=20.0$ Hz



(b) Case 10: $Re=10.7$, $f=18.0$ Hz

Figure 3.22: Computed instantaneous film thickness distributions for cases 9 and 10.

(cases 1-10) with the author's own corresponding experimental data, which will be presented and discussed in greater detail in chapter 5. For all cases, the agreement with respect to maximal film thickness and capillary wave topology is good. Further, for case 1, figure 3.19(b) shows that the streamwise evolution of the wave topology from the inlet to the fully developed state is predicted accurately by the numerical simulation.

In addition to the comparison of wave topology, figures 3.27 and 3.28 compare numerical and experimental[†] time traces of the liquid phase streamwise velocity component evaluated at a fixed point in the fully developed region of the flow. Since experimental velocity data were obtainable only in the specifically designed vertical optical test setup (see subsection 4.1.1), comparison was

[†]Obtained by the author using LDV (see chapter 4).

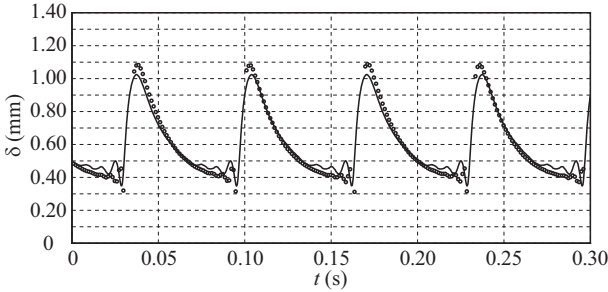
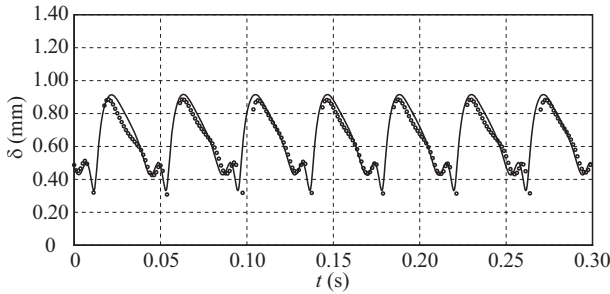


Figure 3.23: Comparison of experimental (circles) and numerical (lines) film thickness time traces in the fully developed region of the flow (numerical data evaluated at $x=200$ mm): case 1.

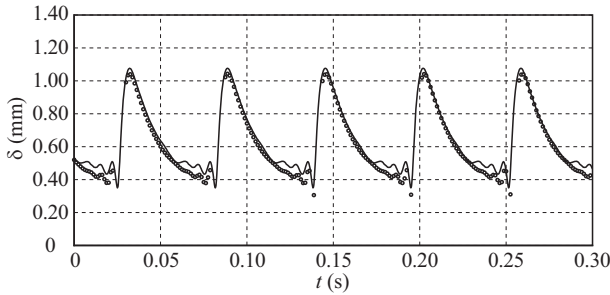
made only for cases 5-10. Results show that agreement between simulation and experiment is good for all cases over the entire period length of a surface wave. Importantly, the modulation of streamwise velocity in the capillary wave region is captured accurately by the simulations as evidenced by the accurate prediction of the number and amplitude of capillary extrema.

Finally, figure 3.29 compares the developed wave topology obtained from the 3-dimensional simulation (case 11) with a shadowgraph recording produced by Park & Nosoko (2003) for the same operating conditions. Agreement between the respective data, as far as this qualitative comparison can indicate, is good.

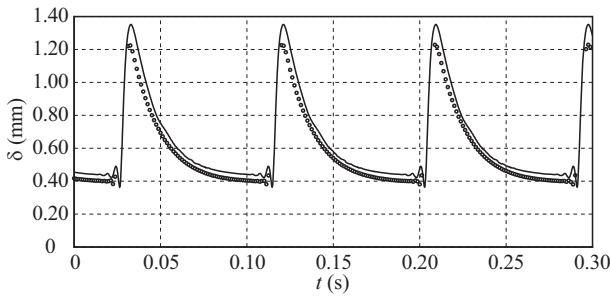
In summary, the elaborations of this chapter have introduced the numerical methodology employed in the context of this thesis and have established its accuracy in terms of the numerical simulation of falling liquid films with specific attention to the capillary wave region, preceding large wave humps. Generic consistency tests as well as detailed direct comparison with experimental data lead to the conclusion that a physically sound representation of the real film dynamics is provided by the numerical simulation, thus warranting a numerically based investigation into the dynamics of capillary flow separation.



(a) Case 2: $Re=21.4$, $f=24.0$ Hz



(b) Case 3: $Re=21.4$, $f=17.7$ Hz



(c) Case 4: $Re=21.4$, $f=11.3$ Hz

Figure 3.24: Comparison of experimental (circles) and numerical (lines) film thickness time traces in the fully developed region of the flow (numerical data evaluated at $x=60$ mm for cases 2 and 3 and $x=150$ mm for case 4): cases 2-4.

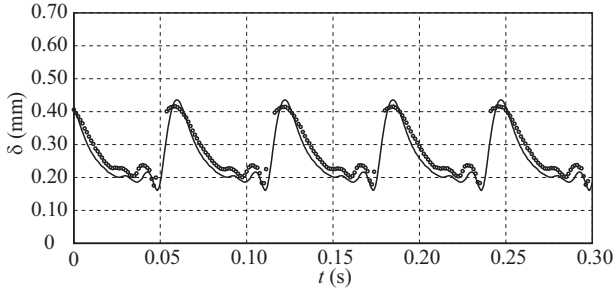
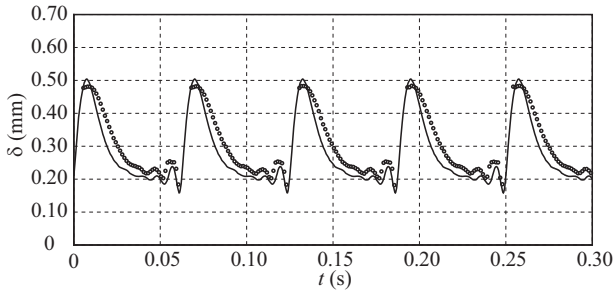
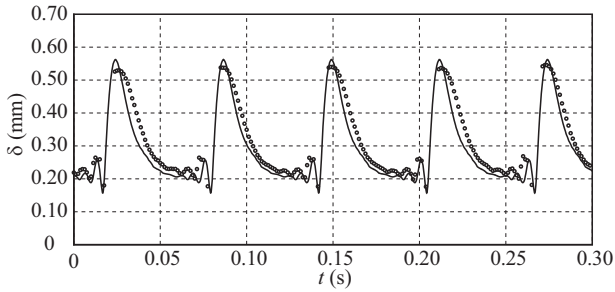
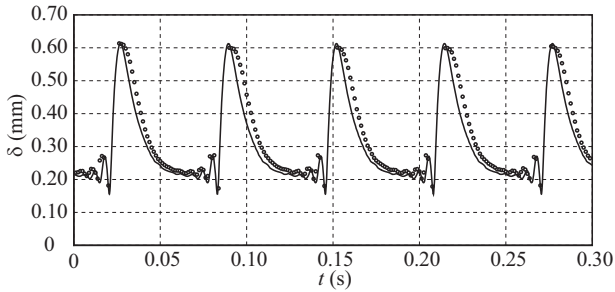
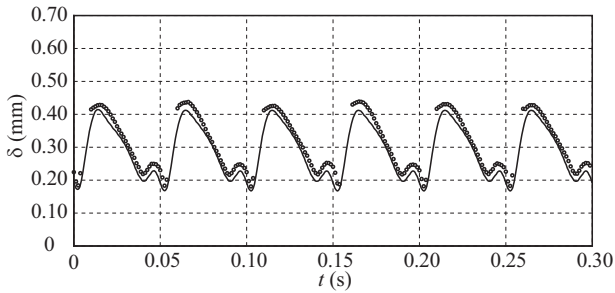
(a) Case 5: $Re=8.6$, $f=16.0$ Hz(b) Case 6: $Re=10.7$, $f=16.0$ Hz(c) Case 7: $Re=12.9$, $f=16.0$ Hz

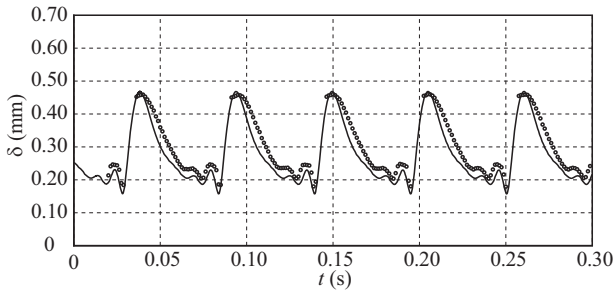
Figure 3.25: Comparison of experimental (circles) and numerical (lines) film thickness time traces in the fully developed region of the flow (numerical data evaluated at $x=56$ mm): cases 5-7.



(a) Case 8: $Re=15.0$, $f=16.0$ Hz



(b) Case 9: $Re=10.7$, $f=20.0$ Hz



(c) Case 10: $Re=10.7$, $f=18.0$ Hz

Figure 3.26: Comparison of experimental (circles) and numerical (lines) film thickness time traces in the fully developed region of the flow (numerical data evaluated at $x=56$ mm): cases 8-10.

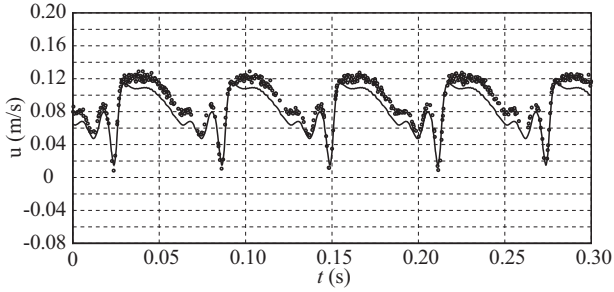
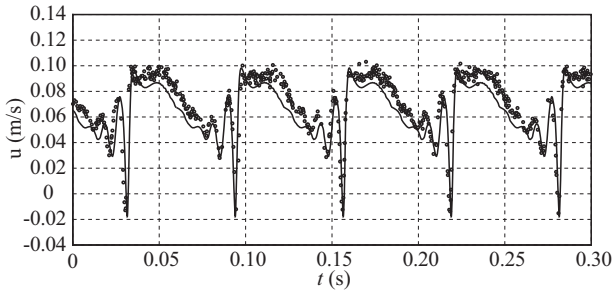
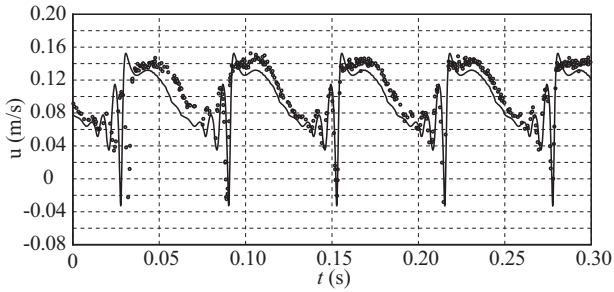
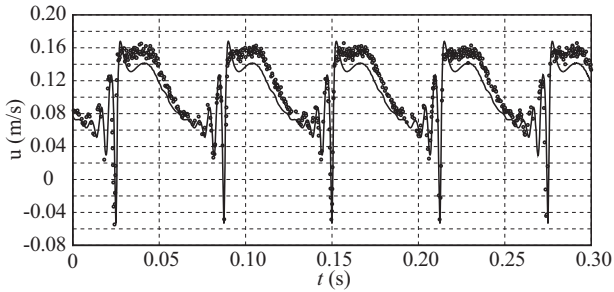
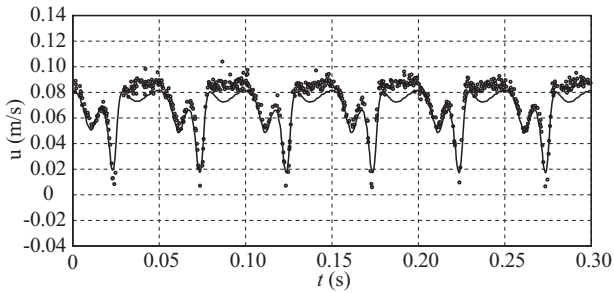
(a) Case 5: $Re=8.6$, $f=16.0$ Hz, $y=120 \mu\text{m}$ (b) Case 6: $Re=10.7$, $f=16.0$ Hz, $y=80 \mu\text{m}$ (c) Case 7: $Re=12.9$, $f=16.0$ Hz, $y=120 \mu\text{m}$

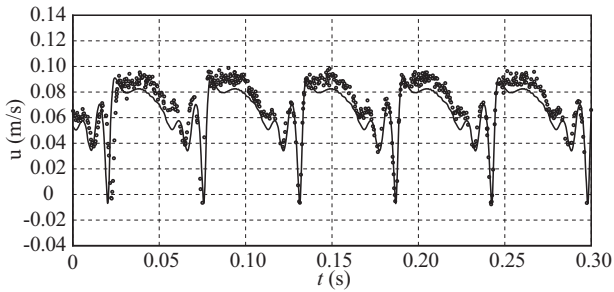
Figure 3.27: Comparison of experimental (circles) and numerical (lines) stream-wise velocity time traces in the fully developed region of the flow at $y=120 \mu\text{m}$ (cases 5 and 7) and $y=80 \mu\text{m}$ (case 6) respectively (numerical data evaluated at $x=56 \text{ mm}$): cases 5-7.



(a) Case 8: $Re=15.0$, $f=16.0$ Hz, $y=120 \mu\text{m}$

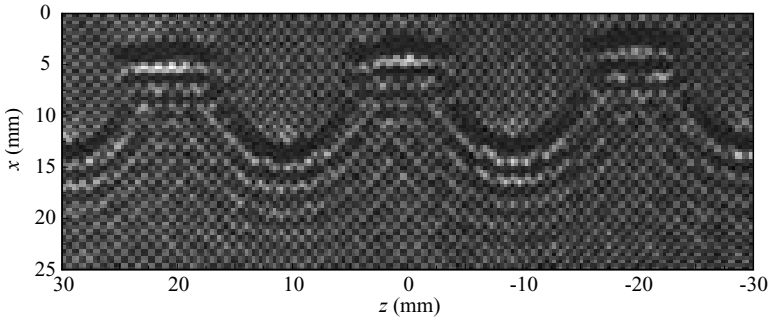


(b) Case 9: $Re=10.7$, $f=20.0$ Hz, $y=80 \mu\text{m}$

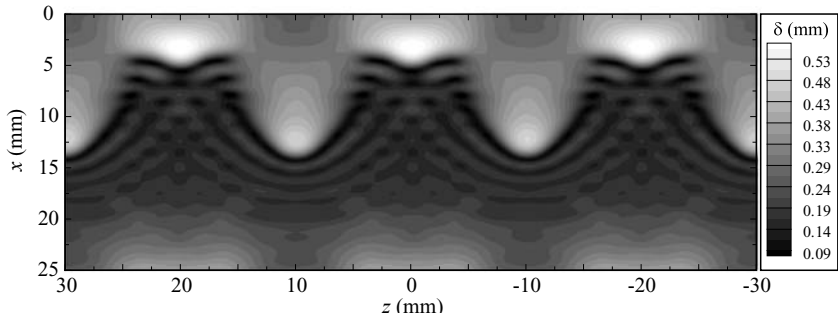


(c) Case 10: $Re=10.7$, $f=18.0$ Hz, $y=80 \mu\text{m}$

Figure 3.28: Comparison of experimental (circles) and numerical (lines) streamwise velocity time traces in the fully developed region of the flow at $y=120 \mu\text{m}$ (case 8) and $y=80 \mu\text{m}$ (cases 9 and 10) respectively (numerical data evaluated at $x=56 \text{ mm}$): cases 8-10.



(a) Shadowgraph taken from Park & Nosoko (2003)



(b) Numerical simulation

Figure 3.29: Comparison of numerical and experimental wave topology for the 3-dimensional simulation: case 11 (see table 3.1).

4 Experimental

Having presented the numerical methodology in chapter 3, this chapter provides a description of experiments performed in the context of this thesis, both in terms of the test setups (section 4.1) employed to realize investigated experimental conditions and in terms of applied measurement techniques (section 4.2). Two test setups, yielding different falling film flow conditions, were employed:

1. A vertical cylindrical test setup, henceforth designated as *optical test setup*, which was specifically designed for liquid phase velocity measurements, using optical techniques, namely *Laser Doppler Velocimetry* (LDV) and *Particle Image Velocimetry* (PIV), as well as simultaneous film thickness measurements, using a *Confocal Chromatic Imaging* (CCI) technique.
2. An inclined plane test setup, henceforth designated as *inclined test setup*, allowing for film thickness measurements with the CCI technique as well as velocity measurements with LDV, although the latter lack crosswise spatial resolution and are included only in order to demonstrate the resolution improvement achieved in the optical test setup.

The goal of the performed experiments was twofold. On the one hand, experimental data served to assess the soundness of numerical data (see subsection 3.3.4). On the other hand, in the form of velocity measurements, they served to clearly prove the existence of capillary flow separation in falling liquid films, showing the occurrence of backflow (by way of LDV) in the capillary wave region and elucidating the topology of the associated Capillary Separation Eddy or CSE (by way of PIV).

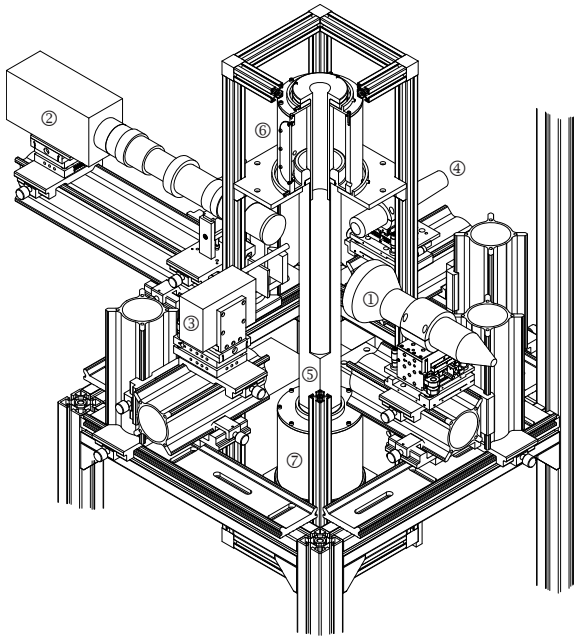


Figure 4.1: Isometric view of the optical test setup including measurement instruments. 1: LDV-probe; 2: CMOS camera and microscopic lens assembly (PIV); 3: light sheet optics (PIV); 4: CCI-probe; 5: glass body; 6: middle reservoir including film inlet; 7: lower reservoir.

4.1 Test setups

4.1.1 Optical test setup

In order to access the film cross section with optical velocity and film thickness measurement techniques, a specifically designed optical test setup (see figures 4.1 and 4.2) was employed. The principal element of the test setup consists of an elongated cuboid quartz glass body that contains a cylindrical bore of 48.9 mm diameter (the glass body was machined by Aachener Quarz-Glas Tech-



Figure 4.2: Photograph of the optical test setup.

nologie Heinrich, using the material HSQ300 produced by Heraeus Quarzglas GmbH & Co. KG) creating an inner surface along which the liquid film develops (see figure 4.3). This configuration provides optical access to the film from all four faces of the glass body. Figure 4.2 depicts a photograph of the glass body, showing the arrangement of velocity and film thickness measuring devices. Wave fronts developing on the liquid film as it flows down the inside of the glass body are also discernible.

To enable the distortion-free imaging of the film cross section, the refractive indices of working liquid and quartz glass were matched. This was achieved by the careful choice of an appropriate working liquid. *Refractive Index Matching* (RIM) is commonly employed for optical measurements in fluid dynamics and a comprehensive review of optically matched systems, consisting of a glass material and a working liquid, can be found in Budwig (1994) and Albrecht *et al.* (2003). In general, two RIM approaches are possible. When the working liquid is a pure substance the adaptation of refractive indices can be achieved by reg-

4 Experimental

Solute	Mass fraction	T (°C)	ρ_l (kg/m ³)	σ (N/m)	ν_l (10 ⁻⁶ m ² /s)
DMSO	83.11%	25.2	1098.3	0.0484	2.85
Glycerol	90.98%	32.6	1230.7	0.0635	93.77

Table 4.1: Liquid properties of the two refractively matched aqueous solutions employed as working liquids in the optical test setup. All measurements were performed at RIM (Refractive Index Matching) temperature with liquid samples containing the tracer particles used for velocity measurements.

ulating the temperature. This is possible because the refractive index of most glass materials increases with temperature as opposed to most liquids which exhibit a refractive index decreasing with temperature. On the other hand, the use of mixtures consisting of two or more liquids enables RIM through the regulation of the mixture composition. In the context of this thesis these two approaches were combined. The employed working liquid consists of an aqueous solution of dimethylsulfoxide (DMSO) whereby the composition of the solution is chosen such that RIM approximately takes place at room temperature. The precise adaptation of the refractive index is then achieved through the regulation of the working temperature. Adomeit & Renz (2000) previously used pure DMSO for measurements in falling liquid films in a similar optically matched setup. However, they employed a cylindrical glass tube (see also Karimi & Kawaji (1998)) as opposed to the glass body shown in figures 4.1 and 4.3, creating the need for further optical measures to enable distortion free imaging[†].

In addition to the DMSO-water solution which was used to investigate the CSE phenomenon, an aqueous glycerol solution was employed. Using this working liquid (due to its large kinematic viscosity) conditions of smooth developed film flow could be achieved in the optical test setup at $Re \approx 1$. By measuring the crosswise velocity profile under these conditions, the LDV measurement technique was validated on the basis of the analytical solution for smooth

[†]Nonetheless, the work of Adomeit & Renz (2000) was the inspiration for the RIM concept developed in this thesis.

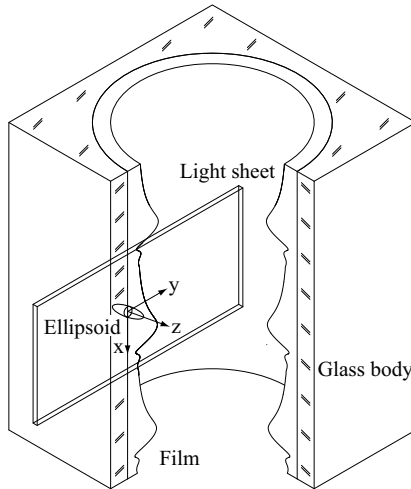


Figure 4.3: Enlarged view of the falling liquid film flowing down the inside of the glass body, showing the thin light sheet used for PIV and the LDV-ellipsoid (objects are individually scaled to illustrate geometrical conditions and size relations between different objects are incorrect).

developed film flow (see equation 2.13).

Table 4.1 displays the properties of the two working liquids as well as the respective solution compositions and the RIM temperature, which was determined with an in situ refraction experiment using the laser beam employed for LDV measurements. In addition, the refractive index of the quartz glass as well as that of the two working liquids was measured ex situ as a function of temperature with an Abbe refractometer (ATAGO CO., LTD., model DR-M2) at wavelengths $\lambda = 514.5$ nm and $\lambda = 488.0$ nm (laser wavelengths employed for LDV and PIV in this thesis are $\lambda = 514.5$ nm and $\lambda = 511.6$ nm respectively). Resulting data are plotted in figure 4.4, where the points of intersection of different curves (for working liquid and glass respectively) define RIM temperatures obtained from these ex situ measurements. Further,

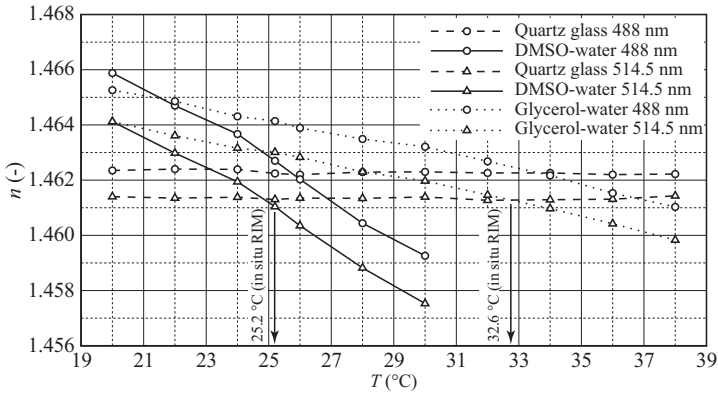


Figure 4.4: Temperature dependence of the refractive index for the quartz glass body and the two aqueous solutions specified in table 4.1 at wavelengths $\lambda = 488$ nm and $\lambda = 514.5$ nm.

RIM temperatures determined from the in situ experiments (as given in table 4.1) are also highlighted. A slight deviation between ex situ and in situ RIM temperatures is evident, which can be attributed to errors in the respective temperature and refractive index measurements. Meanwhile, the magnitude of this temperature deviation corresponds to only a very small deviation between refractive indices of approximately $3 \cdot 10^{-4}$ and is thus not significant.

The optical test setup displayed in figure 4.1 is integrated into a standard closed liquid circuit. The working liquid is pumped from the lower reservoir (item 7 in figure 4.1) to an upper buffer reservoir (not pictured in figure 4.1) situated above the optical test setup by a gear pump. This reservoir is equipped with an overflow allowing for the damping of flow rate oscillations and decouples the pressurized part of the circuit from the falling film section as the liquid leaving the reservoir is accelerated only by gravity. In order to regulate the working liquid temperature, a heat exchanger is integrated into the circuit between the lower and upper reservoirs. The liquid in the secondary circuit of the heat exchanger was thermally regulated with a laboratory thermostat, limiting tem-

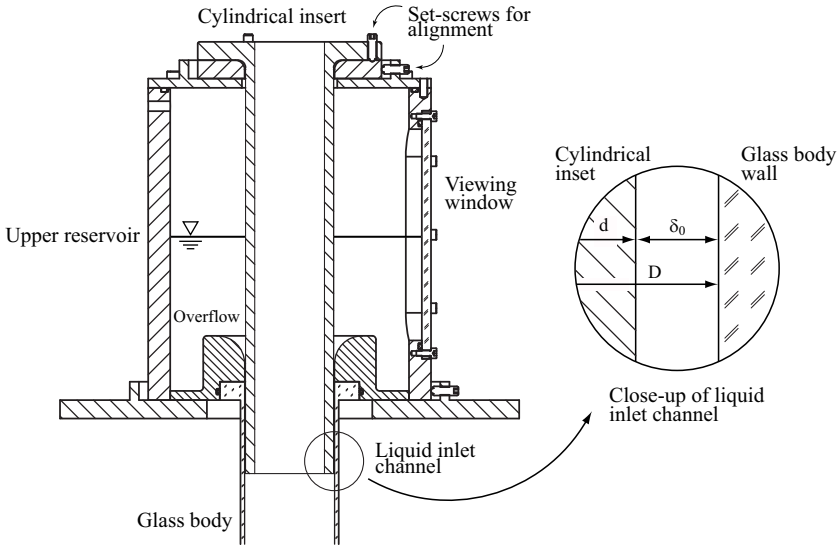


Figure 4.5: Close-up view of liquid inlet conditions in the optical test setup.

perature variations to $\pm 0.01\text{K}$. The volume flow rate of the working liquid was measured with a positive displacement flow meter between the heat exchanger and the upper reservoir. For all experiments, the ambient temperature of the laboratory was conditioned to $T = 25\text{ }^\circ\text{C}$. The flow of working liquid leaving the upper reservoir is divided and radially fed to the middle reservoir shown in figure 4.1 through two separate entry ports. Upon entering the middle reservoir, the liquid impinges on a cylindrical overflow further dissipatively damping flow oscillations. The inner surface of the overflow is rounded in order to avoid flow separation as the working liquid enters the glass body. The actual inlet for the falling liquid film consists of an annulus created between the glass body and a cylindrical insert (see figure 4.5). The thickness δ_0 of the annular inlet channel could be varied incrementally through the choice of the insert diameter. Further, the radial position of the insert as well as the orientation of its axis

Solute	Re	Ka	We	f (1/s)	δ_0 (μm)	Case
DMSO	8.6	509.5	20.3	16.0	250	5
DMSO	10.7	509.5	14.1	16.0	340	6
DMSO	12.9	509.5	10.3	16.0	340	7
DMSO	15.0	509.5	8.0	16.0	340	8
DMSO	10.7	509.5	14.1	24.0	340	-
DMSO	10.7	509.5	14.1	20.0	340	9
DMSO	10.7	509.5	14.1	18.0	340	10
Glycerol	1.1	5.6	6.9	-	1365	-

Table 4.2: Flow regimes investigated in the optical test setup. Numbers in the last column pertain to corresponding simulation cases (see table 3.1).

could be precisely set with micrometric set-screws (see figure 4.5). Using these set-screws, the cylindrical insert was oriented concentrically to the glass body bore before each measurement series in dry state. For this, the film thickness measurement technique described in the following subsection was employed to evaluate the annulus thickness variation in the axial direction. In a second step, the radial insert orientation was optimized by visually evaluating the azimuthal uniformity of wave fronts once the film flow had developed. Finally, before each measurement series, it was verified that the amplitude of measured film thickness time traces for the respective lowest frequency waves did not deviate by more than 3% from values predicted by the empirical correlation of Nosoko *et al.* (1996). During experiments, the temperature of the liquid in the middle reservoir was measured with a resistive thermometer (Pt 100) with an error of $\pm 0.1\text{K}$. The air volume above the liquid level developing in the middle reservoir was connected to an external loudspeaker-driven resonator, enabling the monochromatic excitation of surface waves in the film flow.

Table 4.2 summarizes the main[†] operating conditions under which measurements were performed in the optical test setup in the context of this thesis. Most of these conditions were also investigated numerically and, accordingly, the number in the last column of table 4.2 refers to the corresponding simula-

[†]Some measurements were performed under additional operating conditions but do not play a central role and are therefore not explicitly quantified here.



Figure 4.6: Photograph of 2-dimensional wave fronts in the optical test setup: $Re=12.9$, $Ka=509.5$, $f=24$ Hz.

tion case in table 3.1.

Figures 4.6 and 4.7 show photographs of the wavy liquid film flow in the optical setup for two representative cases listed in table 4.2. The first case is characterized by surface waves of short wavelength (caused by a relatively large excitation frequency of $f=24$ Hz). The corresponding photograph in figure 4.6 shows that surface waves travel at a constant distance from one another without interacting over a large portion of the glass body. The second case is characterized by surface waves of larger wavelength (caused by a smaller excitation frequency of $f=18$ Hz), developing precursory capillary waves, as is slightly discernible in the close-up photograph presented in figure 4.7. This picture also shows that wave fronts are 2-dimensional over the entire width of one of the glass body's faces. It must be stated that slight azimuthal modulations of wave fronts over the rest of the cylindrical bore's circumference were observed during experiments. However, for all investigated cases, wave fronts traveled as

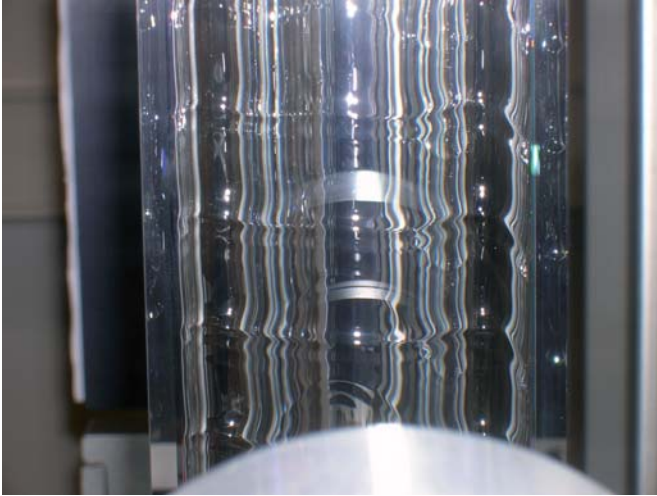


Figure 4.7: Photograph of 2-dimensional wave fronts in the optical test setup: $Re=12.9$, $Ka=509.5$, $f=18$ Hz.

simply connected rings well separated from one another and their amplitude at the measurement position was checked with the empirical correlation of Nosoko *et al.* (1996).

In order to gain a quantitative overview of wave kinematics realized in the optical test setup, figures 4.10 to 4.12 show film thickness time traces of 2-dimensional externally excited surface waves measured with the CCI technique (which will be introduced in section 4.2) over a range of Reynolds number and wave frequency values. Maximal and minimal wave frequency values delimit the range of flow regimes allowing the external imposition of 2-dimensional monochromatic surface waves (all cases of wavy film flow listed in table 4.2 lie within this range). Transgressing these extremal values led to the occurrence of an irregular wave pattern, resembling the one obtained without external forcing.

All measurements in the optical test setup were performed at a streamwise

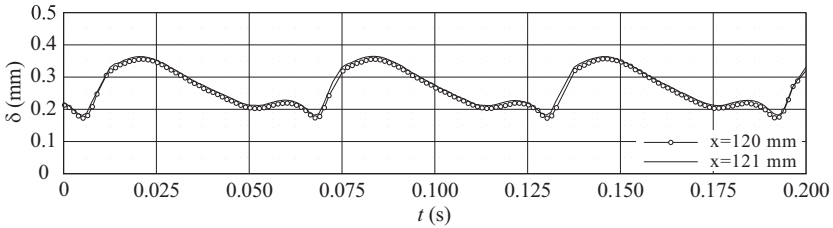


Figure 4.8: Film thickness time traces measured in the optical test setup at streamwise positions $x=120$ mm and $x=121$ mm (measured from the bottom of the cylindrical insert): $Re=6.8$, $Ka=509.5$, $f=16$ Hz.

position of $x = 120$ mm (measured from the bottom of the cylindrical insert). Preliminary experiments showed that, for all investigated flow conditions, surface waves were developed at that position. Experimental evidence to that extent is displayed in figure 4.8, where film thickness time traces at two different streamwise positions ($x=120$ mm and $x=121$ mm) are plotted[†] for the wavy regime with lowest wave growth rate. The latter is obtained at the smallest Reynolds number (i.e. $Re=6.8$) and wave frequency (i.e. $f=16$ Hz) value, as can be deduced from figure 4.9, which plots wave growth rate αc_i (see equation 2.33) against wave frequency for different Reynolds number values. Graphs were computed from the approximate solution of the Orr-Sommerfeld equation according to Anshus & Goren (1966) (see subsection 2.2.2 and figure 2.3 therein).

Film thickness time traces depicted in figures 4.10 to 4.12 cover the range of investigated flow conditions (see table 4.2). The figures show that both the Reynolds number and the excitation frequency significantly influence interface topology. At $Re = 15.0$ and $f = 16$ Hz (see figure 4.10(a)) for instance, the liquid-gas interface is characterized by large wave humps preceded by three capillary waves. As the frequency is increased to 22 Hz (see figure 4.10(b)) the amplitude of the large waves decreases while all but one of the capillary waves are suppressed. These effects are of course well established in the literature

[†]The two time traces were superimposed in this representation to facilitate comparison.

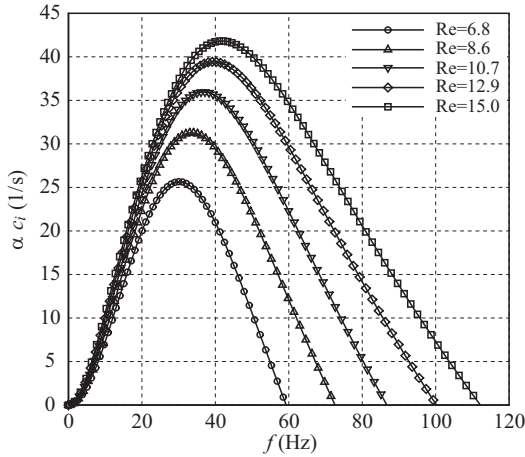


Figure 4.9: Growth rates αc_i (see equation 2.33) obtained from linear stability analysis, according to Anshus & Goren (1966) (see subsection 2.2.2), for wave regimes realized in the optical test setup: $Ka=509.5$.

(see Liu *et al.* (1993) and Nosoko *et al.* (1996)) and are due to the interaction of large waves as their separation decreases. The same frequency dependence as for $Re = 15.0$ can be observed for lower values of the Reynolds number (see figures 4.10(c) to 4.11(d) and 4.12), whereby, at high frequencies, the wave separation is so small that capillary waves are suppressed altogether (see figures 4.11(a), 4.11(d), 4.12(b) and 4.12(c)). This of course significantly affects the CSE phenomenon as will be established in section 5.4. The Reynolds number influence acts contrary to that of the frequency as can be deduced from figures 4.10(a), 4.10(c), 4.11(b) and 4.12(a). This is due to the fact that wave separation decreases with frequency yet increases with the Reynolds number (see e.g. Nosoko *et al.* (1996)). Another observation resulting from figures 4.10, 4.11 and 4.12 is that the minimal film thickness (observed in the capillary wave region) is scarcely influenced by the varied quantities.

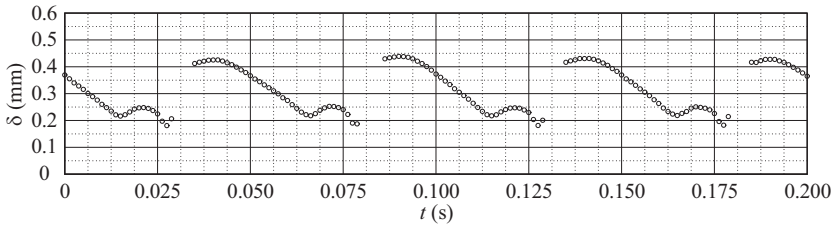
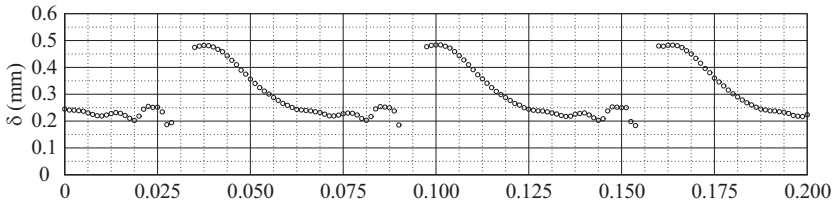
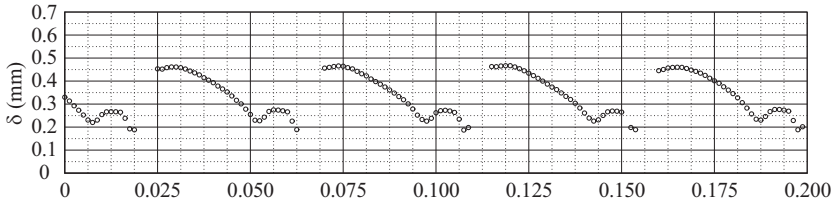
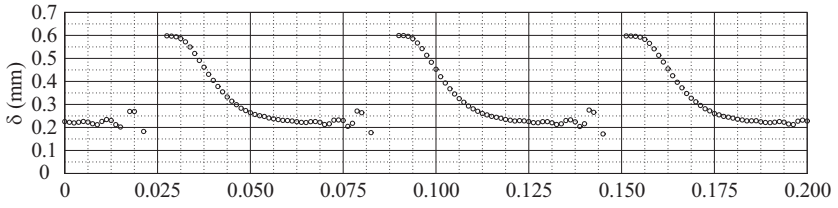
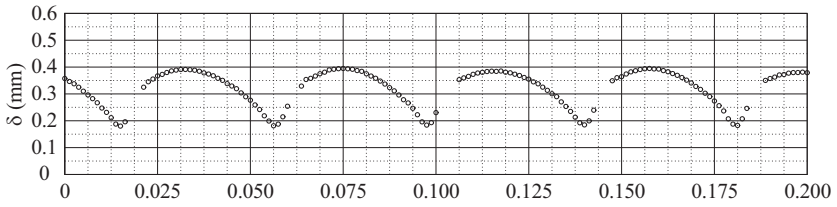
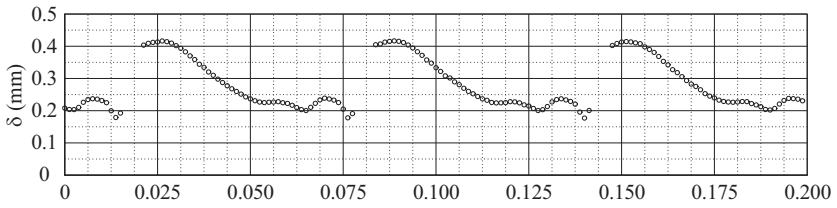


Figure 4.10: Film thickness time traces measured in the optical test setup in the region of developed waves ($x=120$ mm).

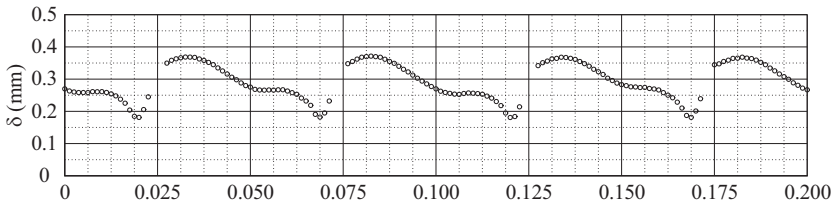
4 Experimental



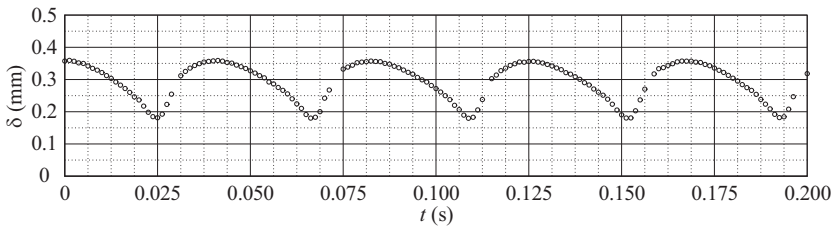
(a) $Re=10.7$, $f=24$ Hz



(b) $Re=8.6$, $f=16$ Hz



(c) $Re=8.6$, $f=20$ Hz



(d) $Re=8.6$, $f=24$ Hz

Figure 4.11: Film thickness time traces measured in the optical test setup in the region of developed waves ($x=120$ mm).

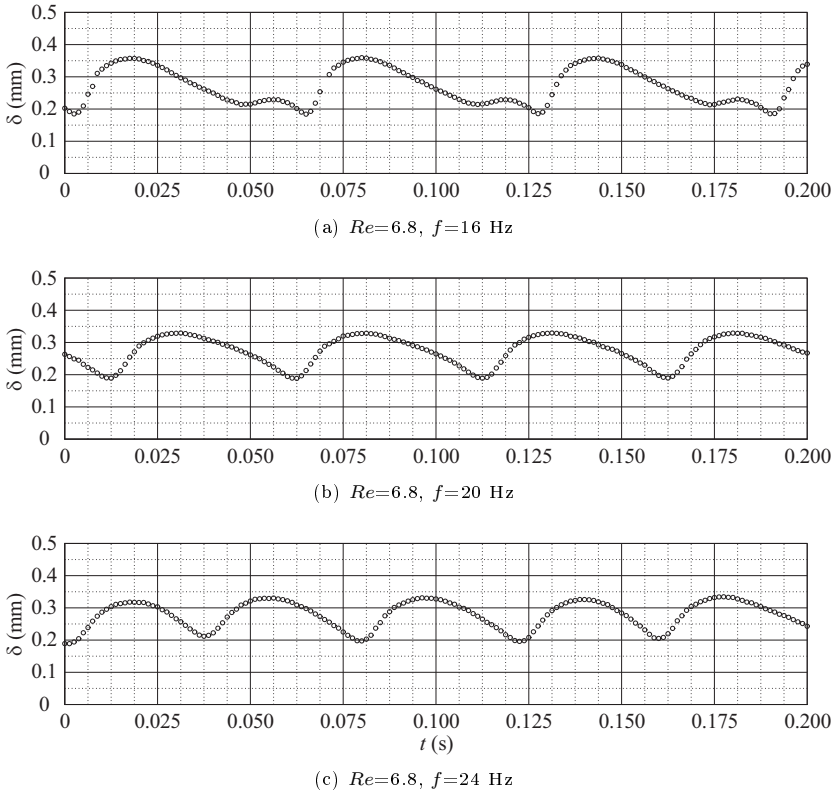


Figure 4.12: Film thickness time traces measured in the optical test setup in the developed region of the flow ($x=120$ mm).

4.1.2 Inclined test setup

Figures 4.13 and 4.14 display a sketch and a corresponding photograph of the inclined test setup. It consists of an acrylic glass plate, inclined at an angle φ to the gravitational acceleration vector, on which the liquid develops into a falling film at the exit of a rectangular inlet channel of width W and channel

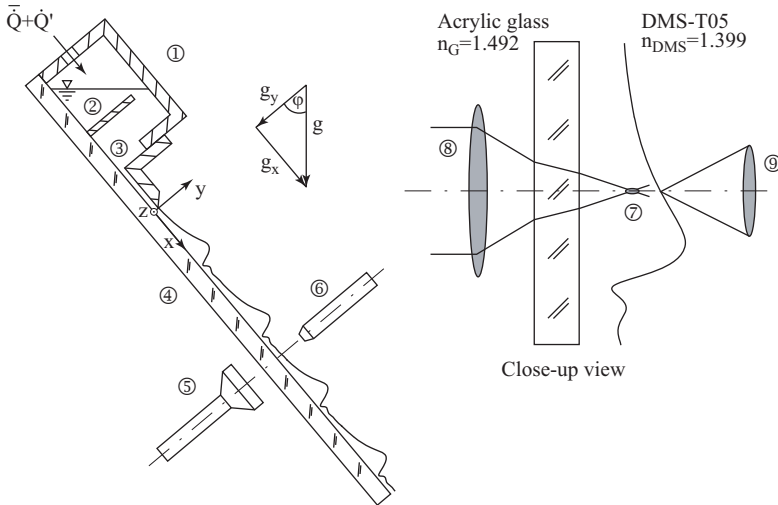


Figure 4.13: Sketch of the inclined test setup, including a close-up view of the measurement position. 1: Reservoir; 2: overflow; 3: inlet channel; 4: acrylic glass plate; 5: LDV-probe; 6: CCI-probe; 7: LDV-ellipsoid; 8: LDV front lens; 9: CCI front lens.

height δ_0 . The liquid is fed to a reservoir upstream of the inlet channel by a gear pump. A fluctuation \dot{Q}' of predefined frequency f and small amplitude is imposed on the mean feeding flow rate \bar{Q} by way of a pressure fluctuation generated with a loud speaker upstream of the reservoir (not pictured). To avoid direct perturbations at the inlet channel by the impinging liquid jet, entering the reservoir, an obstructing overflow is integrated. As working liquid, a *Dymethylsiloxane* (DMS) or *silicone oil* with the designation DMS-T05 (Gelest, Inc.) was employed. Two sets of experiments, using two different batches of the liquid (designated as batch 1 and batch 2) were performed. The working liquid was seeded with titanium dioxide particles acting as tracers for LDV measurements. The properties of the particle laden liquid (for both batches) were measured at the working temperature $T = 25^\circ\text{C}$ and are listed in table

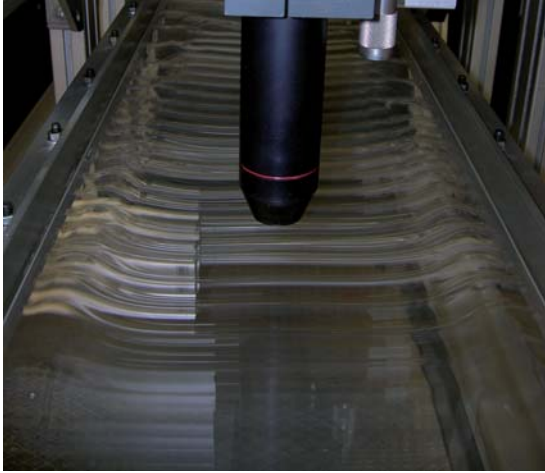


Figure 4.14: Photograph of wave fronts in the inclined test setup: $Re=15.6$, $Ka=133.6$, $f=15.0$ Hz.

4.3.

Table 4.4 quantifies experimental conditions for film flow regimes realized in the inclined test setup. Only those regimes, which are of primary concern in the context of this thesis are specified here (conditions for auxiliary experiments will be specified where necessary). The first column of table 4.4 specifies the batch of DMS-T05 employed for the respective measurements, while the number listed in the last column refers to the corresponding simulation case specified in table 3.1. For all experiments performed in the inclined test setup, the inlet channel height was set to the same value i.e. $\delta_0=635$ μm , as the precise adjustment of the knife bounding the inlet channel on the upper side was extremely difficult. To a practically achievable extent, this value corresponds to the primary film thickness $\delta_{Nu}=646$ of case 1 and was chosen as a result of the different priorities of cases 1-4. As mentioned in subsection 3.2.5, case 1 forms the basis for the investigation of the streamwise development of the

4 Experimental

Batch	ρ_1 (kg/m ³)	σ (N/m)	ν_1 (10 ⁻⁶ m ² /s)	k_1 (W/mK)	c_1 (J/kgK)
1	909.3	0.022	5.70	0.12	1540
2	908.5	0.0204	5.21	-	-

Table 4.3: Liquid properties for the two batches of DMS-T05 (Gelest, Inc.) used in the inclined test setup. All properties (except k_1 and c_1 , which were obtained from the manufacturer) were measured at $T=25.0$ °C.

batch	Re	Ka	We	Fr	φ (deg)	f (1/s)	δ_0 (μm)	Case
1	15.6	133.6	2.0	1.9	35	15.0	635	1
2	21.4	139.8	1.2	2.2	35	24.0	635	2
2	21.4	139.8	1.2	2.2	35	17.7	635	3
2	21.4	139.8	1.2	2.2	35	11.3	635	4

Table 4.4: Flow regimes investigated in the inclined test setup. Numbers in the last column pertain to corresponding simulation cases (see table 3.1).

capillary flow separation, whereas for cases 2-4 only the developed state of the phenomenon is of interest. Consequently, as the inlet channel height has no influence on developed wave topology, δ_0 was chosen in accordance with case 1. Meanwhile, Alekseenko *et al.* (1994) showed for smooth film flow that, for a given inlet channel height, the film thickness tends to δ_{Nu} in streamwise direction, which also applies to the wavy flow as far as the mean film thickness is concerned for laminar regimes dominated by viscous and capillary forces (see e.g. Lel *et al.* (2005)). Consequently, by setting $\delta_0 = \delta_{Nu}$, an unnecessary streamwise change in the mean film thickness is avoided, whereby the wave development process can be isolated to some extent. However, it must be considered that, due to the discontinuous change in boundary conditions at the inlet to the two-phase region (not considered by Alekseenko *et al.* (1994)), a certain streamwise development of the mean flow takes place nonetheless.

The film flow regimes realized in the inclined test setup displayed monochromatic 2-dimensional solitary waves preceded by small capillary waves, which developed from the forced inlet disturbance of frequency f imposed by a loud

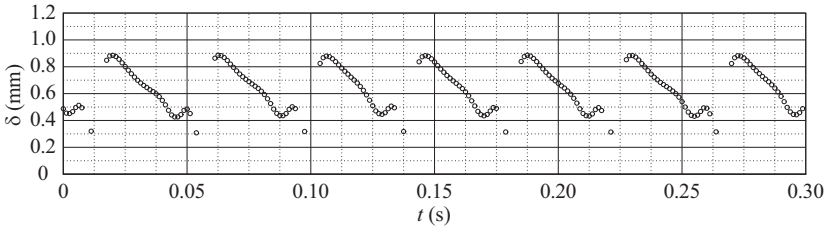
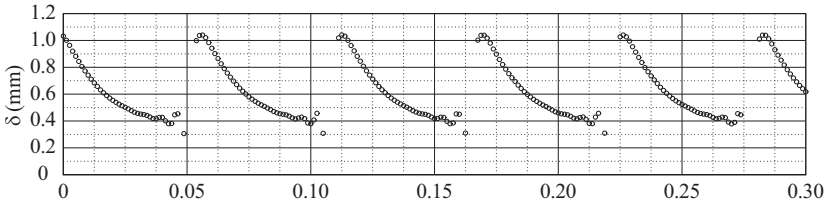
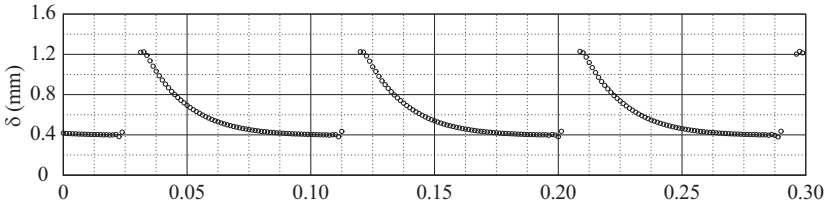
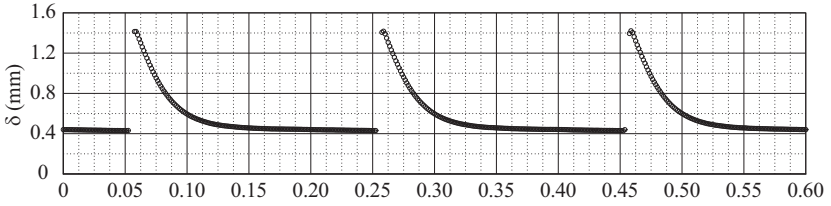


Figure 4.15: Film thickness time traces measured in the inclined test setup in the region of developed waves ($x=215$ mm) using batch 2 of DMS-T05: $Ka=139.8$.

speaker (Alekseenko *et al.* (1994) introduced the term *stationary two dimensional waves* to designate the regime in question). These 2-dimensional waves attained a constant amplitude in the top part of the test setup (see figure 3.19(b)) before secondary instability led to their break-up into 3 dimensional structures. Figure 4.14 displays a photograph of 2-dimensional surface waves in the top part of the inclined test setup for flow conditions corresponding to the first case in table 4.4 (i.e. simulation case 1). From this picture, it can be discerned that the side-walls of the test section caused a localized distortion of wave fronts, which, however, remained confined to a small insignificant outer region over the entire development process of waves. Similar observations were also reported by Nosoko *et al.* (1996).

Figure 4.15 illustrates film thickness time traces measured in the inclined test setup for a range of representative (in terms of the investigations in this thesis) operating conditions, using batch 2 of DMS-T05. Subfigures 4.15(b) to 4.15(d) depict time traces for the last three cases in table 4.4 (i.e. simulation cases 2 to 4), while the wave frequency for subfigure 4.15(a) marks the lower bound for the imposition of externally forced monochromatic waves (incidentally, subfigure 4.15(d) represents the corresponding upper frequency bound). Figure 4.15 thus shows the effect of excitation frequency on wave kinematics, confirming observations in the vertically falling film (see figures 4.10 and 4.11). Indeed, a decrease in frequency is shown to increase wave amplitude and to cause long (in time) stretches of unperturbed residual layer. At the same time, capillary waves increase in number and decrease in wavelength (compare figures 4.15(c) and 4.15(d)). For the two lowest frequencies (figures 4.15(a) and 4.15(b)) measurement data only *indicate* the presence of capillary waves, which is due to an insufficient temporal resolution of the measurement technique. Measurements were performed at a streamwise position of $x=215$ mm (measured from the bottom of the knife, bounding the inlet channel), which lies in the developed region of the flow for all cases. Experimental proof of this is illustrated in figures 4.16 and 4.17, which show the streamwise evolution of film thickness time traces for cases corresponding to the two extremal frequencies.

In addition, these plots show some interesting features. For the lowest fre-

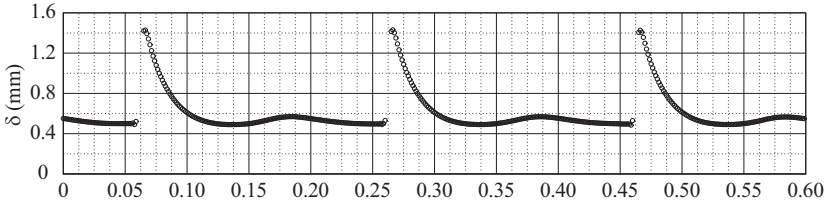
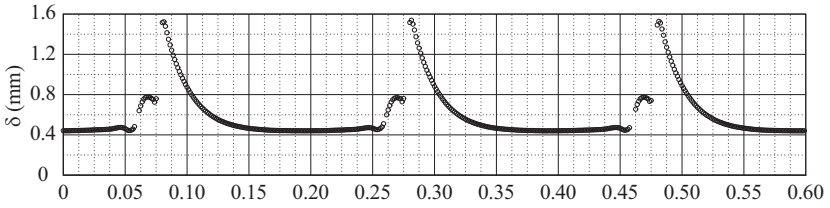
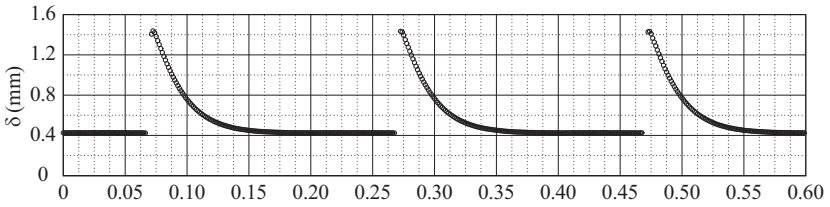
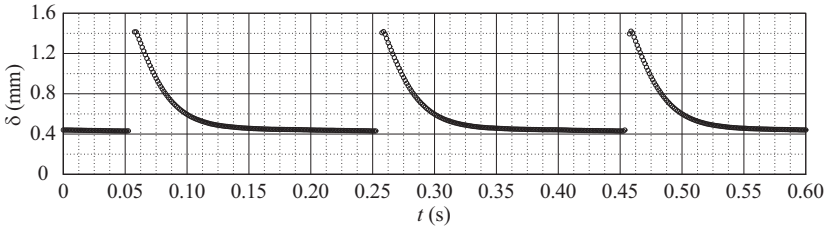
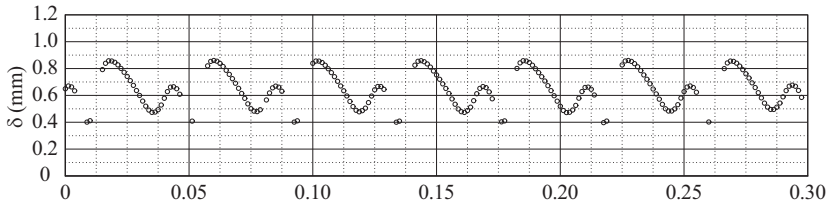
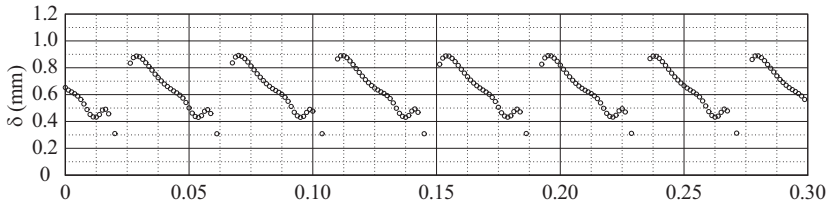
(a) $f=5.0$ Hz, $x=95$ mm(b) $f=5.0$ Hz, $x=135$ mm(c) $f=5.0$ Hz, $x=175$ mm(d) $f=5.0$ Hz, $x=215$ mm

Figure 4.16: Streamwise evolution of film thickness time traces measured in the inclined test setup: $Re=21.4$, $Ka=139.8$, $f=5.0$ Hz.

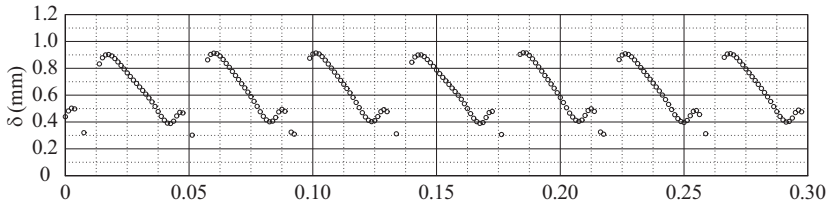
4 Experimental



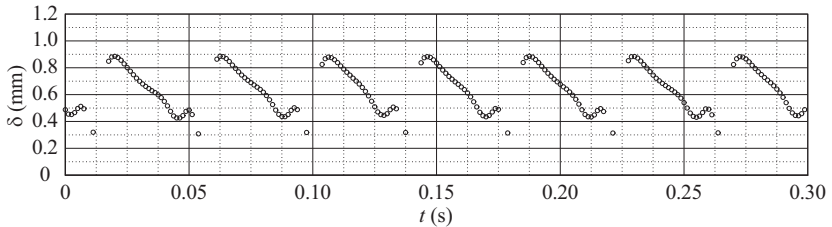
(a) $f=24.0$ Hz, $x=95$ mm



(b) $f=24.0$ Hz, $x=135$ mm



(c) $f=24.0$ Hz, $x=175$ mm



(d) $f=24.0$ Hz, $x=215$ mm

Figure 4.17: Streamwise evolution of film thickness time traces measured in the inclined test setup: $Re=21.4$, $Ka=139.8$, $f=24.0$ Hz.

quency, $f=5$ Hz, a small wave hump is shown to appear on the residual layer between two large waves at $x=95$ mm. Further downstream ($x=135$ mm), this hump has been caught-up by the succeeding large wave and both are at the point of merging, causing the maximal film thickness to increase. At the most downstream positions $x=175$ mm and $x=215$ mm, the additional wave hump has disappeared and large waves have attained a constant maximal film thickness. For the highest frequency, $f=24$ Hz, time series plots in figure 4.17 show the streamwise evolution of a capillary wave, from a relatively large subsidiary wave occurring between two large waves (see figure 4.17(a)). Further, a slight change in the topology of the wave back of large waves is discernible between positions $x=135$ mm and $x=215$ mm in the form of small amplitude parasitic waves. At $x=135$ mm wave backs of large waves display one such parasitic wave, which has disappeared at $x=175$ mm, before reappearing further downstream at $x=215$ mm. This streamwise oscillation of wave topology is a result of the secondary instability evoked in section 2.2.1.

4.2 Measurement techniques

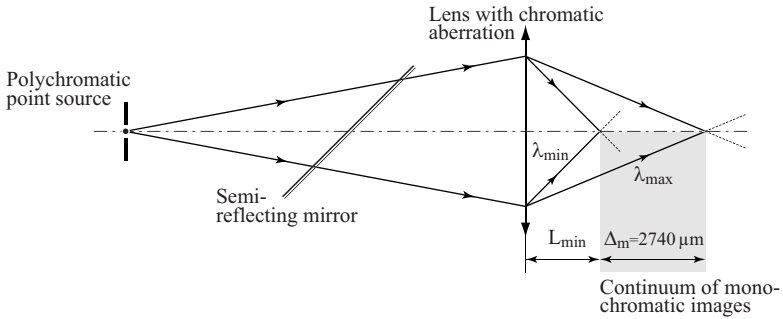
Three measurement techniques were employed in this thesis, namely Laser Doppler Velocimetry (LDV) and Particle Image Velocimetry (PIV) for velocity measurements and a distance measuring technique based on Confocal Chromatic Imaging (CCI) for film thickness measurements. The principles of these measurement techniques are well established in the literature (see e.g. Albrecht *et al.* (2003), Raffel *et al.* (2007) and Cohen-Sabban *et al.* (2001) respectively) and attention in the following subsections shall be focused merely on their specific application to the optical test setup pictured in figures 4.1 and 4.2 and the inclined test setup pictured in figures 4.13 and 4.14.

4.2.1 Confocal Chromatic film thickness measurement

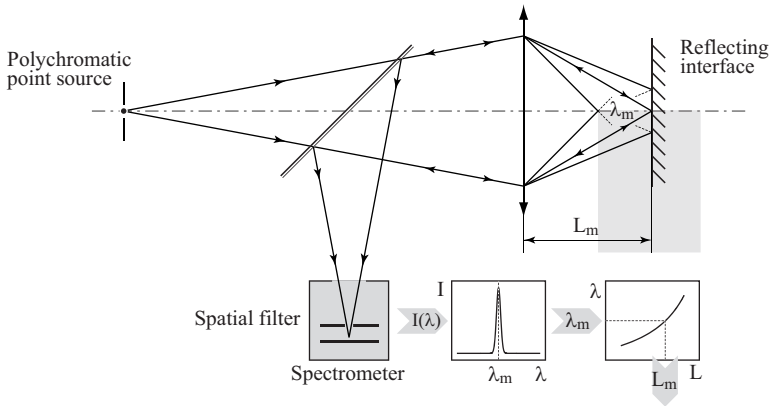
In terms of film thickness measurements in falling liquid films, an excellent review of different methods employed over the years was compiled recently by

Clark (2002). In this thesis, a distance measuring technique based on Confocal Chromatic Imaging and developed by Cohen-Sabban *et al.* (2001) (originally for surface sensing) was applied for temporally resolved film thickness measurements, basically by measuring both the distance to the liquid-gas interface and the bounding wall of the film. Using the same measurement device but a different approach to obtaining film thickness data, Lel *et al.* (2004) previously performed measurements in falling liquid films and compared results to simultaneous film thickness measurements obtained with the Laser Induced Fluorescence technique. The authors showed good agreement between data obtained from the two techniques and discussed their respective practical advantages.

Figure 4.18 depicts two sketches, illustrating the measurement principle of the CCI technique. According to subfigure 4.18(a), light from a polychromatic point source passes through a semi-reflecting mirror before being focused by a biconvex front lens. Due to the lens' chromatic aberration, light beams of different wavelength are focused onto different points on the optical axis, creating a continuum of monochromatic images of the point source. If, as pictured in subfigure 4.18(b), a reflecting interface is positioned in this continuum of depth Δ_m , light of wavelengths within a selective interval (the size of which is determined by the resolution of the technique) is reflected toward the front lens, which would image the interfacial reflection point onto the point source. However, due to the presence of a semi-reflecting mirror, reflected light is diverted into the signal detection unit of the system. There, the spectral intensity distribution of incoming light is measured with a spectrometer in discretized (in time and wavelength) form. Subsequently, the wavelength λ_m of maximal intensity, which is directly linked to the distance L_m , is determined from the distribution. The measurement result L_m is finally obtained from λ_m with a calibration curve (see figure 4.19) measured by the manufacturer. In terms of hardware, the measurement system employed for this thesis (STIL SA, model CHR 450) consists of two components. A controller unit, which comprises the light source, semi-reflecting mirror, spectrometer and data processing hardware, and an optical probe (see figures 4.1 and 4.7), which holds the front lens.



(a) Confocal chromatic imaging principle.



(b) Signal generation by a reflecting interface.

Figure 4.18: Measurement principle of the Confocal Chromatic Imaging (CCI) technique employed for film thickness measurements (sketch adapted from Cohen-Sabban *et al.* (2001)).

Both parts of the system are connected with an optical fiber. Specifications of the measurement system as it was employed for this thesis are quantified in table 4.5. The repetition frequency (which is directly coupled to the exposure time of the spectrometer) for measurements in falling liquid films was limited

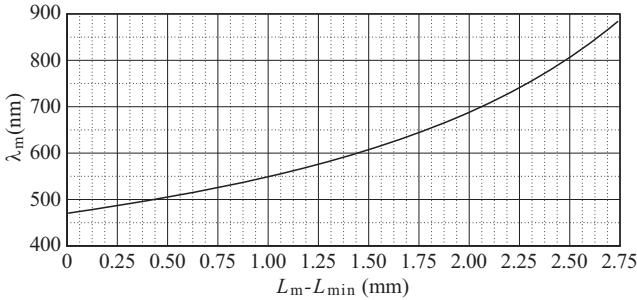


Figure 4.19: Calibration relation for the CCI distance measurement (see figure 4.18): wavelength versus measurement distance.

Working distance L_{\min}	Measurement interval Δ_m	Repetition frequency	Distance measurement error	Transverse resolution
1.6 mm	2740 μm	800 Hz	1 μm	10 μm

Table 4.5: Specifications of the CCI measurement system (STIL SA, model CHR 450) employed for film thickness measurements.

to 800 Hz by the signal strength obtained from the liquid-gas interface and the transversal resolution of the distance measurement is determined by the size of the point source and the imaging characteristics of the front lens. As can be deduced from film thickness time traces in figures 4.10 to 4.12 and 4.15, both the temporal and streamwise spatial resolution of the CCI technique are sufficient in the context of this thesis.

The CCI measurement device allows for simultaneous processing of signals from two separate interfaces positioned within the measurement interval. Consequently, by providing the refractive index of the material between the interfaces, its thickness can be measured. However, due to the weakness of the signal emanating from the bounding wall of the liquid film both in the optical (where the signal vanishes due to RIM) and inclined test setup, a direct film thickness measurement could not be realized. In this thesis, only the sig-

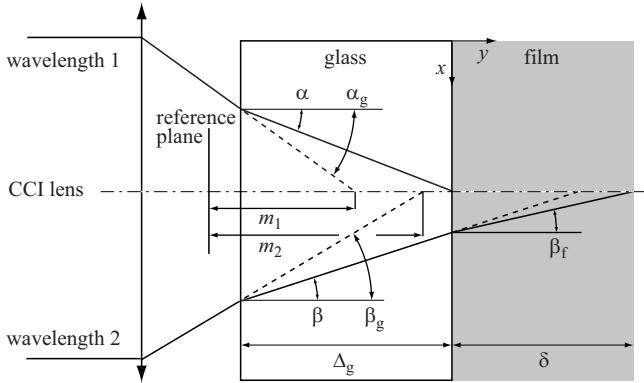


Figure 4.20: Application of the CCI film thickness measuring technique to the optical test setup. Solid lines (actual beam paths) and dashed lines (beam paths in the absence of refraction) show light beams reflected by the glass wall (wavelength 1) and the free surface of the film (wavelength 2). Measured quantities: m_1 , m_2 .

nal from the liquid-gas interface was measured instantaneously, whereas the reference signal from the bounding wall was measured and stored before each measurement series in dry state. Preliminary measurements in both test setups showed that the reference signal did not change (to an extent resolvable by the CCI technique) over the time span of a measurement series. Depending on optical access to the liquid-gas interface (which was different for the two test setups), different post processing approaches were necessary to obtain film thickness data from the two signals. These will be presented next.

In the optical test setup, the liquid-gas interface was accessed through the glass body wall and liquid film as pictured in figure 4.20. Applying geometrical optics, the film thickness δ can be expressed in terms of the distances m_1 and m_2 associated with the signals generated by the liquid-gas interface (instantaneously) and the wall (a priori) respectively:

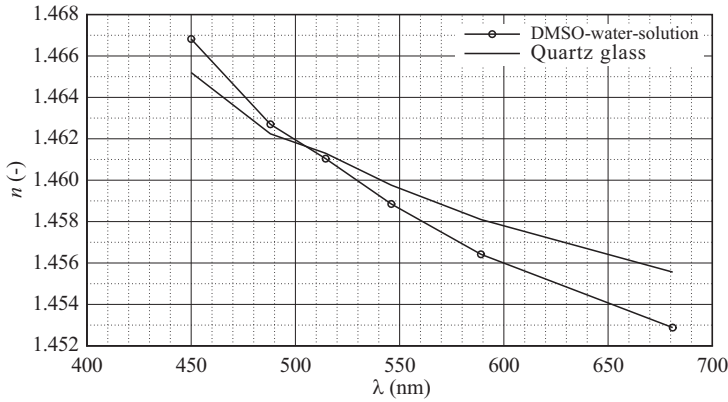


Figure 4.21: Spectral dependence of the refractive index for quartz glass body and DMSO-water solution in the visible range at $T=25.2$ °C.

$$\delta = \left[m_2 - m_1 + \Delta_g \left(\frac{1}{n_g^1} \frac{\cos \alpha_g}{\cos \alpha} - \frac{1}{n_g^2} \frac{\cos \beta_g}{\cos \alpha} \right) \right] n_f^2 \frac{\cos \beta_f}{\cos \beta} \quad (4.1)$$

For the considered conditions, all angles are negligibly small so that the film thickness is given in good approximation by:

$$\delta \approx \left[m_2 - m_1 + \Delta_g \left(\frac{1}{n_g^1} - \frac{1}{n_g^2} \right) \right] n_f^2, \quad (4.2)$$

where the numerical indices refer to the wavelengths associated with the respective signals. The glass thickness Δ_g was also measured before each experiment series in dry state whereas the spectral distribution of the refractive indices of quartz glass and working liquid were measured at RIM temperature using an Abbe refractometer (see figure 4.21). Evaluation of the total differential of δ according to equation 4.2 (with measurement errors of $1 \mu\text{m}$ for m_1 and m_2 and 0.0002 for the refractive indices) yields an absolute film thickness measurement error of $4 \mu\text{m}$. In this configuration, film thickness measurements were performed with an acquisition frequency of 800 Hz. During LDV experiments (see subsection 4.2.2) the film thickness was measured simultaneously (and at

the same circumferential position as the LDV) to enable correlation of film thickness and velocity data. However, a small streamwise offset of about 2 mm was inevitable to avoid disturbance of the film thickness measurements by the LDV laser beams.

As can be seen in figures 4.10 and 4.11 the film thickness measurements do not resolve wave fronts equally well for all cases (see for instance figures 4.10(a) to 4.10(d)). This is due to a combination of effects linked to the large wave front inclination angle for the cases in question. On the one hand, the intensity of light reflected back into the CCI emitter-receiver decreases with increasing steepness of the wave front due to elementary geometrical optics. On the other hand, as the wave fronts grow steeper their transit time in x -direction decreases, thus reducing the number of measurement points captured by the measurement device (operating at a constant acquisition frequency). In addition, steeper wave fronts coincide with larger values of the wave celerity also causing the transition time to decrease. It is also discernible from the film thickness time traces that capillary wave fronts of comparable steepness are resolved better than large wave fronts. This results from the fact that free surface signal intensity is larger for capillary wave fronts since the distance to the CCI emitter-receiver is smaller compared to large wave fronts.

In the inclined test setup, the liquid-gas interface was accessed from the gas-side of the film flow (see figure 4.13). The liquid film thickness was obtained by subtracting the instantaneously measured distance to the interface from the reference distance to the inclined wall, which was measured a priori in dry state. For this case, the film thickness measurement error is $2\ \mu\text{m}$. For simultaneous film thickness (using the CCI technique) and velocity (using the LDV technique) measurements, the CCI-probe was positioned with its optical axis parallel to that of the LDV probe (see figure 4.13) at the same streamwise position. However, the probes were distanced in spanwise direction by about 5 mm to avoid damage to the CCI device by the LDV laser beams.

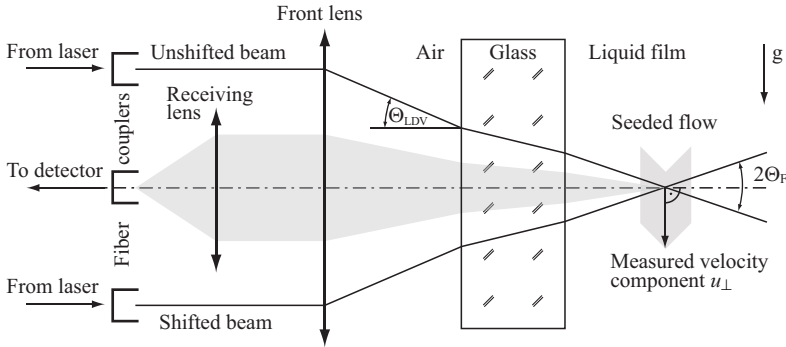


Figure 4.22: Sketch of the integrated fiber-based emitting and receiving optics (Dantec Dynamics A/S, model FiberFlow) employed for LDV measurements, showing optical paths to and from the measurement position in the liquid film.

4.2.2 Laser Doppler Velocimetry

As mentioned in subsection 2.3.1, first velocity measurements in falling liquid films were performed by Wilke (1962), using an intrusive technique. Since then, an array of optical techniques was employed, using diluted tracer substances or tracer particles. For instance, Wilkes & Nedderman (1962), Ho & Hummel (1970) and Karimi & Kawaji (1998) performed velocity measurements with the Laser Induced Fluorescence (LIF) technique. More recently, velocimetry techniques widely used in single-phase flow, such as Laser Doppler Velocimetry (LDV) and Particle Image Velocimetry (PIV) have been applied to measurements in falling liquid films.

LDV measurements in falling liquid films have been performed by Mudawar & El-Masri (1986), Paras & Karabelas (1992), Mudawar & Houpt (1993*a*), Mudawar & Houpt (1993*b*), Wierschem *et al.* (2002) and Leefken *et al.* (2004). In these investigations the film flow was either accessed through the interface (creating the need to reconstruct velocity data), a plane bounding wall (causing resolution problems) or, in the case of the measurements of Professor Mudawar

Laser wave-length, λ_{LDV}	Beam separation	Front lens focal length	Intersection angle, Θ_{LDV}	Beam diameter
514.5 nm	38 mm	80 mm	13.36°	2.2 mm

Table 4.6: Optical quantities specifying the fiber-optic LDV-probe pictured in figure 4.22.

and coworkers, through the side-walls of a specifically designed sampling channel (which, conceivably, alters the characteristic of the film flow).

In this thesis, LDV was employed for instantaneous point measurements of the liquid phase streamwise velocity in the optical test setup for film flow regimes listed in table 4.2. Additionally, one LDV measurement was performed in the inclined test setup and corresponding data (see figures 4.31 and 4.32) are presented only in order to demonstrate the resolution improvement achieved in the optical test setup. The principles of LDV are well established in experimental fluid mechanics and are therefore not recapitulated here (the reader is referred to the books of Durst *et al.* (1976) and Albrecht *et al.* (2003)). Instead, the technique's specific application to test setups employed in this thesis will be detailed.

Figure 4.22 sketches the general situation (encountered in both test setups) in terms of optical access to the liquid film for the employed LDV optics. The latter are fully integrated into a fiber-based LDV-probe (Dantec Dynamics A/S, model FiberFlow), which acts both as emitter and receiver. On the emitting side, two laser beams of wavelength (in air) $\lambda_{LDV}=514.5$ nm, Gaussian beam diameter 2.2 mm and beam separation 38 mm are focused by a front lens with a focal length of 80 mm (see table 4.6). These beams are obtained from a single Argon-Ion laser (Spectra-Physics) beam, which is split up and coupled into two separate optical fibers connected to the LDV-probe (see figure 4.22). Because the film flow is accessed through a glass wall, the beams are refracted at the gas-glass and glass-liquid interfaces (the second refraction does not occur in the optical test setup due to RIM) respectively, before intersecting at the measurement position. The depicted configuration enables measurement of the

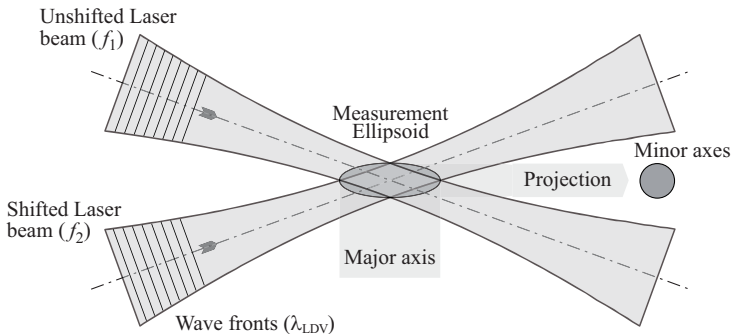


Figure 4.23: Close-up schematic view of the intersection volume of LDV laser beams, illustrating the measurement ellipsoid.

velocity component u_{\perp} normal to the optical axis, lying in the same plane as the LDV beams. A close-up sketch of the measurement region is provided in figure 4.23. It shows the intersection volume of the two Gaussian LDV beams, which has the shape of an ellipsoid[†]. The ellipsoid's major axis is considerably longer than the two minor axes, themselves of equal length. The actual dimensions of the ellipsoid depend on the beams' intensity distributions and their intersection angle in the liquid, which itself depends on the refractive indices of glass material and working liquid (see table 4.7).

It follows from figure 4.23 that it is the measurement ellipsoid's orientation (and principally that of its major axis) relative to the velocity field's gradient that determines the spatial resolution of the LDV measurement. In this respect, conditions in the two test setups were fundamentally different, as will be elaborated next. In falling liquid films with 2-dimensional surface waves, only velocity variations in the streamwise and crosswise directions take place. Consequently, in order to maximize spatial resolution, the measurement ellipsoid should be oriented with its major axis pointing in spanwise direction. This is

[†]Note that the spatial extent of the intersection volume is defined by the local intensity (i.e. the sum of the two laser intensities) in relation to the maximal intensity and not the geometrical intersection of the two pictured Gaussian beams.

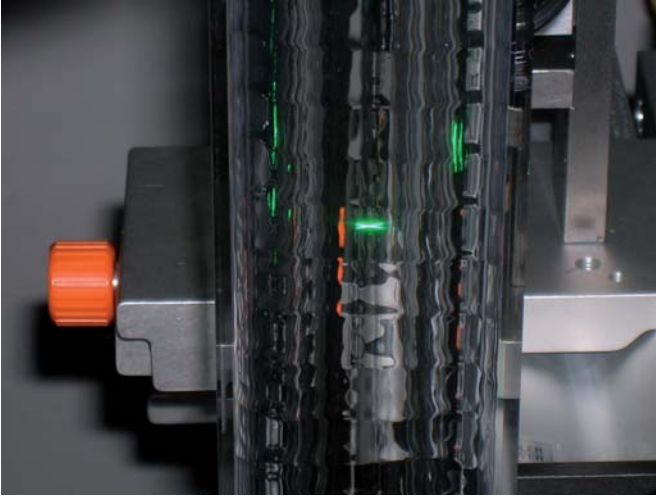


Figure 4.24: Photograph of intersecting LDV laser beams in the optical test setup.

not possible in the inclined test setup, where optical access is obtained through the plane acrylic glass wall, bounding the film. In this case, the ellipsoid's major axis is necessarily oriented in crosswise direction (see figure 4.13), which is the most inconvenient scenario. In the optical test setup however, due to the glass body's geometry, the liquid film can be optically accessed from the spanwise direction (see photograph in figure 4.24), which leads to a spanwise orientation of the ellipsoid's major axis (see figure 4.3). The streamwise resolution of the measurement is optimal in both orientations.

Tracer particles dispersed in the liquid film scatter light of both laser beams as they pass through the ellipsoid. This light is collected and re-collimated by the front lens of the LDV-probe before being focused by a receiving lens onto an optical output fiber (see figure 4.22). In this back-scattering mode the LDV technique yields a large signal intensity, which resulted in data rates of up to 3000 Hz for the experiments performed in this thesis compared to

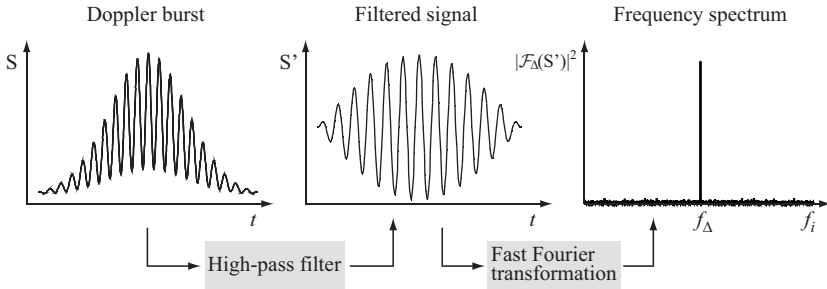


Figure 4.25: Signal processing operations performed by the Burst Spectrum Analyzer.

wave frequencies of the order of 10 Hz. The optical signal is transduced to an electrical signal with a photomultiplier (not pictured). With this, the intensity oscillation frequency f_{Δ} of light scattered by a particle, moving through the interference pattern within the ellipsoid, is measured. In good approximation, f_{Δ} is related to the velocity component u_{\perp} as follows:

$$f_{\Delta} = (f_1 - f_2) + 2 \sin(\Theta_{\text{LDV}}) \lambda_{\text{LDV}} u_{\perp}, \quad (4.3)$$

where $2\Theta_{\text{LDV}}$ is the intersection angle of the unrefracted LDV beams (see figure 4.22). Further, f_1 and f_2 designate the light frequency of the upper and lower LDV beam respectively (see figure 4.23). These are not equal, as the lower beam's frequency is shifted by 40 MHz below that of the upper beam ($f_2 = f_1 - 40 \text{ MHz}$), using a Bragg Cell (not pictured in figure 4.22). This frequency shift is negligibly small compared to the light frequencies f_1 and f_2 so that it does not measurably alter the wavelength of the shifted beam. However, it significantly alters the measurement relation 4.3 in the sense that negative values of u_{\perp} are now detectable[†]. For velocity measurements in the capillary wave region of falling liquid films, which is characterized by flow reversal, this property is essential. Further, it can be discerned from equation 4.3 that f_{Δ} is

[†]The measured quantity f_{Δ} is always larger than zero.

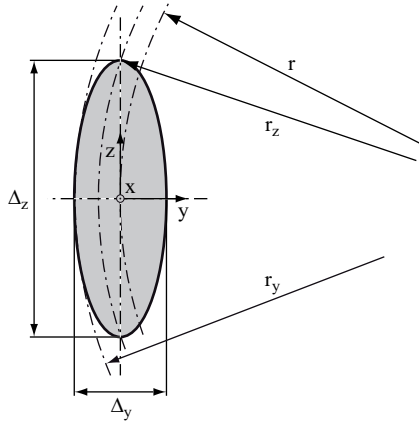


Figure 4.26: Sketch of the LDV measurement ellipsoid (in the optical test setup) with Cartesian and radial coordinates. The origin of the radial coordinate is situated on the axis of the glass body bore and the dimensions of the ellipsoid are $\Delta_x = \Delta_y = 24 \mu\text{m}$ and $\Delta_z = 151 \mu\text{m}$ respectively.

independent of the optical properties of the materials through which the LDV beams pass.

In order to detect the frequency f_Δ , a series of processing operations are performed on the signal obtained from the photomultiplier. These operations are executed online (i.e. with a repetition rate of up to 3000 Hz in the case of measurements performed in this thesis) by hardware components integrated in a so called *Burst Spectrum Analyzer* (BSA). In the context of this thesis, a BSA purchased from Dantec Dynamics A/S (model P80) was employed. Figure 4.25 illustrates the two main processing steps. The leftmost figure shows a typical signal *Doppler burst* obtained from a single particle moving through the measurement ellipsoid. It exhibits a low frequency modulation caused by the Gaussian intensity distribution of the two LDV beams, which is omitted by a high-pass filter in a preprocessing step. In the second step, a *Fast Fourier*

Test setup	n_G	n_F	Θ_F ($^\circ$)	Δ_x (μm)	Δ_y (μm)	Δ_z (μm)
Optical	1.462	1.462	9.09	24.12	23.82	150.80
Inclined	1.492	1.399	9.51	24.00	144.20	23.82

Table 4.7: Dimensions of the LDV-ellipsoid (see figure 4.23) in the liquid film for the optical (figures 4.3 and 4.24) and inclined (figure 4.13) test setup (G and F refer to glass material and film liquid respectively).

Transformation is performed on the filtered signal, yielding the frequency f_Δ . To complete the specification of the LDV technique as it was implemented for experiments in this thesis, two data processing validation criteria need to be quantified. These criteria fix a threshold for the validation or falsification of Doppler bursts recorded by the BSA. The first of these prescribes a lower limit for the signal to noise ratio of the burst and was set to $10^{0.5}$. The second prescribes a lower limit for the ratio between the powers of the two strongest frequencies of the burst's frequency power spectrum and was set to 16.

Following this qualitative description of the employed LDV methodology, a detailed quantitative account of LDV measurement conditions realized in the optical test setup is provided next. The subsection is concluded with a brief description of LDV measurement conditions realized in the inclined test setup with the goal of documenting and explaining the substantial spatial resolution improvement obtained in the optical test setup.

In the optical test setup (see figure 4.3), the size of the measurement ellipsoid in x- and y-direction was $\Delta_x = \Delta_y = 24 \mu\text{m}$ as opposed to a size of $\Delta_z = 151 \mu\text{m}$ in z-direction (see table 4.7). By way of comparison, the minimal film thickness (which is associated with the capillary wave region) for regimes investigated in the optical test setup is of the order of $200 \mu\text{m}$ (see figures 4.10 to 4.12). The extent of the ellipsoid in z-direction does not limit the spatial resolution of the measurement, as changes of the velocity in z-direction are negligible in the considered case of 2-dimensional waves. Variation over the z-axis of the ellipsoid takes place solely due to the fact, that the film flow is cylindrical and not Cartesian (see figure 4.26). It shall be shown here, on the basis of a smooth developed cylindrical film flow, that this effect is negligible.

For this case, the radial distribution of the streamwise velocity component is given by (see Mudawar & Houpt (1993a)):

$$u(r) = \frac{1}{2} \frac{g}{\nu_1} \left[\frac{1}{2} (R^2 - r^2) - R_\delta^2 \ln \left(\frac{R}{r} \right) \right], \quad (4.4)$$

where $R = 24.46$ mm is the radius of the glass body bore and R_δ the radius of the liquid-gas interface, which depends on the flow regime. Following equation 4.4, the ratio between velocity variations over the measurement volume in y- and z-direction is:

$$\frac{\Delta u_z}{\Delta u_y} = \frac{u|_r - u|_{r=r_z}}{u|_r - u|_{r=r_y}} = \frac{0.5 (r_z^2 - r^2) - R_\delta^2 \ln (r_z/r)}{0.5 (r_y^2 - r^2) - R_\delta^2 \ln (r_y/r)} \quad (4.5)$$

$$r_z = (r^2 + 0.25 \Delta_z^2)^{0.5}, \quad r_y = r + 0.50 \Delta_y,$$

where geometric quantities are illustrated in figure 4.26. Assuming a film thickness of $\delta = R - R_\delta = 300 \mu\text{m}$ (corresponding approximately to the mean film thickness of the falling liquid films investigated in the optical test setup; see figures 4.10 to 4.12) evaluation of the above relation at $r = R$ (where the gradient of the velocity profile is maximal) yields $\Delta u_z / \Delta u_y = 0.009$. The velocity variation in z-direction is thus roughly two orders of magnitude smaller than the corresponding variation in y-direction.

Solid tracer particles of Titanium dioxide with a mean diameter of $d_P = 2 \mu\text{m}$ and a density of 4500 kg/m^3 were employed. As established in Dietze *et al.* (2008) fluid elements in the CSE region follow loop shaped path lines of small characteristic length. In order to ensure that the LDV measurements resolve the CSE phenomenon accurately it is thus necessary to assess the ability of the tracer particles to follow the flow in the region of interest. This was done on the basis of the Basset-Boussinesq-Oseen (BBO) equation, which governs the movement of a particle in a non steady flow. Hjempfelt & Mockros (1966) derived the frequency response of the particle velocity to an oscillation in fluid velocity from the BBO equation. This result enables the computation of the amplitude ratio η and the angular phase shift $\Delta\phi$ between the particle and

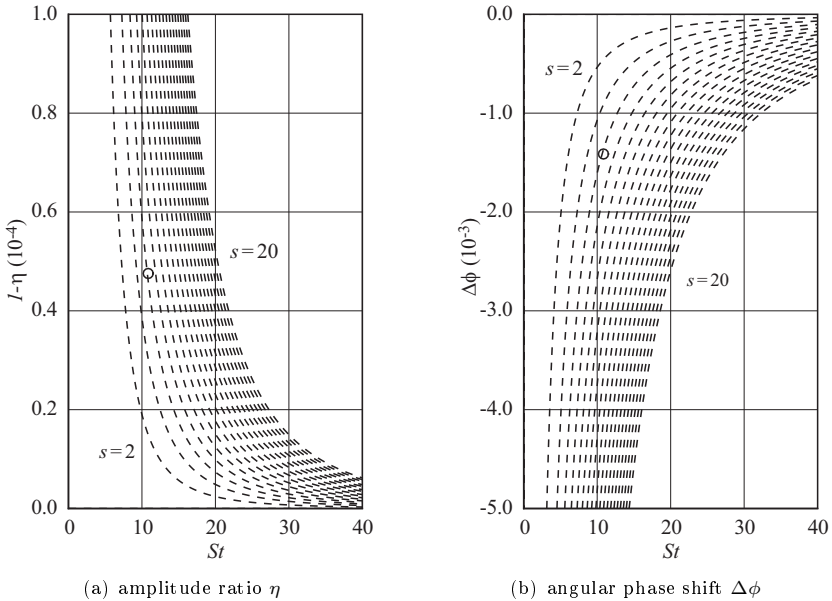


Figure 4.27: Particle frequency response to an oscillating flow. Dashed lines: solutions of the BBO-equation according to Hjelmfelt & Mockros (1966) as a function of solid to liquid density ratio s and Stokes number St . Circles: Titanium dioxide particles in DMSO-water solution (St formulated with characteristic time of CSE i.e. 10^{-3} s).

fluid velocity oscillation for a given excitation frequency. Both quantities are indicators for the capacity of the particle to follow the surrounding flow and are plotted in figure 4.27 as a function of the solid to liquid density ratio s and the Stokes number $St = \Delta t \nu_l / (2\pi d_p^2)$. In addition, circles displayed in figures 4.27(a) and 4.27(b) highlight points corresponding to the measurement conditions encountered in the optical test setup i.e. Titanium dioxide particles dispersed in the DMSO-water solution (see table 4.1). Thereby, the Stokes number was formulated with the characteristic time of the CSE phenomenon

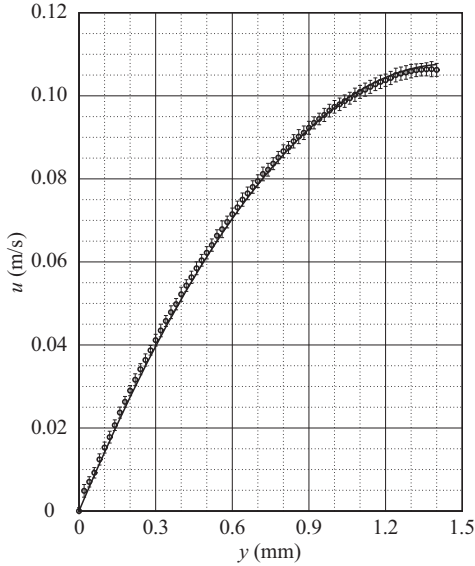


Figure 4.28: Radial streamwise velocity profile in the smooth water-glycerol film: $Re=1.1$ (see table 4.1). Circles: LDV data (bars demarcate standard deviation); solid line: analytical solution for smooth developed cylindrical film flow (see e.g. Mudawar & Houpt (1993*a*)).

($\Delta t = 0.001$ s; see figure 4.29). From the figures, the conclusion can be drawn that under the conditions considered here the employed tracer particles follow the liquid flow well.

Finally, the LDV measurement in the optical test setup was validated on the basis of measurements performed in a smooth developed film flow using the water-glycerol solution detailed in table 4.1. The crosswise profile of the streamwise velocity under these conditions is given by the analytical solution in equation 4.4 (R_δ was thereby obtained by integrating equation 4.4 and iteratively solving it for the volume flow rate). Figure 4.28 illustrates a comparison for $Re \approx 1$ between this analytical solution and measurement data obtained

by LDV, showing good agreement between the two data sets. Further, it can be observed that the standard deviation of the measurement data for a given measurement position is negligible in relation to the measured velocity which is due to the extremely high spatial resolution of the setup. The different measurement positions were set using a three-axis micrometric traversing system, as shown in figure 4.1, in incremental steps of $20\ \mu\text{m}$ with a positioning error of only $\pm 0.1\ \mu\text{m}$

Figures 4.29 and 4.30 depict exemplary LDV data obtained in the optical test setup at different crosswise measuring positions for one of the flow regimes in table 4.2 ($Re=15.0$, $Ka=509.5$, $f=16.0\ \text{Hz}$). The first three measurement positions lie within the residual layer of the liquid film (see subfigures 4.29(a) to 4.29(c)), while subfigures 4.30(a) and 4.30(b) depict velocity time traces outside of the residual layer. The latter are characterized by intermittent bursts of data points, while large waves pass through the LDV measurement volume, separated by stretches without data, when the measurement volume lies in the gaseous phase. In general, the experimental data display a small scatter, which results from the extremely high spatial resolution (i.e. $\Delta x = \Delta y = 24\ \mu\text{m}$) of the LDV technique as it was implemented in this thesis and are shown to be reproducible, as evidenced by their periodicity. Further, LDV measurements are shown to temporally resolve all characteristic features of velocity time traces at the different crosswise positions in the liquid film. A detailed discussion of the measurement data in figure 4.29 from a physical point of view will be performed in subsection 5.1.2.

In the inclined test setup (see figure 4.13), the LDV beam intersection angle in the liquid is $\Theta_{\text{LDV}} = 19.02^\circ$. The dimension of the measurement ellipsoid in x- and z-direction is $24\ \mu\text{m}$, while its dimension in y-direction is $144\ \mu\text{m}$ (see table 4.7). The minimal film thickness encountered for the only case of inclined liquid film flow, for which LDV measurements were performed, is approximately $300\ \mu\text{m}$ (see figure 4.31), leading to a minimal film thickness to ellipsoid height ratio of 2. The same tracer particles as in the optical test setup were employed, exhibiting the same capacity to follow the flow. Indeed, evaluations based on the BBO-equation showed that at flow oscillation frequencies

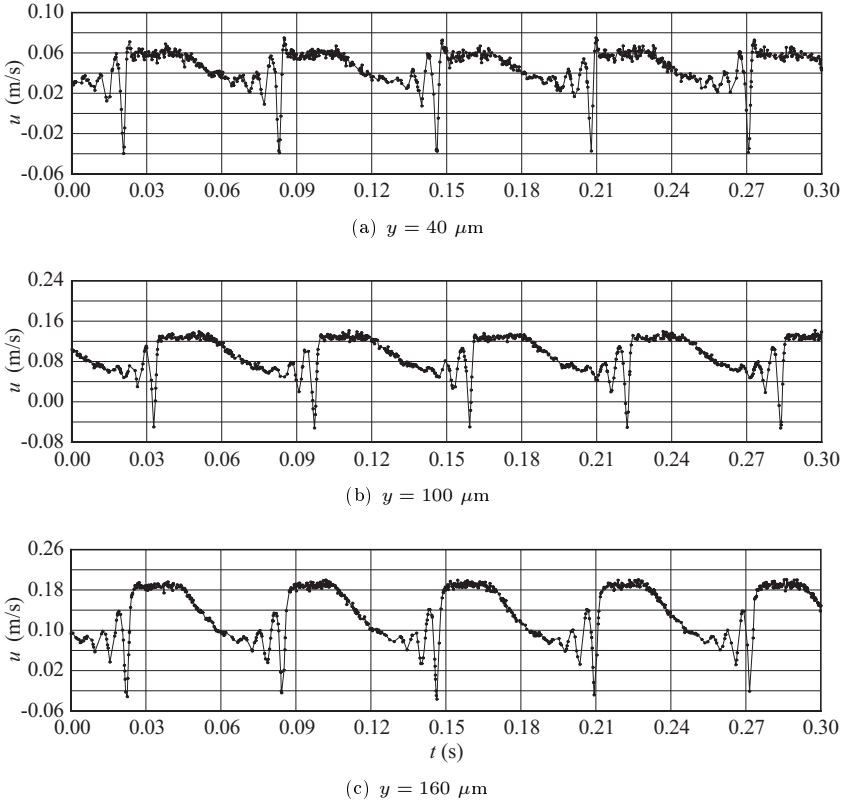


Figure 4.29: Liquid phase streamwise velocity time traces in the residual layer measured with LDV in the optical test setup: $Re=15.0$, $Ka=509.5$, $f=16.0$ Hz.

of up to 10.000 Hz, the deviation of particle kinematics from flow kinematics is negligible. Figures 4.31 and 4.32 depict streamwise velocity time traces measured with LDV in the inclined test setup for one of the regimes listed in table 4.4 ($Re=15.6$, $Ka=133.6$, $f=15.0$ Hz) at three different crosswise positions[†].

4 Experimental

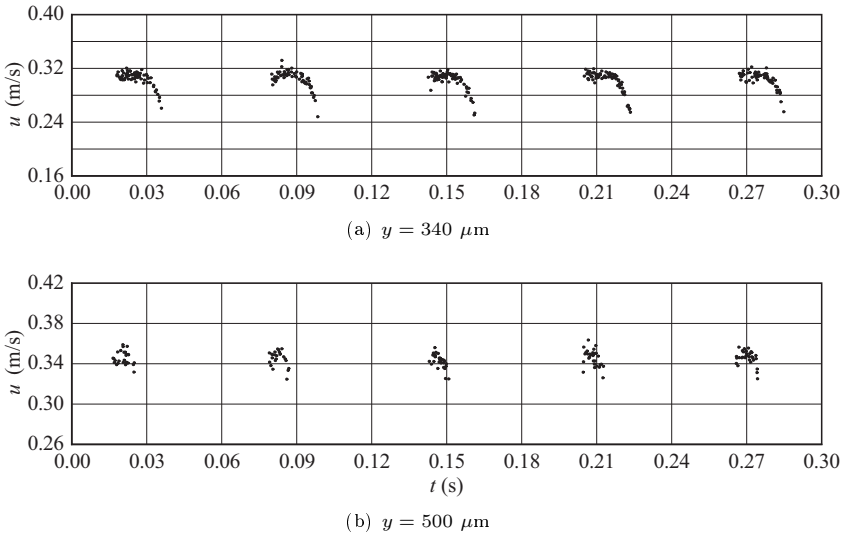


Figure 4.30: Liquid phase streamwise velocity time traces in the large wave humps measured with LDV in the optical test setup: $Re=15.0$, $Ka=509.5$, $f=16.0$ Hz.

In addition, simultaneous film thickness time traces measured with the CCI technique are also displayed. Qualitatively, the velocity time traces are similar to those obtained in the optical test setup (see figures 4.29 and 4.30). However, they exhibit a drastically larger scatter, which results from the substantially lower spatial resolution of the LDV technique as it was implemented in the inclined test setup, due to an inadequate orientation of the measurement ellipsoid (compare figure 4.13 with figure 4.3).

[†]The figures also show velocity time traces obtained from the corresponding numerical simulation (case 1).

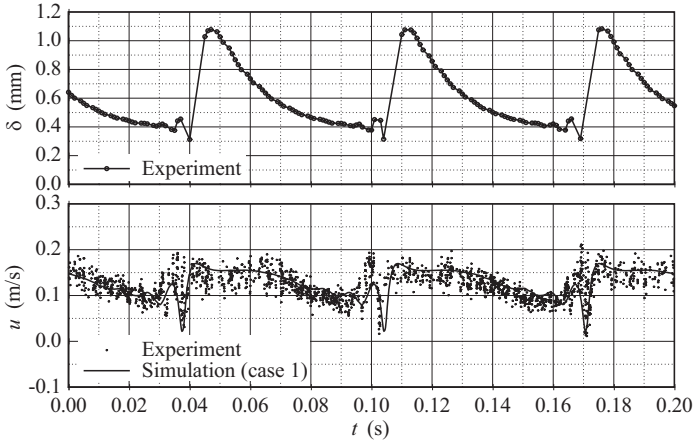
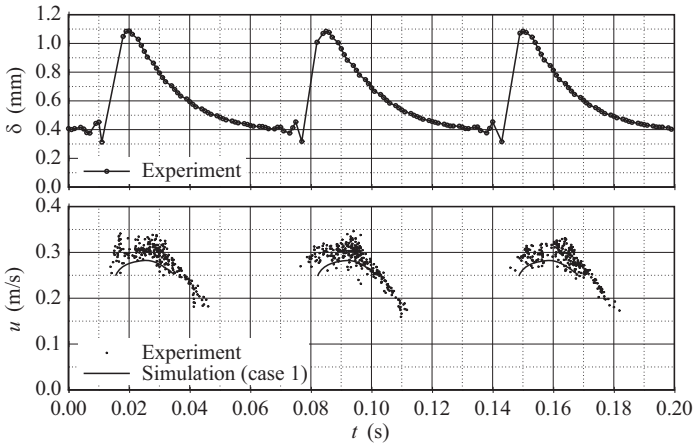
(a) residual layer: $y=200 \mu\text{m}$ (b) intermediate position: $y=596 \mu\text{m}$

Figure 4.31: Liquid phase streamwise velocity time traces in the residual layer and intermediate region (measured with LDV) and corresponding film thickness time traces (measured with CCI) obtained in the inclined test setup: $Re=15.6$, $Ka=133.6$, $f=15.0$ Hz, $x=200$ mm.

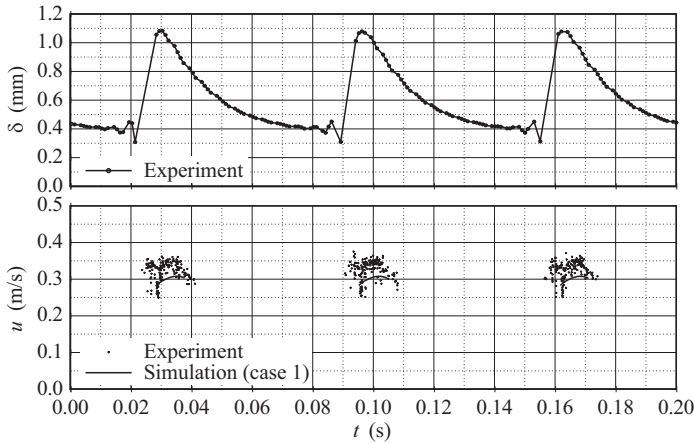
(a) wave crest: $y=794 \mu\text{m}$

Figure 4.32: Liquid phase streamwise velocity time trace in the large wave humps (measured with LDV) and corresponding film thickness time trace (measured with CCI) obtained in the inclined test setup: $Re=15.6$, $Ka=133.6$, $f=15.0$ Hz, $x=200$ mm.

4.2.3 Particle Image Velocimetry

To conclude this chapter on experimental methodology, the third of the employed measurement techniques i.e. Particle Image Velocimetry (PIV) will be addressed in this subsection. As was the case for LDV, a discussion of the principles of the technique is forgone, since it is well established in experimental fluid mechanics. Instead, the reader is referred to the monograph by Raffel *et al.* (2007). Here, only the technique's specific application to velocity measurements in falling liquid films, using the optical test setup introduced in subsection 4.1.1, is discussed.

A few previous works, treating the application of PIV to velocity measurements in falling liquid films can be found in the literature. Cook & Clark (1971) and Nakoryakov *et al.* (1977) used a precursor to the PIV technique more akin



Figure 4.33: Photograph of the PIV laser light sheet illuminating the wavy liquid film in the optical test setup.

to *Particle Tracking Velocimetry* (PTV), while PIV measurements in the modern sense of the technique were performed by Adomeit & Renz (2000), Moran *et al.* (2002), Wierschem *et al.* (2003), Wierschem & Aksel (2004) and Alekseenko *et al.* (2007). However, in the latter three works, considerably different flow conditions (compared to those investigated in this thesis) were treated. Indeed, Wierschem *et al.* (2003) and Wierschem & Aksel (2004) investigated film flows developing on a corrugated inclined surface, while Alekseenko *et al.* (2007) investigated rivulet flow developing on an inclined tube.

In this thesis, the PIV technique was employed for the measurement of velocity vectors in the falling film's x-y-plane, using the optical test setup (see figure 4.3). The resulting data provide a field view of velocity in the liquid phase and in particular the capillary wave region, where flow separation occurs, and complement the pointwise velocity information obtained from LDV. The conjunction of these two velocimetry techniques thus provides the means to fully capture the flow separation phenomenon's kinematics.

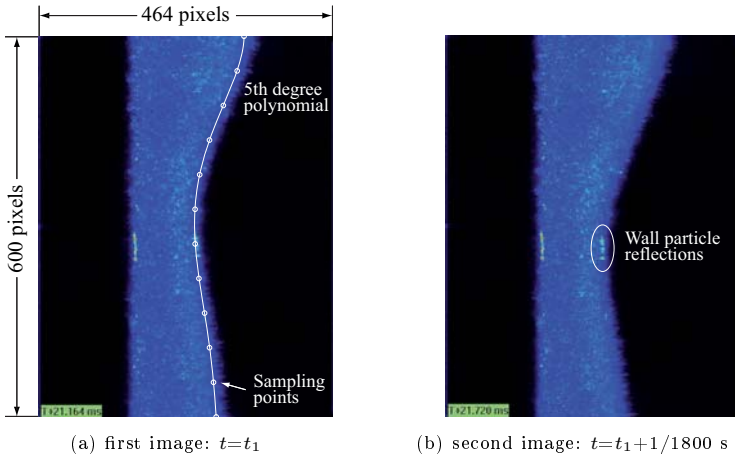


Figure 4.34: Two successive digital PIV images recorded with the CMOS camera using an acquisition frequency of 1800 Hz in the region of the first capillary minimum.

The PIV technique was used in its cross-correlation mode, i.e. velocity information was obtained from pairs of successively recorded images of tracer particles[†] dispersed in the liquid film. For image acquisition, particles in the x - y -plane of the liquid film were illuminated with a laser light sheet of approximately 1 mm thickness as illustrated in figure 4.3. As light source, a pulsed copper vapour laser (Oxford Lasers Ltd., model CU15-A) with a wavelength of $\lambda=511.6$ nm was employed. The laser beam was coupled into an optical fiber connected to the light sheet optics (Oxford Lasers Ltd., model FibreSheet), which are pictured as item 3 in figure 4.1, and which could be oriented relative to the glass body using opto-mechanical linear and tilting stages. Figure 4.33 shows a photograph of the laser light sheet illuminating the wavy liquid film in the glass body.

Illuminated particles were imaged and recorded with a high-speed digital

[†]The same titanium dioxide particles also used for LDV measurements were employed.

Complementary Metal Oxide Semiconductor (CMOS) colour camera (Vision Research, Inc., model Phantom v4.3) equipped with a microscopic lens assembly, its optical axis oriented in z-direction i.e. normal to the laser light sheet, as illustrated in figure 4.1. The camera chip consisted of 600x800 quadratic picture elements (pixels) of edge length $22 \mu\text{m}$ each digitizing light intensity levels with 8 bits. The lens assembly (Infinity Photo-Optical Company, model K2) allowed for a tenfold magnification of the liquid film, resolving the minimal film thickness of $\delta \approx 200 \mu\text{m}$ with roughly 100 camera pixels.

Figure 4.34 shows an example of a pair of successive digital images recorded with this assembly in the region of the first capillary minimum. The two subfigures represent the digitized light intensity I , which was obtained from the corresponding spectral intensities recorded by the colour camera's pixels, i.e. $I = (I_R + I_G + I_B)/3$, where R, G, and B pertain to red, green and blue[†]. Direct reflection of laser light by the liquid-gas interface did not pose a problem as the latter is only slightly curved in azimuthal direction and thus reflects incident light away from the lens assembly. However, reflections at the interface of light scattered by particles adhering to the wall were visible in camera images after sustained operation of the setup when a particle layer had formed at the wall. In subfigure 4.34(b), an example of such reflections is highlighted. Because the film interface is concave in azimuthal direction, wall particle reflections did not limit the capacity to resolve the liquid phase velocity field in the x-y-plane. Nonetheless, the inner surface of the glass body was cleaned regularly between measurement series to minimize this effect.

Figure 4.35 illustrates the logistic illumination and imaging sequence employed to record PIV image pairs (quantitative settings and properties for the CMOS camera and copper vapour laser are listed in table 4.8). During image acquisition, particles were illuminated with laser pulses of repetition rate 9000 Hz, pulse length 10 ns and pulse energy 2 mJ for all experiments. Particle images were continuously recorded with the CMOS camera over several wave period lengths at a frame repetition rate of which the laser pulse frequency is

[†]It should be noted here that the use of a color camera was not necessary for the PIV measurements in this thesis and resulted simply out of availability.

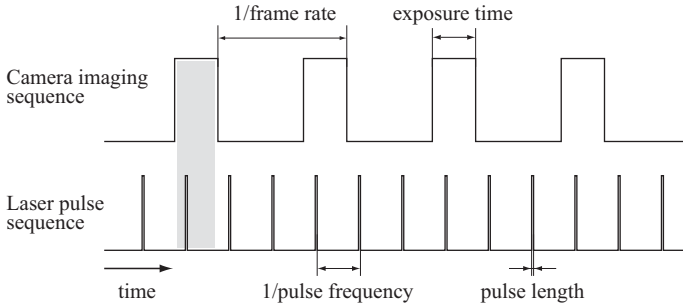


Figure 4.35: Typical illumination and imaging sequence employed for PIV recordings.

CMOS camera		Copper vapour laser			
exposure time	frame rate	wavelength	pulse frequency	pulse length	pulse energy
111 μ s	1.5-4.5 kHz	511.6 nm	9000 Hz	10 ns	2 mJ

Table 4.8: Settings and properties of the CMOS camera and copper vapour laser employed for PIV recordings.

a multiple. The exposure time of the camera chip was set to 111 μ s, which is slightly inferior to the period length of laser pulse repetition 111.1 μ s. Using these settings, it was ensured that each camera recording was illuminated by exactly one laser pulse, and that the time between two successive particle images was given by the pulse frequency (accurate to within 10^{-9} Hz) and the number of pulses between two recordings (which was constant in time). For all investigated flow regimes, image sequences were recorded at several frame repetition rates spanning from 1500 Hz to 4500 Hz (the range of active picture elements on the camera chip was adapted accordingly), in order to account for varying velocity magnitudes in different regions of the falling liquid film. Since two images are needed for the evaluation of velocity vectors at a given time (using the cross-correlation method), the liquid film velocity field was resolved with half the camera frame repetition rate i.e. between 750 Hz and 2250 Hz,

which is much greater than the maximal wave frequency of 24 Hz. The sample digital PIV image pair pictured in figure 4.34 was recorded at a frame rate of 1800 Hz.

Liquid film velocity vectors were obtained by applying a series of post processing steps to the raw digitized particle images (see figure 4.34), subsequently designated as *frames*, recorded with the CMOS camera in the above described manner. In the first step, particle displacement vectors were computed from a given pair of frames by applying a PIV cross-correlation algorithm. The algorithm basically minimizes the *Cross Correlation Function* (CCF) $R(I_1, I_2)$ of the discrete intensity distributions $I_1(i_x, i_y)$ and $I_2(i_x, i_y)$ (i_x and i_y index the position of the considered pixel), corresponding to the first and second frame respectively, evaluated over a quadratic *interrogation area* of edge length N :

$$R(i_x^{\min}, i_y^{\min}, \Delta i_x, \Delta i_y) = \sum_{j=i_y^{\min}}^{i_y^{\min}+N} \sum_{i=i_x^{\min}}^{i_x^{\min}+N} I_1(i, j) \cdot I_2(i + \Delta i_x, j + \Delta i_y) \quad (4.6)$$

with respect to the displacement vector components Δi_x and Δi_y . The obtained displacement vector $[\Delta i_x, \Delta i_y]^T$ is then representative for all pixels within the interrogation area delimited by $i_x^{\min} \leq i_x \leq i_x^{\min} + N$, $i_y^{\min} \leq i_y \leq i_y^{\min} + N$.

The commercially available software Davis 7.1 (LaVision GmbH) was employed for PIV processing of the raw frames obtained from the CMOS camera. Settings pertaining to the PIV cross-correlation algorithm as it was applied in the context of this thesis will be briefly described next. Displacement vectors were computed in consecutive cross-correlation steps performed on an iteratively refined grid, starting with an interrogation area size of 64x64 pixels and ending with one of 6x6 pixels. In each cross-correlation step (except the first one), displacement information from the previous step was employed to shift the intensity distribution I_2 of the second frame in the direction of the flow. This allows for the detection of particle displacements larger than the interrogation area length and thus a maximization of spatial resolution. For measurements in the capillary wave region of falling liquid films this procedure

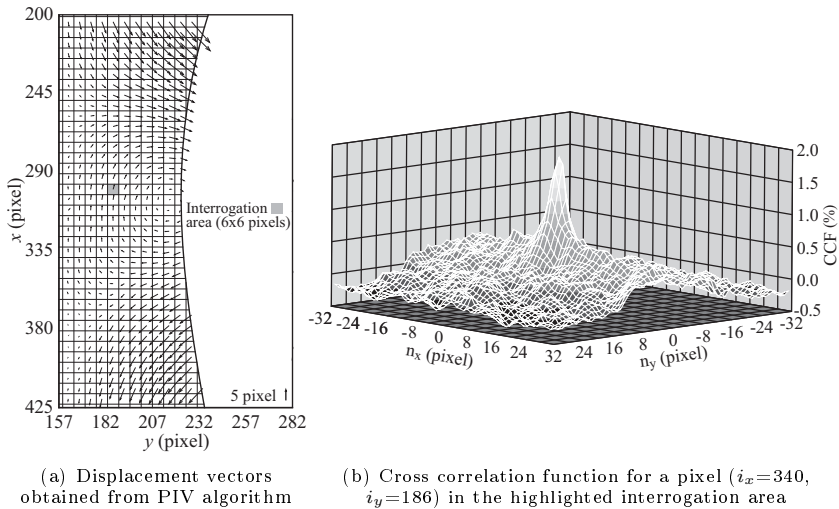


Figure 4.36: Displacement vectors obtained from the application of the PIV algorithm to the image pair in figure 4.34, using the first order Cross Correlation Function (CCF).

is particularly helpful, as spatial velocity gradients there are large. Within each refinement step, the cross-correlation algorithm was performed three times in succession (only twice for the finest resolution), applying the intensity distribution shift mentioned above, in order to center the cross-correlation function and thus increase the signal to noise ratio (see Raffel *et al.* (2007)). In this process, computed displacement vectors were validated using median filtering (see Westerweel (1994)), whereby vectors of magnitudes differing from the median of neighbouring interrogation area values by more than twice their root mean square were removed. Excluded vectors were replaced by interpolating between displacement vectors of surrounding interrogation areas.

Subfigure 4.36(a) shows displacement vectors computed with the above described PIV algorithm from the raw camera frames pictured in figure 4.34,

clearly showing the occurrence of flow reversal at the first capillary minimum. Grid lines demarcate interrogation areas employed for the final cross-correlation step (i.e. of size 6x6 pixels) and thus the spatial resolution of the displacement vector field. The interface, is approximated by a fifth order polynomial, which was fitted to the twelve sampling points highlighted in figure 4.34. These points were defined subjectively for each processed displacement vector field. Subfigure 4.36(b) displays the CCF evaluated over a region of 64x64 pixels surrounding a pixel within the interrogation area highlighted in subfigure 4.36(a). The CCF exhibits the characteristic principal peak from which displacement information is computed. In this case, the ratio of the principle CCF peak to the second largest peak is roughly 5. For the PIV data presented in this thesis, this ratio was in excess of 1.2 for all displayed displacement vectors.

In order to obtain velocity information from the displacement vectors computed with the procedure described above, the imaging factor φ , relating displacements in the object and image planes[†], and the time between two camera frames, which is the reciprocal value of the camera frame rate f_c , is necessary:

$$[u,v]^T = \varphi \cdot f_c \cdot [\Delta i_x, \Delta i_y]^T. \quad (4.7)$$

In the traditional application of PIV, φ is determined by imaging a predefined metric target positioned in the object plane. This procedure could not be employed here due to the geometric constraints of the optical test setup. Instead, PIV measurements were calibrated with corresponding LDV data once for every measurement series. Figure 4.37 illustrates the employed procedure for the calibration of φ . Therein, the leftmost subfigure displays displacement vectors in the region of the first capillary minimum obtained from the PIV algorithm. Conversely, the bottom right subfigure displays a corresponding (i.e. measured under the same flow conditions) streamwise velocity time trace measured with LDV at a given crosswise position y_{LDV} . The global minimum displayed by this time trace is associated with the first capillary minimum, as will be established in chapter 5. Consequently, this characteristic point can also be identified in

[†]More precisely, the length of the projection of a pixel into the object plane.

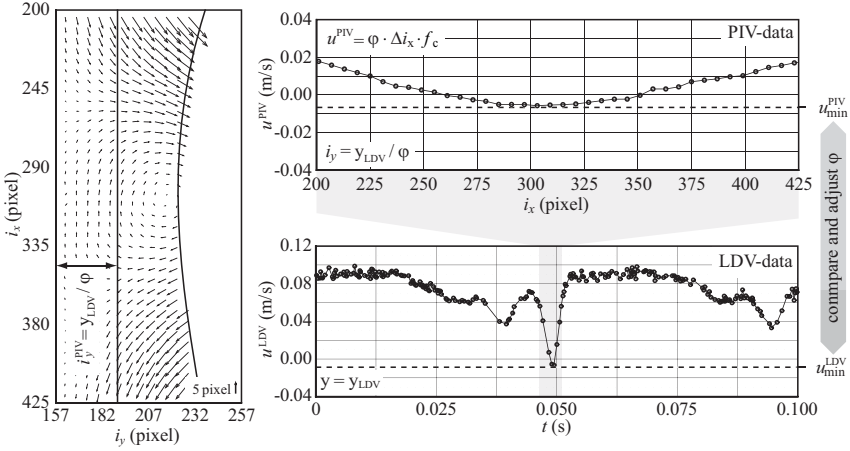


Figure 4.37: Calibration of the imaging factor φ for PIV measurements. Left: particle displacement vectors obtained from PIV algorithm; top right: streamwise velocity ($u^{PIV} = \varphi f_c \Delta i_x$) profile computed from streamwise particle displacements Δi_x at $i_y = y_{LDV} / \varphi$; bottom right: streamwise velocity time trace measured with LDV at $y = y_{LDV}$.

the displacement vector map, given the correct imaging factor φ . This opens the possibility to inversely determine φ , which was done as follows. Starting with an initial guess for φ , the crosswise position in the displacement vector map, corresponding to the LDV measurement position was determined from $i_y^{PIV} = y_{LDV} / \varphi$. The profile of the streamwise velocity component (computed with equation 4.7, using the current guess for φ) evaluated at that position is displayed in the top right subfigure. By comparing the minimum of this profile with the global minimum of the LDV time trace[†] (both should be identical), a better guess for φ was determined. By applying this procedure iteratively, the correct imaging factor was obtained. The deviation of PIV data from LDV data for the first capillary extremal values (first capillary minimum and first

[†]To be precise, the average over LDV minima in four successive waves was employed.

capillary maximum[†]) of the streamwise velocity component was smaller than 5% of the total change in the corresponding LDV time trace (this remaining error is of the same magnitude as the variation of LDV data between waves) for all such measurements presented in this thesis.

[†]This characteristic point is also identifiable in both data sets.

5 Capillary flow separation

After having introduced the employed numerical and experimental methods for the investigation of momentum and scalar transport in 2-dimensional (and 3-dimensional) laminar falling liquid films, this chapter presents the main results of this thesis. Although various numerical and experimental results have already been introduced in previous chapters, this was done for the purpose of illustrating established knowledge (see chapter 2) or validating numerical (chapter 3) and experimental (chapter 4) methods. By contrast, results presented in this chapter represent a new contribution to the field of falling liquid film research.

In essence, it was discovered (see Dietze *et al.* (2008, 2009)) that the flow in the capillary wave region of laminar falling liquid films separates at the wall under certain flow conditions, thus explaining previous observations of back-flow by Kapitza (1948) and others (see subsection 2.3.1). The elucidation of this *capillary flow separation* from its phenomenology through its governing dynamics to its effect on liquid phase scalar transport under 2-dimensional (and 3-dimensional) flow conditions is at the center of this thesis. The phenomenon's discovery provides a hitherto missing piece in the phenomenology of the liquid phase velocity field and thereby valuable input for the development of simplified wave dynamics models based on Shkadov's integral approach. Indeed, as established in subsection 2.2.3, such models rely on assumptions concerning the streamwise velocity profile. Further, the effect of capillary flow separation on liquid phase scalar transport represents a partial explanation for the intensification of scalar transfer to the capillary wave region of falling liquid films (see subsection 2.3.2) for both 2-dimensional (and 3-dimensional) wave dynamics.

The chapter is structured as follows. In sections 5.1 to 5.3, a detailed account

of the fundamental mechanisms of 2-dimensional capillary flow separation will be rendered on the basis of two representative flow regimes. Therein, the kinematics of the phenomenon will be established first in section 5.1 with the help of numerical data as well as experimental velocity data obtained from PIV and LDV measurements. Second, the governing dynamics driving these kinematics will be elucidated in section 5.2 on the basis of numerical data. Third, the intensifying effect of capillary flow separation on liquid phase scalar transport and the resulting wall-side scalar transfer will be established in section 5.3 based on numerical simulations of heat transfer. In section 5.4, the influence of two principal control parameters, namely the Reynolds number and the wave frequency, on the fluid mechanical aspects of capillary flow separation (i.e. kinematics and governing dynamics) will be demonstrated with numerical data as well as PIV and LDV measurement results. To conclude the chapter, characteristics of capillary flow separation under 3-dimensional flow conditions will be treated in section 5.5 based on a single 3-dimensional numerical simulation.

5.1 Kinematics

In order to introduce capillary flow separation, a purely kinematic description of the phenomenon, both in terms of the velocity field and the out of plane vorticity field, is provided in this section. The goal being to establish what the phenomenon “looks like” before addressing questions about its cause and effect. This is done on the basis of two representative flow regimes. An *inclined liquid film* (case 1 in table 3.1) and a *vertically falling liquid film* (case 8 in table 3.1).

5.1.1 Spatio-temporal visualisation

A simple visualization of capillary flow separation as it occurs in falling liquid films is provided in figures 5.1 and 5.2. These display the spatio-temporal evolution of simulated liquid phase streamlines in the region of the first capillary

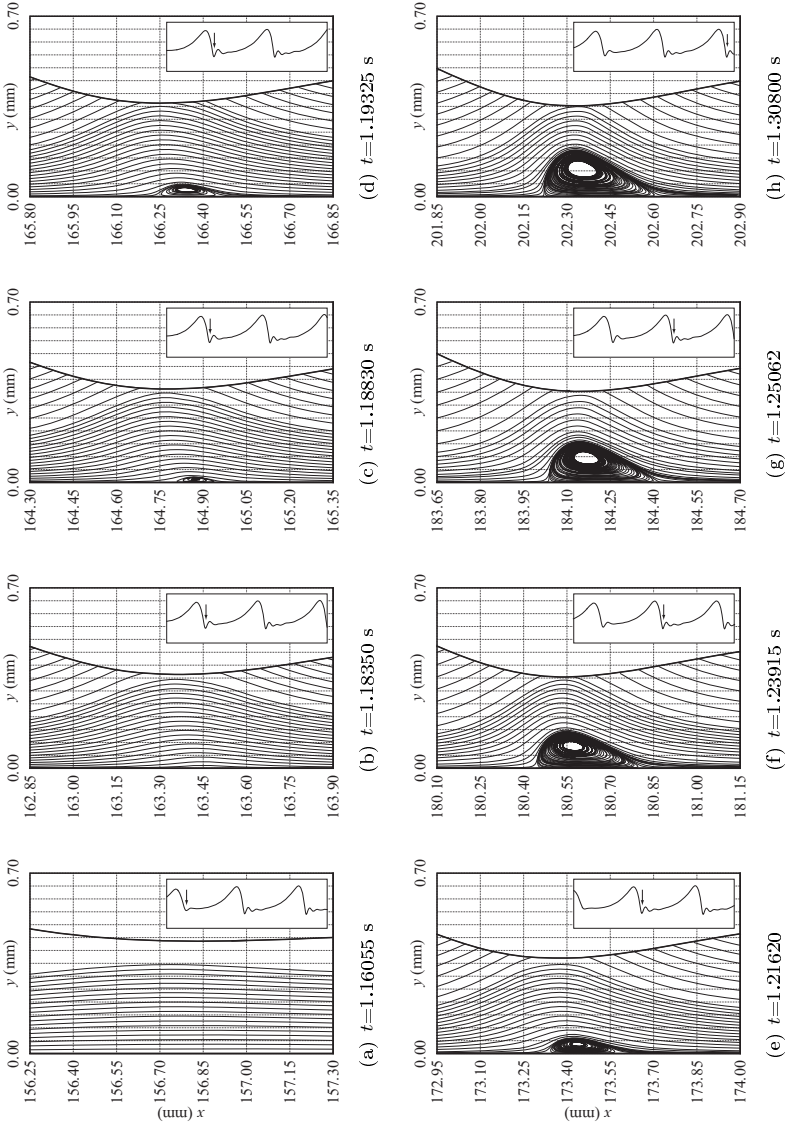


Figure 5.1: Simulated streamlines in the capillary wave region for case 1 in table 3.1 (inclined film).

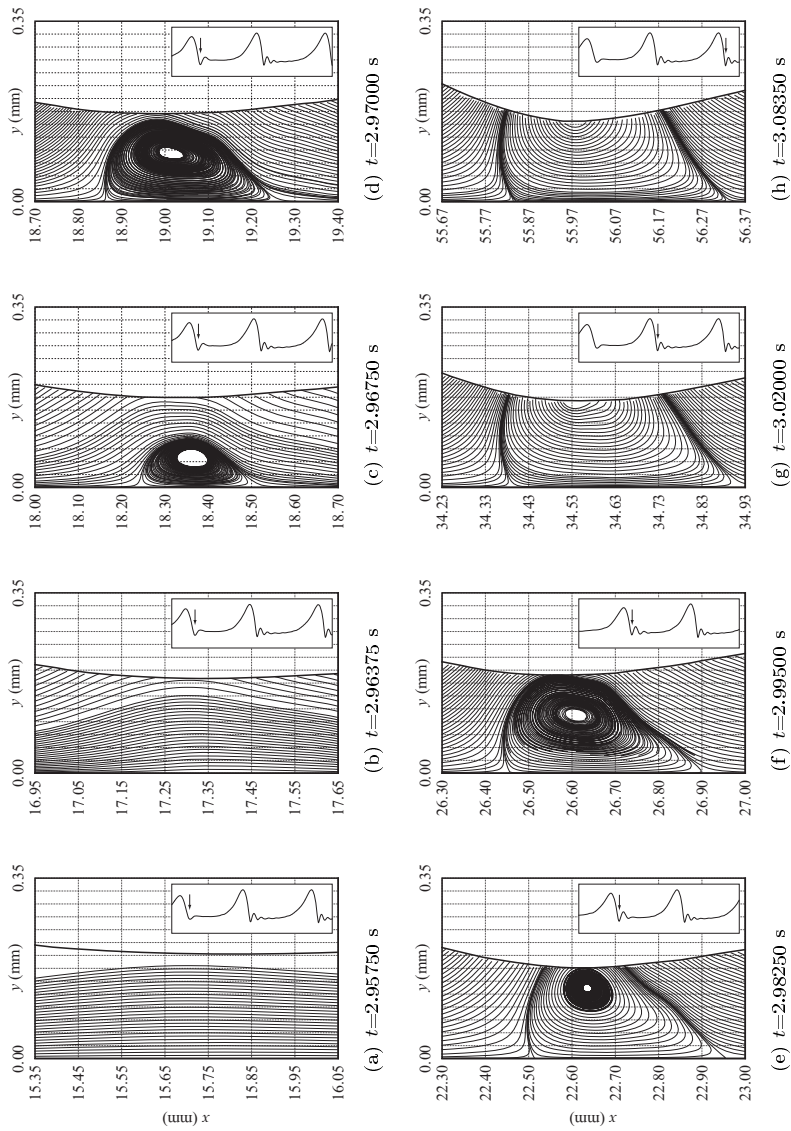


Figure 5.2: Simulated streamlines in the capillary wave region for case 8 in table 3.1 (vertical film).

minimum for the two investigated cases. A pictogram of the corresponding streamwise film thickness distribution, highlighting the region depicted in the streamline plot with an arrow, is also included in each subfigure. This highlighted region moves downstream with wave celerity, tracking the capillary wave region of a single wave during its entire development.

Both streamline plot sequences exhibit the same behaviour in the initial stages of wave development. As the first capillary minimum takes shape, streamlines underneath it distort into a pattern typically associated with decelerated and re-accelerated flow. Indeed, tracking a streamline in streamwise direction, the latter moves away from the wall while approaching the capillary minimum and re-converges toward it after passing the minimum. Streamlines attain their maximal distance from the wall slightly downstream of the wave trough. Since, for a given time, the volume flow per unit width between 2 streamlines is constant (the film liquid being incompressible), the mean flow is consequently decelerated and re-accelerated in streamwise direction. This streamline distortion grows more pronounced as the capillary waves develop, until the flow separates by detaching and subsequently re-attaching to the bounding wall (see subfigures 5.1(c), 5.1(d) and 5.2(c)) similar to classical flow separation. In the process, a *Capillary Separation Eddy* (CSE) is formed, which subsequently grows until it attains a constant size once the capillary wave topology is fully developed.

In this respect, a significant difference between the inclined and vertical film is evident. In the first case, the CSE stays fully contained in the liquid phase (see figure 5.1(h)), assuming a crosswise size of approximately half the minimal film thickness. In the second case, the CSE outgrows the liquid film, assuming an open shape with streamlines ending at the liquid-gas interface (see subfigure 5.2(h)). The possibility of such a scenario was in principle established by Rood (1994), who investigated vortex interactions with a free surface and stated that, when a vortex breaks up and “attaches” to a free surface, interfacial vorticity transport takes place. Accordingly, a discussion of the out of plane vorticity field in the CSE region for this case is provided in subsection 5.1.3. Interestingly, the streamline pattern in subfigure 5.2(h) confirms the flow struc-

ture conjectured by Kapitza (1948) (see figure 2.15) and Massot *et al.* (1966). Moreover, Malamataris & Balakotaiah (2008) have recently obtained similar results by way of numerical simulation, introducing the term cellular pattern to describe the flow structure at the first capillary minimum.

Further, subfigures 5.2(e) to 5.2(g) show that, before attaining its final open shape (subfigure 5.2(h)), the CSE reverts back to a closed shape (subfigures 5.2(e) and 5.2(f)), suggesting a two-way coupling between the flow separation phenomenon and capillary wave dynamics. Consequently, it can be envisaged that capillary flow separation may play a role in the (secondary) instability of wavy liquid films.

5.1.2 Velocity field

In order to provide a quantitative account of the capillary flow separation's kinematics, the corresponding velocity field is investigated in greater detail in this subsection. To that end, figures 5.3(a), 5.3(c) and 5.4(a) represent a larger view of streamline patterns near the inclined liquid film's first capillary minimum at three distinctive time points of the evolution shown in figure 5.1. The first one, shortly before the initiation of flow separation, the second one shortly after and the third one after full development of the phenomenon. These time points delimit three principal developmental episodes of the capillary flow separation, which are linked to the evolution of capillary waves i.e. flow deceleration, CSE nucleation and CSE growth. Figures 5.3(b), 5.3(d) and 5.4(b) depict corresponding profiles of the streamwise velocity component at different streamwise positions in the vicinity of the first capillary minimum.

In figure 5.3(a) the flow is shown to decelerate and re-accelerate at the first capillary minimum without the occurrence of separation. This is evident, from a qualitative perspective, in the shape of near-wall streamlines, as discussed in subsection 5.1.1. Quantitative evidence is provided by the corresponding streamwise velocity profiles. Indeed, figure 5.3(b) shows a significant deceleration (from $x=163.02$ mm to $x=163.46$ mm) and re-acceleration (from $x=163.46$ mm to $x=164.00$ mm) of the flow. As evidenced by comparison of the profiles

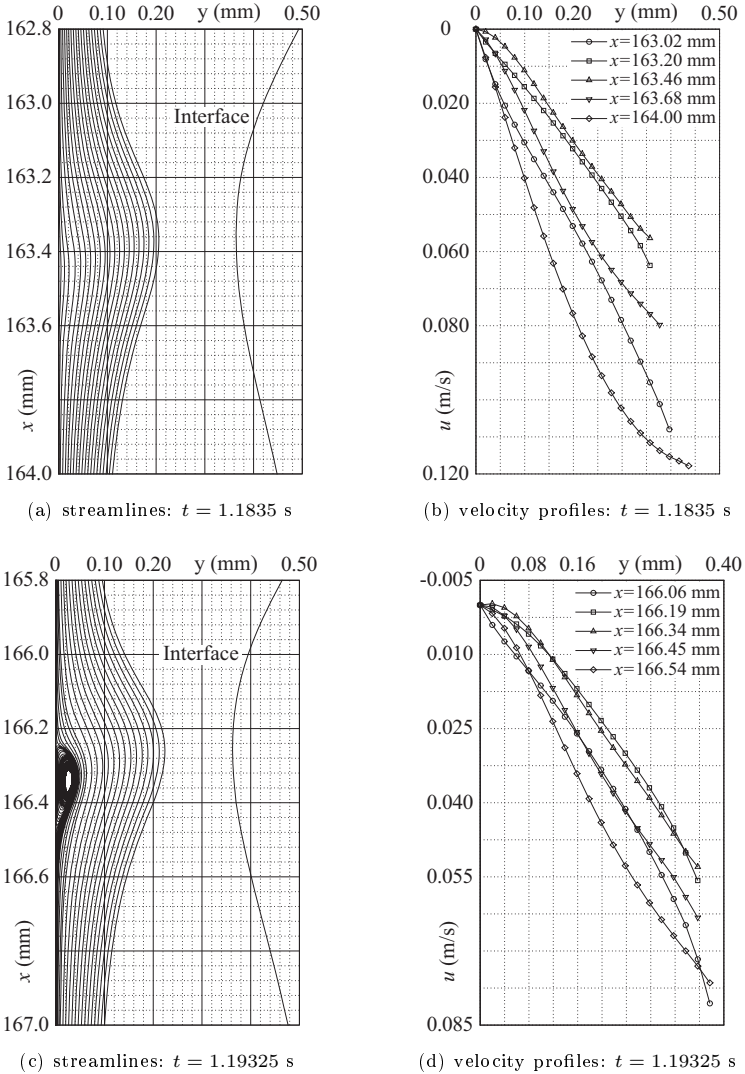


Figure 5.3: Simulated near-wall streamlines and streamwise velocity profiles at the first capillary minimum for different points in time during wave development (case 1 in table 3.1): $Re=15.6$, $Ka=133.6$, $f=15.0$ Hz.

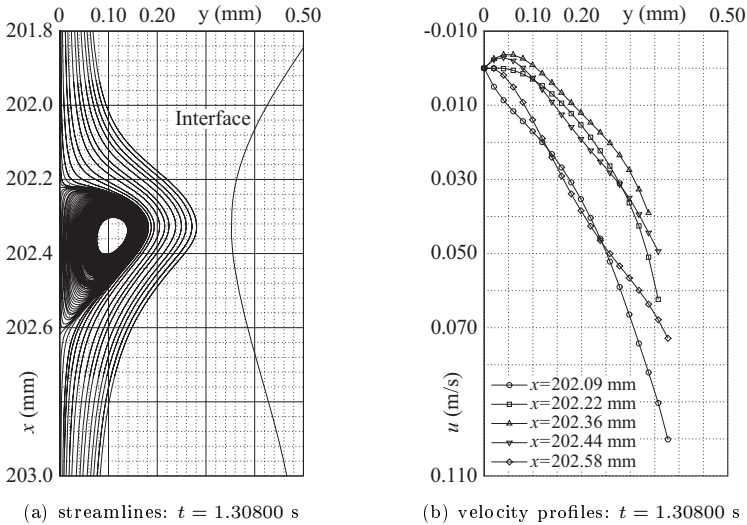


Figure 5.4: Simulated near-wall streamlines and streamwise velocity profiles at the first capillary minimum in the developed region (case 1 in table 3.1): $Re=15.6$, $Ka=133.6$, $f=15.0$ Hz.

at $x=163.02$ mm and $x=163.46$ mm, the deceleration is associated with a sign change of the second order crosswise derivative near the wall from negative to positive. This is due to the stronger deceleration of fluid elements closer to the wall with lower kinetic energy, leading to a turning point in the profile at $x=163.46$ mm. This change in shape of the velocity profile is characteristic for the separation of wall bounded flows. Further, between positions $x=163.20$ mm and $x=163.46$ mm, the first order crosswise derivative at the wall approaches but does not attain the value zero, signifying that flow separation is imminent. As the flow re-accelerates in streamwise direction downstream of the wave trough (from $x=163.46$ mm to $x=164.00$ mm) the second order crosswise derivative of the velocity profile re-converges toward a negative value near the wall.

Figure 5.3(c) shows the CSE shortly after its nucleation at the bounding wall. Correspondingly, the velocity profile at $x=166.34$ mm (see figure 5.3(d)) manifests a slightly negative value of the streamwise velocity component near the wall. During the growth phase of the CSE, the latter attains its developed size of approximately 50% of minimal film thickness as illustrated in figure 5.4(a). Figure 5.4(b) shows the same qualitative behaviour of the near wall velocity profile upstream of the CSE (between $x=202.09$ mm and $x=202.22$ mm) as shown in figure 5.3(b). However, here, the streamwise change in the shape of the near wall profile is such that the threshold of a vanishing first order crosswise derivative at the wall is reached at $x=202.22$ mm. At this position, flow separation takes place. Downstream of the separation point, between $x=202.36$ mm and $x=202.44$ mm, the velocity profiles are characterised by a second root next to the one at the wall. Between the two roots, the streamwise velocity component is negative, confirming the flow reversal discernible in figure 5.4(a). Moving further downstream, the velocity profile re-approaches its pre-separation shape as the flow re-accelerates. The general sequence of streamwise deceleration and re-acceleration at the first capillary minimum is also discernible in subfigure 4.31(a), which depicts a streamwise velocity time trace measured with LDV at $y=200$ μm (i.e. above the CSE center) in the developed region of the inclined film. However, as previously mentioned, the relatively low resolution of LDV data obtained in the inclined test setup only allows for qualitative assessments. When discussing the velocity field for the vertically falling liquid film, the superior resolution of LDV data obtained in the optical test setup will be exploited to extract quantitative information.

Next to revealing regions of back flow, velocity profiles in subfigures 5.3(b), 5.3(d) and 5.4(b) indicate the velocity distribution's complexity in the capillary wave region. Recently, as established in subsection 2.2.3, accurate models of wave dynamics based on long wave theory have been published by Scheid *et al.* (2006), Mudunuri & Balakotaiah (2006), Nguyen & Balakotaiah (2000) and Ruyer-Quil & Manneville (2000). An essential assumption in their approach concerns the degree of freedom of polynomials representing the crosswise distribution of streamwise velocity. Results in subfigures 5.3(b), 5.3(d) and 5.4(b)

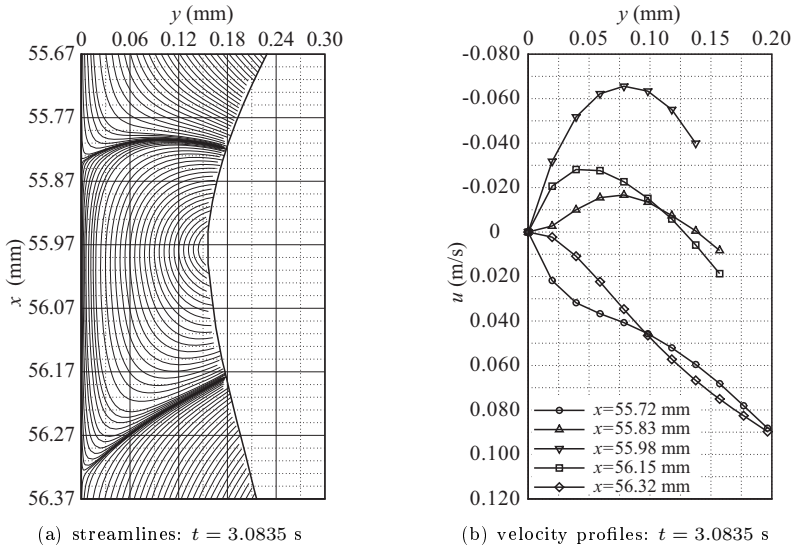


Figure 5.5: Simulated near-wall streamlines and streamwise velocity profiles at the first capillary minimum in the developed region (case 8 in table 3.1): $Re=15.0$, $Ka=509.5$, $f=16.0$ Hz.

could serve as a physical justification of such modelling assumptions. Indeed, in order to account for flow separation, polynomials representing the streamwise velocity component should obviously be at least of third order. This is not the case for lowest order models, which are based on a local approximation of the velocity profile with a second order polynomial.

For the vertically falling liquid film (see capillary streamline evolution in figure 5.2), figure 5.5 depicts streamwise velocity profiles (subfigure 5.5(b)) evaluated at different streamwise positions within the fully developed CSE (visualised by the streamline pattern in subfigure 5.5(a)) as obtained from numerical simulation. These profiles exhibit the same principle characteristics as corresponding profiles for the inclined film flow (compare subfigure 5.5(b))

with subfigure 5.4(b)) with two exceptions. Firstly, the velocity profile passing through the center of the CSE ($x=55.98$ mm) exhibits a maximal negative value approximately ten times larger than the corresponding profile for the inclined liquid film. At this position, a considerable volume flux per unit width of approximately $3 \cdot 10^{-6}$ m²/s, yielding a local Reynolds number value of approximately 1, flows counter to the gravitational acceleration. Secondly, the profile evaluated at the upstream separation point ($x=55.83$ mm) exhibits negative velocity values at a certain distance from the wall, which results from a streamwise bulge in the shape of the open CSE.

In addition to the numerical data displayed in figure 5.5, corresponding experimental data measured with PIV and LDV in the optical setup were also obtained for the vertically falling liquid film (i.e. the fourth case in table 4.2). Figure 5.6 depicts liquid phase velocity vectors measured in the developed capillary wave region using PIV. Different images capture the velocity field at different times in the evolution of a surface wave. Thereby, the vector plots are arranged in the order in which an observer would see the corresponding wave regions pass by, starting with the second capillary minimum (subfigure 5.6(a)), followed by the first capillary maximum (subfigure 5.6(b)) and minimum (subfigure 5.6(c)) and ending with the large wave front (figure 5.6(d)). In each subfigure, a pictogram highlighting the considered region of the film is included. Also, underneath each pictogram, a reference vector of adequately chosen length is displayed.

Figure 5.6(a) depicts velocity vectors in the region of the second capillary minimum, showing a strong deceleration and subsequent re-acceleration of the flow in streamwise direction. This is evidenced by the small velocities at the capillary minimum as well as the fact that upstream of the minimum, vectors point away from the wall ($\partial v/\partial y > 0 \leftrightarrow \partial u/\partial x < 0$) whereas they point toward the wall further downstream ($\partial v/\partial y < 0 \leftrightarrow \partial u/\partial x > 0$). The flow near the first capillary maximum (see figure 5.6(b)) is accelerated and subsequently decelerated as it approaches the second capillary minimum. Meanwhile, flow velocities attain considerably larger values compared to figure 5.6(a).

In the region of the first capillary minimum, pictured in figure 5.2(h), velocity

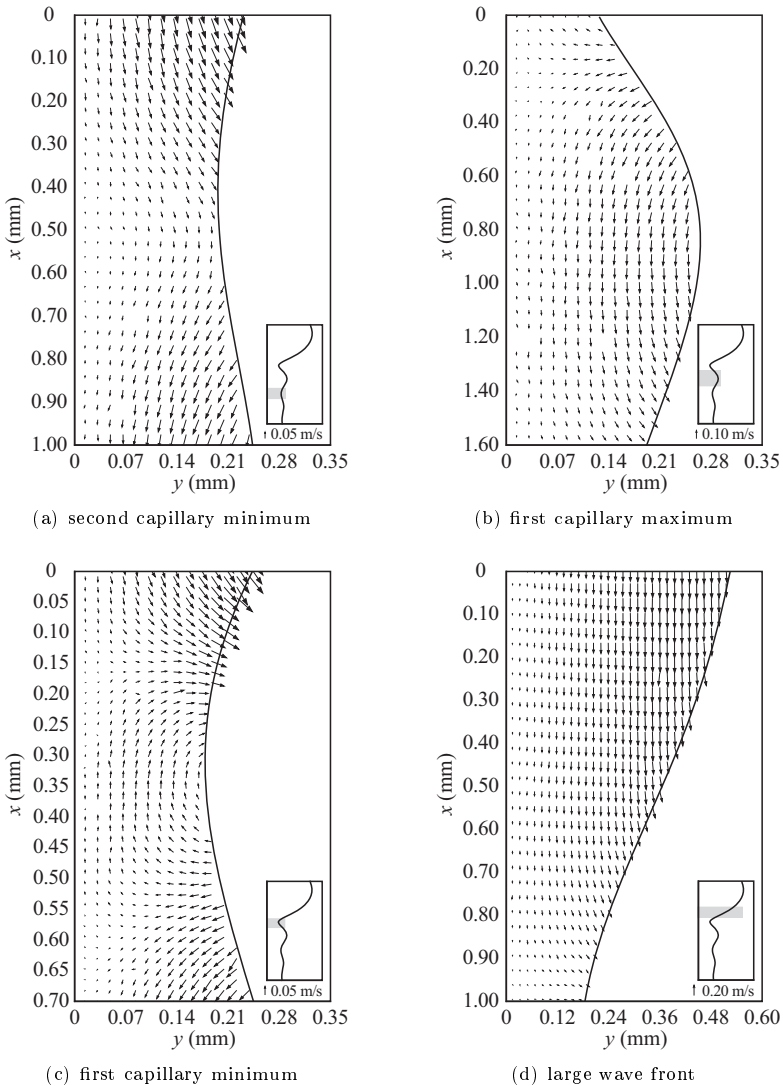
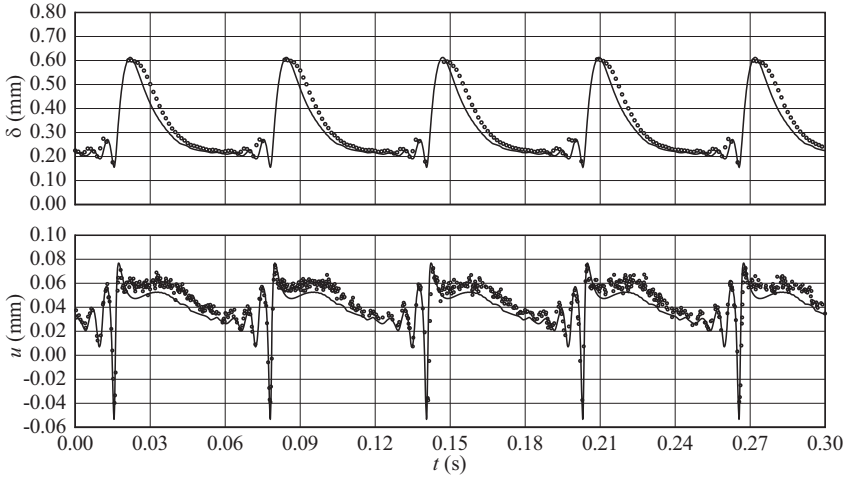


Figure 5.6: Liquid phase velocity vectors in the capillary wave region measured in the optical test setup using PIV (subfigures are scaled differently): $Re=15.0$, $Ka=509.5$, $f=16.0$ Hz.

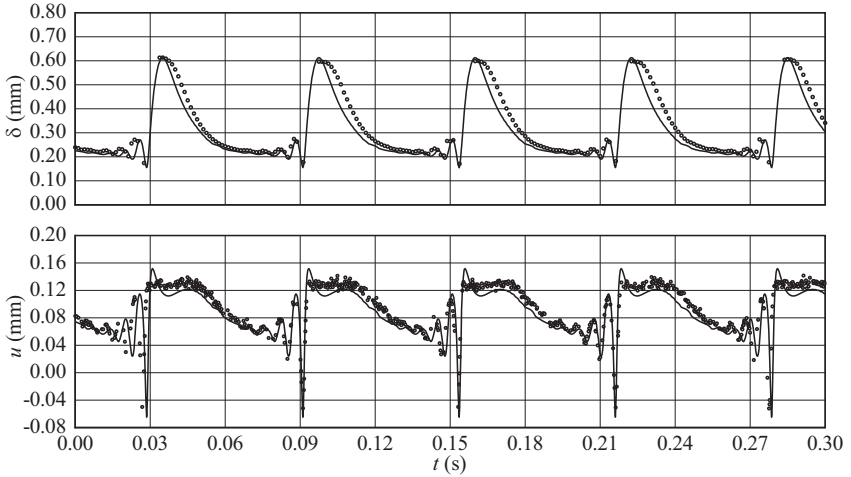
vectors clearly indicate the CSE in its open shape. This vector plot constitutes the first clear experimental evidence of the existence of flow separation in the capillary wave region of falling liquid films. A portion of the CSE is also seen at the top of figure 5.6(b). Finally, figure 5.6(d) shows the velocity field in the large wave, exhibiting significantly larger velocities than in all other regions. The vector plot also shows that the crosswise velocity component is negligible in the wave crest and only increases as the flow decelerates while approaching the CSE.

Vector plots in figure 5.6 suggest a strong influence of the capillary wave topology on the liquid phase velocity field. This can be more rigorously investigated on the basis of simultaneous streamwise velocity and film thickness time traces, which were measured in the optical test setup, using LDV and the CCI technique respectively. Figures 5.7, 5.8 and 5.9 depict such time traces over several wave periods evaluated at five distinctive crosswise positions in the vertically falling liquid film (for the fourth case in table 4.2). In these figures, corresponding (i.e. for case 8 in table 3.1) film thickness and streamwise velocity time traces obtained from numerical simulation are also plotted with the help of solid lines. The reason for their inclusion stems from the inevitable small streamwise shift between the LDV and CCI measurement positions evoked in subsection 4.2.1. This spatial shift causes a time shift between the film thickness and velocity time traces of approximately 2 ms. By plotting experimental time traces such that their characteristic points match those of corresponding numerical time traces (the latter were evaluated at exactly the same position for film thickness and streamwise velocity), this small shift was corrected. This correction is only applied here, as the correlation of film thickness and streamwise velocity is of interest. In subsequent sections, simultaneously measured LDV and CCI data are presented in their raw form (see subsection 5.4 in particular). The same sequence of LDV time traces without the addition of numerical data is displayed in figures 4.29 and 4.30 of subsection 4.2.2.

From the perspective of capillary flow separation, velocity and film thickness time traces in the residual layer of the film, which are depicted in subfigures 5.7(a) to 5.8(b), are of most interest. These display two main characteristics.



(a) $y = 40 \mu\text{m}$



(b) $y = 100 \mu\text{m}$

Figure 5.7: Liquid phase streamwise velocity time traces in the residual layer (near-wall region) measured in the optical test setup using LDV: $Re=15.0$, $Ka=509.5$, $f=16.0$ Hz.

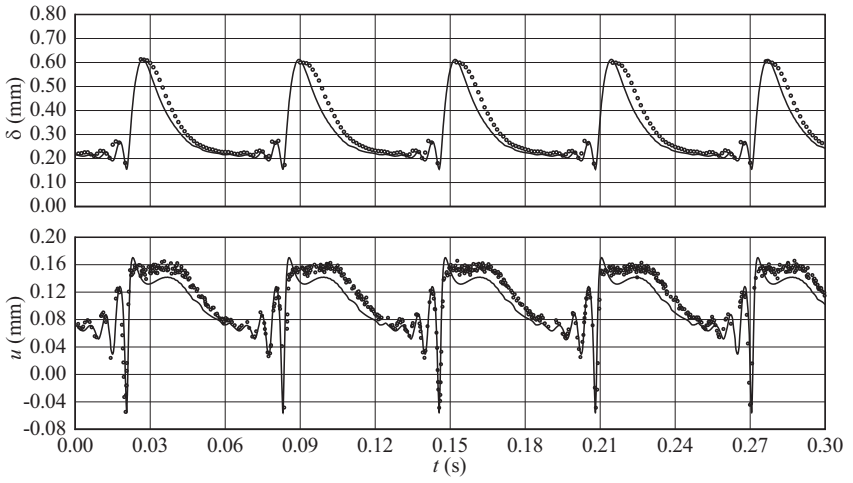
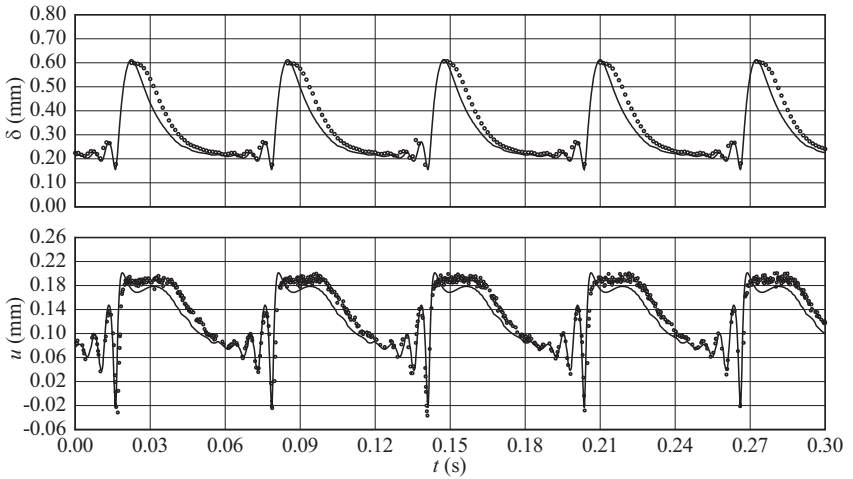
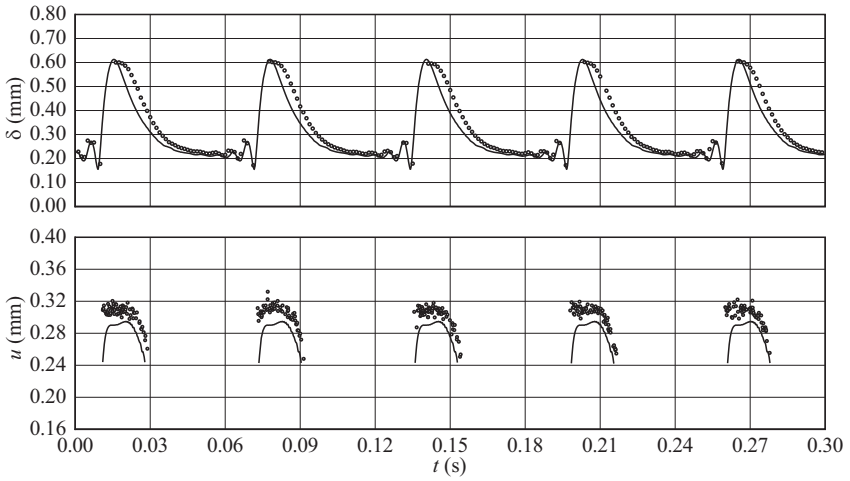
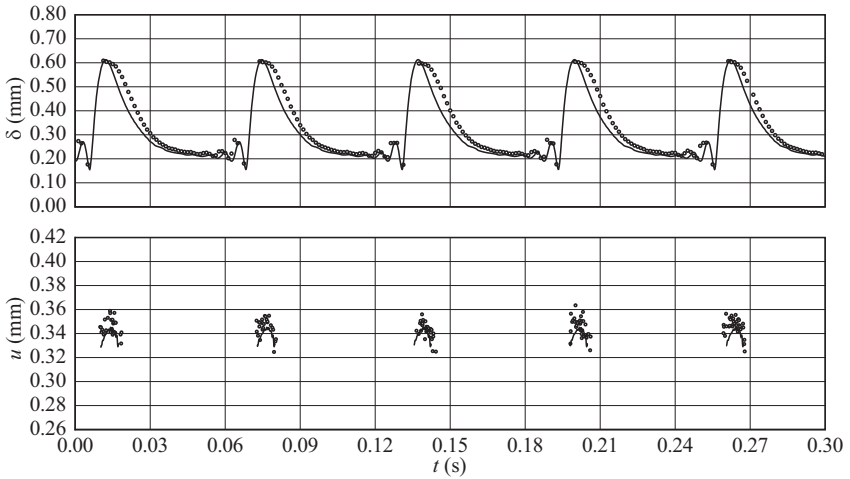
(a) $y = 120 \mu\text{m}$ (b) $y = 160 \mu\text{m}$

Figure 5.8: Liquid phase streamwise velocity time traces in the residual layer (intermediate region) measured in the optical test setup using LDV: $Re=15.0$, $Ka=509.5$, $f=16.0$ Hz.



(a) $y = 340 \mu\text{m}$



(b) $y = 500 \mu\text{m}$

Figure 5.9: Liquid phase streamwise velocity time traces in the large wave humps measured in the optical test setup using LDV: $Re=15.0$, $Ka=509.5$, $f=16.0$ Hz.

First and foremost, they exhibit negative values of the streamwise velocity component in each wave at the position of the first capillary minimum. This constitutes further clear experimental evidence of the existence of backflow in falling liquid films. Thereby, the global minimum of the velocity time trace is shown to decrease with increasing wall distance from $y=40\ \mu\text{m}$ to $y=100\ \mu\text{m}$ and to increase with wall distance between $y=100\ \mu\text{m}$ and $y=160\ \mu\text{m}$, in accordance with the streamwise velocity profile at $x=55.98\ \text{mm}$ in subfigure 5.5(b) (see also PIV vector plot in subfigure 5.6(c)).

Second, figures 5.7 and 5.8 show velocity and film thickness time traces to be strongly correlated. This is most evident in the capillary wave region downstream of the main wave. There, velocity time traces oscillate in a similar manner as the film thickness, each capillary extremal value being associated with a corresponding extremal value in the velocity time trace. Meanwhile, the amplitude of velocity oscillations increases with increasing wall distance suggesting an increase in wave influence on the flow field. This will be explained when addressing the effect of capillary flow separation on liquid phase scalar transport in section 5.3.

Finally, figure 5.9 depicts velocity time traces at positions outside of the residual layer. Accordingly, LDV time traces are characterized by intermittent bursts of data points obtained as large waves pass through the LDV measurement volume, separated by stretches without data when the measurement volume lies in the gaseous phase. Correspondingly, numerical velocity data were restricted to the liquid phase to allow for a clear comparison. The main observation to be deduced from these plots is that film thickness and streamwise velocity are also strongly correlated within large waves. Indeed, velocity time traces display a similar shape to that of the crests of these waves.

5.1.3 Vorticity field

A striking feature of the CSE as it occurs in the vertically falling liquid film (see figure 5.2) is its open shape, with streamlines ending at the liquid-gas interface. As mentioned previously, the possibility of such a scenario was in

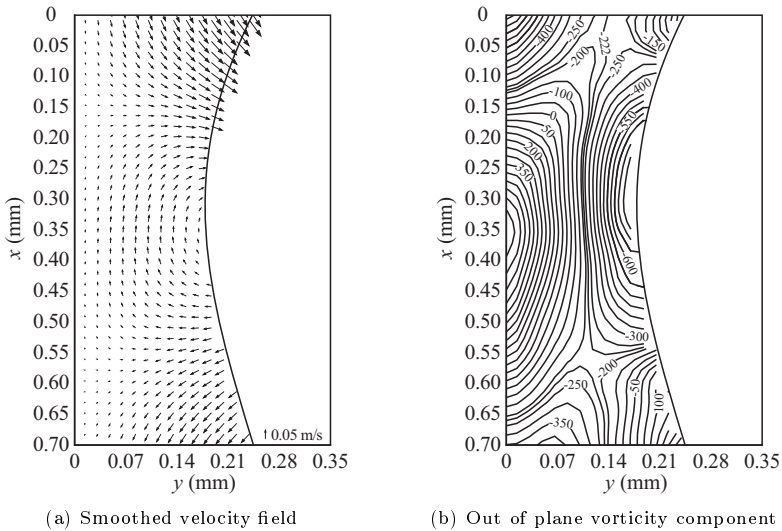


Figure 5.10: Smoothed velocity field resulting from the application of a moving average filter to the raw velocity data of figure 5.6(c) and contour plot (including contour values) of the out of plane vorticity component $\omega_z = \partial v / \partial x - \partial u / \partial y$ derived from the smoothed field.

principle established by Rood (1994), who investigated vortex interactions with a free surface. Rood (1994) stated that when a vortex breaks up and attaches to a free surface, interfacial vorticity transport takes place. In principle the CSE region displayed in subfigures 5.6(c) and 5.5(a) fits this description, and consequently, a detailed discussion of vorticity transport within this region is included here.

For this, the out of plane vorticity component $\omega_z = \partial v / \partial x - \partial u / \partial y$ corresponding to the velocity field pictured in subfigure 5.6(c) was evaluated. Contours of ω_z are displayed in figure 5.10(b). For the calculation of ω_z , the velocity field of figure 5.6(c) was smoothed with a moving average filter (which takes into account only the immediate crosswise and streamwise neighbours of a consid-

ered data point), yielding the velocity plot displayed in figure 5.10(a)[†]. The necessity of smoothing PIV velocity data in order to obtain vorticity fields was discussed by Luff *et al.* (1999) and stems from the amplification of measurement errors as a result of numerical differentiation. The derivatives $\partial v/\partial x$ and $\partial u/\partial y$ were approximated by their first order central difference discretization (forward or backward difference discretization was employed at the boundaries, depending on available neighbouring data points). Because it is derived from smoothed velocity data, the contour plot in figure 5.10(b) should be considered only as a qualitative indicator of vorticity distribution in the CSE region.

It shows that the CSE is divided into two distinct vorticity regions (in what follows the term vorticity shall be used to designate ω_z) which can be clearly attributed to the mechanisms of vorticity generation at the wall (see e.g. Morton (1984)) and the liquid-gas interface (see Wu (1995)) respectively. At the wall, vorticity is generated by the resulting action of adverse streamwise pressure derivative and gravitational acceleration and is instantly diffused into the liquid film. Following Morton (1984) (see also Green (1996)) the local *diffusional vorticity flux*[‡] normal to the wall is then given by:

$$-\nu_1 \left. \frac{\partial \omega_z}{\partial y} \right|_{y=0} = \frac{1}{\rho_1} \left. \frac{\partial p}{\partial x} \right|_{y=0} - g, \quad (5.1)$$

where the terms on the right hand side are responsible for the generation of vorticity. In the CSE region, the resulting upstream pressure force on a fluid element surpasses the downstream gravitational force[§], which means that positive vorticity is generated at the wall (i.e. the right hand side of equation 5.1 is positive). According to Lundgren & Koumoutsakos (1999), vorticity at the free surface, assuming negligible tangential shear stress, is given by the following

[†]The smoothed velocity vector field in subfigure 5.10(a) does not differ substantially from the raw data in subfigure 5.6(c).

[‡]This has a unit of flow rate per time and area (see e.g. Morton (1984)) and should be understood as a diffusional flux contributing to a change in vorticity.

[§]This will be established in section 5.2.

relation:

$$\omega_z = 2 \vec{\nabla} \cdot \vec{\tau} (\vec{u} \cdot \vec{n}) - 2 \kappa \vec{u} \cdot \vec{\tau}, \quad \kappa = \frac{\partial^2 \delta / \partial x^2}{(1 + (\partial \delta / \partial x)^2)^{3/2}},$$

$$\vec{n} = (\partial \delta / \partial x, -1, 0)^T (\partial \delta / \partial x^2 + 1)^{-1/2}, \quad (5.2)$$

$$\vec{\tau} = (-1, -\partial \delta / \partial x, 0)^T (\partial \delta / \partial x^2 + 1)^{-1/2},$$

where \vec{n} and $\vec{\tau}$ form an orthonormal surface coordinate system in the x - y -plane with \vec{n} pointing into the liquid phase (as opposed to the system defined in 2.2, and κ designates the interface curvature. From the above equation it is clear that interfacial vorticity in the CSE region should be negative, which concurs with figure 5.10(b). In order to identify the generating source of this negative vorticity, the normal vorticity flux at the interface is introduced (see Lundgren & Koumoutsakos (1999) for a derivation):

$$-\nu \vec{\nabla} \cdot \vec{n} \omega_z = -\vec{u} \cdot \vec{n} \left[\vec{\nabla} \cdot \vec{\tau} (\vec{u} \cdot \vec{n}) + \kappa \vec{u} \cdot \vec{\tau} \right] - \frac{d}{dt} (\vec{u} \cdot \vec{\tau}) + \frac{1}{\rho} \vec{\nabla} \cdot \vec{\tau} p - \vec{g} \cdot \vec{\tau}. \quad (5.3)$$

Following Wu (1995), the net vorticity generation rate per unit interfacial area[†] can be determined from an interfacial vorticity balance as the sum of liquid-side and gaseous-side diffusive vorticity fluxes, given by equation 5.3 (assuming that the normal vector always points into the considered phase). In this balance all right hand side terms of equation 5.3 except the tangential pressure derivative cancel out, due to the continuity of velocity across the interface. The vorticity generation rate is then given by the interfacial jump of the term $(1/\rho) \vec{\nabla} \cdot \vec{\tau} p$ and thus has a baroclinic origin. Assuming, for simplicity, a constant pressure in the gaseous phase, and considering the negative tangential liquid-side pressure gradient (which follows from the positive streamwise pressure gradient and the definition of the tangential coordinate according to equation 5.2), the interfacial vorticity generation rate in the CSE region must be negative i.e.

[†]Which has a unit of flow rate per time and area and should be understood as the source feeding the vorticity fluxes.

negative vorticity is produced at the interface and diffuses into both phases. In summary, the CSE region is thus characterized by the cross diffusion and partial annihilation of two vorticity fluxes of opposing sign generated at the respective crosswise boundaries. Wu (1995) proposed an alternative to the concept of annihilation of vorticities of opposing sign (introduced by Morton (1984)), preferring to describe the process as the dissipation of enstrophy (i.e. one half the volume integral of the square of vorticity) between the wall and the free surface.

5.2 Governing dynamics

From elaborations concerning the kinematics of capillary flow separation in section 5.1, it is clear that this phenomenon is quite similar to “classical” *boundary layer separation* of wall-bounded single-phase flows (see e.g. Prandtl (1961) and Sychev (1998)) at least in the early stages of its development (see subfigures 5.1(a) to 5.1(g) and 5.2(a) to 5.2(c)). This also holds for the developed state of the phenomenon if the CSE stays contained within the liquid film’s residual layer, as is the case for the inclined film in subfigure 5.1(h). If however, the CSE outgrows the local film thickness, as is the case for the vertically falling liquid film in subfigure 5.2(h), this similarity is no longer valid and considerably different kinematics take hold. Indeed, as discussed in subsection 5.1.1 regarding the break-up of the CSE and in subsection 5.1.3 regarding capillary vorticity transport, kinematics are considerably altered by the interaction between CSE and interface.

An even more important difference with respect to “classical” boundary layer separation concerns the governing dynamics of capillary flow separation. While the driving cause of boundary layer separation is an adverse pressure gradient imposed by the *external flow*, falling liquid films under investigation in this thesis flow in a largely quiescent gaseous atmosphere (any flow developing in the gaseous phase is driven by the liquid film and confined to the interfacial region), which is virtually unbounded on the far-field side. Consequently, the driving cause for capillary flow separation cannot stem from the external

gaseous phase and therein lies the difference with “classical” boundary layer separation. Accordingly, it is the goal of this section to establish the distinct governing dynamics of capillary flow separation in laminar falling liquid films. This will be done on the basis of numerical data for the two cases also treated in section 5.1, i.e. an inclined (see case 1 in table 3.1 and figure 5.1) and a vertically falling (see case 8 in table 3.1 and figure 5.2) liquid film, since these permit an evaluation of liquid phase forces, which were not experimentally accessible.

The occurrence of flow separation in falling liquid films, especially in the case of a vertical arrangement, is at first unexpected, since this means that liquid flows in the direction opposite to gravity, which accelerates the film downward in the first place. Thus, the principal question to be answered concerns the force causing such flow reversal. Obviously, this force must act in upstream direction. Considering that the wall parallel component of the gravitational force acts in downstream direction and that viscosity forces are inner forces, only the resulting pressure force on a fluid element can be retained as such[†] (see the illustration on the right hand side of figure 5.11). Moreover, since capillary flow separation initiates at the bounding wall, it is the wall distribution of static pressure, that is of principal interest. Accordingly, one can conjecture that capillary flow separation must be caused by a positive streamwise wall pressure derivative occurring in the capillary wave region. The elucidation of the mechanism generating this positive pressure derivative represents one of the main contributions of this thesis. In order to explain it, the nature of the relation between liquid phase static pressure and interface topology is recalled here. This relation is given by the normal coupling condition (see equations 2.4 and 2.17) between liquid and gaseous phase, which was previously introduced in section 2.1.

For considerations in the capillary wave region, the normal coupling condition can be considerably simplified. Indeed, in this region, it can be assumed that contributions of pressure and surface tension forces are dominant. This follows from the large Kapitza number values exhibited by the employed work-

[†]Solutocapillary and thermocapillary forces were previously excluded from investigations in the context of this thesis.

ing liquids, meaning that capillary forces dominate viscous forces. Further, as established in subsection 5.1.2 in regard to subfigure 5.5(b), the local Reynolds number value at the first capillary minimum is of order unity[†]. Bearing in mind that $We = 3^{1/3} Ka Re^{-5/3}$, the above established conditions ($Ka \gg 1$, $Re \approx 1$) signify that the local Weber number in the capillary wave region is large ($We \approx 700$ for conditions represented in subfigure 5.5(b)). As can be deduced from the dimensionless form of the normal coupling condition in equation 2.17 (if local length and velocity scales are introduced), this formally establishes that viscous terms can be neglected. The interfacial pressure jump being the only other remaining term (neglecting the effect of viscous forces in the gaseous phase), it must have the same magnitude as the capillary term.

Introducing the above assumptions and assuming negligible pressure variations in the gaseous phase, the normal coupling condition in equation 2.4 yields the following simple relation between the streamwise derivative of interfacial liquid pressure and the film thickness:

$$\frac{\partial p_1}{\partial x} = -\sigma \frac{\partial \kappa}{\partial x}, \quad \kappa = \frac{\partial^2 \delta / \partial x^2}{\left(1 + \left(\frac{\partial \delta}{\partial x}\right)^2\right)^{3/2}}, \quad (5.4)$$

or in dimensionless form:

$$\frac{\partial p_1^*}{\partial x^*} = -\frac{\epsilon We}{3^{1/3}} \frac{\partial \kappa^*}{\partial x^*}, \quad \kappa^* = \frac{\epsilon \partial^2 \delta^* / \partial x^{*2}}{\left(1 + \epsilon^2 \left(\frac{\partial \delta^*}{\partial x^*}\right)^2\right)^{3/2}}. \quad (5.5)$$

According to this relation, the interfacial liquid pressure distribution in falling liquid films is imposed by surface tension forces, attaining influence due to a wave-induced distortion of the interface, the degree of which is expressed by the streamwise derivative of interface curvature κ .

The physical mechanism underlying equation 5.4 results from the interfacial pressure jump caused by tensile forces, which was previously discussed in section 2.2.1, regarding capillary waves on a horizontal liquid layer, and is

[†]“Inertial” and viscous forces are thus of the same magnitude and both dominated by surface tension forces.

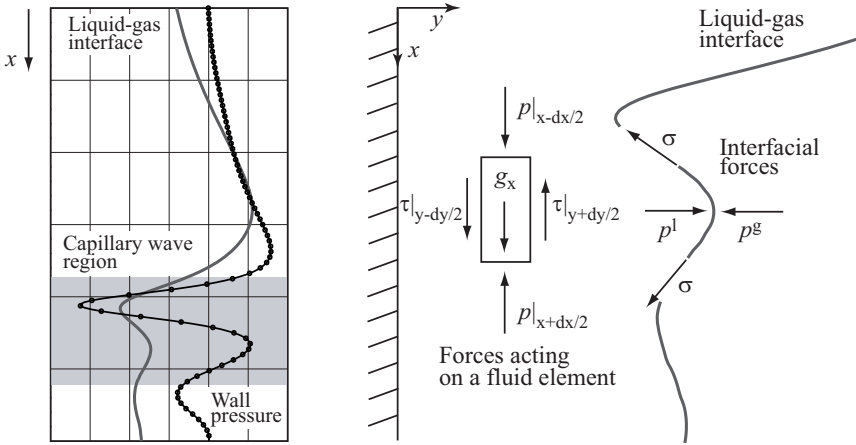


Figure 5.11: Sketch illustrating the relation between interface topology and liquid phase static pressure given by equation 5.6.

given by equation 2.24. A corresponding illustration pertaining to falling liquid films is provided on the right hand side of figure 5.11. According to this, the interfacial pressure jump (from liquid to gas) must act in opposition to tensile forces to maintain the interface's distortion. Consequently, it is negative in a wave hump and positive in a wave trough (as illustrated in figure 2.2). Neglecting pressure variations in the gaseous phase, this means that liquid pressure increases from wave trough to wave hump. As a result, assuming a streamwise succession of wave trough and wave hump, this yields a positive (or adverse) streamwise pressure derivative. Or, in other words, a resulting pressure force directed upstream. At the same time, the streamwise change in interface curvature from positive in the wave trough to negative in the wave hump is negative, which is in accordance with equation 5.4. However, in the case of a smooth film $\partial\kappa/\partial x = 0$, leading to a constant interfacial liquid pressure. Finally, as can be deduced from equation 5.5, the coupling between interface distortion ($\partial\kappa^*/\partial x^*$) and pressure derivative ($\partial p_l^*/\partial x^*$) is scaled by the Weber number,

which consequently is one of the governing dimensionless groups of capillary flow separation.

In falling liquid films, the interfacial pressure distribution is largely imposed on the bounding wall, due to the mainly hydrostatic nature of crosswise pressure variations, as established by Malamataris *et al.* (2002). Indeed, resulting from relatively small crosswise velocity values in most parts of the liquid film's capillary wave region (see vector plots in figure 5.6), the pressure term and the gravitational term are dominant in the crosswise momentum equation. Admittedly, these dynamical conditions are altered somewhat by the CSE, as evidenced by the vector plot in subfigure 5.6(c) and the corresponding streamline plot in subfigure 5.5(a) (see also PIV data in subfigure 5.36(d) of section 5.4). These show that, in the vicinity of the separation streamlines bounding the CSE in streamwise direction, velocity vectors point in crosswise direction, leading to a larger contribution of crosswise "inertial" and viscous forces, and challenging the assumption of a purely hydrostatic crosswise pressure variation. Indeed, Malamataris *et al.* (2002) observed deviations from the hydrostatically predicted wall pressure minimum at the first capillary minimum, where, as established in subsection 5.1.1, the CSE develops, showing the actual wall pressure to be larger. However, this deviation was rather small for most flow conditions and confined almost discontinuously to the position of the pressure minimum. Meanwhile, the rest of the capillary pressure distribution closely followed the hydrostatic prediction. Consequently, the streamwise modulation of interfacial pressure is close to preserved at the wall. Moreover, the direction of causality between pressure distribution and capillary flow separation is clear, the pressure distribution being the cause and flow separation the effect. Therefore, when considering the inception of the CSE, assuming the wall pressure distribution to be imposed by the corresponding interfacial pressure distribution (allowing for hydrostatic variation) is admissible.

In summary, for the purpose of explaining the governing dynamics of capillary flow separation, it can be stated that the liquid pressure distribution (and more specifically the wall pressure distribution) in the capillary wave region of falling liquid films is largely imposed by the interfacial topology there.

Thereby, the streamwise derivative of wall pressure is approximately given by the corresponding streamwise derivative of interfacial pressure:

$$\left. \frac{\partial p}{\partial x} \right|_{y=0} \approx \frac{\partial p_i}{\partial x} = -\sigma \frac{\partial \kappa}{\partial x}. \quad (5.6)$$

Consequently, the sign and absolute value of the streamwise wall pressure derivative (for a given liquid) are defined by the streamwise derivative of the interface curvature.

Therewith, a potential cause for the adverse streamwise wall pressure derivative, conjectured to be at the root of capillary flow separation in falling liquid films, has been identified. It is a negative streamwise derivative of interface curvature. In order to assess the occurrence of such conditions (conducive to flow separation) in falling liquid films, figures 5.12 and 5.13 illustrate streamwise distributions of wall pressure and film thickness (subfigures 5.12(b) and 5.13(b)) as well liquid phase contour plots of the streamwise velocity component (subfigures 5.12(a) and 5.13(a)) over one wavelength for the inclined and vertically falling liquid film respectively. To be precise, the difference between wall pressure $p_{y=0}$ and a gaseous phase reference pressure $p_r=101325$ Pa is plotted in subfigures 5.12(b) and 5.13(b) for convenience[†]. A qualitative representation of typical (for the liquid films considered in this thesis) wall pressure and film thickness distributions is also plotted on the left hand side of figure 5.11.

From this figure as well as subfigures 5.12(b) and 5.13(b) it is evident that the general interface topology of solitary waves with preceding capillary waves exhibits several regions with a positive (or adverse) streamwise wall pressure derivative, which are thus conducive to flow separation. First of all, this is the case for the wave back, where the interface curvature changes slightly from positive to negative while approaching the wave crest. Correspondingly, a slight increase in wall pressure is evident there. A much stronger streamwise increase of wall pressure arises between the first capillary minimum and first capillary

[†]Similar plots were previously introduced in section 2.3 in the form of figures 2.17(b) and 2.17(c).

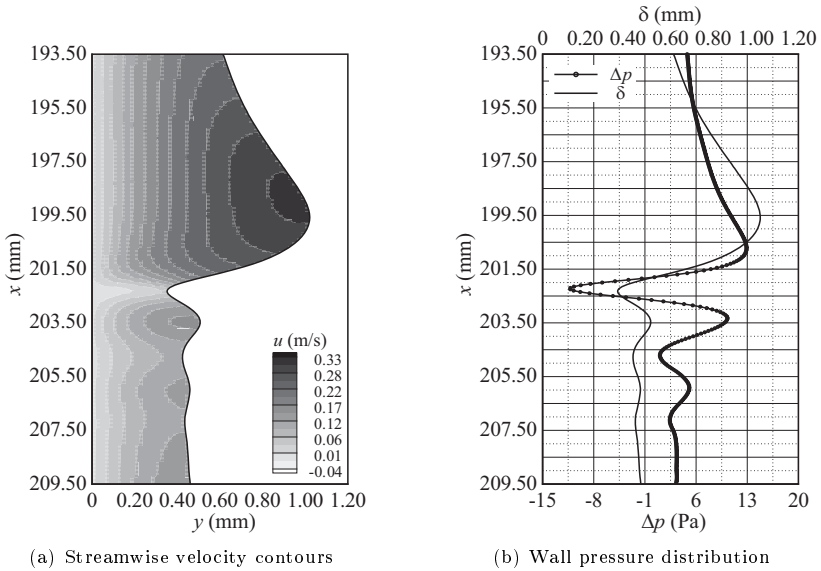


Figure 5.12: Wave topology, streamwise velocity contours and corresponding wall pressure difference ($\Delta p = p|_{y=0} - p_r$) distribution for case 1.

maximum. This drastic increase results from the small length of the first capillary wave and the large curvature magnitude of its wave trough and wave hump, both characteristics contributing to a large negative streamwise derivative of interface curvature. The region between the second capillary minimum and maximum also displays a strong adverse wall pressure derivative, which is larger than that in the wave back yet considerably smaller than that in the first capillary wave. Based on the nature of capillary waves and the relation in equation 5.6 it can be extrapolated that a positive wall pressure derivative occurs in every capillary wave. It can therewith be concluded that the capillary wave region, and especially the first capillary wave, is the most conducive to flow separation in falling liquid films, which is in accordance with the kinematic observations in figures 5.1, 5.2 and 5.6, which show the CSE to develop exactly

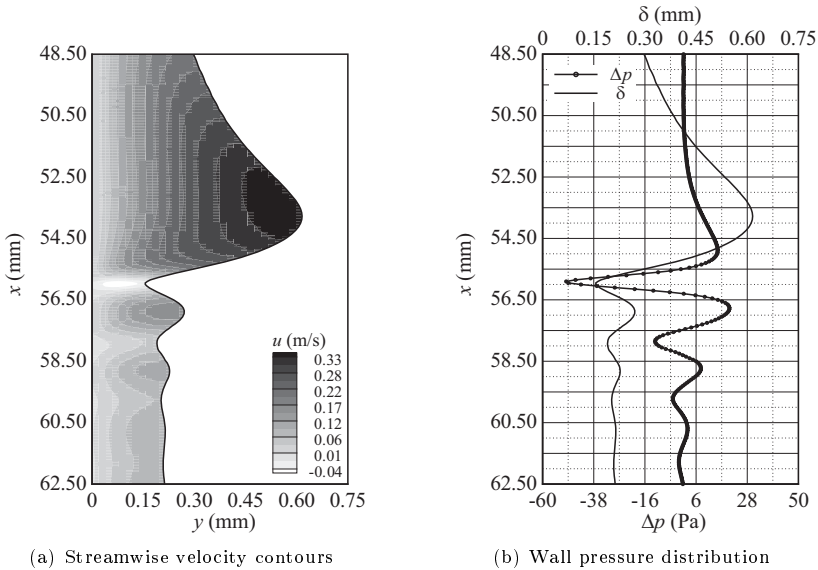


Figure 5.13: Wave topology, streamwise velocity contours and corresponding wall pressure difference ($\Delta p = p|_{y=0} - p_r$) distribution for case 8.

there.

A comparison of subfigures 5.12(b) and 5.13(b) yields another interesting observation. Indeed, the increase in wall pressure from first capillary minimum to first capillary maximum is significantly larger (approximately by a factor of 3) for case 8 compared to case 1, which can be explained on the basis of equation 5.6. According to this, the fact that the surface tension for case 8 is larger than for case 1 by a factor of 2.2 (see table 3.2) accounts for the major share in the increase. The rest stems from a smaller capillary wavelength for case 8, the curvature at the first capillary extrema being approximately equal for both cases. In the rest of the capillary wave region the wall pressure distribution for case 8 also displays stronger modulations than for case 1, which corresponds

to stronger modulations of the streamwise velocity component as illustrated in subfigures 5.12(a) and 5.13(a).

In order to assess the above elaborations in greater detail, dynamical conditions in the capillary wave region for the two representative falling liquid films, i.e. cases 1 and 8 in table 3.1, will be investigated quantitatively in the remaining part of this section. Figures 5.14(a), 5.15(a) and 5.16(a) depict streamwise distributions of film thickness and static wall pressure difference $\Delta p = p|_{y=0} - p_r$ for the inclined liquid film (case 1 in table 3.1) at points in time corresponding to the streamline plots in subfigures 5.3(a), 5.3(c) and 5.4(a). This permits an assessment of the adverse wall pressure derivative in the first capillary wave as the latter develops over time. Indeed, an increase in the pressure derivative's magnitude is clearly discernible in the succession of subfigures 5.14(a), 5.15(a) and 5.16(a) as the capillary waves grow. This evolution concurs with the episodes of flow deceleration, CSE nucleation and CSE growth illustrated in subfigures 5.3(a), 5.3(c) and 5.4(a). However, in order to assess the possibility of flow separation, it does not suffice to investigate the pressure distribution along the wall. Rather, the resulting streamwise pressure force acting on a fluid element (given by $-\partial p/\partial x|_{y=0}$) must be compared to the streamwise component of the gravitational force (given by $\rho_l g_x$), as illustrated on the right hand side of figure 5.11. Only if the former surmounts the latter, the resulting streamwise external force acts in upstream direction, enabling flow deceleration and eventually flow reversal and separation. Or, in terms of a quantitative criterion:

$$\left. \frac{\partial p}{\partial x} \right|_{y=0} > \rho_l g_x \quad \text{or} \quad \left. \frac{\partial p^*}{\partial x^*} \right|_{y=0} > \frac{2g_x/g_y}{\varepsilon Fr^2}. \quad (5.7)$$

Expressing the pressure derivative in terms of the interface curvature according to equation 5.6 then yields the following condition:

$$\frac{\partial \kappa}{\partial x} < -\frac{2g_x}{\sigma} \quad \text{or} \quad \frac{\partial \kappa^*}{\partial x^*} < -3^{1/3} \frac{2g_x/g_y}{\varepsilon^2 Fr^2 We}. \quad (5.8)$$

Consequently, the dimensionless groups scaling capillary flow separation are the

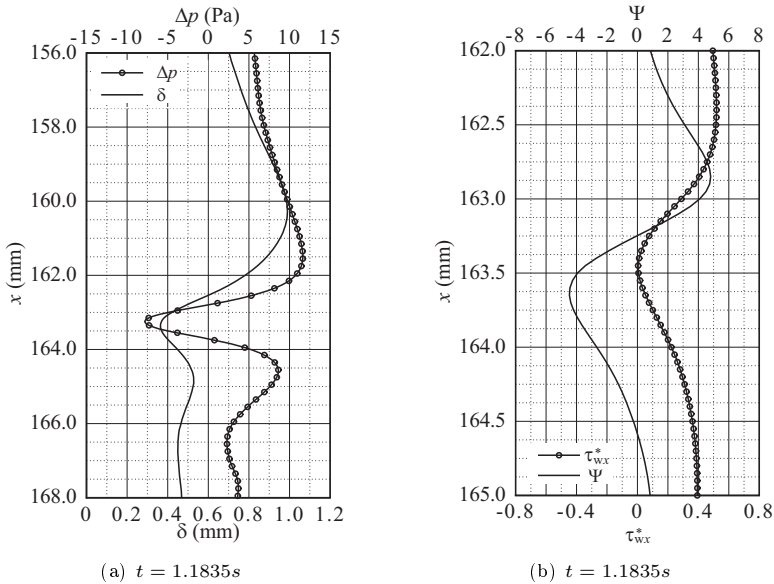


Figure 5.14: Numerical data corresponding to streamlines in figure 5.3(a). (a): static wall pressure difference and film thickness for one wave; (b): dimensionless wall shear stress and force ratio Ψ at the first capillary minimum (note the change in ordinate scale).

Weber number We , the Froude number Fr and the ratio g_x/g_y , which defines the film's inclination[†]. The above criterion is merely necessary and not sufficient, as the effect of viscous forces is not accounted for. However, its general form is correct, since viscous forces would only influence its quantitative threshold.

In order to assess the fulfillment of this criterion by the pressure distributions in subfigures 5.14(a), 5.15(a) and 5.16(a), the ratio Ψ of resulting streamwise pressure force per unit volume (evaluated at the wall) $-\partial p/\partial x|_{y=0}$ to streamwise gravitational force per unit volume $\rho_1 g_x$ as well as the dimensionless

[†]Alternatively, g_x/g_y can be expressed in terms of Re and Fr .

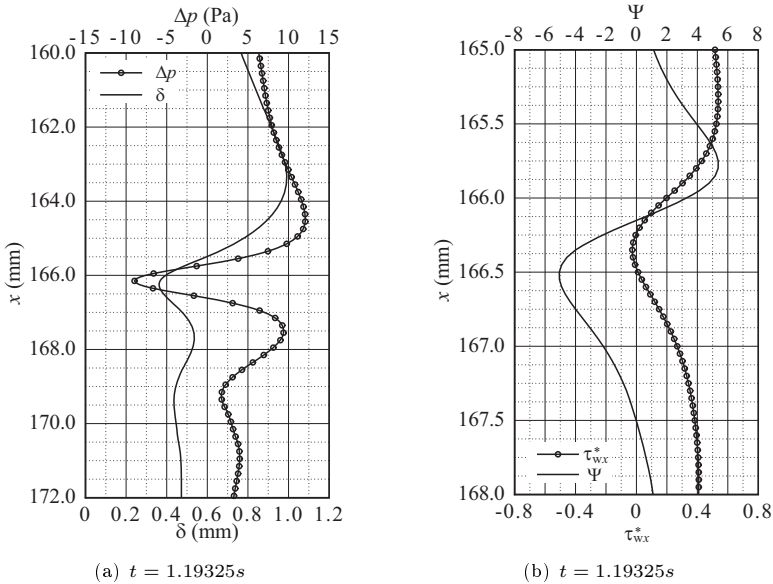


Figure 5.15: Numerical data corresponding to streamlines in figure 5.3(c). (a): static wall pressure difference and film thickness for one wave; (b): dimensionless wall shear stress and force ratio Ψ at the first capillary minimum (note the change in ordinate scale).

streamwise wall shear stress τ_{wx}^* :

$$\Psi = - \left. \frac{\partial p}{\partial x} \right|_{y=0} \rho_l g x, \quad \tau_{wx}^* = \frac{2}{Re} \left. \frac{\partial u^*}{\partial y^*} \right|_{y^*=0} \quad (5.9)$$

are plotted in figures 5.14(b), 5.15(b) and 5.16(b) for the points in time corresponding to figures 5.14(a), 5.15(a), and 5.16(a). Thereby, if $\Psi < -1$ condition 5.7 is fulfilled. Subfigures 5.14(b), 5.15(b) and 5.16(b) show that Ψ falls below -1 only in the capillary wave region, which consequently is the only one where flow separation can take place. Indeed, $\Psi < -1$ occurs in the first capillary wave for all three points in time. Thereby, the minimal value of Ψ decreases

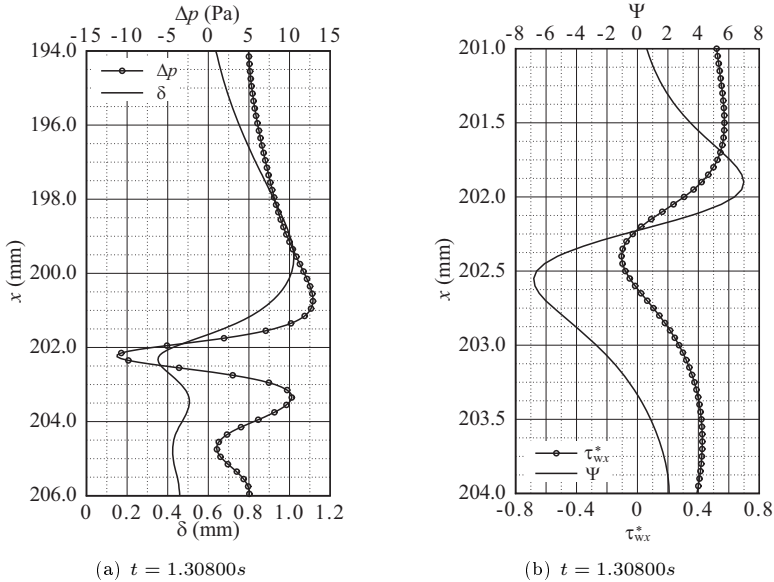


Figure 5.16: Numerical data corresponding to streamlines in figure 5.4(a). (a): static wall pressure difference and film thickness for one wave; (b): dimensionless wall shear stress and force ratio Ψ at the first capillary minimum (note the change in ordinate scale).

drastically as the capillary waves grow more pronounced (compare subfigures 5.14(b), 5.15(b) and 5.16(b)). This confirms that it is the adverse pressure distribution exhibited by subfigures 5.14(a), 5.15(a) and 5.16(a), that causes the episodes of flow deceleration, CSE nucleation and CSE growth shown in subfigures 5.3(a), 5.3(c) and 5.4(a).

However, flow separation, evidenced by a sign change in the dimensionless wall shear stress τ_{wx}^* , does not occur as soon as $\Psi < -1$. Indeed, subfigure 5.14(b) does not exhibit flow separation at all although Ψ attains a minimal value of approximately -5. Further, at the upstream separation point (defined by

$\tau_{wx}^*=0$) in subfigure 5.15(b), Ψ is significantly inferior to -1. This delay is caused by the effect of viscous forces, which are not accounted for in inequality 5.7. Granted, as long as the second order derivative of the streamwise velocity component at the wall ($\partial^2 u / \partial y^2|_{y=0}$) is negative (as is the case at $x=163.02$ mm in subfigure 5.3(b)), the resulting viscous force on a fluid element acts upstream and thus supports flow reversal. However, the path to flow separation leads through a sign change of $\partial^2 u / \partial y^2|_{y=0}$ as evidenced by the streamwise evolution of velocity profiles in subfigures 5.3(d) and 5.4(b). Consequently, as soon as $\partial^2 u / \partial y^2|_{y=0} > 0$, the resulting viscous force acts counter to the adverse pressure derivative and represents an additional[†] finite threshold the latter needs to surmount in order for flow separation to occur. For the point in time represented by subfigures 5.14(b) and 5.3(b) this does not occur as the resulting upward external force is compensated by the resulting downward viscous force arising from the positive curvature of near-wall velocity profiles (see profiles at $x=163.46$ mm and $x=163.68$ mm in subfigure 5.3(b)).

Similarly, the positive second derivative $\partial^2 u / \partial y^2|_{y=0}$ near the upstream separation point in subfigure 5.3(c) (see corresponding velocity profile at $x=166.19$ mm in subfigure 5.3(d)) is relatively large, necessitating a lower value for Ψ , as evidenced by subfigure 5.15(b).

However, once the CSE is developed (see subfigures 5.4(a), 5.4(b) and 5.16(b)), the criterion $\Psi=-1$ is closely met at the upstream separation point. This results from the shape of the developed CSE in subfigure 5.4(a), which displays a steepened separation streamline at its upstream front. Indeed, the corresponding velocity profile at the upstream separation point ($x=202.22$ mm in subfigure 5.4(b)) exhibits an almost vanishing curvature at the wall, reducing the effect of viscous forces there. To be precise, Ψ is slightly larger than -1 at the upstream separation point, which can be attributed to inertia. Indeed tracking a near-wall fluid element in subfigure 5.4(a) as it approaches the separation point from below, the latter does not suddenly reverse its flow direction as soon as it enters the region where $\Psi > -1$ (i.e. where a resulting downstream force acts upon it), but requires a certain time for deceleration.

[†]In addition to that represented by gravity.

Finally, it must be considered that a fluid element flowing downstream is exposed to the adverse pressure gradient caused by the capillary waves only for a limited time span, since the wave celerity is larger than the fluid velocity in the residual layer[†]. Thus, the resulting adverse force acting on a fluid element must be sufficiently large to decelerate the latter to the point of flow reversal and beyond within this short time span in order for flow separation to occur. A detailed investigation of this aspect would be highly interesting as it is specific to flow separation in falling liquid films. However, this must be deferred to future work, as it exceeds the scope of this thesis.

To conclude this section, a dynamical analysis of flow separation in the vertically falling liquid film (case 8 in table 3.1) is performed next. Therein, rather than rigorously repeating the quantitative analysis performed for the inclined film, two further aspects will be discussed. First, it will be established to what extent the streamwise distribution of Ψ can explain the PIV vector plots in the capillary wave region depicted in figure 5.6. Second, the break-up and subsequent “contraction” of the CSE as it interacts with the interface (see subfigures 5.2(d) to 5.2(f)) will be analysed from a dynamical perspective.

Subfigures 5.17(a), 5.18(a), 5.19(a) and 5.20(a) depict liquid phase velocity vectors evaluated from numerical data for the four characteristic regions also represented in figure 5.6, i.e. the second capillary minimum, the first capillary maximum and minimum and the wave front. First of all, comparing experimental and numerical vector plots, good agreement between the two data sets can be established[‡]. In subfigures 5.17(a), 5.18(a), 5.19(a) and 5.20(a), contours of the liquid pressure difference $\Delta p = p - p_r$ are additionally displayed in order to assess the capillary effect driving flow in the capillary wave region. These contours show, in accordance with equation 2.24, positive pressure differences in the wave humps and negative values in the wave troughs as well as the resulting pressure gradients between these regions.

In order to evaluate the resulting driving external force on a fluid element,

[†]A detailed discussion of this aspect will be presented in section 5.3.

[‡]Numerical data were scaled the same way as corresponding PIV data to facilitate comparison.

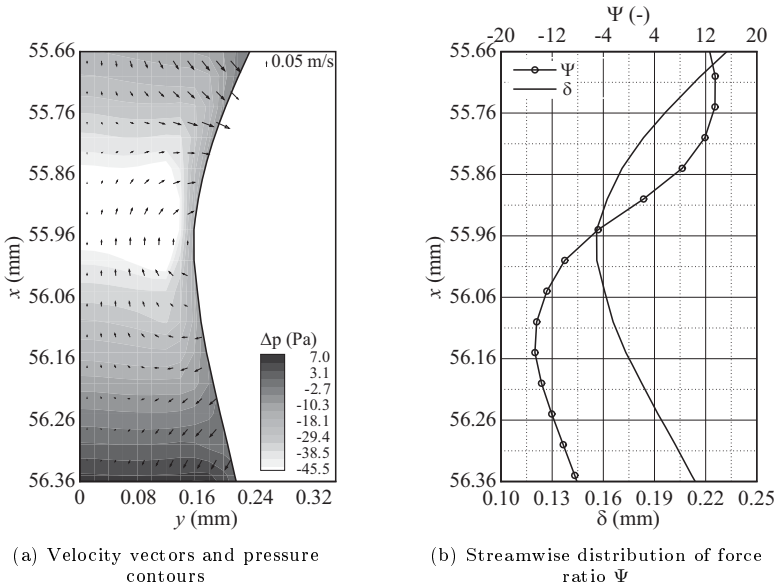


Figure 5.17: Simulated liquid phase velocity vectors and pressure contours as well as streamwise distribution of the force ratio Ψ for case 8: first capillary minimum.

streamwise distributions of the force ratio Ψ and the film thickness, corresponding to subfigures 5.17(a), 5.18(a), 5.19(a) and 5.20(a) are plotted in subfigures 5.17(b), 5.18(b), 5.19(b) and 5.20(b) respectively.

The Ψ -distribution in the region of the first capillary minimum (where the CSE occurs) exhibits two interesting features (see subfigure 5.17(b)). First, Ψ attains a minimum of approximately -16, which is 2.5 times lower than the corresponding value for the inclined film (see subfigure 5.16(b)). This follows from the significantly larger (by a factor of 3.5) adverse pressure derivative as discussed in regard to figures 5.12(b) and 5.13(b), the effect of which is partially mitigated by the larger (by a factor of 1.7) streamwise component of

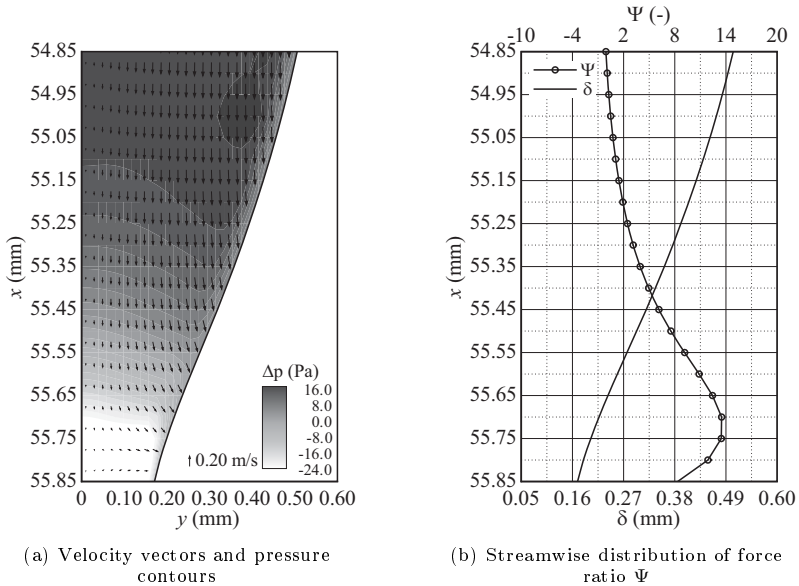


Figure 5.18: Simulated liquid phase velocity vectors and pressure contours as well as streamwise distribution of the force ratio Ψ for case 8: wave front.

gravitational acceleration. These conditions explain the significantly “stronger” backflow exhibited by the vertically falling liquid film, as evidenced by the velocity profiles in subfigure 5.5(b) (compare to profiles in subfigure 5.4(b)). Moreover, they explain the larger crosswise size of the CSE. Indeed, as Ψ^\dagger attains smaller values for the vertical film, “faster” fluid elements traveling further from the wall can be decelerated to the point of reversal and beyond during the transition time of the capillary wave region.

Second, the upstream separation point identifiable in subfigure 5.17(a) lies significantly farther upstream than the point at which $\Psi=-1$ (see subfigure

[†]Although Ψ is defined at the wall it is representative for the film’s cross section due to the hydrostatic nature of crosswise pressure variations.

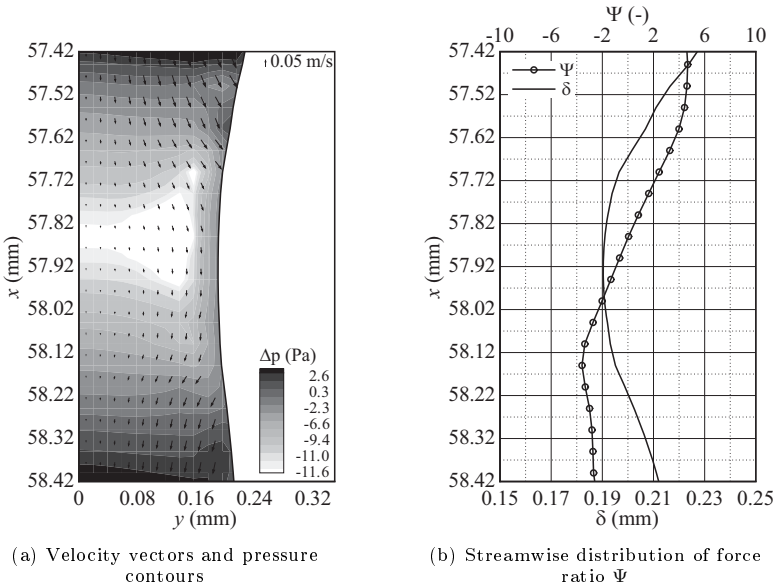


Figure 5.19: Simulated liquid phase velocity vectors and pressure contours as well as streamwise distribution of the force ratio Ψ for case 8: second capillary minimum.

5.17(b)). This follows from the inertial effect discussed with respect to the inclined film. In the vertically falling film this effect is stronger, since fluid elements traveling upward in the CSE exhibit a significantly larger (by a factor of 14) velocity (compare subfigures 5.5(b) and 5.4(b)).

In the region of the wave front (see figure 5.18), Ψ exceeds -1 over the entire displayed length, attaining its maximum slightly upstream of the wave trough. At this position, rather surprisingly, the flow is decelerated instead of being accelerated, as opposed to the rest of the region farther upstream. This is due to the effect of the CSE, which to a certain degree extends upstream. By way of explanation, at the separation streamline of the CSE (see subfigure 5.5(a)), two

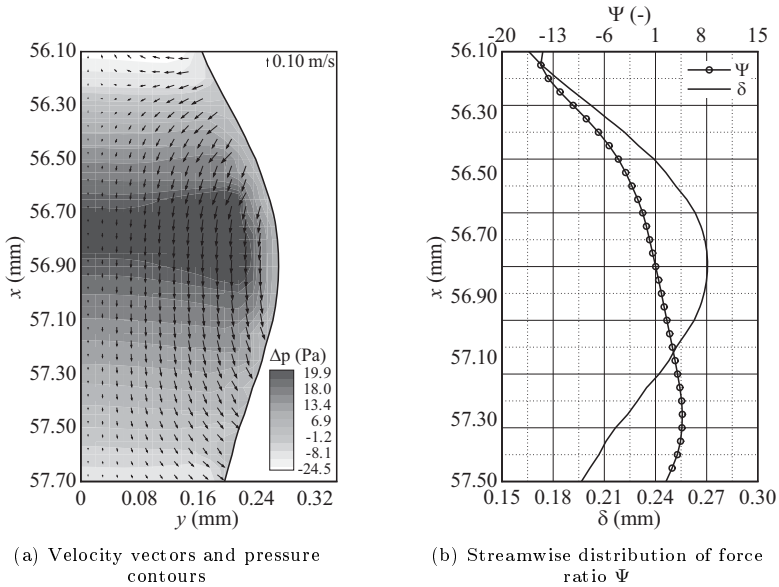


Figure 5.20: Simulated liquid phase velocity vectors and pressure contours as well as streamwise distribution of the force ratio Ψ for case 8: first capillary maximum.

flows impinge on one another. One approaches from the wave front above and the other from the CSE below. Thus, the streamwise position of the separation streamline depends on the momentum[†] of these respective flows. In the case considered here, the momentum of the CSE dominates, resulting from the fact that the magnitude of the Ψ -distribution's minimum $\Psi_{\min} \approx -16$, which lies in the CSE region (see subfigure 5.17(b)), is larger than that of the distribution's maximum $\Psi_{\max} \approx 14$, which lies in the region of the wave front (see 5.18(b)). In other words, the cause driving the upward flow from below is stronger than that driving the downward flow from above.

[†]More precisely, the associated inertia.

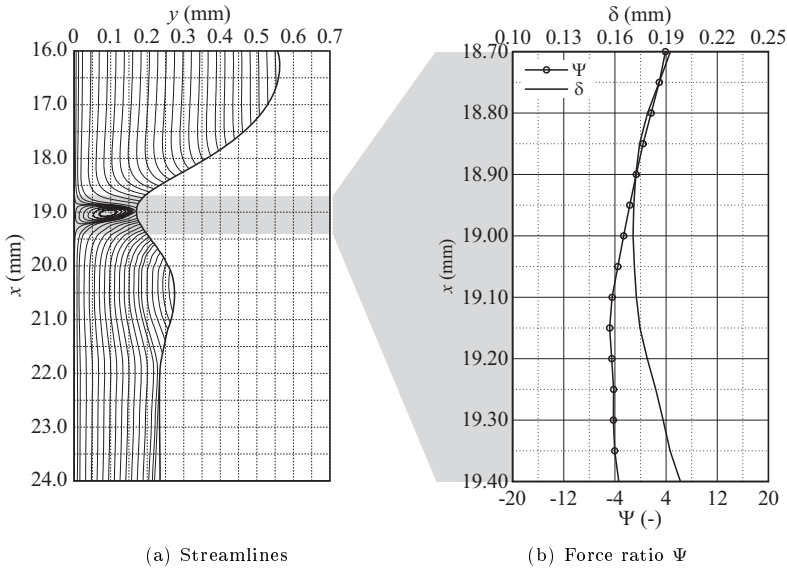


Figure 5.21: Streamlines in the capillary wave region and streamwise distribution of the force ratio Ψ for simulation case 8: $t=2.97000$ s.

In the regions of the second capillary minimum and first capillary maximum, as displayed in subfigures 5.19(b) and 5.20(b), the magnitude of the Ψ -distribution's local extrema is considerably smaller than for the two other regions (subfigures 5.17(b) and 5.18(b)). This leads to an increase in the effect of inertia, as evidenced by the shift between the flow's state of acceleration (discernible in subfigures 5.19(a) and 5.20(a)) and the corresponding value of Ψ (discernible in subfigures 5.19(b) and 5.20(b)). In other words, the flow in these regions cannot adapt sufficiently fast to new dynamical conditions imposed by the propagating wavy interface.

Finally, subfigures 5.21(a), 5.22(a), 5.23(a) and 5.24(a) depict streamlines in the entire capillary wave region for points in time corresponding to subfigures 5.2(d) to 5.2(g). These show the initial break-up, re-“contraction” and final

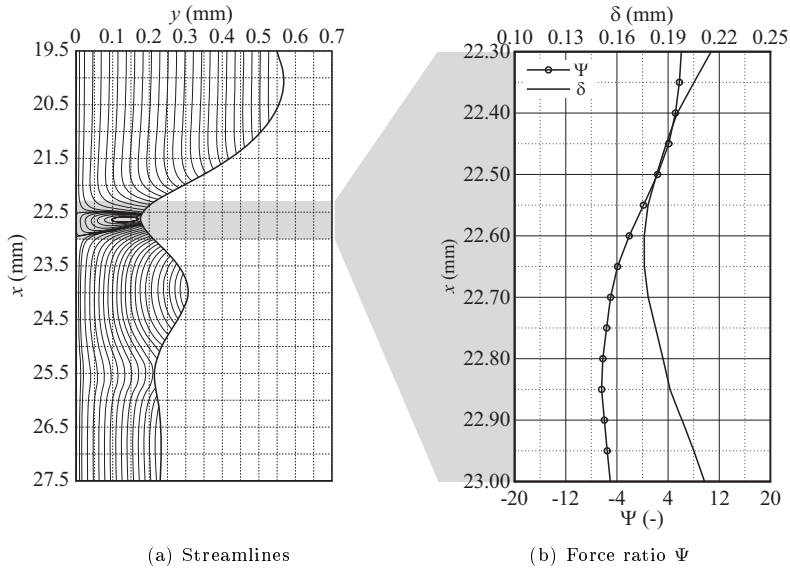


Figure 5.22: Streamlines in the capillary wave region and streamwise distribution of the force ratio Ψ for simulation case 8: $t=2.98250$ s.

break-up of the CSE, which were discussed in section 5.1.1. In order to assess the cause for this change in CSE topology, corresponding streamwise distributions of film thickness and force ratio Ψ are plotted in subfigures 5.21(b), 5.22(b), 5.23(b) and 5.24(b). Thereby, only the region surrounding the first capillary minimum is displayed. It is clear from these subfigures that the initial break-up is caused by the growth of the CSE, which is driven by a decrease in the minimum of the force ratio Ψ (from -4 to -7) as evidenced by subfigures 5.21(b) and 5.22(b). However, for all subsequent time steps, the value of Ψ_{\min} stays unchanged. Consequently, the closing of the CSE, the result of which is displayed in subfigure 5.23(a), cannot stem from a contraction on its part. Indeed, comparing the film thickness distributions in subfigures 5.22(a) and 5.23(a), it is evident that the change in CSE topology is caused by a

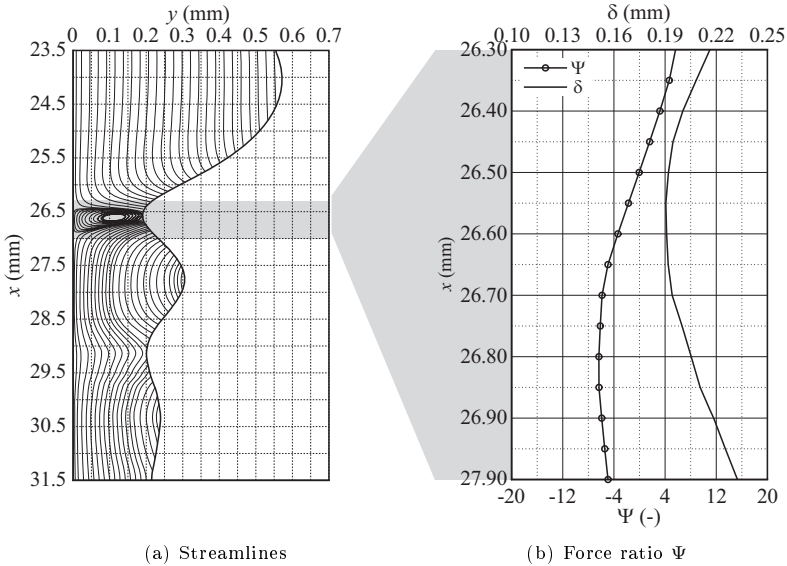


Figure 5.23: Streamlines in the capillary wave region and streamwise distribution of the force ratio Ψ for simulation case 8: $t=2.99500$ s.

film thickness increase at the first capillary minimum. This increase coincides with the growth of the second capillary wave (compare subfigures 5.22(a) and 5.23(a)) and is reversed once the capillary topology is established and the CSE has reached its final open shape (see subfigure 5.24(a)).

5.3 Effect on wall-side heat transfer

In the context of the literature review presented in section 2.3.2, it was established that wall-side heat and mass transfer to a liquid film are intensified by surface waves. Specifically, the reader is referred to the reviews by Seban & Faghri (1978) and Alekseenko *et al.* (1994) as well as landmark investigations by Wilke (1962), Oliver & Atherinos (1968), Frisk & Davis (1972), Brauner &

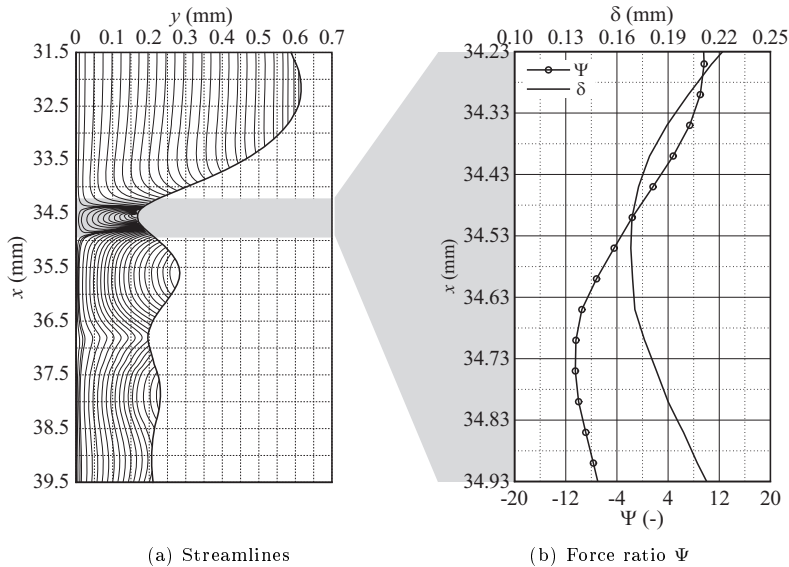


Figure 5.24: Streamlines in the capillary wave region and streamwise distribution of the force ratio Ψ for simulation case 8: $t=3.02000$ s.

Moalem Maron (1982) and Miyara (1999). Moreover, detailed experiments and numerical simulations have demonstrated that a drastic increase of the wall-side transfer coefficient occurs at the first capillary minimum for flow regimes exhibiting a pronounced capillary wave region (see the works of Adomeit *et al.* (2000), Miyara (2001), Kunugi & Kino (2005) and Schagen *et al.* (2006)). Finally, a number of investigations regarding *interfacial transfer* to falling liquid films have shown that the intensifying effect of waves is much stronger for this scenario as compared to *wall-side transfer* (see the reviews by Seban & Faghri (1978) and Alekseenko *et al.* (1994) as well as the works of Yoshimura *et al.* (1996) and Rastaturin *et al.* (2006)).

It is with these last two points in mind that the effect of capillary flow separation on wall-side heat transfer is investigated in this section. In accordance

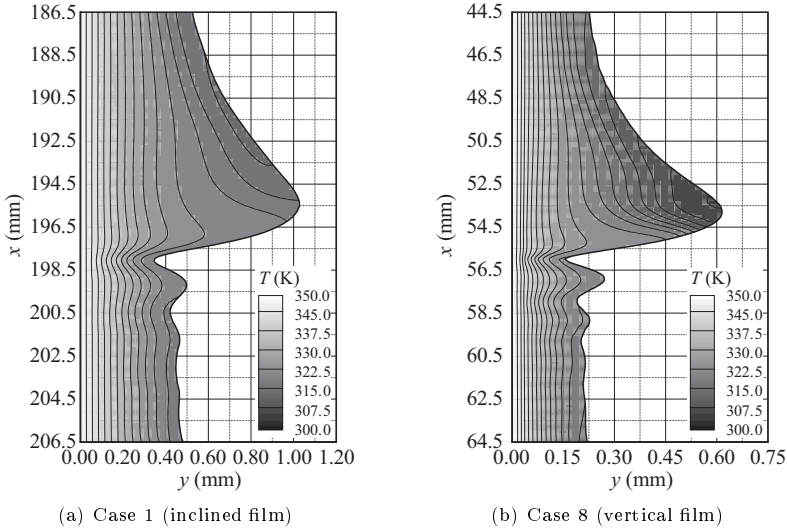


Figure 5.25: Simulated temperature contours in a single wave in the hydrodynamically and thermally developed region of the liquid film for cases 1 and 8.

with previous sections, this will be done on the basis of two representative flow regimes, namely cases 1 and 8 in table 3.1. For these two cases, heat transfer simulations were performed for a single set of thermal boundary conditions. These are quantified in table 3.5 along with thermal properties of the respective working liquids. Importantly, the case of constant wall temperature was investigated here. Numerical results of the two simulations are presented in figures 5.25 and 5.26 in the form of liquid phase temperature contours (5.25(a) and 5.25(b)) and profiles (5.26(a) and 5.26(b)) within a single surface wave evaluated in the hydrodynamically and thermally developed region of the film. In figure 5.25 it can be discerned that near-wall temperature contours are significantly distorted at the first capillary minimum for both investigated cases. This distortion occurs from above in the sense that near-wall temperature contours

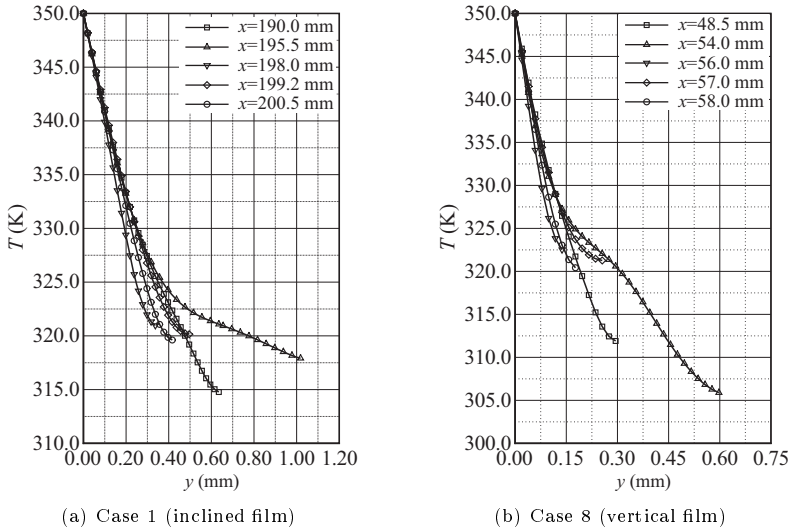


Figure 5.26: Simulated temperature profiles in a single wave in the hydrodynamically and thermally developed region of the liquid film for cases 1 and 8.

are compressed by a region of lower temperature gradient near the interface. Thereby, the extent of the compression decreases with decreasing wall distance and is barely discernible very close to the wall. This is also evident in the corresponding temperature profiles at $x = 198.0$ mm and $x = 56.0$ mm (displayed in subfigures 5.26(a) and 5.26(b)) respectively, which exhibit a crosswise derivative diminishing with wall distance. Meanwhile, the crosswise derivative at the wall is greatest at the position of the first capillary minimum. Thus, it can be concluded that the numerical data represented in figures 5.25 and 5.26 are in accordance with the two characteristics of liquid phase scalar transfer accentuated at the start of this section.

Based on the streamline plots illustrated in subfigures 5.4(a) and 5.5(a) corresponding to subfigures 5.25(a) and 5.25(b), which show a drastic effect of

the CSE on the velocity field in the region of the first capillary minimum, it is to be expected that the above described temperature field distortion in this region is caused by the capillary flow separation. Under this assumption, the underlying transport mechanism responsible for the transfer intensification is that of convection. Consequently, in the remainder of this section, the effect of the CSE on liquid phase convective transport as well as the resulting wall-side transfer characteristics will be investigated in greater detail.

As discussed in subsection 2.3.2, the conjecture that small eddies preceding large waves could be responsible for the intensification of scalar transfer to wavy liquid films has been proposed by a number of researchers (see e.g. Portalski (1964a) and Kunugi & Kino (2005)). Without attempting a detailed explanation of the underlying mechanism, it was assumed that such eddies would mix the liquid in the capillary wave region and thus increase the driving potential for scalar transfer. This conforms with an *Eulerian view* of the liquid phase velocity field, which has been duly employed in this thesis to introduce the kinematics of capillary flow separation and the associated CSE. In this view, the capillary flow separation is characterized by an eddy (the CSE) made up of annular streamlines and, consequently, one would assume that the associated mixing length is of the order of the eddy's size.

However, such an Eulerian view of the phenomenon does not account for an important aspect of wavy liquid films. Indeed, because the wave celerity is larger than the mean flow velocity in the residual layer, surface waves repeatedly pass over fluid elements traveling there. Consequently, the latter are subjected to the CSE's kinematics only for a more or less short transition period during which the capillary wave region passes over their current position. Conversely, this means that fluid elements are not trapped in the CSE but are rather swept-up and shed by it as it passes through. Thus, in order to elucidate the CSE's influence on liquid phase convective transport, it seems more promising to adopt a *Lagrangian view* of capillary flow separation.

Accordingly, figures 5.27 and 5.28 display the temporal evolution of fluid element pathlines in the residual layer of the liquid film for case 1. Thereby, subfigures 5.27(a) to 5.28(a) show the pathlines at five different points in time

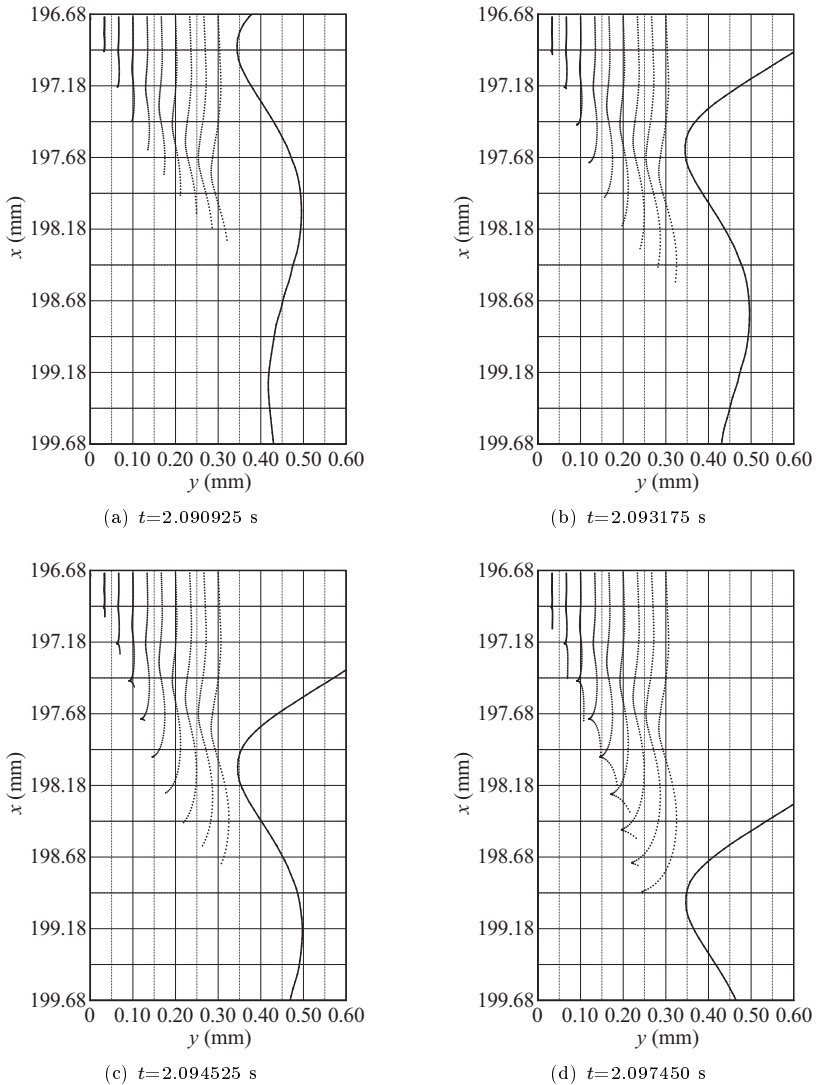


Figure 5.27: Simulated fluid element pathlines in the residual layer for case 1 (calculated from the starting time $t=2.075625$ s) at different time points during the transition of the first capillary minimum.

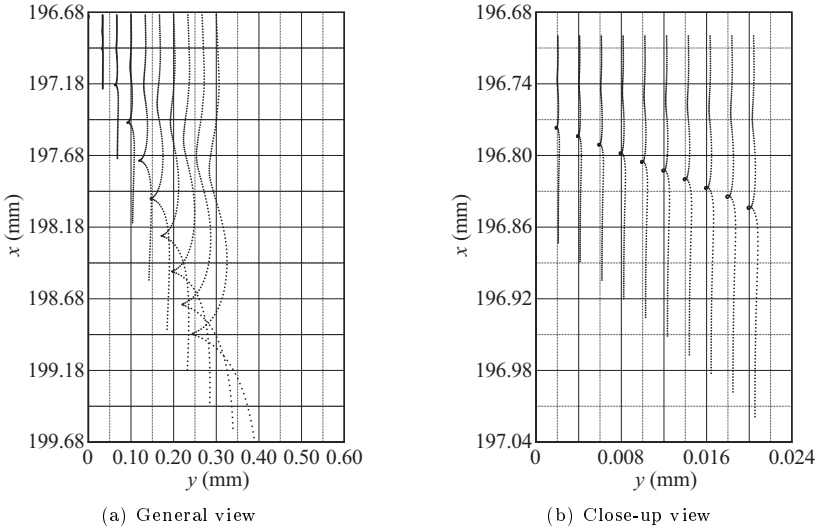


Figure 5.28: General and close-up view of pathlines (calculated from the starting time $t=2.075625$ s) for case 1 at $t=2.103075$ s, exhibiting “hook” and “loop”-shaped distortions caused by the CSE.

during the transition of the first capillary minimum through a constant stream-wise interval stretching from $x=196.68$ mm to $x=199.68$ mm (which lies in the hydrodynamically and thermally developed region of the film). In each subfigure, the corresponding instantaneous film thickness distribution in this region is also displayed. These distributions show the first capillary minimum entering the displayed region at $t=2.090925$ s (subfigure 5.27(a)) traveling across it between $t=2.090925$ s and $t=2.097450$ s (subfigures 5.27(a) to 5.27(d)) and having left it at $t=2.103075$ s (subfigure 5.28(a)). Pathlines were calculated from starting points equidistantly distributed in crosswise direction at $x=196.68$ mm on the basis of instantaneous numerical velocity data stored at 54 time steps between $t=2.075625$ s and $t=2.103075$ s.

The pathline sequence shows fluid elements describing “loop”- or “hook”-

shaped trajectories as the first capillary minimum passes over their position, depending on their wall distance at the time the CSE attains their position[†]. Fluid elements traveling above the CSE center (which according to subfigure 5.4(a) is approximately positioned at $y=0.1$ mm) follow “hook”-shaped pathlines since they do not encounter flow reversal as opposed to near-wall elements, which follow “loop”-shaped pathlines. Since the “loop”-shaped distortions are extremely small, a close-up view of the near-wall region is represented in subfigure 5.28(b). This shows pathlines calculated from starting points distributed over a considerably shorter crosswise distance at $x=196.70$ mm over the same time interval as pathlines in subfigure 5.28(a).

Due to the decrease in flow velocity toward the wall, trajectories of fluid elements traveling near the wall are influenced at an earlier stage by the passing waves compared to those of fluid elements traveling further from the wall. Hence, the streamwise position of the characteristic “loops” or “hooks” moves downstream as the wall distance of the pathline starting point increases. Moreover, pathlines increase in length as the wall distance increases, since “faster” fluid elements travel farther during the displayed time interval (i.e. $t=2.075625$ s to $t=2.103075$ s).

The “loop”- and “hook”-shaped pathline distortions cause fluid elements to approach the wall and subsequently move away from it, which results from the streamline pattern of the CSE (see subfigure 5.4(a)). Indeed, fluid elements engulfed by the CSE are first exposed to streamlines oriented in the direction of the wall (causing them to approach it) and subsequently to streamlines leading away from the wall (causing them to move away from it) after having passed a point of vanishing crosswise velocity component. Thereby, the crosswise dimension of “loop”- or “hook”-shaped pathline distortions represents the local *mixing length* l .

Subfigures 5.27(a) to 5.28(b) show that the mixing length increases with the wall distance of the pathline starting position. This also results from the above established increase in streamwise velocity with wall distance. Indeed,

[†]A streamline plot showing the CSE in its developed state was previously introduced in the form of subfigure 5.4(a).

with decreasing relative streamwise velocity between a considered fluid element and the passing capillary wave[†], the exposure time of the fluid element to the kinematics of the CSE, and in particular those regions exhibiting large crosswise velocity, increases. This effect on the local mixing length l can be expressed with the following relation:

$$l = \frac{1}{2} \tilde{v} \Delta t \approx \frac{1}{2} \tilde{v} \frac{\Lambda_c}{(c - u)}, \quad (5.10)$$

where \tilde{v} designates the characteristic crosswise velocity induced by the CSE, c signifies the wave celerity, u the local streamwise velocity component prior to the wave transit, which approximately satisfies a quadratic profile in the residual layer (as established in subsection 2.3.1) and Λ_c the capillary wave length, which approximately defines the streamwise extent of the CSE. This simple relation, in addition to the pathline sequence in subfigures 5.27(a) to 5.28(b), allows to explain the two observations regarding scalar transfer to liquid films accentuated at the onset of this section. First, the CSE clearly induces crosswise convective transport toward and subsequently away from the wall, whereby the resulting mixing length scales with the characteristic crosswise velocity \tilde{v} and wavelength Λ_c of the CSE. Second, the near-wall mixing length is far smaller than the one close to the interface, as l scales inversely with $c - u$. Consequently, the effect of the CSE on scalar transport is much larger near the interface. Importantly, the mixing length is in general significantly smaller than the size of the CSE.

In order to assess the consequences of the CSE induced transport intensification for wall-side heat transfer, figure 5.29 depicts time traces of streamwise wall shear stress $\tau_{wx} = \mu_l \partial u / \partial y|_{y=0}$ (subfigure 5.29(a)) and wall Nusselt number $Nu = h \delta_{Nu} / k_l^{\ddagger}$ (subfigure 5.29(b)) for case 1. In both subfigures, the corresponding film thickness time trace is also displayed. Time traces were evaluated at $x=198.0$ mm, which corresponds to the cusp in the fifth pathline from the wall in subfigures 5.27(c) and 5.28(a). This cusp occurs at the time

[†]The wave celerity is larger than the liquid velocity in the residual layer.

[‡]With $h = -k_l \partial T / \partial y|_{y=0} / (T_w - T_0)$, where $T_w = 350$ K designates the wall temperature and $T_0 = 300$ K a reference temperature in the gaseous phase.

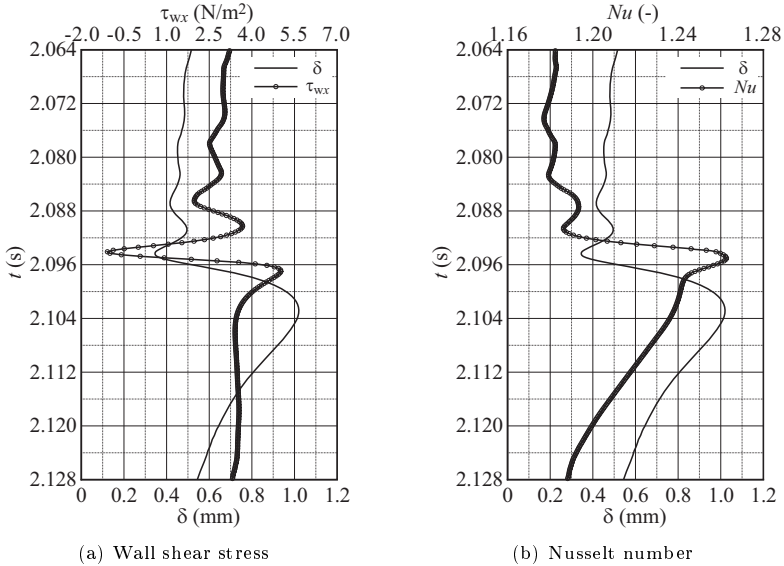


Figure 5.29: Simulated time traces of film thickness, wall shear stress and Nusselt number for case 1 evaluated over one period length at $x=198.0$ mm (see subfigure 5.27(c)).

point $t=2.094525$ s, which is represented in subfigure 5.27(c).

Concerning the Nusselt number time trace, subfigure 5.29(b) shows that Nu correlates inversely and proportionally with film thickness in the residual layer up to the second capillary maximum. As discussed in subsection 2.3.2, this behaviour has frequently been explained by the proportionality of crosswise conduction resistance and film thickness. However, in film flows, streamwise convective transport cannot be neglected[†]. Instead, a more physically sound explanation can be derived from the elaborations of subsections 2.3.1 and 2.3.2.

[†]Indeed, considering equation 2.21, and that in the capillary wave region $\epsilon \approx 1$, streamwise convective transport is not negligible compared to crosswise conduction, due to the large local Péclet number value $Pe=Re Pr \approx 100$.

There, it was established that the streamwise velocity profile in the residual layer is locally developed (more precisely parabolic with a vanishing crosswise derivative at the interface). Consequently, the local Nusselt number can be approximated by $Nu' = 1.88$ (see table 2.7) if the local film thickness is introduced as length scale, i.e. $Nu' = h \delta / k_1$. Then, expressing the Nusselt number represented in subfigure 5.29(b) in terms of this, yields $Nu = h \delta_{Nu} / k_1 \sim \delta_{Nu} / \delta$.

Tracking the Nusselt time trace upstream of the second capillary maximum, it is clear that the above established proportionality no longer holds. Indeed, a relatively strong modulation of Nu is evident at the second capillary minimum and an even stronger one at the first capillary minimum. Formally, these modulations must be associated with a departure of the velocity field from the locally developed state, which indeed takes place at the second and first capillary minimum as a result of the flow deceleration and re-acceleration as well as the occurrence of the CSE there (see figure 5.4). Further, as shown in subfigures 5.27(a) to 5.28(a), the first and second capillary minimum are associated with crosswise convective transport evidenced by the “loop”- and “hook”-shaped pathline distortions[†]. Indeed, at $t = 2.094525$ s, which corresponds to the drastic increase of the Nusselt number in subfigure 5.29(b), the fifth pathline from the wall in subfigure 5.27(c) reaches its minimal wall distance. Meanwhile, the sign change of the wall shear stress in subfigure 5.29(a) shows that this point in time is associated with the CSE. From a heat transfer perspective, the “loop”- or “hook”-shaped pathlines transport “cold” liquid, emanating from regions further away, to the wall where it is “heated up” before moving it away again. This increases the driving potential at the wall similarly to the effect of turbulence. From an Eulerian perspective the pathline distortions induce liquid mixing, resulting in the temperature contour distortion evidenced by figure 5.25(a).

After having attained its maximum, the Nusselt number in subfigure 5.29(b) decreases with film thickness in the large wave hump. Thereby, the initial decrease is drastic and associated with fluid elements moving away from the wall and assuming a larger and further constant wall distance as shown in

[†]The smaller “hook”-shaped pathline distortions preceding the large distortions (see e.g. 5.28(a)) are associated with the second capillary minimum.

subfigure 5.28(a) (or, from an Eulerian perspective, with the decompression of temperature contours in subfigure 5.25(a)). For the regime investigated here, the CSE induced increase of the Nusselt number is not as dramatic as reported in the work of Kunugi & Kino (2005) and its influence on the temporally averaged Nusselt number is therefore not dominant.

To conclude this subsection on heat transfer intensification, the analysis performed above for case 1 will be applied to case 8 in order to assess in what way conditions are altered by the significantly different open shape of the CSE in the latter case (compare streamline plots in subfigures 5.4(a) and 5.5(a)). Accordingly, subfigures 5.30(a) to 5.31(a) depict pathlines and the corresponding film thickness distribution in the fully developed region of the film for case 8 calculated over a time interval ranging from $t=3.253050$ s to $t=3.280750$ s. Compared to the pathline sequence for case 1 (see subfigures 5.27(a) to 5.28(a)) two principal differences can be discerned. First, all pathlines independent of their wall distance exhibit “loop”-shaped distortions, which of course results from the fact that the open CSE induces flow reversal over the entire film thickness. In subfigure 5.31(a) a photographic insert is included, which shows a “loop”-shaped pathline obtained experimentally by Al-Sibai (1998) under somewhat different flow conditions[†]. Further, subfigure 5.31(b) shows a close-up view of near-wall “loop”-shaped pathlines. Second, the local mixing length is significantly larger than for case 1, which can be attributed to the larger characteristic crosswise velocity \tilde{v} (see equation 5.10) induced by the open CSE. A larger “hook”-shaped distortion induced by the second capillary minimum is also evident in subfigures 5.30(a) to 5.31(a), resulting from the relatively strong deceleration and re-acceleration of the flow there, as illustrated in figure 5.6(a).

Figures 5.32(a) and 5.32(b) depict time traces of film thickness, wall shear stress and wall Nusselt number for case 8 evaluated at $x=56.0$ mm, which corresponds to the minimum of the seventh “loop”-shaped pathline from the wall attained at $t=3.271050$ s (see subfigure 5.30(d)). The Nusselt number time

[†]Experiments were performed in the optical setup developed by Adomeit & Renz (2000), using pure DMSO.

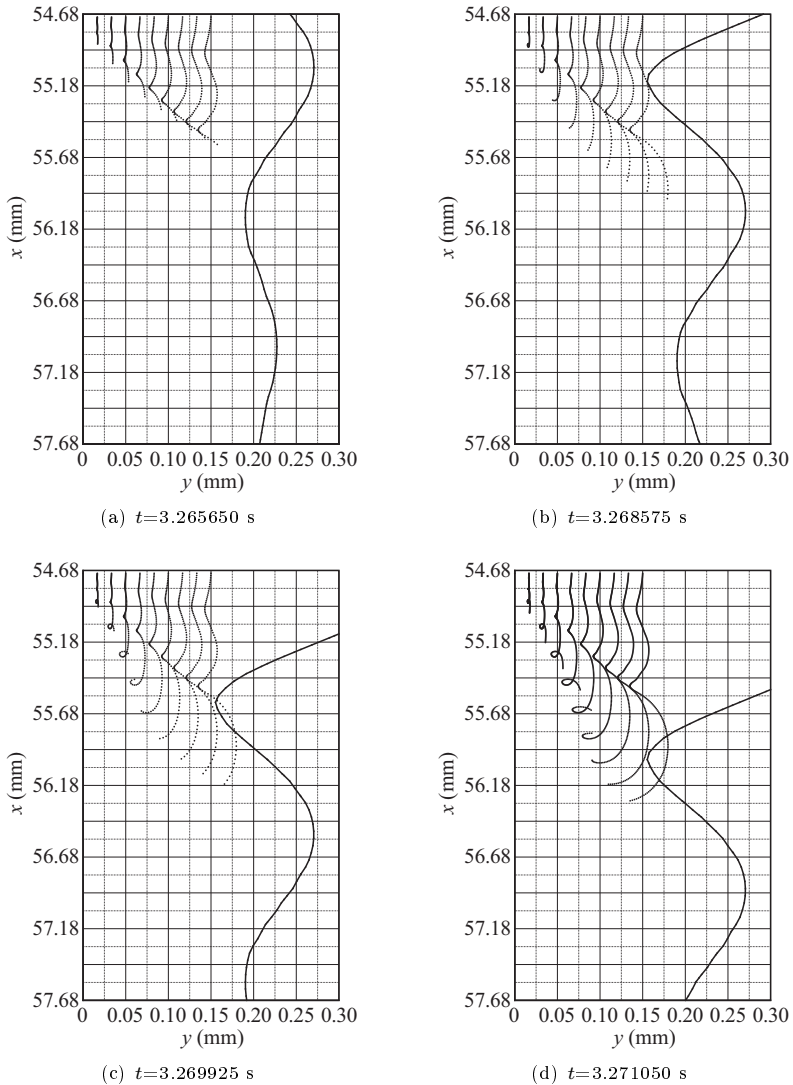


Figure 5.30: Simulated fluid element pathlines in the residual layer for case 8 (calculated from the starting time $t = 3.253050$ s) at different time points during the transition of the first capillary minimum.

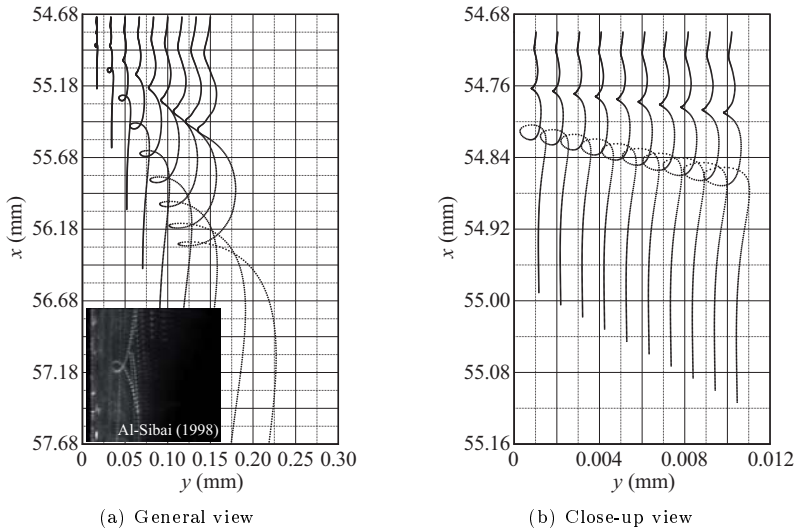


Figure 5.31: General and close-up view of pathlines (calculated from the starting time $t=3.25305$ s) for case 8 at $t=3.280275$ s, exhibiting “loop”-shaped distortions caused by the CSE.

trace is strikingly similar to the corresponding time trace for case 1 (see subfigure 5.29(b)), although the mean mixing length is considerably larger. However, a closer look at the pathlines in subfigures 5.31(a) and 5.28(a) reveals that pathlines very close to the wall, which are the most relevant from the point of view of wall-side heat transfer, exhibit a very small mixing length for both cases[†]. This, of course, is due to the large velocity difference $c - u$ (see equation 5.10) close to the wall. Judging from the very large pathline distortions near the interface in subfigure 5.31(a), it can be inferred that interfacial heat transfer is affected to a much larger extent by the CSE, which would confirm the experimental and numerical evidence from the literature mentioned at the onset

[†]In accordance with the relatively weak distortion of temperature contours close to the wall illustrated in figure 5.25.

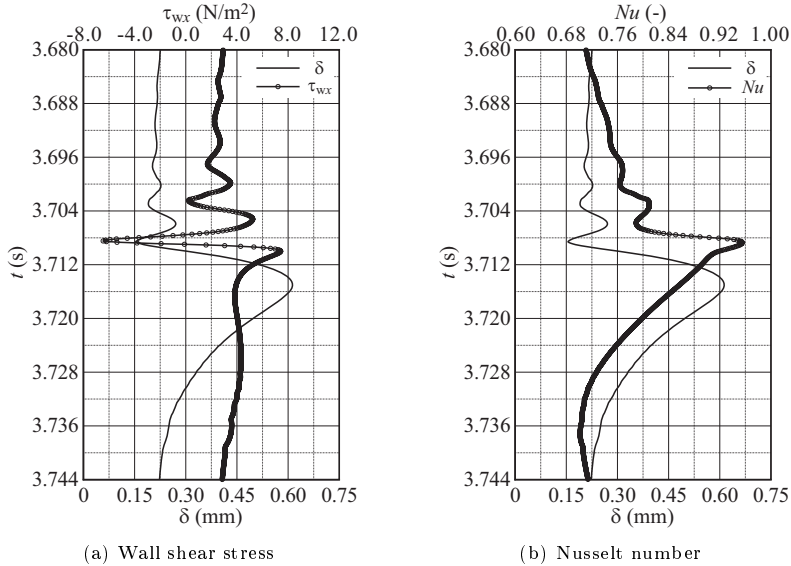


Figure 5.32: Simulated time traces of film thickness, wall shear stress and Nusselt number evaluated over one period length for case 8: $x=56.0$ mm (see subfigure 5.30(c)).

of this subsection. Due to the simulation method employed in this thesis it was unfortunately not possible to consider the case of interfacial transfer. Such investigations have to be deferred to future work.

5.4 Influence of control parameters

Before concluding the elaborations on 2-dimensional capillary flow separation, the influence of two principal control parameters on the previously established kinematics and dynamics of the phenomenon, namely the Reynolds number Re and the wave frequency f , will be addressed in this subsection. This will be done on the basis of experimental data from PIV and LDV measurements as well as

numerical data. For this, the parameters Re and f were varied in a series of experiments and 2-dimensional numerical simulations, which are characterized in tables 4.2 and 3.1. The Reynolds number influence was established for the vertically falling liquid film by varying Re from 8.6 to 15.0 at a constant wave frequency of $f=16$ Hz. Experiments realizing this parameter variation (which were performed in the optical test setup) are quantified by the first four lines in table 4.2. The corresponding numerical simulations are quantified in table 3.1 in the form of cases 5, 6, 7 and 8.

The influence of wave frequency was established through two sets of parameter variations. For the vertically falling liquid film, the wave frequency was varied from 16 Hz to 24 Hz at $Re=10.7$. Corresponding experiments are quantified by the second and fifth to seventh entries in table 4.2, while numerical conditions are quantified in table 3.1 in the form of cases 6, 9 and 10[†]. For the inclined film, the wave frequency was varied from 11.3 Hz to 24.0 Hz at $Re=21.4$. Here, only numerical simulations were performed, which are quantified as cases 2 to 4 in table 3.1.

5.4.1 Reynolds number influence

The Reynolds number influence on kinematics in the capillary wave region is illustrated in figures 5.33 to 5.38. Figure 5.33 depicts streamwise film thickness distributions for the four different Reynolds number values (i.e. $Re=8.6, 10.7, 12.9, 15.0$). As discussed in subsection 2.2.2, the wavelength of large waves increases with Re according to the empirical correlation of Nosoko *et al.* (1996). This leads to an increase in the number and amplitude of capillary waves preceding the large wave and a decrease in their wavelength, which is clearly discernible in figure 5.33. Tihon *et al.* (2006) made the same observation (see subsection 2.3.1), conjecturing that to “stabilize” large waves of increasing amplitude (caused by an increasing wavelength) capillary waves of larger amplitude and smaller wavelength are needed.

[†]The case $f=24$ Hz was not simulated numerically due to difficulties concerning the outlet boundary condition in connection with secondary instabilities.

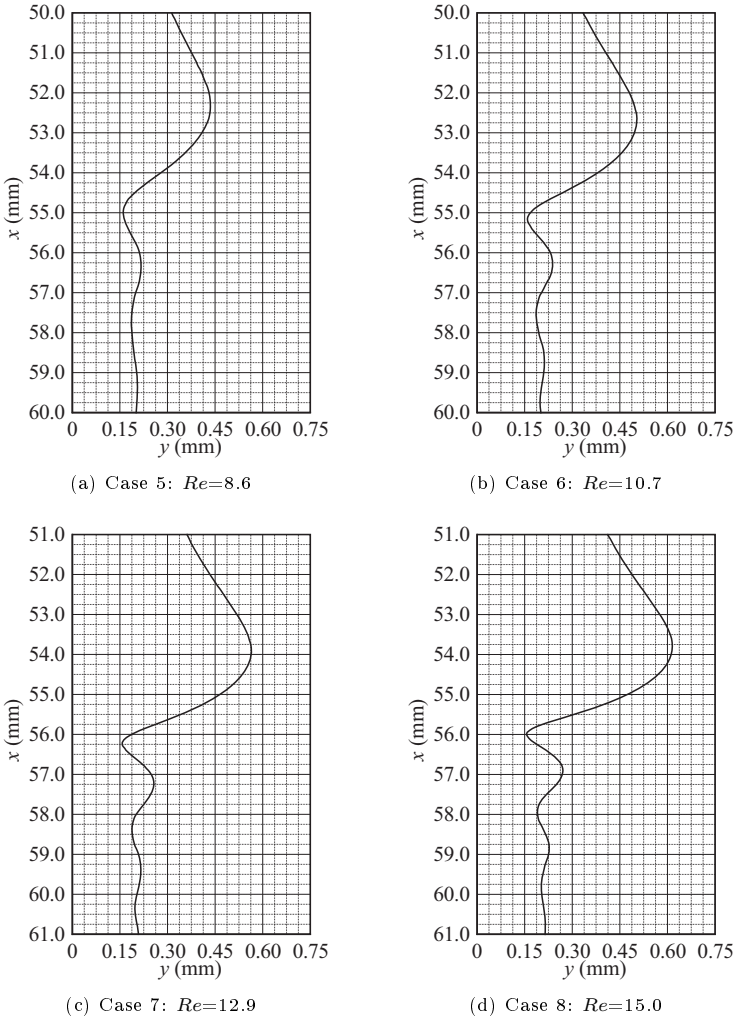
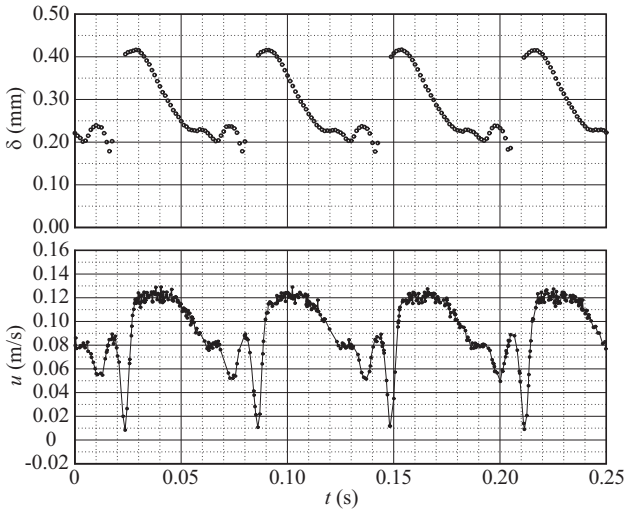
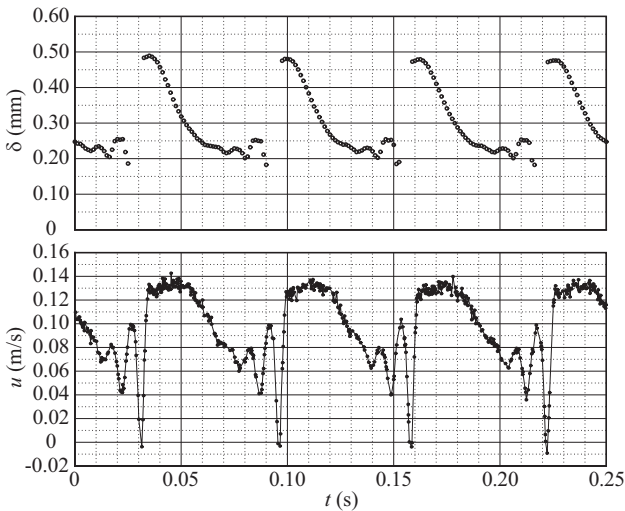


Figure 5.33: Simulated streamwise film thickness distribution over a single wave for cases 5 to 8 in table 3.1: $Ka=509.5$, $f=16.0$ Hz.



(a) $Re=8.6$, $Ka=509.5$, $f=16.0$ Hz



(b) $Re=10.7$, $Ka=509.5$, $f=16.0$ Hz

Figure 5.34: Film thickness and streamwise velocity time traces measured in the optical test setup using CCI and LDV (at $y=120 \mu\text{m}$).

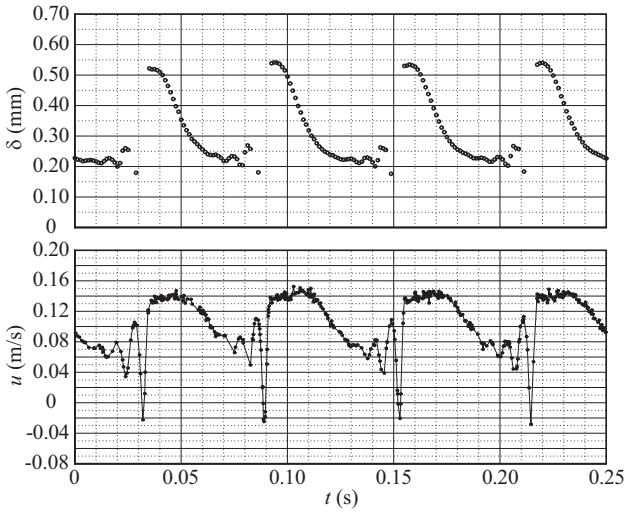
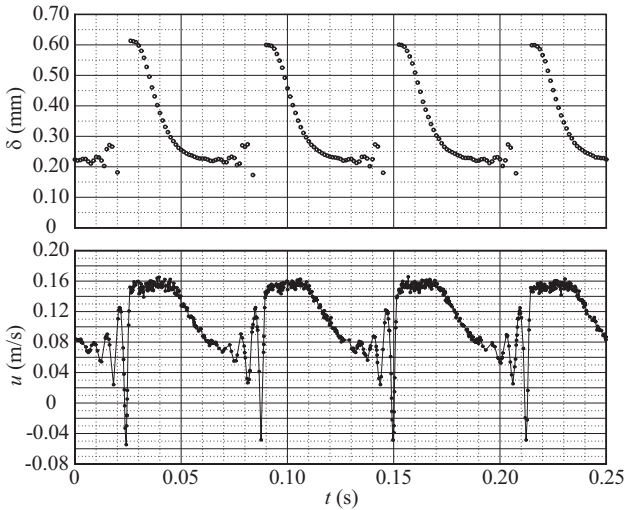
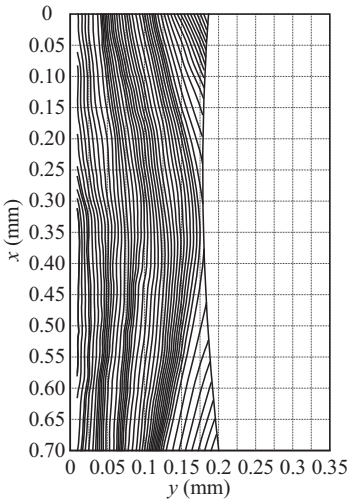
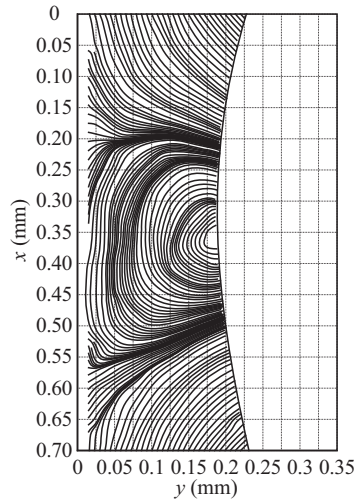
(a) $Re=12.9$, $Ka=509.5$, $f=16.0$ Hz(b) $Re=15.0$, $Ka=509.5$, $f=16.0$ Hz

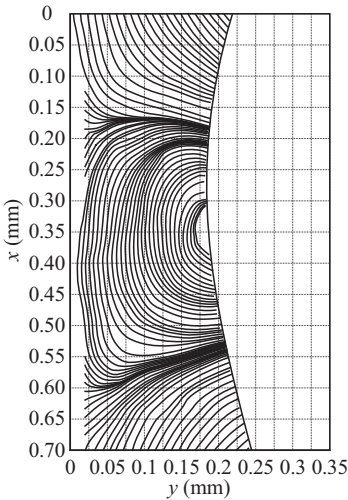
Figure 5.35: Film thickness and streamwise velocity time traces measured in the optical test setup using CCI and LDV (at $y=120 \mu\text{m}$).



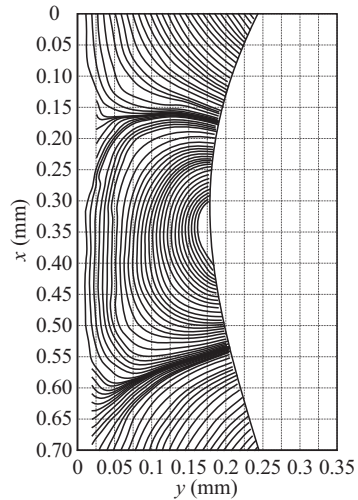
(a) $Re=8.6$, $Ka=509.5$, $f=16$ Hz



(b) $Re=10.7$, $Ka=509.5$, $f=16$ Hz



(c) $Re=12.9$, $Ka=509.5$, $f=16$ Hz



(d) $Re=15.0$, $Ka=509.5$, $f=16$ Hz

Figure 5.36: Streamlines at the first capillary minimum obtained from PIV measurements in the optical test setup: Reynolds number influence.

The effect of the Reynolds number on interface topology is also evident in figures 5.34 and 5.35, which depict experimental film thickness (obtained with CCI) and streamwise velocity (obtained with LDV) time traces for the four Reynolds number values. However, the wavelength of capillary waves cannot be determined from these *time traces*. Meanwhile, the LDV time traces, which were measured at a constant crosswise position of $y=120\ \mu\text{m}$ in the residual layer, show that the streamwise velocity component strongly correlates with film thickness as was established in subsection 5.1.2 (see figures 5.7 and 5.8). Indeed, the number of subsidiary extrema in the capillary wave region is the same in both sets of time traces. Concerning the Reynolds number influence, streamwise velocity time traces in figures 5.34 and 5.35 display a modulation amplitude in the capillary wave region, which increases with Re , in accordance with the increase in capillary film thickness modulation discussed with respect to figure 5.33. In particular, this concerns the deceleration occurring at the first capillary minimum. Indeed, for $Re=8.6$ (see subfigure 5.34(a)), although the streamwise velocity component attains small values, it stays positive. For the larger Reynolds number values, $Re=10.7$, 12.9 and 15.0 (see subfigures 5.34(b) to 5.35(b)), the streamwise velocity does attain negative minimal values, which increase in magnitude with Re . Meanwhile, the maximal streamwise velocity (which is attained within the large wave) also increases with Re .

These streamwise velocity time traces suggest that flow separation occurs for all considered Reynolds number values except $Re=8.6$, which is confirmed by the corresponding streamline plots in the region of the first capillary minimum depicted in figure 5.36 and obtained from PIV measurements. These show that for $Re=8.6$, the flow is merely decelerated and re-accelerated (see subfigure 5.36(a)), while for the other Reynolds number values, capillary flow separation occurs (see subfigures 5.36(b) to 5.36(d)). Thereby, the size of the CSE increases with the Reynolds number.

In order to investigate the Reynolds number influence on the dynamics underlying the above discussed kinematics, figures 5.37 and 5.38 display numerical data corresponding to subfigures 5.36(a) to 5.36(d). Thereby, subfigures 5.37(a), 5.37(c), 5.38(a) and 5.38(c) depict streamlines in the region of the

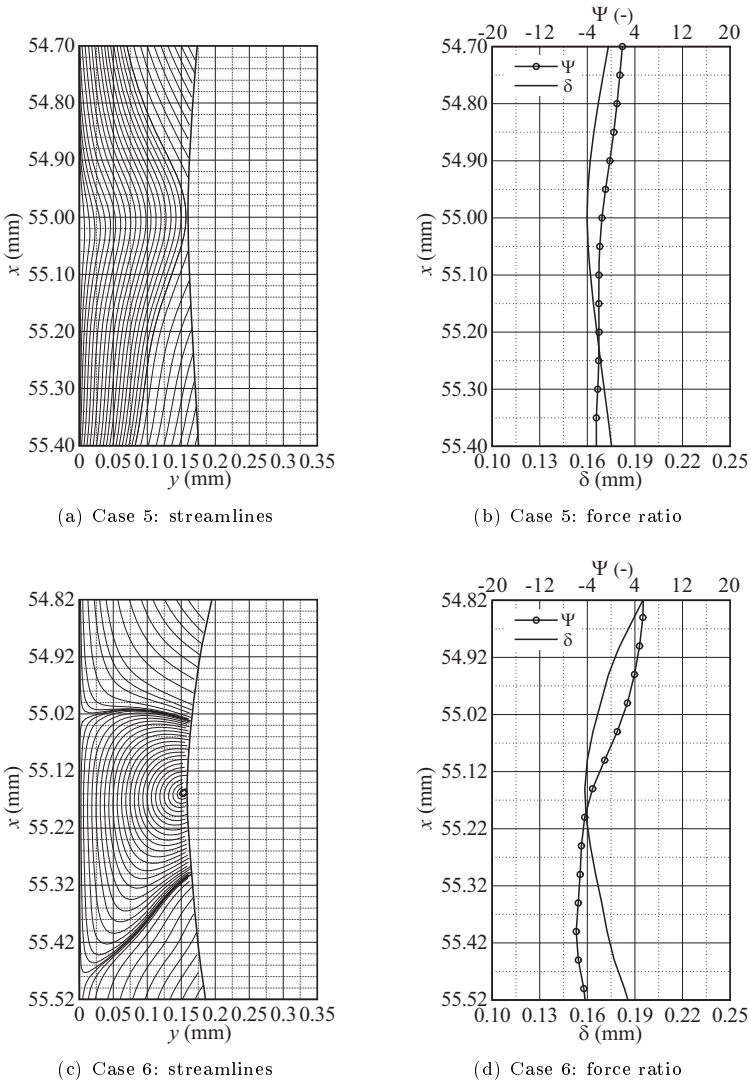


Figure 5.37: Streamlines and streamwise distributions of film thickness and force ratio Ψ at the first capillary minimum for simulation cases 5 ($Re=8.6$) and 6 ($Re=10.7$): $Ka=509.5$, $f=16.0$ Hz.

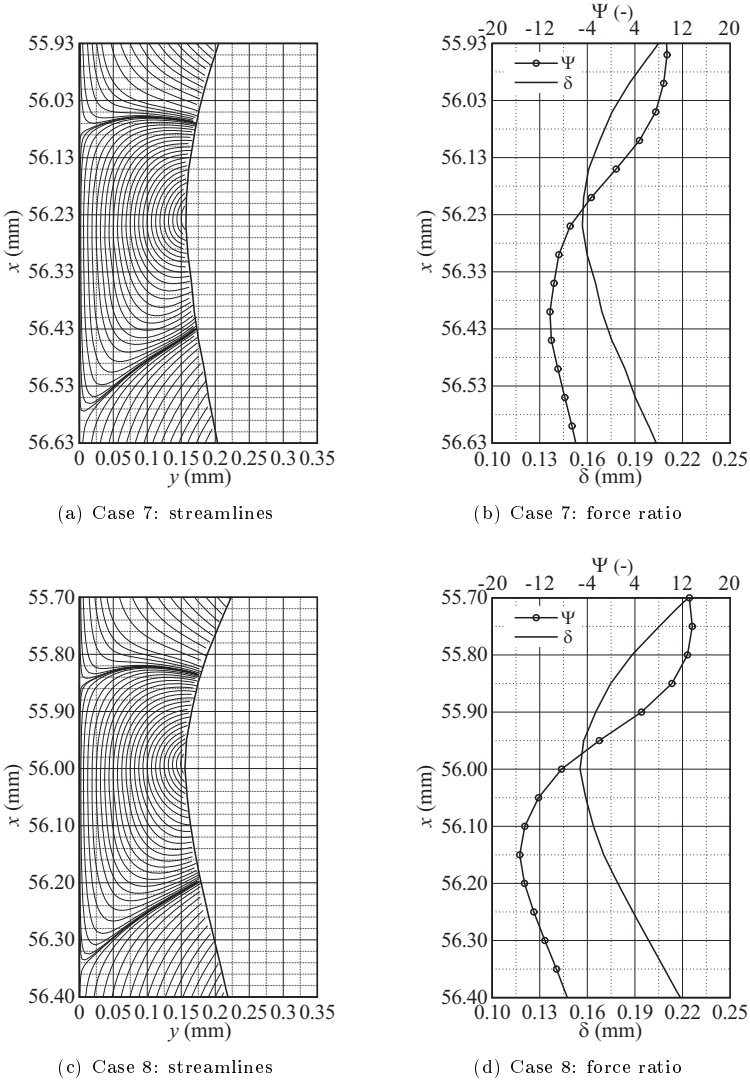


Figure 5.38: Streamlines and streamwise distributions of film thickness and force ratio Ψ at the first capillary minimum for cases 7 ($Re=12.9$) and 8 ($Re=15.0$): $Ka=509.5$, $f=16.0$ Hz.

first capillary minimum, while subfigures 5.37(b), 5.37(d), 5.38(b) and 5.38(d) depict the corresponding streamwise distributions of film thickness and force ratio Ψ . The figures show that, as the Reynolds number increases, the minimal (negative) value of Ψ decreases causing the initiation and growth of the CSE. As discussed in subsection 5.2 (see equation 5.6 there), the cause for this decrease in Ψ_{\min} is an increase in magnitude of the negative streamwise interface curvature derivative $\partial\kappa/\partial x$ (i.e. toward larger negative values $\partial\kappa/\partial x$) at the first capillary minimum. Thereby, the increase in $|\partial\kappa/\partial x|$ is caused by an increase in capillary amplitude and decrease in capillary wavelength, as evidenced by the film thickness distributions in figures 5.33, 5.37 and 5.38. In summary, an increase in the Reynolds number leads to larger wave separation, producing more pronounced capillary waves, which in turn cause a larger adverse pressure gradient, leading to the initiation and growth of the CSE.

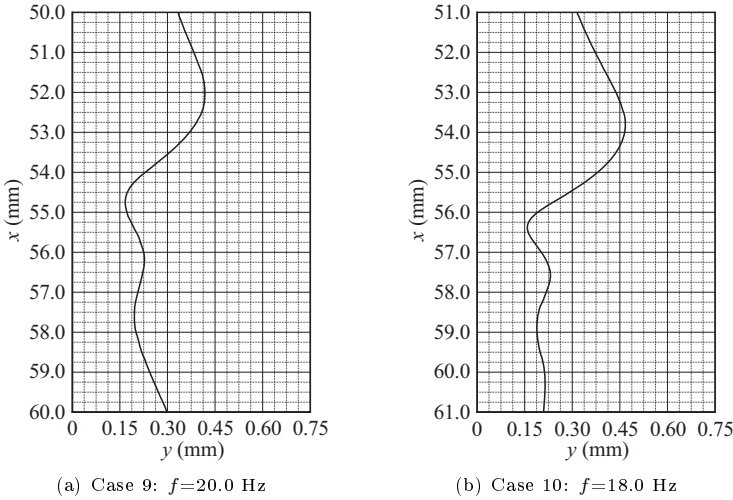
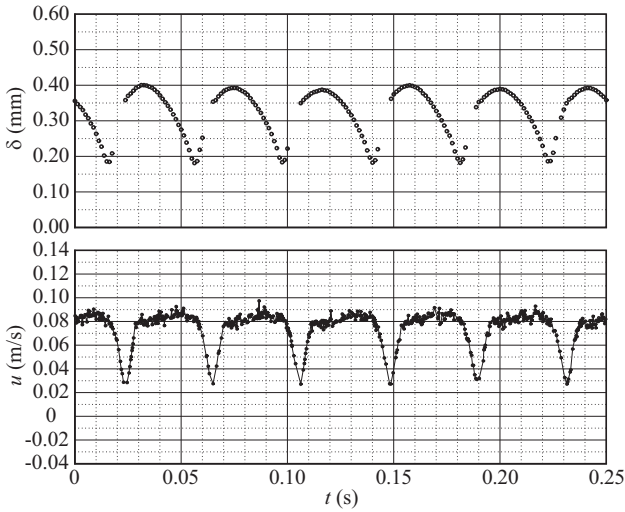


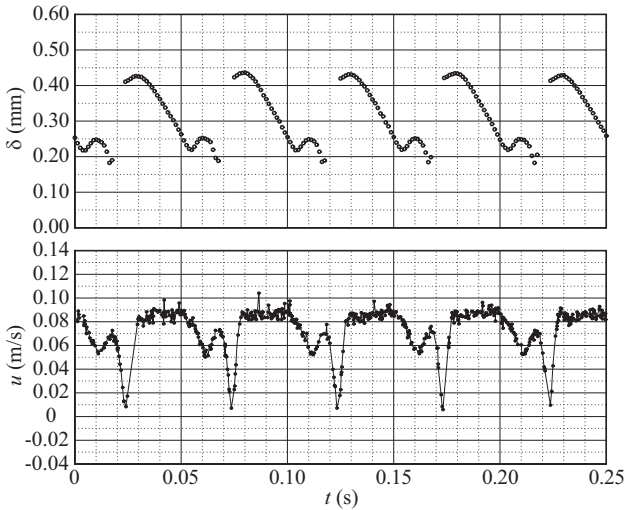
Figure 5.39: Simulated streamwise film thickness distribution over a single wave for cases 9 and 10 in table 3.1: $Re=10.7$ Hz, $Ka=509.5$.

5.4.2 Wave frequency influence

In analogy to subsection 5.4.1, the influence of wave frequency on the kinematics and dynamics in the region near the first capillary minimum for the vertically falling liquid film is represented in the form of figures 5.39 to 5.43, in addition to subfigures 5.37(c), 5.37(d) and 5.33(b), which pertain to case 6. Thereby, figure 5.39 depicts numerical streamwise film thickness distributions for the frequencies $f=18$ Hz and $f=20$ Hz, adding to the previously introduced film thickness distribution for $f=16$ Hz in figure 5.33(b). Figures 5.40 and 5.41 depict experimental film thickness (obtained with CCI) and streamwise velocity (obtained with LDV) time traces evaluated at $y=80 \mu\text{m}$ for all four investigated frequencies $f=16$ Hz, 18 Hz, 20 Hz and 24 Hz. Figure 5.42 depicts corresponding streamline plots in the region of the first capillary minimum obtained from PIV measurements. Finally, figure 5.43 displays numerical streamline plots



(a) $Re=10.7$, $Ka=509.5$, $f=24$ Hz



(b) $Re=10.7$, $Ka=509.5$, $f=20$ Hz

Figure 5.40: Film thickness and streamwise velocity time traces measured in the optical test setup using CCI and LDV (at $y=80 \mu\text{m}$).

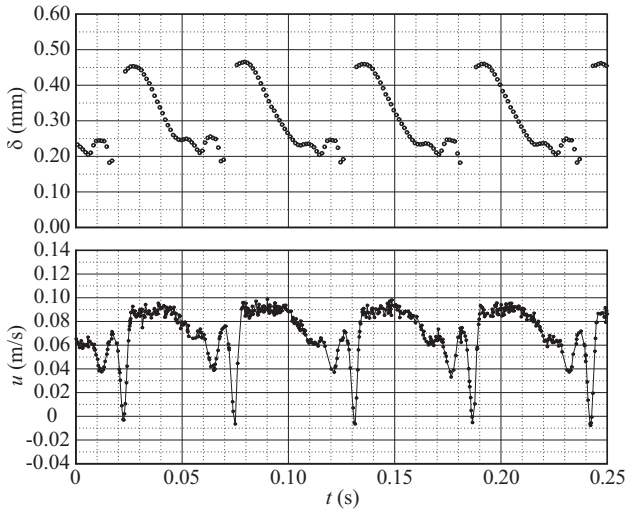
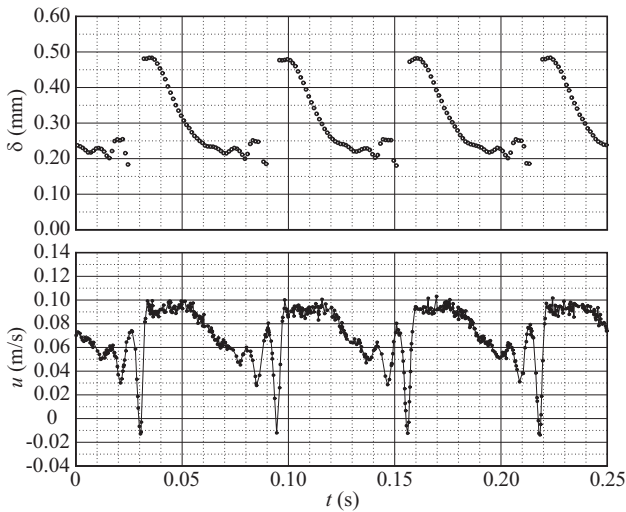
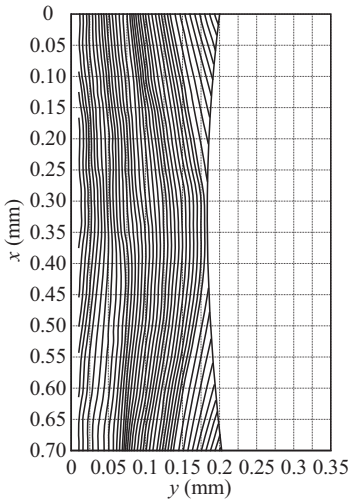
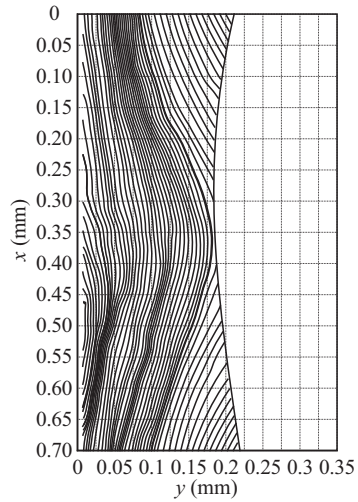
(a) $Re=10.7$, $Ka=509.5$, $f=18$ Hz(b) $Re=10.7$, $Ka=509.5$, $f=16$ Hz

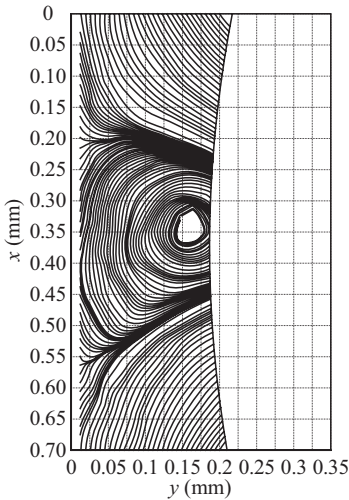
Figure 5.41: Film thickness and streamwise velocity time traces measured in the optical test setup using CCI and LDV (at $y=80 \mu\text{m}$).



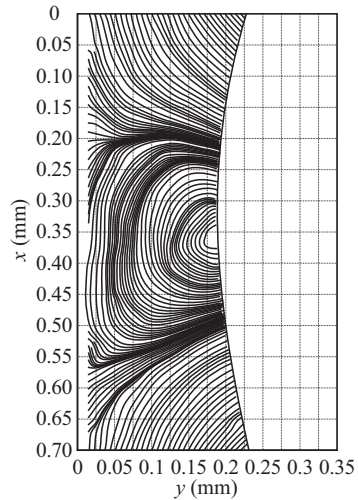
(a) $Re=10.7$, $Ka=509.5$, $f=24$ Hz



(b) $Re=10.7$, $Ka=509.5$, $f=20$ Hz



(c) $Re=10.7$, $Ka=509.5$, $f=18$ Hz



(d) $Re=10.7$, $Ka=509.5$, $f=16$ Hz

Figure 5.42: Streamlines at the first capillary minimum obtained from PIV measurements in the optical test setup: wave frequency influence.

and corresponding distributions of the force ratio Ψ for $f=18$ Hz and 20 Hz, which add to the corresponding plots for $f=16$ Hz, previously introduced in the form of subfigures 5.37(c) and 5.37(d).

The influence of the wave frequency on these results can be understood when considering its effect on wave separation. Indeed, wave separation increases with decreasing wave frequency (see e.g. the empirical correlation of Nosoko *et al.* (1996)) so that the effect of wave frequency acts counter to that of the Reynolds number. This is evident in subfigures 5.33(b), 5.39(a) and 5.39(b), which show an increase in capillary wave amplitude and decrease in capillary wave length with decreasing wave frequency, leading to a larger flow deceleration at the first capillary minimum as evidenced by subfigures 5.40(a) to 5.41(b). Thereby, for $f=24$ Hz and $f=20$ Hz no flow reversal takes place. For $f=24$ Hz, where the flow deceleration is weakest, the interface does not display capillary waves altogether. Correspondingly, the PIV streamlines in figure 5.42 exhibit flow separation only for the lowest frequencies $f=16$ Hz and 18 Hz. Finally, subfigures 5.37(c) and 5.37(d) and figure 5.43 show that as expected the minimal value of Ψ decreases with decreasing wave frequency.

Concluding this section, figures 5.44 to 5.46 illustrate the wave frequency influence on capillary flow separation for the inclined film on the basis of numerical data for cases 1 to 4, corresponding to wave frequencies of $f=11.3$ Hz, 15.0 Hz, 17.7 Hz and 24 Hz. Case 1 was included here although the associated Reynolds number is lower than for the other three cases. Figure 5.44 depicts film thickness distributions, while figures 5.45 and 5.46 depict streamlines and corresponding distributions of the force ratio Ψ in the region of the first capillary minimum. In summary, these results exhibit the same effect of wave frequency as for the vertically falling liquid film.

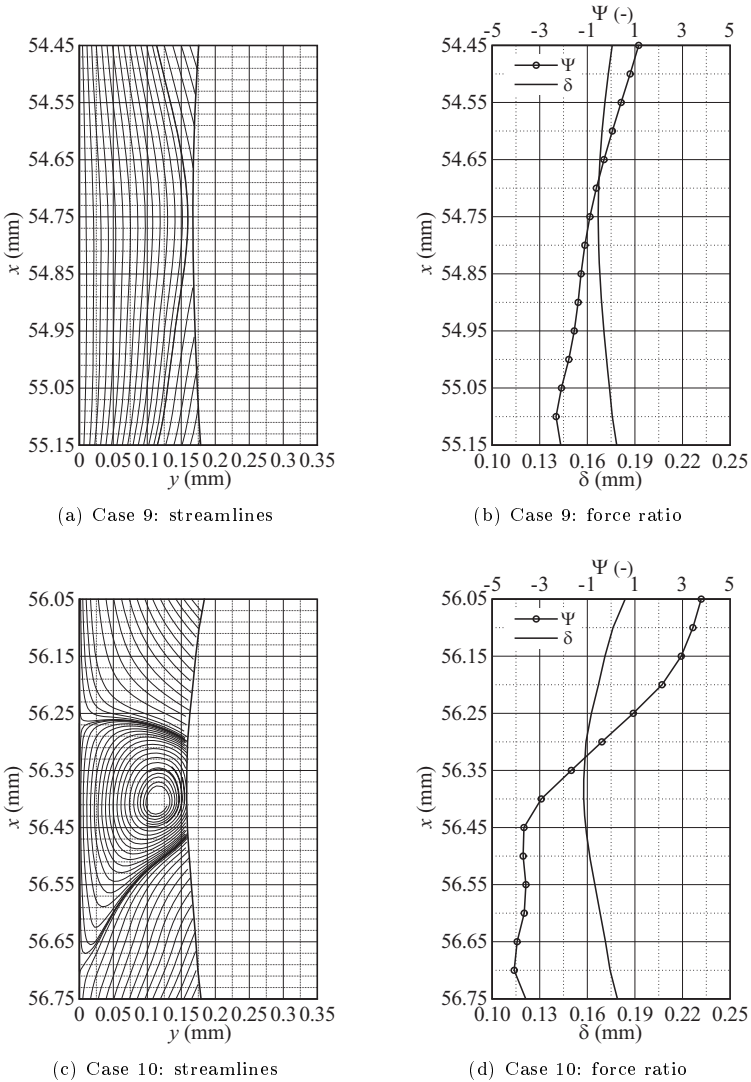
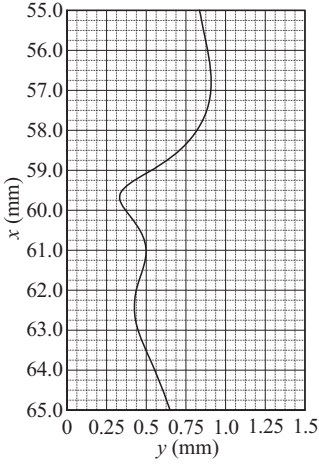
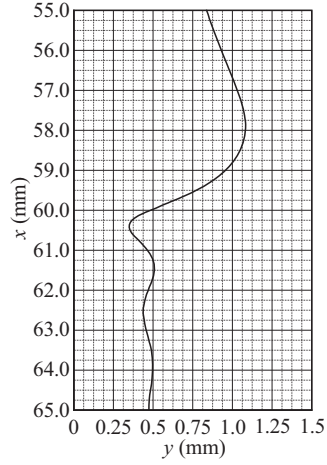


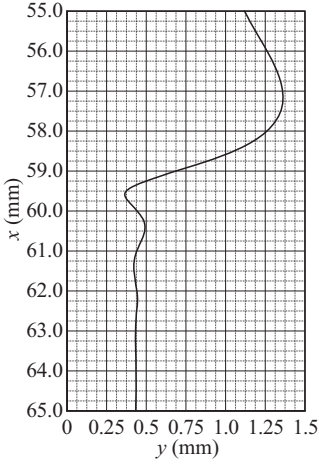
Figure 5.43: Streamlines and streamwise distributions of film thickness and force ratio Ψ at the first capillary minimum for simulation cases 9 ($f=20.0$ Hz) and 10 ($f=18.0$ Hz): $Re=10.7$, $Ka=509.5$.



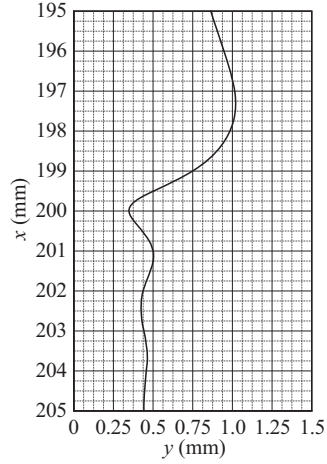
(a) Case 2: $Re=21.4$, $Ka=139.8$,
 $f=24.0$ Hz



(b) Case 3: $Re=21.4$, $Ka=139.8$,
 $f=17.7$ Hz



(c) Case 4: $Re=21.4$, $Ka=139.8$,
 $f=11.3$ Hz



(d) Case 1: $Re=15.6$, $Ka=133.6$,
 $f=15.0$ Hz

Figure 5.44: Simulated streamwise film thickness distribution over a single wave for cases 1 to 4 in table 3.1.

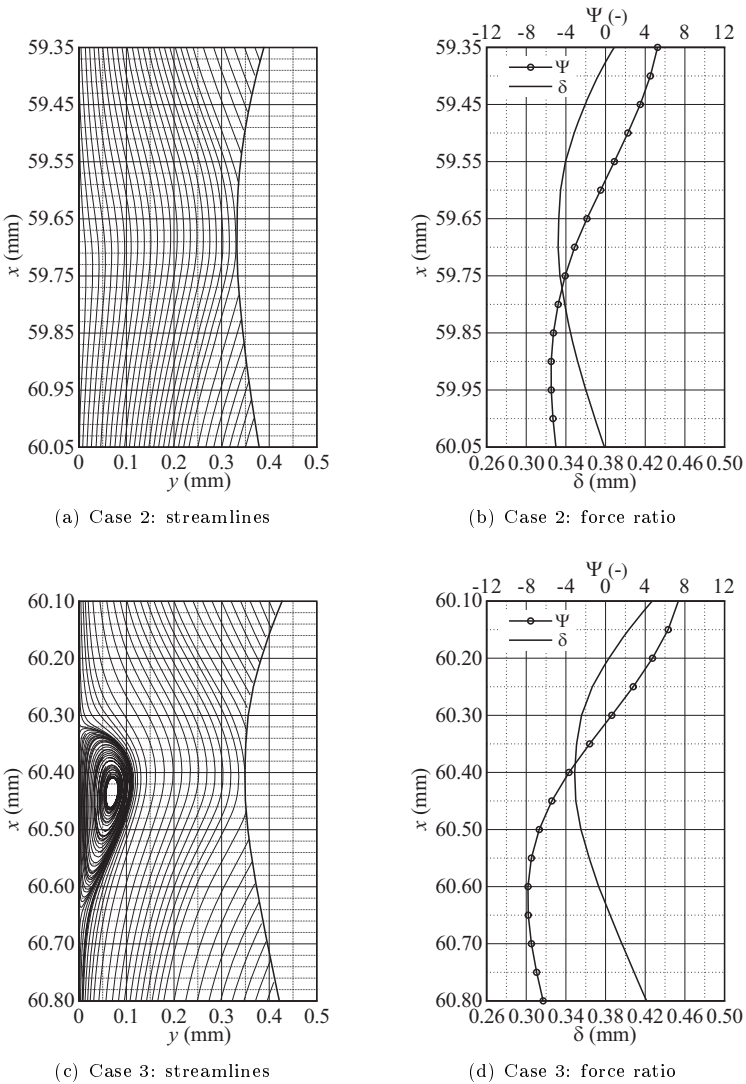


Figure 5.45: Streamlines and streamwise distributions of film thickness and force ratio Ψ at the first capillary minimum for simulation cases 2 ($f=24.0$ Hz) and 3 ($f=17.7$ Hz): $Re=21.4$, $Ka=139.8$.

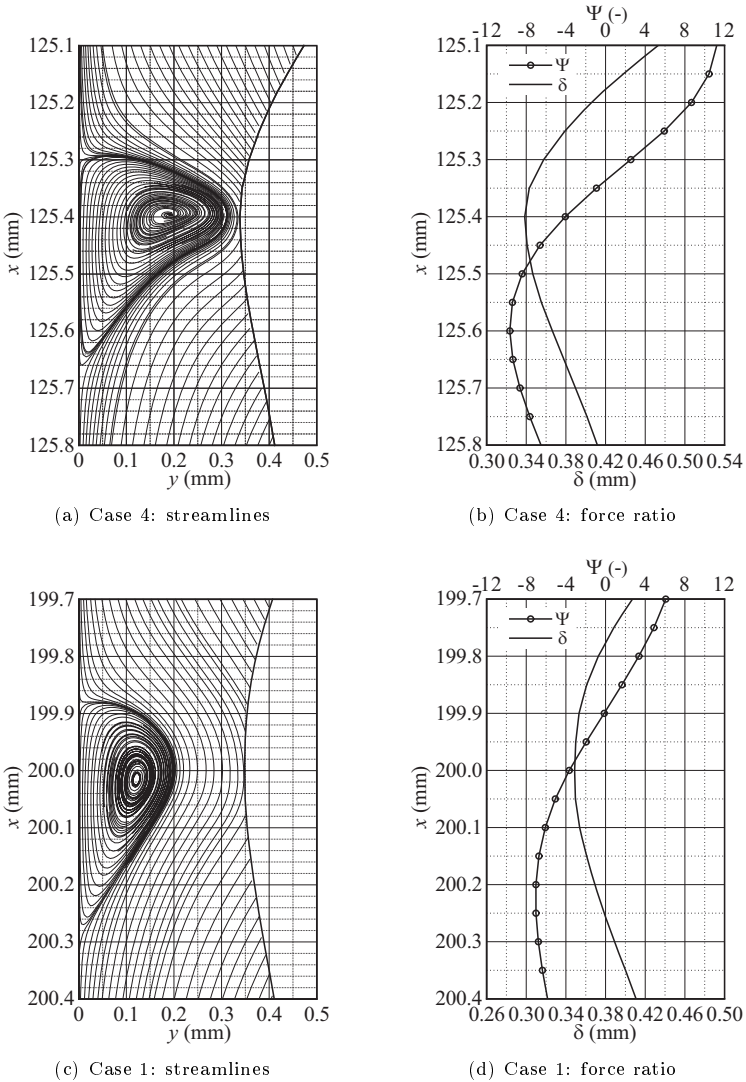


Figure 5.46: Streamlines and streamwise distributions of film thickness and force ratio Ψ at the first capillary minimum for simulation cases 4 ($Re=21.4$, $f=11.3$ Hz) and 1 ($Re=15.6$, $f=15.0$ Hz).

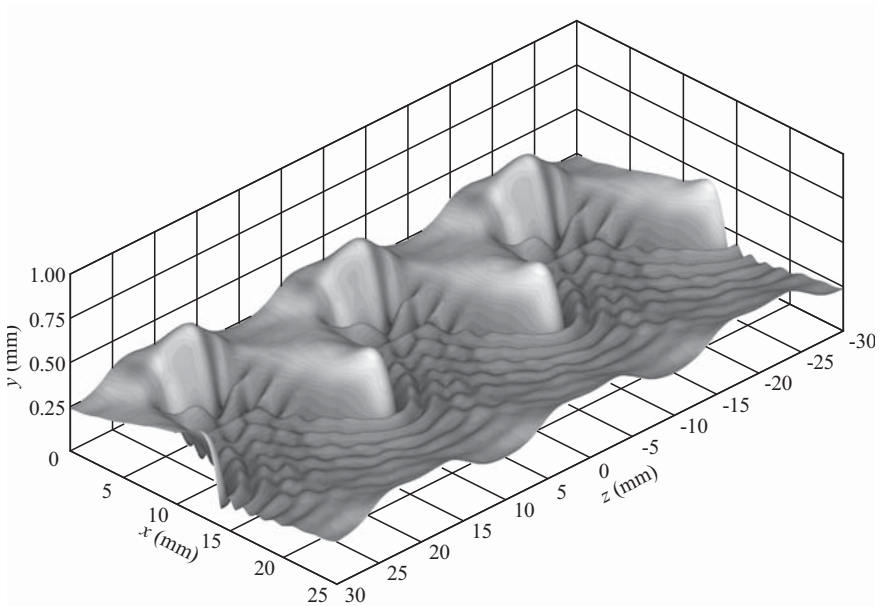


Figure 5.47: Interface topology for the 3-dimensional simulation (case 11 in table 3.1).

5.5 3-dimensional capillary flow separation

To conclude the analysis of capillary flow separation conducted in this thesis, an investigation of the phenomenon under 3-dimensional conditions is provided next. This will be done on the basis of the numerical simulation of a vertically falling water film with 3-dimensional wave dynamics, namely case 11 in table 3.1. Figure 5.47 represents the fully developed interface topology for this case over one streamwise wavelength and three spanwise wavelengths. As established in subsection 3.2.1, only the region $-10 \leq z \leq 10$ (corresponding to one spanwise wavelength) was actually computed. Data outside this region were obtained by mirroring data within it and are displayed only for the purpose of

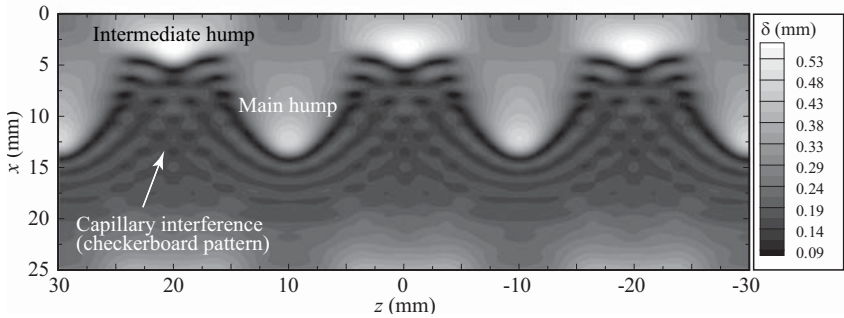
providing a better overview of the 3-dimensional flow.

Similar to the 2-dimensional case, the interface topology is characterised by large wave humps preceded by approximately five capillary waves of considerable amplitude. However, in contrast to the 2-dimensional case, wave fronts of large wave humps are distorted into horseshoe-like shapes as established in subsection 2.2.2. At the position where two horseshoe-shaped wave fronts meet, a large intermediate hump, representing the global film thickness maximum, occurs. As a further consequence of the horseshoe-shaped wave fronts, capillary waves (the wave fronts of which are also horseshoe-shaped) preceding two adjacent large wave humps interfere with one another in much the same way as waves caused by rain drops on a water surface. This region of capillary interference is characterised by capillary wave humps and troughs alternating in streamwise and spanwise direction in the form of a checkerboard or *herringbone pattern*[†]. Thereby, capillary waves preceding the large intermediate hump caused by the intersection of large wave fronts are particularly pronounced, i.e. exhibit a large amplitude and small wavelength. Further, they display almost horizontal wave fronts.

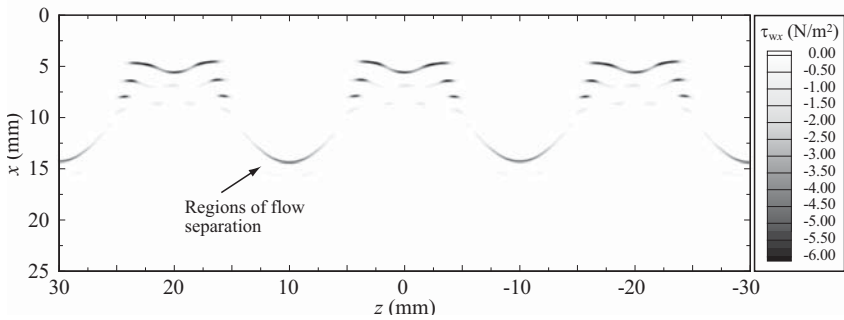
Based on the 3-dimensional representation of wave topology in figure 5.47 and the corresponding top view of the film thickness distribution represented in subfigure 5.48(a), it can be stated that a large part of the considered film's interface is affected by capillary wave dynamics. In order to assess their influence on the liquid phase flow field, subfigures 5.48(b) and 5.48(c) depict contours of the streamwise $\tau_{wx} = \mu_1 \partial u / \partial y|_{y=0}$ and spanwise $\tau_{wz} = \mu_1 \partial w / \partial y|_{y=0}$ wall shear stress corresponding to the representation of film thickness contours in subfigure 5.48(a). The contour levels in subfigure 5.48(b) are chosen such that only negative values of τ_{wx} are associated with gray scales other than white. This allows to identify regions of flow reversal (i.e. regions coloured in any gray scale other than white) and consequently capillary flow separation. Accordingly, capillary flow separation is seen to occur in three distinct regions.

At the first capillary minimum, flow separation is seen to occur over almost

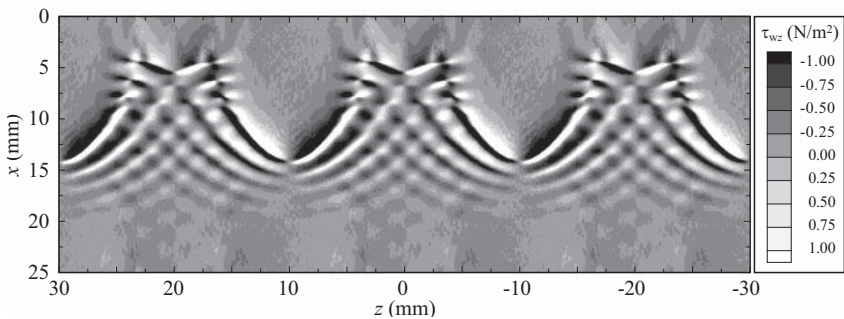
[†]These terms were previously introduced by Chang *et al.* (1994) and Liu *et al.* (1995) respectively to describe the interface topology of interacting 3-dimensional large waves.



(a) Film thickness



(b) Streamwise wall shear stress: $\tau_{wx} = \mu_1 \partial u / \partial y|_{y=0}$



(c) Spanwise wall shear stress: $\tau_{wz} = \mu_1 \partial w / \partial y|_{y=0}$

Figure 5.48: Contours of film thickness as well as streamwise and spanwise wall shear stress for the 3-dimensional film (case 11).

the entire spanwise wavelength. Thereby, in front of the intermediate hump, the streamwise wall shear stress attains the largest positive values, indicating strong backflow, as is expected from the large interface distortion (i.e. change in interface curvature) there. In front of the large wave humps, the region of capillary flow separation (associated with negative values of τ_{wx}) is shaped in the form of a horseshoe (in accordance with the shape of capillary wave fronts). This region extends in principle to the capillary wave region of the intermediate hump but is interrupted by a stretch without flow reversal. In addition to the first capillary minimum, flow separation also takes place at the second and third capillary minima. However, this is the case only in the region preceding the intermediate hump, owing to the larger interface distortion there.

A more detailed look at capillary flow separation in the regions identified in subfigure 5.48(b) is provided by figures 5.49 and 5.50. These depict liquid phase velocity components in the region of the first and second capillary minimum. More precisely, subfigures 5.49(a) to 5.50(d) display the velocity field within planes parallel to the x-y-plane at different spanwise positions between the symmetry planes of the intermediate ($z=0$) and main wave ($z=-10$ mm) hump respectively. Thereby, subfigures 5.49(a) to 5.49(d) resolve the capillary wave region of the intermediate hump in spanwise direction, while subfigures 5.50(a) to 5.50(d) do the same for that of the main wave hump. Since subfigures 5.49(a) ($z=0$) and 5.50(d) ($z=-10$ mm) correspond to planes of symmetry, the spanwise velocity component there vanishes and streamlines were chosen to represent the velocity field. Conversely, in subfigures 5.49(b) to 5.50(c), the spanwise velocity component is illustrated with contours, while the streamwise and crosswise components are represented with the help of vectors. Thereby the displayed vectors result from a projection of the 3-dimensional velocity vector field into the respective planes.

In accordance with the distribution of τ_{wx} depicted in subfigure 5.48(b), subfigure 5.49(a) shows the occurrence of two open CSE's (associated with the first and second capillary minimum respectively) in front of the intermediate hump at $z=0$. With increasing spanwise distance, the second CSE is seen to disappear at $z=-1.42857$ mm (see subfigure 5.49(b)) before re-appearing

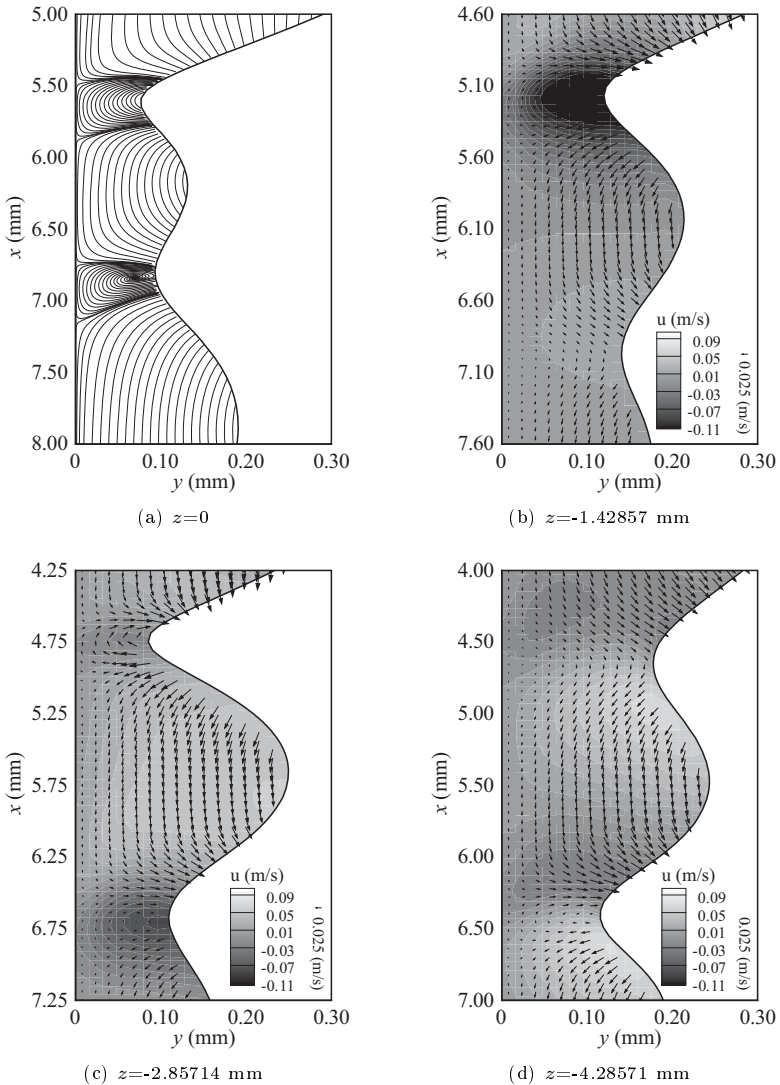


Figure 5.49: Streamlines and velocity vectors (projected into x-y planes) near the first two capillary minima projected into x-y planes at different z-positions for case 11.

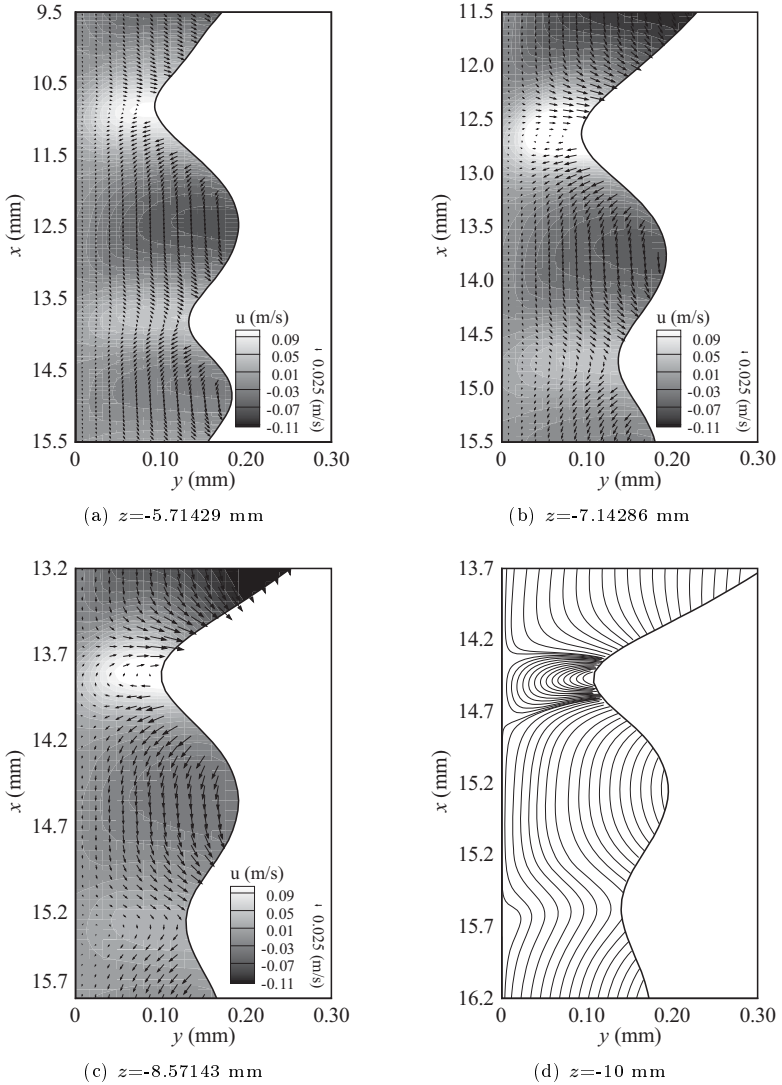


Figure 5.50: Streamlines and velocity vectors (projected into x - y planes) near the first two capillary minima at different z -positions for case 11.

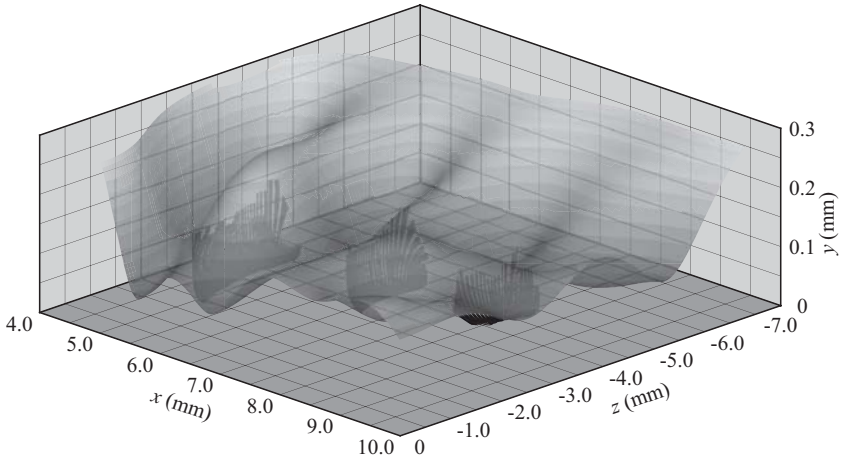
at $z=-2.85714$ mm and $z=-4.28571$ mm (see subfigures 5.49(c) and 5.49(d)). From contours of the spanwise velocity component it is evident that the CSE is associated with strong spanwise flow at $z=-1.42857$ mm (see subfigure 5.49(b)). This is in accordance with the orientation of the capillary wave front there, which is not horizontal, in contrast to the other spanwise positions, as can be deduced from subfigure 5.48(a). The occurrence of strong spanwise flow within the CSE suggests a corkscrew-type flow in this region[†].

Subfigures 5.50(b) to 5.50(d) show the occurrence of only a single CSE at the first capillary minimum, preceding the main wave hump. This CSE is maintained over a spanwise interval ranging from $z=-10$ mm to $z=-7.14286$ mm. At $z=-5.71429$ mm (see subfigure 5.50(a)) no flow separation takes place, since this position lies within the stretch of positive streamwise wall shear stress previously identified in subfigure 5.48(b).

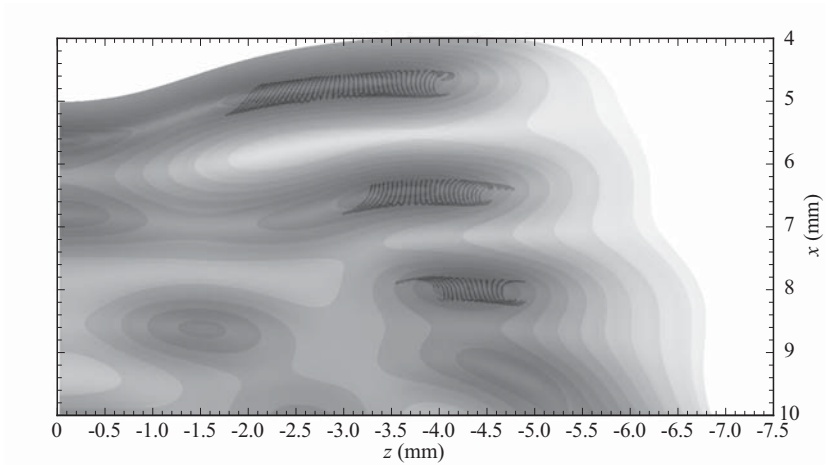
In order to gain a topological insight into the 3-dimensional capillary flow separation occurring in the considered water film, figures 5.51 and 5.52 depict liquid phase streamlines evaluated for the different regions highlighted in subfigure 5.48(b). Therein, 3-dimensional CSE's are shown to take the form of vortex tubes, the axes of which are shaped like the corresponding capillary wave fronts. Moreover, the vortex tube associated with the second capillary minimum preceding the intermediate hump exhibits corkscrew-shaped streamlines as previously inferred with respect to subfigure 5.49(b). It should be mentioned here that those parts of streamlines depicted in figures 5.51 and 5.52, lying in the gaseous phase were blanked in order to highlight liquid phase conditions. The full streamlines do indeed form closed vortex tubes.

A distinctly 3-dimensional capillary feature of the flow is exhibited by the region of capillary interference shown in figure 5.47 and subfigure 5.48(a). Indeed, considering the governing mechanism of capillary flow separation established in section 5.2, it can be inferred that the spanwise modulation of film thickness associated with the checkerboard pattern there causes spanwise flow. Moreover, since the spanwise component of gravitational acceleration is non

[†]Oliver & Atherinos (1968) and Portalski (1964*a*) conjectured (and in the latter case refuted) the existence of such a flow in falling liquid films.

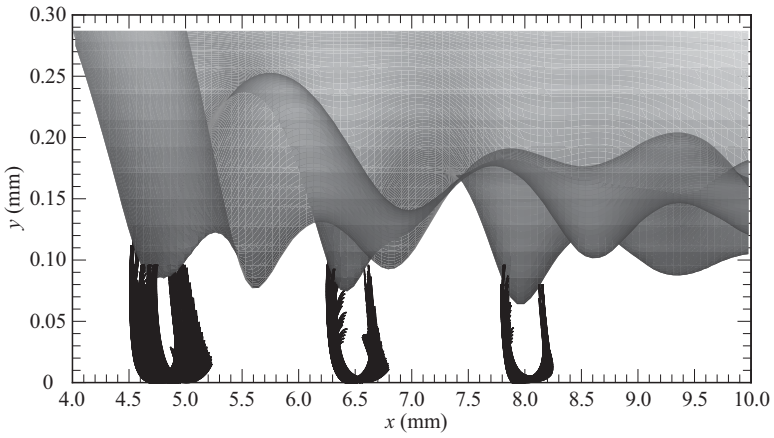


(a) Perspective view

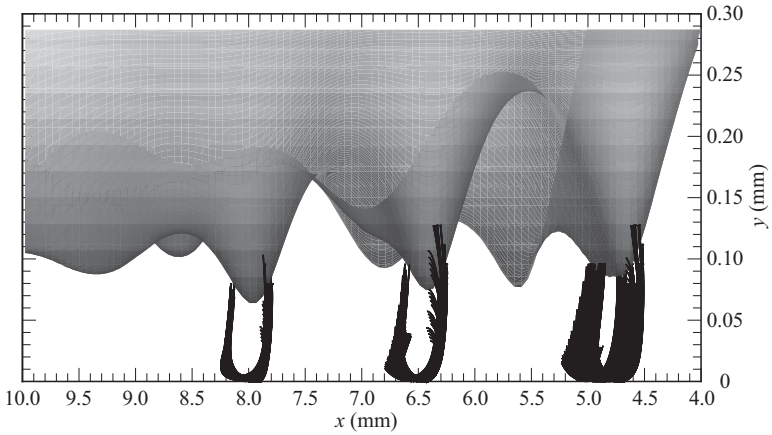


(b) Top view

Figure 5.51: Liquid phase streamlines in the capillary wave region of the 3-dimensional film (case 11): perspective and top view.



(a) inner side view



(b) outer side view

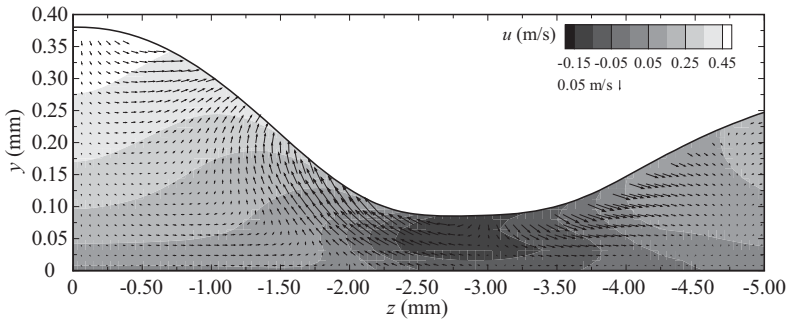
Figure 5.52: Liquid phase streamlines in the capillary wave region of the 3-dimensional film (case 11): inner and outer side views.

existent, it can be expected that this capillary-induced spanwise flow is relatively strong. This is confirmed by the distribution of the spanwise wall shear stress τ_{wz} depicted in subfigure 5.48(c), showing τ_{wz} to attain large magnitudes in the interference region. Further, the distribution of τ_{wz} clearly shows that the previously discussed interfacial checkerboard pattern is also imposed on the flow.

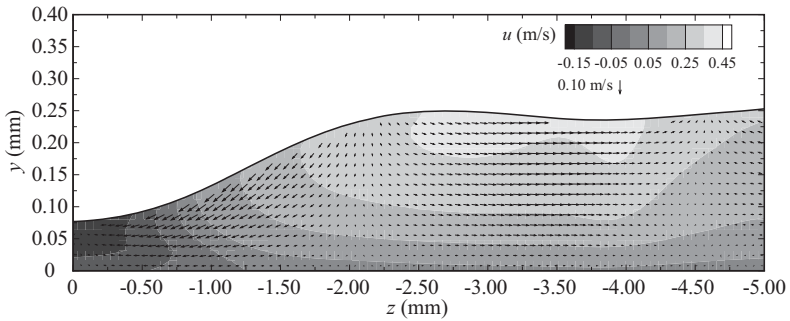
The occurrence of a checkerboard flow structure raises an interesting prospect from a transport perspective. Indeed, considering a fluid element traveling at a given spanwise position, the latter is subjected to spanwise flow of alternating direction as the region of capillary interference passes over its position. This causes the fluid element to move back and forth in spanwise direction causing strong lateral mixing. In addition, the fluid element is subjected to oscillating streamwise and crosswise velocity components, causing it to adopt a corkscrew-shaped pathline.

In order to investigate the spanwise flow caused by the checkerboard pattern in greater detail, figures 5.53 to 5.55 depict liquid phase velocity components within planes parallel to the y - z -plane at different streamwise positions. These positions were chosen such that the corresponding planes “cut through” subsequent capillary extrema. In these figures, the streamwise velocity component is represented with contours, while spanwise and crosswise velocity components are illustrated with projections of the 3-dimensional velocity vector field into the respective planes.

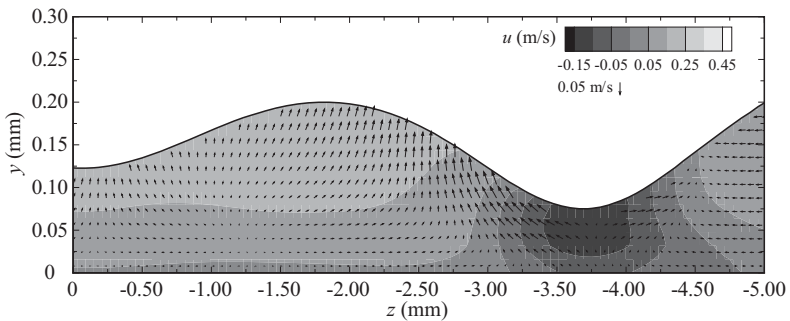
The most striking feature of the vector plots in subfigures 5.53(a) to 5.55(b) is the cellular flow pattern caused by the spanwise modulation of film thickness. This pattern is similar to that arising in a horizontal wavy liquid layer as depicted in figure 2.2 or in Marangoni convection. Therein, each capillary wave is associated with two open cells, resembling the open CSE in figures 5.49 and 5.50. These cells are associated with strong spanwise flow from the wave humps to the wave troughs. As the position of the latter alternates in spanwise direction, so does the direction of the spanwise flow. Indeed, considering the spanwise position $z=-2.75$ mm, a fluid element traveling in the residual layer is first subjected to spanwise flow in negative (see subfigure 5.55(b)) then positive



(a) $x=4.75$ mm



(b) $x=5.60$ mm



(c) $x=6.40$ mm

Figure 5.53: Velocity vectors (projected into z - y planes) at different x -positions in the region of capillary interference: case 11.

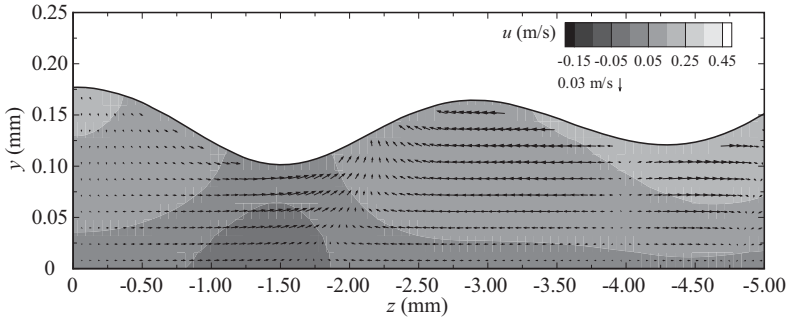
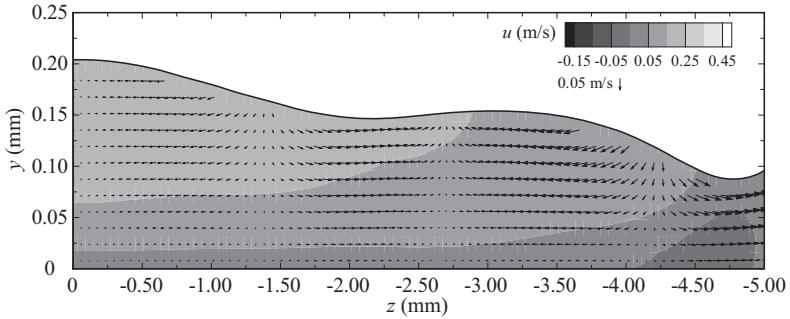
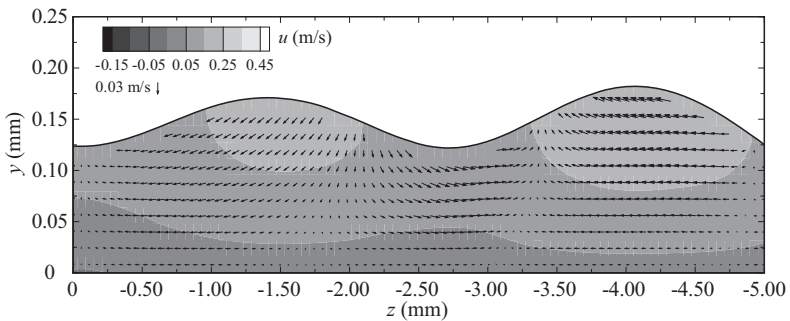
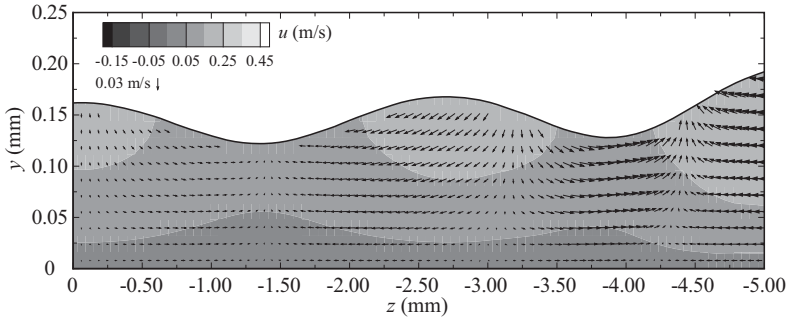
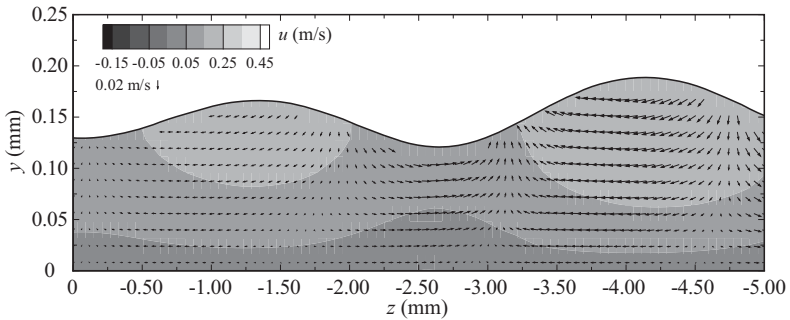
(a) $x=8.60$ mm(b) $x=9.35$ mm(c) $x=10.42$ mm

Figure 5.54: Velocity vectors (projected into z - y planes) at different x -positions in the region of capillary interference: case 11.



(a) $x=12.00$ mm



(b) $x=13.50$ mm

Figure 5.55: Velocity vectors (projected into z - y planes) at different x -positions in the region of capillary interference: case 11.

(see subfigure 5.55(a)) and again in negative (see subfigure 5.54(c)) z -direction before moving in positive y -direction (see subfigure 5.54(b)). Subsequently, as discernible in subfigures 5.54(a), 5.53(c), 5.53(b) and 5.53(a) respectively, the fluid element moves in positive z -direction, positive y -direction, negative z -direction, and finally in positive z -direction. Thereby, the strongest span-wise flow is encountered in the region of the first capillary wave preceding the intermediate hump, i.e. at $x=4.75$ mm (see subfigure 5.53(a)).

From a scalar transport perspective, the above discussed intense mixing, caused both by capillary flow separation and the spanwise cellular pattern in the region of capillary interference, is expected to drastically increase the local driving potential, leading to a significant wave-induced intensification of scalar transfer, which could explain the strong increase in transfer rates to 3-dimensional falling liquid films. Finally, the especially intense spanwise mixing in the capillary wave region preceding the intermediate hump could exert a stabilizing effect on thermo-capillary film rupture, since it would tend to homogenise the spanwise temperature distribution and thus reduce thermo-capillary forces driving film rupture.

6 Conclusion

In this thesis, a complete account of a hitherto unknown phenomenon taking place in falling liquid films has been provided. The phenomenon in question is that of flow separation in the capillary wave region, hence the designation *capillary flow separation*. At the onset of the work documented in this thesis lies the discovery of the phenomenon in 2-dimensional falling liquid films (see Dietze *et al.* (2008)). Subsequently, the kinematics of the phenomenon were elucidated as well as its governing dynamics. Further, the effect of capillary flow separation on liquid phase convective transport and wall-side heat transfer was demonstrated. Having established the fundamental transport processes characterising the phenomenon, the influence of two important control parameters, namely the Reynolds number and the wave frequency was elucidated. Finally, the kinematics of capillary flow separation as it occurs in falling liquid films with 3-dimensional wave dynamics were established for one example of such flows.

In the context of this thesis, numerical and experimental methods were employed to investigate the above listed aspects of capillary flow separation, exploiting their respective advantages. Laser Doppler Velocimetry (LDV) along with simultaneous film thickness measurements using a Confocal Chromatic Imaging (CCI) technique and Particle Image Velocimetry (PIV), respectively providing a temporal and field view of liquid phase velocity, were employed to investigate the kinematics of the phenomenon in its developed state, and for the validation of numerical data. These experiments were in large part conducted in a specifically designed optical test setup (see Dietze *et al.* (2009, 2010)). On the other hand, numerical simulations were performed to fill “gaps” inaccessible or difficultly accessible to experimental investigation, such as the

spatio-temporal evolution and governing dynamics of capillary flow separation, as well as its effect on liquid phase convective transport and wall-side heat transfer. Thereby, agreement between numerical and available experimental data (from LDV, CCI and PIV) was shown to be good overall.

The main conclusions of this thesis are as follows. During the spatio-temporal development of capillary waves preceding large wave humps in wavy falling liquid films, the flow in this region is decelerated at the respective capillary minima. Thereby, the strongest deceleration takes place at the first capillary minimum, which immediately precedes the large wave hump. As the amplitude of capillary waves grows (and their wavelength diminishes) the associated flow deceleration increases, leading to a change in sign of the near-wall second order crosswise derivative of the streamwise velocity profile from negative to positive. This in turn produces a near wall point of inflexion in the profile similar to classical boundary layer separation. Further growth of the capillary amplitude (and decrease of the capillary wavelength) then leads to the separation of the flow at the wall, producing a separation eddy. This *Capillary Separation Eddy* (CSE) causes upstream flow to detach from the wall and reattach further downstream, and is the cause for flow reversal or backflow in falling liquid films, which has been debated by a number of researchers over the years (see e.g. Kapitza (1948), Kapitza (1948), Massot *et al.* (1966), Demekhin *et al.* (1987), Adomeit *et al.* (2000) and Adomeit *et al.* (2000)). The crosswise dimension of the CSE grows with the capillary waves until the latter attain their developed state. Depending on the developed capillary wave topology, the fully developed CSE assumes one of two distinctly different forms. Either a closed form if its size is inferior to the local minimal film thickness or an open shape with streamlines ending at the liquid-gas interface if its size exceeds the residual layer. The latter scenario was previously established in principle by Rood (1994), who investigated vortex interactions with a liquid-gas interface and stated that in such cases vorticity is transported across the interface. Correspondingly, based on velocity field data from PIV measurements the vorticity transport within the CSE was investigated. These data revealed that the open CSE is characterized by the cross-diffusion of two vorticity fluxes of opposing sign, emanating from the re-

spective crosswise boundaries (i.e. the wall and the liquid-gas interface), which annihilate one another within the liquid phase. The source of these respective vorticity fluxes can be attributed to the established mechanisms of vorticity generation at fixed walls and liquid-gas interfaces, which are determined by the capillary flow separation's governing dynamics.

In terms of the liquid phase velocity field in the region of capillary flow separation, two further important conclusions were drawn from the respective numerical and experimental data. First, streamwise velocity profiles in the region of the CSE are characterized by a large number of degrees of freedom in terms of their crosswise variation, that cannot be captured by the simplest integral boundary layer models based on Shkadov's approach (see e.g. Shkadov (1967)), which assume parabolic profiles. Indeed, from the general kinematics of capillary flow separation it follows that the streamwise velocity profile should be at least of third order to allow for a near-wall point of inflexion. Second, simultaneous film thickness and velocity time traces (measured with the CCI technique and LDV respectively) revealed that streamwise velocity and film thickness are strongly correlated in the capillary wave region. Indeed, it was shown that each capillary film thickness extremum is associated with a corresponding local streamwise velocity extremum.

Regarding the governing dynamics of capillary flow separation, it was established that, similar to classical boundary layer separation, the phenomenon is caused by an adverse streamwise wall pressure derivative, occurring in the capillary wave region. However, in contrast to boundary layer separation, this adverse pressure derivative has an origin stemming from the multiphase nature of the film flow. Indeed, it is caused by tensile forces, gaining influence due to the interface distortion (i.e. change in interface curvature) in the capillary wave region. This leads to larger static pressure within capillary wave humps (exhibiting negative interface curvature) as compared to capillary wave troughs (displaying positive interface curvature), producing a pressure increase from trough to hump. The magnitude of the associated positive streamwise pressure derivative is thereby scaled by the amplitude and wavelength (inversely) of capillary waves, which determine the streamwise change in interface curvature.

Further, based on numerical data, it was shown that this magnitude is largest at the first capillary minimum, where it can exceed the streamwise gravitational force per unit volume, yielding a resulting upward external force acting on a fluid element, which is the prerequisite for flow separation. In this context it was established that this force must exceed a finite threshold in order for capillary flow separation to occur, which can be attributed to the stabilizing effect of viscous forces. Further, the fact that the resulting streamwise pressure force per unit volume (given by the streamwise pressure derivative) surmounts the streamwise gravitational force per unit volume serves to explain the generation of positive vorticity at the wall (in a right hand coordinate system) and negative vorticity at the interface, the latter production process having a baroclinic origin.

Regarding the effect of capillary flow separation on scalar transfer to falling liquid films, the following conclusions were drawn. In essence, the CSE causes crosswise convective transport, which in turn leads to mixing in the capillary wave region, increasing the local driving potential for scalar transfer. As a result, the corresponding transfer coefficient increases, which was demonstrated with the help of numerical simulations of wall-side heat transfer, confirming previous observations by Adomeit *et al.* (2000) and Kunugi & Kino (2005). Further, through the detailed analysis of the CSE induced crosswise convective transport, two interesting conclusions were obtained. First, it was established that the crosswise mixing length induced by the CSE is inferior to the size of the latter, which runs counter to intuition in terms of an Eulerian view of the phenomenon. However, due to the fact that fluid elements traveling in the residual layer are exposed to the CSE's kinematics for only a limited time during the passage of the capillary wave region over their position (the wave celerity being larger than the fluid velocity in the residual layer), a Lagrangian view is more adequate. Indeed, based on fluid element pathlines in the residual layer, calculated from numerical data, it was established that the latter are only temporarily disturbed into “loop”-shaped (if the fluid element travels above the CSE center) or “hook”-shaped (if the fluid element travels beneath the CSE center) structures as the CSE region passes by. Based on these data, a second

interesting conclusion with respect to crosswise convective transport intensification was drawn. Indeed, it was shown that the mixing length increases with wall distance owing to the fact that “faster” fluid elements traveling further from the wall are exposed to the CSE’s kinematics over a longer period. This in turn explains the much stronger intensification of interfacial scalar transfer as compared to wall-side scalar transfer, which has been observed in the literature (see e.g. Alekseenko *et al.* (1994)). Moreover, it was shown that the open CSE leads to much larger mixing lengths compared to the closed CSE, owing to the steeper separation streamlines in the open case. Finally, a mechanistic modelling of the mixing length (taking into account the above mentioned aspects) could prove useful in the formulation of effective (thermal) diffusivity models for falling liquid films (see e.g. Dietze *et al.* (2005, 2006)).

Based on the above mentioned kinematic, dynamic and transport related aspects of capillary flow separation, the influence of two important control parameters, namely the Reynolds number and the wave frequency, was investigated by way of numerical and experimental (LDV and PIV) parameter studies. The following conclusions can be drawn from the obtained results. The governing property scaling the capillary flow separation phenomenon is the separation of large waves, which increases with increasing Reynolds number and decreasing wave frequency. Thereby, an increase in wave separation is accompanied by an increase in capillary amplitude and decrease in capillary wavelength, which confirms results obtained by Tihon *et al.* (2006). Consequently the adverse streamwise wall pressure derivative in the capillary wave region increases in magnitude, leading to stronger flow separation and larger CSE’s respectively.

Finally, the properties of capillary flow separation as it occurs in falling liquid films with 3-dimensional wave dynamics were investigated based on a single numerical simulation of a 3-dimensional water film, yielding the following conclusions. In principle, the kinematics and dynamics of 3-dimensional CSE’s are similar to those in the 2-dimensional case. However, due to the spanwise extension of the 3-dimensional flow, these assume the shape of vortex tubes the axes of which follow the corresponding capillary wave fronts (more precisely they follow the position of the corresponding capillary minima). In the investigated

case, the latter are horseshoe shaped. A distinctly 3-dimensional aspect of capillary flow separation arises due to the interaction of the large horseshoe shaped wave fronts as well as their preceding capillary waves. Indeed, due to this interaction a large intermediate hump arises where large wave fronts intersect, which is preceded by several very large capillary waves, developing large tubular CSE's. Due to the non-horizontal nature of the large capillary waves these CSE's exhibit corkscrew shaped streamlines in some regions, causing spanwise convective transport. The large capillary waves preceding the intermediate hump are themselves preceded by a large region of capillary interference exhibiting a checkerboard or herringbone pattern of capillary wave humps and wave troughs. In this region, spanwise flow occurs due to the same governing mechanism causing capillary flow separation as a consequence of spanwise film thickness modulations. Due to the checkerboard pattern the direction of this flow alternates in streamwise progression causing fluid elements to assume corkscrew shaped pathlines. This feature along with the previously mentioned strong spanwise flow in the region of large capillary waves preceding the intermediate hump could explain the wave-induced intensification of scalar transfer to 3-dimensional falling liquid films. Finally, the strong mixing caused by this process along with the CSE's could explain the stabilisation of thermo-capillary "finger" structures in heated 3-dimensional falling liquid films.

References

- ABDOU, M. A. 1999 Exploring novel high power density concepts for attractive fusion systems. *Fusion Engineering and Design* **45**, 145–167.
- ADOMEIT, P., LEEFKEN, A. & RENZ, U. 2000 Experimental and numerical investigations on wavy films. In *Proceedings of the 3rd European thermal sciences conference* (ed. E. W. P. Hahne, W. Heidemann & K. Spindler), pp. 1003–1009. Heidelberg: ETS.
- ADOMEIT, P. & RENZ, U. 2000 Hydrodynamics of three-dimensional waves in laminar falling films. *International Journal of Multiphase Flow* **26**, 1183–1208.
- AL-SIBAI, F. 1998 Simultane Messung der Strömungs- und Oberflächenstruktur von Rieselfilmen mit zwei- und dreidimensionaler Welligkeit. Master's thesis, RWTH-Aachen University.
- AL-SIBAI, F., LEEFKEN, A., LEL, V. V. & RENZ, U. 2003 Measurement of transport phenomena in thin wavy films. In *2nd International Berlin Workshop-IBW2 on Transport Phenomena with Moving Boundaries* (ed. F.-P. Schindler), *Fortschritt-Berichte VDI*, vol. 3, pp. 1–15. Düsseldorf: VDI Verlag.
- AL-SIBAI, F., LEEFKEN, A. & RENZ, U. 2002 Local and instantaneous distribution of heat transfer rates through wavy films. *International Journal of Thermal Sciences* **41**, 658–663.
- ALBRECHT, H., E., BORYS, M., DAMASCHKE, N. & TROPEA, C. 2003 *Laser Doppler and Phase Doppler Measurement Techniques*. Berlin: Springer.
- ALEKSEENKO, S. V., ANTIPIN, V. A., BOBYLEV, A. V. & MARKOVICH, D. M. 2007 Application of PIV to velocity measurements in a liquid film flowing down an inclined cylinder. *Experiments in Fluids* **43** (2-3), 197–207.

References

- ALEKSEENKO, S. V., ANTIPIN, V. A., GUZANOV, V. V., KHARLAMOV, S. M. & MARKOVICH, D. M. 2005 Three-dimensional solitary waves on falling liquid film at low Reynolds numbers. *Physics of Fluids* **17** (121704), 1–4.
- ALEKSEENKO, S. V., NAKORYAKOV, V. E. & POKUSAEV, B. G. 1994 *Wave Flow of Liquid Films*. Begell House.
- ALEKSEENKO, S. V., NAKORYAKOV, V. E. & POKUSAEV, B. G. 1996 Wave effect on the transfer processes in liquid films. *Chemical Engineering Communications* **141–142**, 359–385.
- ALEKSEENKO, S. V., NAKORYAKOV, V. Y. & POKUSAEV, B. G. 1985 Wave formation on a vertical falling liquid film. *AIChE Journal* **31** (9), 1446–1460.
- ALEKSEENKO, S. V., NAKORYAKOV, V. Y., POKUSAEV, B. G. & KRISTOFOROV, V. V. 1973 Friction during downward film flow along a vertical wall. *Journal of Engineering Physics and Thermophysics* **24** (5), 584–588.
- ANSHUS, B. E. & GOREN, S. L. 1966 A method of getting approximate solutions to the Orr-Sommerfeld equation for flow on a vertical wall. *AIChE Journal* **12** (5), 1004–1008.
- BACH, P. & VILLADSEN, J. 1984 Simulation of the vertical flow of a thin, wavy film using a finite-element method. *Journal of Heat Transfer* **27** (6), 815–827.
- BALAKOTAIAH, V. & MUDUNURI, R. R. 2004 Balakotaiah and Mudunuri Reply. *Physical Review Letters* **93** (19), 199402–1.
- BALMFORTH, N. J. & MANDRE, S. 2004 Dynamics of roll waves. *Journal of Fluid Mechanics* **514**, 1–33.
- BANERJEE, S., RHODES, E. & SCOTT, D. S. 1967 Mass transfer to wavy falling liquid films at low Reynolds numbers. *Chemical Engineering Science* **22**, 43–48.
- BANERJEE, S., SCOTT, D. S. & RHODES, E. 1968 Mass transfer to falling wavy liquid films in turbulent flow. *Industrial & Engineering Chemistry Fundamentals* **7** (1), 22–27.
- BENNEY, D. J. 1966 Long waves on liquid films. *Journal of Mathematics and Physics* **45**, 150–155.

- BLYTH, M. G. & POZRIKIDIS, C. 2004 Effect of surfactant on the stability of film flow down an inclined plane. *Journal of Fluid Mechanics* **521**, 241–250.
- BONTOZOGLOU, V. 1998 A numerical study of interfacial transport to a gas-sheared wavy liquid. *International Journal of Heat and Mass Transfer* **41** (15), 2297–2305.
- BRACKBILL, J. U., KOTHE, D. B. & ZEMACH, C. 1992 A continuum method for modelling surface tension. *Journal of Computational Physics* **100**, 335–354.
- BRAUER, H. 1956 Strömung und Wärmeübergang bei Rieselfilmen. *VDI-Forschungsheft* **457** (22), 1–40.
- BRAUER, H. 1971 *Stoffaustausch einschließlich chemischer Reaktion*. Aarau: Verlag Sauerländer.
- BRAUNER, N. & MOALEM MARON, D. 1982 Characteristics of inclined thin films, waviness and the associated mass transfer. *International Journal of Heat and Mass Transfer* **25** (1), 99–110.
- BRAUNER, N. & MOALEM MARON, D. 1983 Modeling of wavy flow in inclined thin films. *Chemical Engineering Science* **38** (5), 775–788.
- BRAUNER, N. & MOALEM MARON, D. 1988 Turbulent withdrawal: Application to wavy flow modelling. *Chemical Engineering Journal* **37**, 1–10.
- BRAUNER, N., MOALEM MARON, D. & TOVEY, I. 1987 Characterization of the interfacial velocity in wavy thin films flow. *International Communications in Heat and Mass Transfer* **14**, 293–302.
- BROOKE BENJAMIN, T. 1957 Wave formation in laminar flow down an inclined plane. *Journal of Fluid Mechanics* **2**, 554–574.
- BROOKE BENJAMIN, T. 1961 The development of three-dimensional disturbances in an unstable film of liquid flowing down an inclined plane. *Journal of Fluid Mechanics* **10**, 401–419.
- BROTHERTON, F. 2002 Alcohol recovery in falling film evaporators. *Applied Thermal Engineering* **22**, 855–860.
- BUDWIG, R. 1994 Refractive index matching methods for liquid flow investigations. *Experiments in Fluids* **17**, 350–355.

References

- CERRO, R. L. & WHITAKER, S. 1971 Stability of falling liquid films. *Chemical Engineering Science* **26**, 742–745.
- CHAND, R. & ROSSON, H.F. 1965 Local heat flux to water film flowing down a vertical surface. *Industrial & Engineering Chemistry Fundamentals* **4** (3), 356–359.
- CHANG, H. C. 1986 Traveling waves on fluid interfaces: Normal form analysis of the Kuramoto-Sivashinsky equation. *Physics of Fluids* **29** (10), 3142–3147.
- CHANG, H. C. 1994 Wave evolution on a falling film. *Annual Review of Fluid Mechanics* **26**, 103–136.
- CHANG, H. C., CHENG, M., DEMEKHIN, E. A. & KOPELEVICH, D. I. 1994 Secondary and tertiary excitation of three-dimensional patterns on a falling film. *Journal of Fluid Mechanics* **270**, 251–275.
- CHANG, H. C. & DEMEKHIN, E. A. 2002 *Complex Wave Dynamics on thin Films. Studies in Interface Science* 14. Amsterdam: Elsevier.
- CHANG, H. C., DEMEKHIN, E. A. & KAL Aidin, E. 1996*a* Simulation of noise-driven wave dynamics on a falling film. *AIChE Journal* **42** (6), 1553–1568.
- CHANG, H. C., DEMEKHIN, E. A., KAL Aidin, E. & YE, Y. 1996*b* Coarsening dynamics of falling-film solitary waves. *Physical Review E* **54** (2), 1467–1477.
- CHANG, H. C., DEMEKHIN, E. A. & KOPELEVICH, D. I. 1993 Nonlinear evolution of waves on a vertically falling film. *Journal of Fluid Mechanics* **250**, 433–480.
- CHANG, H. C., DEMEKHIN, E. A. & SAPRIKIN, S. S. 2002 Noise-driven wave transitions on a vertically falling film. *Journal of Fluid Mechanics* **462**, 255–283.
- CHENG, M. & CHANG, H. C. 1995 Competition between subharmonic and sideband secondary instabilities on a falling film. *Physics of Fluids* **7** (1), 34–54.
- CHU, K. J. & DUKLER, A. E. 1974 Statistical characteristics of thin, wavy films: Part II. studies of the substrate and its wave structure. *AIChE Journal* **20** (4), 695–706.

- CLARK, W. W. 2002 Liquid film thickness measurement. *Multiphase Science and Technology* **14** (1), 1–74.
- COHEN-SABBAN, J., GAILLARD-GROLEAS, J. & CREPIN, P.-J. 2001 Quasi-confocal extended field surface sensing. In *Proceedings of SPIE* (ed. A. Duparre & B. Singh), *Optical Metrology Roadmap for the Semiconductor, Optical, and Data Storage Industries II*, vol. 4449, pp. 178–183.
- COOK, R. A. & CLARK, R. H. 1971 The experimental determination of velocity profiles in smooth falling liquid films. *Canadian Journal of Chemical Engineering* **49**, 412–416.
- CORNISH, V. 1934 *Ocean Waves and Kindred Geophysical Phenomena*. London: Cambridge University Press.
- DANKWERTS, P. V. 1951 Significance of liquid-film coefficients in gas absorption. *Industrial and Engineering Chemistry* **43** (6), 1460–1467.
- DATE, A. W. 2005 Solution of transport equations on unstructured meshes with cell-centered colocated variables. Part I: Discretization. *International Journal of Heat and Mass Transfer* **48**, 1117–1127.
- DEMEKHIN, E. A., DEMEKHIN, I. A. & SHKADOV, V. YA. 1983 Solitons in viscous films flowing down a vertical wall. *Fluid Dynamics* **18** (4), 500–507.
- DEMEKHIN, E. A., KAL Aidin, E. N., KALLIADASIS, S. & VLASKIN, S. YU. 2007 Three-dimensional localized coherent structures of surface turbulence. I. scenarios of two-dimensional-three-dimensional transition. *Physics of Fluids* **19** (114103), 1–15.
- DEMEKHIN, E. A., KAPLAN, M. A. & SHKADOV, V. YA. 1987 Mathematical models of the theory of viscous liquid films. *Fluid Dynamics* **22** (6), 885–893.
- DIETZE, G., LEL, V. V. & KNEER, R. 2005 Experimental investigation and modeling of wavy film flow. In *Proceedings of the 3rd International Berlin Workshop (IBW3) on Transport Phenomena with Moving Boundaries*, pp. 159–173.
- DIETZE, G., LEL, V. V. & KNEER, R. 2006 Modelling of heat transfer in stable wavy film flow based on effective thermal diffusivity. In *Proceedings of the 13th International Heat Transfer Conference*. Sydney.

References

- DIETZE, G. F., AL-SIBAI, F. & KNEER, R. 2009 Experimental study of flow separation in laminar falling liquid films. *Journal of Fluid Mechanics* **637**, 73–104.
- DIETZE, G. F., HORSKY, M., AL-SIBAI, F. & KNEER, R. 2010 Selected transport phenomena in falling liquid films. In *Proceedings of the 5th International Berlin Workshop (IBW5) on Transport Phenomena with Moving Boundaries*, p. in print.
- DIETZE, G. F., LEEFKEN, A. & KNEER, R. 2008 Investigation of the backflow phenomenon in falling liquid films. *Journal of Fluid Mechanics* **595**, 435–459.
- DRAZIN, P. G. & JOHNSON, R. S. 1989 *Solitons: an introduction*. Cambridge University Press.
- DRESSLER 1949 Mathematical solution of the problem of roll waves in inclined channel flows. *Communications on Pure and Applied Mathematics* **2**, 149–194.
- DUKLER, A. E. 1976 The role of waves in two phase flow: some new understandings. *Chemical Engineering Education* **11** (3), 108–117.
- DURST, F., MELLING, A. & WHITELAW, J. H. 1976 *Principles and Practice of Laser-Doppler Anemometry*. London: Academic Press.
- EMMERT, R. E. & PIGFORD, R. L. 1954 A study of gas absorption in falling liquid films. *Chemical Engineering Progress* **50** (2), 87–93.
- FAGHRI, A. & SEBAN, R. A. 1985 Heat transfer in wavy liquid films. *International Journal of Heat and Mass Transfer* **28** (2), 506–508.
- FISENKO, S. P., PETRUCHIK, A. I. & SOLODUKHIN, A. D. 2002 Evaporative cooling of water in a natural draft cooling tower. *International Journal of Heat and Mass Transfer* **45**, 4683–4694.
- FREEZE, B., SMOLENTSEV, S., MORLEY, N. & ABDU, M. 2003 Characterization of the effect of Froude number on surface waves and heat transfer in inclined turbulent open channel water flows. *International Journal of Heat and Mass Transfer* **46**, 3765–3775.
- FRENKEL, A. L. & INDIRESHKUMAR, K. 1996 *Mathematical modeling and simulation in hydrodynamic stability*, chap. Derivations and simulations of evolution equations of wavy film flows. Singapore: World Scientific.

-
- FRIEDMAN, S. J. & MILLER, C. O. 1941 Liquid films in the viscous flow region. *Industrial & Engineering Chemistry Fundamentals* **33** (7), 885–891.
- FRISK, D. P. & DAVIS, E. J. 1972 The enhancement of heat transfer by waves in stratified gas-liquid flow. *International Journal of Heat and Mass Transfer* **15**, 1537–1552.
- FULFORD, G. D. 1964 The flow of liquids in thin films. *Advances in Chemical Engineering* **5**, 151–263.
- GANCHEV, B. G. & TRISHIN, V. V. 1987 Fluctuation of wall temperature in film cooling. *Fluid Mechanics: Soviet Research* **16**, 17–23.
- GAO, D., MORLEY, N. B. & DHIR, V. 2003 Numerical simulation of wavy falling film flow using VOF method. *Journal of Computational Physics* **192**, 624–642.
- GERENDAS, M. & WITTIG, S. 2001 Experimental and numerical investigation on the evaporation of shear-driven multicomponent liquid wall films. *Journal of Engineering for Gas Turbines and Power* **123**, 580–588.
- GJEVIK, B. 1970 Occurrence of finite-amplitude surface waves on falling liquid films. *The Physics of Fluids* **13** (8), 1918–1925.
- GREEN, S. I. 1996 *Fluid Vortices*, chap. 1, p. 22. Dordrecht: Kluwer Academic Publishers.
- GRIMLEY, S. S. 1945 Liquid flow conditions in packed towers. *Chemical Engineering Research and Design* **23a**, 228–235.
- GROENVELD, P. 1970 Laminar withdrawal with appreciable inertial forces. *Chemical Engineering Science* **25**, 1267–1273.
- HENSTOCK, W. H. & HANRATTY, T. J. 1979 Gas absorption by a liquid layer flowing on the wall of a pipe. *AIChE Journal* **25** (1), 122–131.
- HIGBIE, R. 1935 The rate of absorption of a pure gas into a still liquid during short periods of exposure. *Transactions of the American Institute of Chemical Engineers* **31**, 365–389.
- HIRT, C. W. & NICHOLS, B. D. 1981 Volume of fluid (VOF) method for the dynamics of free boundaries. *Journal of Computational Physics* **39**, 201–225.

References

- HJEMFELT, A.T. & MOCKROS, L.F. 1966 Motion of discrete particles in a turbulent fluid. *Applied Scientific Research* **16**, 149.
- HO, F. C. K. & HUMMEL, R. L. 1970 Average velocity distributions within falling liquid films. *Chemical Engineering Science* **25**, 1225–1237.
- HO, L.-W. & PATERA, A. T. 1990 A legendre spectral element method for simulation of unsteady incompressible viscous free-surface flows. *Computer Methods in Applied Mechanics and Engineering* **80**, 355–366.
- HOLLENBECK, K. J. 1998 Invlap.m: a MATLAB function for numerical inversion of Laplace transforms by the de Hoog algorithm. Website, <http://cambridge.org/us/engineering/author/nellisandklein/downloads/invlap.m>.
- DE HOOG, F. R., KNIGHT, J. H. & STOKES, A. N. 1982 An improved method for numerical inversion of Laplace transforms. *SIAM Journal on Scientific and Statistical Computing* **3**, 357–366.
- IBRAHIM, G. A., NABHAN, B. W. & ANABTAWI, M. Z. 1995 An investigation into a falling film type cooling tower. *International Journal of Refrigeration* **18** (8), 557–564.
- IRIBARNE, A., GOSMAN, A. D. & BRIAN, D. B. 1967 A theoretical and experimental investigation of diffusion controlled electrolytic mass transfer between a falling liquid film and a wall. *International Journal of Heat and Mass Transfer* **10**, 1661–1676.
- ISHIGAI, S., NAKANISI, S., KOIZUMI, T. & OYABU, Z. 1972 Hydrodynamics and heat transfer of vertically falling liquid films. *Bulletin of the JSME* **15** (83), 594–601.
- ISSA, R. I. 1985 Solution of the implicitly discretised fluid flow equations by operator-splitting. *Journal of Computational Physics* **62**, 40–65.
- JAMET, D., TORRES, D. & BRACKBILL, J. U. 2002 On the theory and computation of surface tension: The elimination of parasitic currents through energy conservation in the second-gradient method. *Journal of Computational Physics* **182** (1), 262 – 276.
- JAYANTI, S. & HEWITT, G. F. 1997 Hydrodynamics and heat transfer of wavy thin film flow. *International Journal of Heat and Mass Transfer* **40** (1), 179–190.

-
- JEBSON, R. S. & CHEN, H. 1997 Performances of falling film evaporators on whole milk and a comparison with performance on skim milk. *Journal of Dairy Research* **64**, 57–67.
- JEPSEN, J. C., CROSSER, O. K. & PERRY, R. H. 1966 The effect of wave induced turbulence on the rate of absorption of gases in falling liquid films. *AIChE Journal* **12**, 186–192.
- JOO, S. W. & DAVIS, S. H. 1992 Instabilities of three-dimensional viscous falling films. *Journal of Fluid Mechanics* **242**, 529–547.
- KAMEI, S. & OISHI, J. 1956 Mass and heat transfer in a falling liquid film of wetted wall tower. *Memoirs of the Faculty of Engineering, Kyoto University* **17**, 277–289.
- KAPITZA, P. L. 1948 Wave flow of thin layer of viscous fluid (in Russian). *Zhurn. Eksper. Teor. Fiz.* **18** (1), 3–28.
- KAPITZA, P. L. & KAPITZA, S.P. 1949 Wave flow of thin layers of viscous fluid (in Russian). *Zhurn. Eksper. Teor. Fiz.* **19** (2), 105–120.
- KAPITZA, P. L. & KAPITZA, S. P. 1965 Wave flow on thin layers of a viscous fluid. In *Collected papers of P. L. Kapitza* (ed. D. Ter Haar), , vol. 2, pp. 662–709. Oxford: Pergamon Press.
- KAPLAN, W. 1991 *Advanced Calculus*, chap. 5.12, pp. 326–330. Reading, MA: Addison-Wesley.
- KARIMI, G. & KAWAJI, M. 1998 An experimental study of freely falling films in a vertical tube. *Chemical Engineering Science* **53** (20), 3501–3512.
- KAYS, W. M. 1966 *Convective Heat and Mass Transfer*. New York: McGraw-Hill, Inc.
- KHESHGI, H. S. & SCRIVEN, L. E. 1987 Disturbed film flow on a vertical plate. *Physics of Fluids* **30**, 990–997.
- KILLION, J. D. & GARIMELLA, S. 2004 Simulation of pendant droplets and falling films in horizontal tube absorbers. *Journal of Heat Transfer* **126**, 1003–1013.

References

- KLINE, S. J., REYNOLDS, W. C., SCHRAUB, F. A. & RUNSTADLER, P. W. 1967 The structure of turbulent boundary layers. *Journal of Fluid Mechanics* **30**, 741–773.
- KORTEWEG, D. J. & DE VRIES, G. 1895 On the change of form of long waves advancing in a rectangular channel, and on a new type of long stationary waves. *The London, Edinburgh and Dublin philosophical magazine and journal of science* **39**, 422–443.
- KREYSZIG, E. 1991 *Differential Geometry*. New York: Dover Publications.
- KUNUGI, T. & KINO, C. 2003 Numerical simulation of oscillatory falling liquid film flows. *Fusion Engineering and Design* **65**, 387–392.
- KUNUGI, T. & KINO, C. 2005 DNS of falling film structure and heat transfer via MARS method. *Computers & Structures* **83** (6-7), 455–462.
- KUNUGI, T., KINO, C. & SERIZAWA, A. 2005 Surface wave structure and heat transfer of vertical liquid film flow with artificial oscillation. In *5th International Symposium on Multiphase Flow, Heat Mass Transfer and Energy Conversion*. XiSan.
- KURAMOTO, Y. & TSUZUKI, T. 1974 Reductive perturbation approach to chemical instabilities. *Progress of Theoretical Physics* **52**, 1399–1401.
- KURAMOTO, Y. & TSUZUKI, T. 1976 Persistent propagation of concentration waves in dissipative media far from thermal equilibrium. *Progress of Theoretical Physics* **55** (2), 356–369.
- LAFaurIE, B., NARDONE, C., SCARDOVELLI, R., ZALESKI, S. & ZANETTI, G. 1994 Modelling merging and fragmentation in multiphase flows with SURFER. *Journal of Computational Physics* **113** (1), 134 – 147.
- LEEFKEN, A., AL-SIBAI, F. & RENZ, U. 2004 LDV measurement of the velocity distribution in periodic waves of laminar falling films. In *Proceedings of the 5th International Conference on Multiphase Flow*. Yokohama.
- LEEFKEN, A. & RENZ, U. 2001 Numerical analysis on hydrodynamics and heat transfer of laminar-wavy falling films. In *1st International Berlin Workshop-IBW1 on Transport Phenomena with Moving Boundaries* (ed. F.-P. Schindler), *Fortschritt-Berichte VDI*, vol. 3, pp. 134–143. Düsseldorf: VDI Verlag.

- LEL, V.V., AL-SIBAI, F., LEEFKEN, A. & RENZ, U. 2005 Local thickness and wave velocity measurement of wavy films with a chromatic confocal imaging method and a fluorescence intensity technique. *Experiments in Fluids* **39** (5), 856–864.
- LEL, V. V., LEEFKEN, A., AL-SIBAI, F. & RENZ, U. 2004 Extension of the chromatic confocal imaging method for local thickness measurements of wavy films. In *Proceedings of the 5th International Conference on Multiphase Flow*. Yokohama.
- LIMBERG, H. 1973 Wärmeübergang an turbulente und laminare Rieselfilme. *International Journal of Heat and Mass Transfer* **16**, 1691–1702.
- LIN, S. P. 1969 Finite-amplitude stability of a parallel flow with a free surface. *Journal of Fluid Mechanics* **36** (1), 113–126.
- LIN, S. P. 1974 Finite amplitude side-band stability of a viscous film. *Journal of Fluid Mechanics* **63**, 417–429.
- LIN, S. P. 1983 *Waves on Fluid Interfaces*, chap. Film Waves, pp. 261–289. New York: Academic Press.
- LIU, J. & GOLLUB, J. P. 1993 Onset of spatially chaotic waves on flowing films. *Physical Review Letters* **70** (15), 2289–2292.
- LIU, J. & GOLLUB, J. P. 1994 Solitary wave dynamics of film flows. *Physics of Fluids* **6** (5), 1702–1712.
- LIU, J., PAUL, J.D. & GOLLUB, J. P. 1993 Measurements of the primary instabilities of film flows. *Journal of Fluid Mechanics* **250**, 69–101.
- LIU, J., PAUL, J. D., BANILOWER, E. & GOLLUB, J. P. 1992 Film flow instabilities and spatiotemporal dynamics. In *Proceedings of the First Experimental Chaos Conference* (ed. S. Vohra, M. Spano, M. Schlesinger, L. M. Pecora & W. Ditto), pp. 225–239. World Scientific.
- LIU, J., SCHNEIDER, J.B. & GOLLUB, J. P. 1995 Three-dimensional instabilities of film flows. *Physics of Fluids* **7** (1), 55–67.
- LUFF, J. D., DROUILLARD, T., ROMPAGE, A. M., LINNE, M. A. & HERTZBERG, J. R. 1999 Experimental uncertainties associated with particle image velocimetry (PIV) based vorticity algorithms. *Experiments in Fluids* **26**, 36–54.

References

- LUNDGREN, T. & KOUMOUTSAKOS, P. 1999 On the generation of vorticity at a free surface. *Journal of Fluid Mechanics* **382**, 351–366.
- LÉVÊQUE, M. A. 1928 Les lois de la transmission de la chaleur par convection. *Annales des Mines de Belgique* **13** (201), 199–415.
- LYU, T. H. & MUDAWAR, I. 1991*a* Determination of wave-induced fluctuations of wall temperature and convection heat transfer coefficient in the heating of a turbulent falling liquid film. *International Journal of Heat and Mass Transfer* **34** (10), 2521–2534.
- LYU, T. H. & MUDAWAR, I. 1991*b* Statistical investigation of the relationship between interfacial waviness and sensible heat transfer to a falling liquid film. *International Journal of Heat and Mass Transfer* **34** (6), 1451–1464.
- MALAMATARIS, N. A. & BALAKOTAIAH, V. 2008 Flow structure underneath the large amplitude waves of a vertically falling film. *AIChE Journal* **54** (7), 1725–1740.
- MALAMATARIS, N. A. & BONTZOGLU, V. 1999 Computer aided analysis of viscous film flow along an inclined wavy wall. *Journal of Computational Physics* **154**, 372–392.
- MALAMATARIS, N. A., VLACHOGIANNIS, M. & BONTZOGLU, V. 2002 Solitary waves on inclined films: Flow structure and binary interactions. *Physics of Fluids* **14** (3), 1082–1094.
- MALAMATARIS, N. T. & PAPANASTASIOU, T. C. 1991 Unsteady free surface flows on truncated domains. *Industrial & Engineering Chemistry Research* **30**, 2211–2219.
- MASSOT, C., IRANI, F. & LIGHTFOOT, E. N. 1966 Modified description of wave motion in a falling film. *AIChE Journal* **12** (3), 445–455.
- MAZURKIEWICZ, J. & TOMASIK, P. 1990 Viscosity and dielectric properties of liquid binary mixtures. *Journal of Physical Organic Chemistry* **3**, 493–502.
- MEZA, C. E. & BALAKOTAIAH, V. 2008 Modeling and experimental studies of large amplitude waves on vertically falling films. *Chemical Engineering Science* **63**, 4704–4734.

-
- MILLER, T. F. & SCHMIDT, F. W. 1988 Use of a pressure-weighted interpolation method for the solution of the incompressible Navier-Stokes equations on a nonstaggered grid system. *Numerical Heat Transfer A* **14**, 213–233.
- MIYA, M., WOODMANEE, D. E. & HANRAFFY, T. J. 1971 A model for roll waves in gas-liquid flow. *Chemical Engineering Science* **26**, 1915–1931.
- MIYARA, A. 1999 Numerical analysis on flow dynamics and heat transfer of falling liquid films with interfacial waves. *Heat and Mass Transfer* **35**, 298–306.
- MIYARA, A. 2000 Numerical simulation of wavy liquid film flowing down on a vertical wall and an inclined wall. *International Journal of Thermal Sciences* **39**, 1015–1027.
- MIYARA, A. 2001 Flow dynamics and heat transfer of wavy condensate film. *Journal of Heat Transfer* **123**, 492–500.
- MOALEM MARON, D., BRAUNER, N. & HEWITT, G. F. 1989 Flow patterns in wavy thin films: numerical simulation. *International Communications in Heat and Mass Transfer* **16**, 655–666.
- MORAN, K., INUMARU, J. & KAWAJI, M. 2002 Instantaneous hydrodynamics of a laminar wavy liquid film. *International Journal of Multiphase Flow* **28**, 731–755.
- MORTON, B. R. 1984 The generation and decay of vorticity. *Geophysical & Astrophysical Fluid Dynamics* **28**, 277–308.
- MUDAWAR, I. & EL-MASRI, M. A. 1986 Momentum and heat transfer across freely-falling turbulent liquid films. *International Journal of Multiphase Flow* **12** (5), 771–790.
- MUDAWAR, I. & HOUPY, R. A. 1993*a* Mass and momentum transport in smooth falling liquid films laminarized at relatively high Reynolds numbers. *International Journal of Heat and Mass Transfer* **36** (14), 3437–3448.
- MUDAWAR, I. & HOUPY, R. A. 1993*b* Measurement of mass and momentum transport in wavy-laminar falling liquid films. *International Journal of Heat and Mass Transfer* **36** (17), 4151–4162.

References

- MUDUNURI, R. R. & BALAKOTAIAH, V. 2006 Solitary waves on thin falling films in the very low forcing frequency limit. *AIChE Journal* **52** (12), 3995–4003.
- NAKANISHI, K., KATO, N. & MARUYAMA, M. 1966 Excess and partial volumes of some alcohol-water and glycol-water solutions. *The Journal of Physical Chemistry* **71** (4), 814–818.
- NAKAYA, C. 1975 Long waves on a thin fluid layer flowing down an inclined plane. *Physics of Fluids* **18** (11), 1407–1412.
- NAKORYAKOV, V. E., POKUSAIEV, B. G. & ALEKSEENKO, S. V. 1976 Stationary two-dimensional rolling waves on a vertical film of fluid. *Journal of Engineering Physics and Thermophysics* **30** (5), 517–521.
- NAKORYAKOV, V. E., POKUSAIEV, B. G. & ALEKSEENKO, S. V. 1982 Desorption of poorly soluble gas from falling wavy liquid films. *Fluid Mechanics: Soviet Research* **11** (5), 116–130.
- NAKORYAKOV, V. E., POKUSAIEV, B. G., ALEKSEENKO, S. V. & ORLOV, V. V. 1977 Instantaneous velocity profile in a wavy fluid film. *Journal of Engineering Physics and Thermophysics* **33** (3), 1012–1016.
- NGUYEN, L. T. & BALAKOTAIAH, V. 2000 Modeling and experimental studies of wave evolution on free falling viscous films. *Physics of Fluids* **12** (9), 2236–2256.
- NOH, W. F. & WOODWARD, P. 1976 SLIC (simple line interface calculation). In *Proceedings of the fifth International Conference on Fluid Dynamics* (ed. A. I. van de Vooren & P. J. Zandbergen), *Lecture Notes in Physics*, vol. 59, pp. 330–340. Berlin: Springer.
- NOSOKO, P., YOSHIMURA, P. N., NAGATA, T. & OYAKAWA, K. 1996 Characteristics of two-dimensional waves on a falling liquid film. *Chemical Engineering Science* **51** (5), 725–732.
- NOSOKO, T. & MIYARA, A. 2004 The evolution and subsequent dynamics of waves on a vertically falling liquid film. *Physics of Fluids* **16** (4), 1118–1126.
- NOSOKO, T., MIYARA, A. & NAGATA, T. 2002 Characteristics of falling film flow on completely wetted horizontal tubes and the associated gas absorption. *International Journal of Heat and Mass Transfer* **45**, 2729–2738.

-
- NUSSELT, W. 1916 Die Oberflächenkondensation des Wasserdampfes. *VDI-Zeitschrift* **60**, 541–546.
- NUSSELT, W. 1923 Der Wärmeaustausch am Berieselungskühler. *VDI-Zeitschrift* **67**, 206–210.
- O'BRIEN, E. E. 1967 On the flux of heat through laminar wavy liquid layers. *Journal of Fluid Mechanics* **28**, 295–303.
- OLIVER, D. R. & ATHERINOS, T. E. 1968 Mass transfer to liquid films on an inclined plane. *Chemical Engineering Science* **23**, 525–536.
- OOSHIDA, T. 1999 Surface equation of falling film flows with moderate Reynolds number and large but finite Weber number. *Physics of Fluids* **11**, 3247–3269.
- PANGA, M. K.R. & BALAKOTAIAH, V. 2003 Low-dimensional models for vertically falling viscous films. *Physical Review Letters* **90** (15).
- PANGA, M. K. R., MUDUNURI, R. R. & BALAKOTAIAH, V. 2005 Long-wavelength equation for vertically falling films. *Physical Review E* **71**.
- PAPANASTASIOU, T. C., MALAMATARIS, N. & ELLWOOD, K. 1992 A new outflow boundary condition. *International Journal of Numerical Methods in Fluids* **14**, 587–608.
- PARAS, S. V. & KARABELAS, A. J. 1992 Measurements of local velocities inside thin liquid films in horizontal two phase flow. *Experiments in Fluids* **13**, 190–198.
- PARK, C. D. & NOSOKO, T. 2003 Three-dimensional wave dynamics on a falling film and associated mass transfer. *AIChE Journal* **49** (11), 2715–2727.
- PATANKAR, S. V. 1980 *Numerical Heat Transfer and Fluid Flow*. Taylor & Francis.
- PEREIRA, A. & KALLIADASIS, S. 2008 Dynamics of a falling film with solutal Marangoni effect. *Physical Review E* **78** (036312), 1–19.
- PETVIASHVILI, V. I. & TSVELODUB, D. Y. 1978 Horseshoe-shaped solitons on a flowing viscous film of fluid. *Soviet Physics Doklady* **23**, 117.

References

- PIERSON, F. W. & WHITAKER, S. 1977 Some theoretical and experimental observations of the wave structure of falling liquid films. *Industrial & Engineering Chemistry Fundamentals* **16** (4), 401–408.
- PORTALSKI, S. 1964a Eddy formation in film flow down a vertical plate. *Industrial & Engineering Chemistry Fundamentals* **3** (1), 49–53.
- PORTALSKI, S. 1964b Velocities in film flow of liquids on vertical plates. *Chemical Engineering Science* **19**, 575–582.
- PORTALSKI, S. & CLEGG, A. J. 1971 Interfacial area increase in rippled film flow in wetted wall columns. *Chemical Engineering Science* **26**, 773–784.
- POZRIKIDIS, C. 1988 The flow of a liquid film along a periodic wall. *Journal of Fluid Mechanics* **188**, 275–300.
- PRANDTL, L. 1938 Zur Berechnung der Grenzschichten. *Zeitschrift für angewandte Mathematik und Mechanik* **18**, 77–82.
- PRANDTL, L. 1961 Über Flüssigkeitsbewegung bei sehr kleiner Reibung. In *Gesammelte Abhandlungen zur angewandten Mechanik, Hydro- und Aerodynamik* (ed. W. Tolmien, H. Schlichting & H. Görtler), , vol. 2, chap. 4. Berlin: Springer-Verlag.
- PROKOPIOU, T., CHENG, M. & CHANG, H.-C. 1991 Long waves on inclined films at high Reynolds number. *Journal of Fluid Mechanics* **222**, 665–691.
- PROSPERETTI, A. 1981 Motion of two superposed viscous fluids. *Physics of Fluids* **24** (7), 1217–1223.
- PROSPERETTI, A. & TRYGGVASON, G., ed. 2007 *Computational Methods for Multiphase Flow*. Cambridge University Press.
- PUCKETT, E. G., ALMGREN, A. S., BELL, J. B., MARCUS, D. L. & RIDER, W. J. 1997 A high-order projection method for tracking fluid interfaces in variable density incompressible flows. *Journal of Computational Physics* **130**, 269–282.
- PUMIR, A., MANNEVILLE, P. & POMEAU, Y. 1983 On solitary waves running down an inclined plane. *Journal of Fluid Mechanics* **135**, 27–50.
- RAFFEL, M., WILLERT, C., WERELEY, S. & KOMPENHANS, J. 2007 *Particle Image Velocimetry: A Practical Guide*, 2nd edn. Berlin: Springer-Verlag.

-
- RAMASWAMY, B., CHIPPADE, S. & JOO, S. W. 1996 A full-scale numerical study of interfacial instabilities in thin-film flows. *Journal of Fluid Mechanics* **325**, 163–194.
- RASTATURIN, A., DEMEKHIN, E. & KALAJDIN, E. 2006 Optimal regimes of heat-mass transfer in a falling film. *Journal of Non-Equilibrium Thermodynamics* **31**, 1–10.
- RENARDY, Y. & RENARDY, M. 2002 PROST: A parabolic reconstruction of surface tension for the Volume-of-Fluid method. *Journal of Computational Physics* **183** (2), 400 – 421.
- RHIE, C. M. & CHOW, W. L. 1983 Numerical study of the turbulent flow past an airfoil with trailing edge separation. *AIAA Journal* **21** (11), 1525–1532.
- ROBERTS, R. M. & CHANG, H.-C. 2000 Wave-enhanced interfacial transfer. *Chemical Engineering Science* **55**, 1127–1141.
- ROOD, E. P. 1994 Interpreting vortex interactions with a free surface. *Journal of Fluids Engineering* **116**, 91–94.
- RUSCHE, H. 2002 Computational fluid dynamics of dispersed two-phase flows at high phase fractions. PhD thesis, Imperial College, University of London.
- RUYER-QUIL, C. 1999 Dynamique d'un film mince s'écoulant le long d'un plan incliné. PhD thesis, Ecole polytechnique.
- RUYER-QUIL, C. & MANNEVILLE, P. 1998 Modeling film flows down inclined planes. *European Physical Journal B* **6** (2), 277–292.
- RUYER-QUIL, C. & MANNEVILLE, P. 2000 Improved modeling of flows down inclined planes. *The European Physical Journal B* **15** (2), 357–369.
- RUYER-QUIL, C. & MANNEVILLE, P. 2002 Further accuracy and convergence results on the modeling of flows down inclined planes by weighted-residual approximations. *Physics of Fluids* **14** (1), 170–183.
- RUYER-QUIL, C. & MANNEVILLE, P. 2004 Comment on "Low-dimensional models for vertically falling viscous films". *Physical Review Letters* **39** (19), 199401–1.

References

- RUYER-QUIL, C. & MANNEVILLE, P. 2005 Thermocapillary long waves in a liquid film flow. Part 1. Low-dimensional formulation. *Journal of Fluid Mechanics* **538**, 199–222.
- SALAMON, T. R., ARMSTRONG, R. C. & BROWN, R. A. 1994 Traveling waves on vertical films: Numerical analysis using the finite element method. *Physics of Fluids* **6**, 2202–2220.
- SARMA, P. K., VIJAYALAKSHMI, B., MAYINGER, F. & KAKAC, S. 1998 Turbulent film condensation on a horizontal tube with external flow of pure vapors. *International Journal of Heat and Mass Transfer* **41** (3), 537–545.
- SCARDOVELLI, R. & ZALESKI, S. 1999 Direct numerical simulation of free-surface and interfacial flow. *Annual Review of Fluid Mechanics* **31**, 567–603.
- SCHAGEN, A. & MODIGELL, M. 2005 Luminescence technique for the measurement of local concentration distribution in thin liquid films. *Experiments in Fluids* **38** (2), 174–184.
- SCHAGEN, A., MODIGELL, M., DIETZE, G. & KNEER, R. 2006 Simultaneous measurement of local film thickness and temperature distribution in wavy liquid films using a luminescence technique. *International Journal of Heat and Mass Transfer* **49** (25–26), 5049–5061.
- SCHEID, B., RUYER-QUIL, C., KALLIADASIS, S., VELARDE, M. G. & ZEYTOUNIAN, R. KH. 2005 Thermocapillary long waves in a liquid film flow. Part 2. Linear stability and nonlinear waves. *Journal of Fluid Mechanics* **538**, 223–244.
- SCHEID, B., RUYER-QUIL, C. & MANNEVILLE, P. 2006 Wave patterns in film flows: modelling and three-dimensional waves. *Journal of Fluid Mechanics* **562**, 183–222.
- SCHLICHTING, H. 1951 *Grenzschicht-Theorie*. Karlsruhe: Verlag G. Braun.
- SEBAN, R. A. & FAGHRI, A. 1978 Wave effects on the transport to falling laminar liquid films. *Journal of Heat Transfer* **100**, 143–147.
- SEMENA, M. G. & MEL'NICHUK, G. A. 1978 Mean-velocity distributions in a falling film. *Fluid Mechanics-Soviet Research* **7** (5), 145–150.

- SHKADOV, V. YA. 1967 Wave flow regimes of a thin layer of viscous fluid subject to gravity. *Fluid Dynamics* **2** (1), 29–34.
- SIVASHINSKY, G. I. & MICHELSON, D. M. 1980 On irregular wavy flow of a liquid film down a vertical plane. *Progress of Theoretical Physics* **63** (6), 2112–2114.
- SLATTERY, J. C. 1990 *Interfacial Transport Phenomena*. New York: Springer-Verlag.
- SQUIRE, H. B. 1933 On the stability for three-dimensional disturbances of viscous fluid flow between parallel walls. In *Proceedings of the Royal Society of London. Series A, Containing Papers of a Mathematical and Physical Character.*, , vol. 142, pp. 621–628.
- STAINTHORP, F. P. & WILD, G. J. 1967 Film flow—the simultaneous measurement of wave amplitude and the local mean concentration of a transferable component. *Chemical Engineering Science* **22**, 701–704.
- STIRBA, C. & HURT, D. M. 1955 Turbulence in falling liquid films. *AIChE Journal* **1** (2), 178–184.
- STUHLTRÄGER, E., MIYARA, A. & UEHARA, H. 1995 Flow dynamics and heat transfer of a condensate film on a vertical wall-II. Flow dynamics and heat transfer. *International Journal of Heat and Mass Transfer* **38** (15), 2715–2722.
- STUHLTRÄGER, E., NARIDOMI, Y., MIYARA, A. & UEHARA, H. 1993 Flow dynamics and heat transfer of a condensate film on a vertical wall-I. Numerical analysis and flow dynamics. *International Journal of Heat and Mass Transfer* **36** (6), 1677–1686.
- SYCHEV, V. V. 1998 *Asymptotic Theory of Separated Flows*. Cambridge University Press.
- TAILBY, S. R. & PORTALSKI, S. 1962 The determination of the wavelength on a vertical film of liquid flowing down a hydrodynamically smooth plate. *Chemical Engineering Research and Design* **40**, 114–122.
- TAKASE, K., YOSHIDA, H., OSE, Y., KANO, T., SATAKE, S. & KUNUGI, T. 2003 Large-scale numerical simulations of multiphase flow behavior in an advanced light-water reactor core. *Tech. Rep.*. Annual Report of the Earth Simulator Center.

- TIHON, J. 2003 Hydrodynamics of the solitary waves travelling down a liquid film. In *2nd International Berlin Workshop-IBW2 on Transport Phenomena with Moving Boundaries* (ed. F.-P. Schindler), *Fortschritt-Berichte VDI*, vol. 3, pp. 260–269. Düsseldorf: VDI Verlag.
- TIHON, J., SERIFI, K., ARGYRIADI, K. & BONTOZOGLOU, V. 2006 Solitary waves on inclined films: their characteristics and the effects on wall shear stress. *Experiments in Fluids* **41**, 79–89.
- TIHON, J., TOVCHIGRECHKO, V., SOBOLIK, V. & WEIN, O. 2003 Electrodiffusion detection of the near-wall flow reversal in liquid films at the regime of solitary waves. *Journal of Applied Electrochemistry* **33**, 577–587.
- TREVELYAN, P. M. J., SCHEID, B., RUYER-QUIL, C. & KALLIADASIS, S. 2007 Heated falling films. *Journal of Fluid Mechanics* **592**, 295–334.
- TRIFONOV, Y. Y. 1990 Bifurcations of two-dimensional into three-dimensional wave regimes for a vertically flowing liquid film. *Fluid Dynamics* **25** (5), 741–745.
- TRIFONOV, Y. Y. 2008 Wavy film flow down a vertical plate: Comparisons between the results of integral approaches and full-scale computations. *Journal of Engineering Thermophysics* **17** (1), 30–52.
- TRIFONOV, Y. Y. & TSVELODUB, O. Y. 1991 Nonlinear waves on the surface of a falling liquid film. Part 1. Waves of the first family and their stability. *Journal of Fluid Mechanics* **229**, 531–554.
- TSVELODUB, O. Y. & TRIFONOV, Y. Y. 1992 Nonlinear waves on the surface of a falling liquid film. Part 2. Bifurcations of the first-family waves and other types of nonlinear waves. *Journal of Fluid Mechanics* **244**, 149–169.
- UCHE, J., ARTAL, J. & SERRA, L. 2002 Comparison of heat transfer coefficient correlations for thermal desalination units. *Desalination* **152**, 195–200.
- UEDA, T. & TANAKA, H. 1975 Measurement of velocity, temperature and velocity fluctuation distribution in falling liquid films. *International Journal of Multiphase Flow* **15**, 261–272.
- VALLURI, P., MATAR, O. K., HEWITT, G. F. & MENDES, M. A. 2005 Thin film flow over structured packings at moderate Reynolds numbers. *Chemical Engineering Science* **60**, 1965–1975.

-
- VILLADSEN, J. & MICHELSON, M. L. 1978 *Solution of differential equation models by polynomial approximation*. New Jersey: Prentice-Hall.
- VÁZQUEZ, G., ALVAREZ, E. & NAVAZA, J. M. 1995 Surface tension of alcohol + water from 20 to 50 °C. *Journal of Chemical & Engineering Data* **40**, 611–614.
- WASDEN, F. K. & DUKLER, A. E. 1989*a* Insights into the hydrodynamics of free falling wavy films. *AIChE Journal* **35** (2), 187–195.
- WASDEN, F. K. & DUKLER, A. E. 1989*b* Numerical investigation of large wave interactions on free falling films. *International Journal of Multiphase Flow* **15** (3), 357–370.
- WASDEN, F. K. & DUKLER, A. E. 1990 A numerical study of mass transfer in free falling wavy films. *AIChE Journal* **36** (9), 1379–1390.
- WESTERWEEL, J. 1994 Efficient detection of spurious vectors in particle image velocimetry data. *Experiments in Fluids* **16**, 236–247.
- WHITHAM, G. B. 1974 *Linear and Nonlinear Waves*. New York: John Wiley & Sons.
- WIERSCHEM, A. & AKSEL, N. 2004 Influence of inertia on eddies created in films creeping over strongly undulated substrates. *Experiments in Fluids* **16** (12), 4566–4574.
- WIERSCHEM, A., SCHOLLE, M. & AKSEL, N. 2002 Comparison of different theoretical approaches to experiments on film flow down an inclined wavy channel. *Experiments in Fluids* **33**, 429–442.
- WIERSCHEM, A., SCHOLLE, M. & AKSEL, N. 2003 Vortices in film flow over strongly undulated bottom profiles at low Reynolds numbers. *Experiments in Fluids* **15** (2), 426–435.
- WILKE, W. 1962 Wärmeübergang an Rieselfilme. *VDI-Forschungsheft* **490** (28), 1–36.
- WILKES, J. O. & NEDDERMAN, R. M. 1962 The measurement of velocities in thin films of liquid. *Chemical Engineering Science* **17**, 177–187.

References

- WOLFF, L. M. & HANRATTY, T. J. 1994 Instantaneous concentration profiles of oxygen accompanying absorption in a stratified flow. *Experiments in Fluids* **16**, 385–392.
- WU, J.-Z. 1995 A theory of three-dimensional interfacial vorticity dynamics. *Physics of Fluids* **7** (10), 2375–2395.
- YIH, C. S. 1954 Stability of liquid flow down an inclined plane. In *Proceedings of the Second US National Congress of Applied Mechanics*, p. 623. ASME, University of Michigan, Ann Arbor, Michigan.
- YIH, C.-S. 1955 Stability of two-dimensional parallel flows for three-dimensional disturbances. *Quarterly of Applied Mathematics* **12**, 434–435.
- YIH, C. S. 1963 Stability of liquid flow down an inclined plane. *The Physics of Fluids* **6** (3), 321–334.
- YILMAZ, E. 2003 Sources and characteristics of oil consumption in a spark-ignition engine. PhD thesis, Massachusetts Institute of Technology.
- YOSHIMURA, P. N., NOSOKO, P. & NAGATA, T. 1996 Enhancement of mass transfer into a falling laminar liquid film by two-dimensional surface waves—some experimental observations and modeling. *Chemical Engineering Science* **51** (8), 1231–1240.
- YOUNGS, D. L. 1982 *Numerical Methods for Fluid Dynamics*, chap. Time-dependent multi-material flow with large fluid distortion, pp. 273–285. New York: Academic Press.
- YU, L.-Q., WASDEN, F. K., DUKLER, A. E. & BALAKOTAIAH, V. 1995 Non-linear evolution of waves on falling films at high Reynolds numbers. *Physics of Fluids* **7** (8), 1886–1902.

Index

- Aris-Taylor dispersion, 102
- asymptotic expansion, 34

- backflow, 65–67, 103
- Benney-type equation, 36
- Bernoulli equation, 140
- boundary layer equations, 33
- boundary layer separation, 247
- bulk liquid temperature, 84
- Burst Spectrum Analyzer, 207

- capillary flow separation, 5, 46, 47, 53, 83, 89, 96, 145, 227
- capillary maximum, 64
- capillary minimum, 64
- Capillary Separation Eddy, 150, 173, 231
- capillary waves, 4, 64
- cellular pattern, 65
- checkerboard instability, 30
- checkerboard pattern, 29, 301, 306, 309
- coarsening dynamics, 26
- colocated, 128
- Complementary Metal Oxide Semiconductor, 219
- complex wave celerity, 17
- Confocal Chromatic Imaging, 173, 195–197
- Continuum Surface Force method, 121

- convection-diffusion equation, 83
- coupling conditions, 7, 12
- critical Reynolds number, 21
- Cross Correlation Function, 221
- crosswise convective transport, 103

- diffusion coefficient, 90
- diffusional vorticity flux, 245
- discretization schemes, 124
- Donor-Acceptor method, 117
- Doppler burst, 207
- Dymethylsiloxane, 188

- Eulerian view, 271
- excited waves, 27

- Fast Fourier Transformation, 208
- film thinning effect, 101
- finite time blow up, 38
- Finite Volume method, 109
- flotsam, 116
- flow reversal, 65
- fully developed, 84, 91, 97

- heat transfer coefficient, 78
- herringbone pattern, 301
- hook-shaped pathline, 274
- horseshoe waves, 29, 301

- Immersed Boundary methods, 113
- inclination angle, 21

- inclined liquid film, 228
- inclined test setup, 173
- interface, 2
- interface curvature, 15
- interfacial cells, 116
- interrogation area, 221

- kinematic condition, 9
- Korteweg-de Vries equation, 39
- Kuramoto-Shivasinsky equation, 39

- Lagrangian view, 271
- Laser Doppler Velocimetry, 173, 195, 202
- Laser Induced Fluorescence, 30, 196, 202
- linear stability analysis, 17
- liquid-gas free surface, 2
- liquid-gas interface, 2
- long-wave approximation, 31
- long-wave equation, 34
- loop-shaped pathline, 69, 274

- mass transfer coefficient, 89
- mean liquid temperature, 84
- mixing length, 274
- momentum-weighted interpolation, 130
- moving frame vortex, 62, 103
- multiple-equation models, 40

- noise sustained, 27
- non-staggered, 128
- Nusselt number, 85

- optical test setup, 173
- Orr-Sommerfeld equation, 17, 183

- parasitic velocities, 153
- parasitic waves, 79
- Particle Image Velocimetry, 173, 195, 202
- Particle Tracking Velocimetry, 217
- passive scalar, 83
- periodic boundary condition, 109
- PISO algorithm, 131
- pressure correction equation, 134
- primary flow, 10
- primary instability, 25
- Péclet number, 93

- reference discretization, 150
- Refractive Index Matching, 175, 198
- residual layer, 4
- Rhie-Chow interpolation, 129
- rivulet flow, 63
- rolling wave, 57, 58

- scalar transfer, 84
- scalar transport, 83
- secondary instability, 26
- self-similar profile, 41, 50
- semi-parabolic profile, 41, 50
- Sherwood number, 90
- Shkadov's 2-equation model, 41
- sideband instability, 26
- silicone oil, 188
- single-fluid, 113
- solitary waves, 25
- soliton, 39
- spurious currents, 153
- streamwise pressure derivative, 75
- streamwise velocity profile, 48
- streamwise wall shear stress, 69, 73
- structured grid, 126
- subharmonic instability, 26
- surface coordinate system, 8
- surface renewal mechanism, 106

surfactant, 81, 82, 88
symmetric boundary condition, 128
synchronous instability, 30

thermal diffusivity, 90
thermally developed, 84, 87
transitional Reynolds number, 82
turbulent spots, 82

upwind, 117
user defined function, 141

vertically falling liquid film, 228
Volume of Fluid method, 113

wall shear stress, 69
wall-fixed coordinate system, 65
wave celerity, 19, 27
wave-fixed reference frame, 58
wavelength, 31

